Winter 2003

An Experimental Study of Flow Control Techniques on a Multi-Element Airfoil

Ira James Walker
Old Dominion University

AN EXPERIMENTAL STUDY OF FLOW CONTROL TECHNIQUES ON A MULTI-ELEMENT AIRFOIL

by

Ira James Walker
B.S.G. May 1974 Villanova University
M.S. May 1980 Old Dominion University

A Dissertation Submitted to the Faculty of
Old Dominion University in Partial Fulfillment of the
Requirement for the Degree of

DOCTOR OF PHILOSOPHY

AEROSPACE ENGINEERING

OLD DOMINION UNIVERSITY
December 2003

Approved by:

Colin P. Britcher (Director)

Drew Landman (Member)

Ponnampalam Balakumar (Member)

Halima Ali (Member)

Oktay Baysal (Member)

ABSTRACT

AN EXPERIMENTAL STUDY OF FLOW-CONTROL TECHNIQUES ON A MULTI-ELEMENT AIRFOIL

Ira James Walker
Old Dominion University, 2003
Director: Dr. Colin P. Britcher

The results of a wind tunnel experiment are reported, which investigated two different flow control techniques that demonstrated the potential of increasing the lift coefficient on a multi-element airfoil. The data also indicated that boundary-layer separation on the trailing-edge flap could be reduced significantly. Results of the investigation revealed that for some test conditions an increased amount of suction occurred on the upper surface of the main element where the flow was attached. One of the techniques that was tested in this investigation involved the use of a pair of piezoelectric devices attached to the model to provide oscillatory motion directly to the flow field of the airfoil. The other technique employed a loudspeaker, which was mounted on the wall of the test section to supply acoustic excitation to the surrounding flow field. During the primary portion of the test, the free stream velocity in the test section was 20 m/s and the model attitude was fixed at 19° angle of attack. The piezoelectric devices were operated at frequencies of 0, 80, 90, 100, and 120, 240, 260 and 320 Hz. The loudspeaker was operated at only two frequencies of 80 and 120 Hz. Velocity profiles were obtained using a TSI® hot-film sensor and anemometer. These velocity profiles were measured on the main element and on the trailing-edge flap. The data showed that increments in mean velocity profile were achieved on the separated

trailing-edge flap when the piezoelectric devices were driven at frequencies of 100 and 120 Hz at 19° angle of attack. When the model was tested at 15° angle of attack, the largest increase in lift was achieved when the devices were driven at 320 Hz. The largest increment in lift occurred when the flow field was acoustically excited at 80 Hz. Linear Stability Analysis was employed to predict the vortex passage frequency behind the slat.

This work is most especially dedicated to my precious wife, Lutricia, whose ever-present support, love, and patience throughout the duration of this project helped to make it all possible. I truly owe her an incalculable amount of gratitude for contributing greatly to my development as a person. A special note of thanks and appreciation is also extended to my two daughters, Tiffany and Danielle, for their encouragement. The author would also like to dedicate this work in memory of his parents, Edward and Mary Walker, who instilled in him from an early age an interest in learning new things.

ACKNOWLEDGEMENTS

The author wishes to sincerely thank Dr. Colin P. Britcher of Old Dominion University for his technical guidance and support while he ably served in the capacity of academic advisor. A debt of gratitude is also owed to the other professors who provided assistance in undertaking this research study. Specifically, thanks go to Dr. Drew Landman of Old Dominion University, who was not only the designer of the test article used in this study, but who also provided much help in the development of the LABVIEW computer software. Additionally, Dr. Ponnampalam Balakumar of NASA/LaRC was instrumental in the formulation of the algorithms that were used in the linear stability analysis. Both Dr. Oktay Baysal of Old Dominion University and Dr. Halima Ali of Hampton University provided very valuable input without which this document would be less complete. The author wishes to also acknowledge Mr. Thomas Galloway for his very valuable technical assistance with the electronic instrumentation that was used in this experiment. The Fabrication Division of the Aerodynamics Research Equipment Section located at NASA Largely Research Center fabricated the test model components. Finally, the author would be remiss if thanks were not extended to Dr. Carolyn B. Morgan of Hampton University for her unwavering support that helped to facilitate this effort.

TABLE OF CONTENTS

LIST OF TABLES

LIST OF FIGURES

Figure Page

Figure Page

Figure Page

NOMENCLATURE

A	Matrix Operator/ Boundary Layer Parameter
AOA	Angle of Attack
A_o	Pulsating Amplitude of Forcing Perturbation
a_{ij}	ith by jth element in Matrix A
B	Matrix Operator/Boundary Layer Parameter
b_{ij}	ith by jth element in Matrix B
C	Airfoil Chord Length
c	Vortex Passage Velocity (m/s)
C_D	Drag Coefficient
C_f	Skin Friction Coefficient
C_L	Lift Coefficient
C_{Lmax}	Maximum Lift Coefficient
C_p	Pressure Coefficient
D	Sensor Coefficient for First Order Term
E	Sensor Calibration Coefficient for Second Order Term
E_b	Anemometer Bridge Voltage
E_{st}	Standard Error of Estimation
F	Sensor Calibration Coefficient for Third Order Term
f_m	Peak Frequency of Unforced Mixing Layer
f_N	Vortex Natural Frequency (Hz)
f_o	Theoretical Most-Amplified Frequency
f_r	Most-Amplified Frequency of the Forced Mixing Layer

G	Sensor Calibration Coefficient for Fourth Order Term
G_F	Flap Gap
G_S	Slat Gap
H	Step Height
h_k	kth Step Size between Grid Nodes
K	Constant Term for Sensor Calibration
KE	Turbulent Kinetic Energy
l	Reference Length Based on Boundary-Layer Thickness (m)
M	Mode Number for Forcing Frequency
m	Fourier Harmonic Frequency
N	Number of Data Points
O_F	Flap Overhang
O_S	Slat Overhang
p_s	Static Pressure (Pa)
p_∞	Free-Stream Static Pressure (Pa)
q_∞	Free-Stream Dynamic Pressure (Pa)
Re	Reynolds Number Based on Stowed Chord length
R_H	Reynolds Number Based on Step Height
$R_{\delta e}$	Reynolds Number Based on Height of Boundary Layer
R_θ	Reynolds Number Based on Momentum Thickness
St	Strouhal Number
T_c	Calibration Temperature of Hot-Film Sensor (° C)
T_e	Experimental Tunnel Air Temperature (° C)

T_s	Operating Temperature of Hot-Film Sensor (° C)
t	Time (seconds)
$\frac{u'}{U_\infty}$	Turbulence Intensity in the Streamwise Direction
U_{edge}	Streamwise velocity at boundary layer edge
U_p	Velocity Predicted by Calibration Coefficients
U_∞	Free-stream Velocity (m/s)
u	Instantaneous Stream-wise Velocity (m/s)
u^+	Boundary Layer Normalized Velocity
V*	Normalized Mean Velocity (m/s)
V^*_{app}	Approximated Mean Velocity (m/s)
v*	Wall-Friction Velocity
V_t	Corrected Sensor Voltage
V_s	Uncorrected Sensor Voltage
v	Instantaneous Transverse Velocity (m/s)
v_k	Velocity at kth Node Point on Computational Grid
w	Instantaneous Lateral Velocity (m/s)
X	Longitudinal Position in Test Section Coordinate System
X/H	Longitudinal Distance Normalized by Step Height
X(m)	Complex Fourier Transform
$X_1(m)$	Real Component of Complex Fourier Transform
$X_2(m)$	Imaginary Component of Complex Fourier Transform
x_n	nth Real-Value Data Point for Spectral Analysis
x_R	Longitudinal Location of Boundary Layer Reattachment

Y	Vertical Position in Test Section Coordinate System
y^+	Boundary Layer Normalized Transverse Location
$\Delta Z/H$	Lateral Distance Normalized by Step Height
Z	Lateral Position in Test Section Coordinate System
Z^*	Normalized Transverse Distance from Model Surface
z_k	kth Node Point on Computational Grid
α	Normalized Wave Number in Free-Stream Direction
β	Normalized Wave Number in Transverse Direction
δ	Complex Wave Number
δ_i	Imaginary Component of Complex Wave Number
δ_r	Real Component of Complex Wave Number
δ_S	Slat Deflection Angle
δ_F	Flap Deflection Angle
δp	$p_s - p_\infty$
γ_p	Forward-Flow Time Fraction
κ	Boundary Layer Parameter
Π	Coles Wake Parameter
ν	Kinematic Viscosity (m^2/s)
μ	Dynamic Viscosity ($kg/(m \cdot s)$)
λ	Vortex Passage Wavelength (m)
ρ	Density of Air (kg/m^3)
θ	Momentum Thickness
ϕ	Phase Difference between Subharmonic and Fundamental

τ_{ij}	ith by jth Element in Shear Stress Matrix
τ_w	Wall Shear Stress
ψ	Finite Difference Solution to Euler-Maclaurin Formula
ω	Angular Frequency (rad/s)

CHAPTER 1

INTRODUCTION

A fundamental and perennial motivation underlying research in fluid mechanics, especially in the field of aerodynamics, is the investigation of techniques that can be used to improve the high-lift performance of aircraft. Much research has been done in the area of modifying the design lines of various aircraft components to augment the total lift, most notably, the wings and other lifting surfaces. Advancements in this area have been aided mainly through the efforts of both experimentalists using wind tunnels and researchers applying Computational Fluid Dynamics (CFD). Additionally, research has also proceeded along the path of employing various flow control techniques for the purpose of improving the high-lift characteristics of aircraft. It is important now to capitalize on this knowledge and to add to the existing database by exploring and devising new and improved techniques to control the flow field surrounding lifting surfaces. This will be done in an attempt to engender improved lift capability of aircraft in an efficient manner. The present experimental investigation documented herein attempts to do just that by employing flow control techniques to influence the flow field surrounding a standard, multi-element airfoil geometry at subsonic speeds.

1.1 Interest in High-Lift Systems

As mentioned in the introduction, the primary motivation behind the development of high-lift systems is to ensure that high aerodynamic lift at low aircraft speeds is maintained during the lift-off and landing phases of the flight. Of course high lift could

---

The model journal for this document is the AIAA Journal.

simply be achieved by adding area to the wing, but this has the obvious disadvantage of increasing the weight and possible complexity of the lifting system.

One option would be to employ conventional lift-augmenting devices such as leading-edge slats and trailing edge-flaps [Kermode, A.C., 1972]. Over the years, various configurations of slats and flaps have been devised to achieve high lift and yet, the challenge has always been to minimize their adverse effects on the other aircraft systems due to aerodynamic interference. It would be ideal, for example, if a system could be developed which provides the required increments in aerodynamic lift, but which also does not cause any significant negative impact on the remaining aircraft systems. The Fowler flap has been included for a long time in the state-of-the-art repertoire of devices to augment the lift by increasing both the camber and plan form area of the wing. However, because of the added mechanical complexity of this arrangement [McClean, J.D. et al., 1999], it would be advantageous if a simpler system could be devised which would provide comparable levels of aerodynamic lift. Other conventional high-lift devices include the Kreuger flap [Kermode, A. C., 1972], which is a relatively simple configuration that consists of a flap that is hinged at the wing leading edge. Additionally, there are slotted leading-edge and trailing-edge devices. Variations of these conventional concepts have been developed which feature either suction or blowing techniques or unsteady oscillatory devices [Talay, T., 1975]. The fundamental rationale behind such approaches is to augment aerodynamic lift by controlling boundary-layer separation. For example, with the suction or blowing technique [Talay, T., 1975] there is either an efflux of low-energy air from the wing surface or a discharge of high-energy air into the boundary layer. Another approach is to transfer high kinetic energy air into the boundary layer by using some type of actuator

that can oscillate. Although suction, blowing, and unsteady oscillation can be employed to increase lift, these methodologies can also be used to provide the added benefit of decreased aerodynamic drag. The reduction of pressure drag on lifting surfaces such as wings or turbine blades are only two examples where these techniques could be employed. Figure 1.1 [Schlichting, H., 1955] shows different arrangements for boundary-layer control. Figure 1.2 [Seifert, A., et al., 1998] shows a sketch of a wind tunnel model that was instrumented with piezoelectric devices that were mounted spanwise and flush-mounted on a two-dimensional airfoil. The data shown in the insert demonstrated the trend of the fluctuating velocity for various free-stream velocities. The excitation frequency was 170 Hz and the model was tested at various angles of attack.

Another application of these high-lift control devices would be for the enhanced effectiveness of tail assembly components, such as rudders, elevators and both vertical and horizontal stabilizers. Conceivably, high-lift control devices could also be used to augment the lateral control system of an aircraft for improved performance in roll and yaw. Although these are powerful techniques for achieving various improved aerodynamic characteristics for a wide range of applications, this dissertation focuses on the use of flow control techniques to control the performance on a multi-element airfoil for the purpose of improving the effectiveness of a high-lift configuration.

There are the inevitable disadvantages to various high-lift concepts, but trade-off studies would need to be conducted for each aircraft application, which includes an assessment of the impact on the other aircraft systems as well as the mission of the vehicle. For example, although oscillatory control can transport additional turbulent

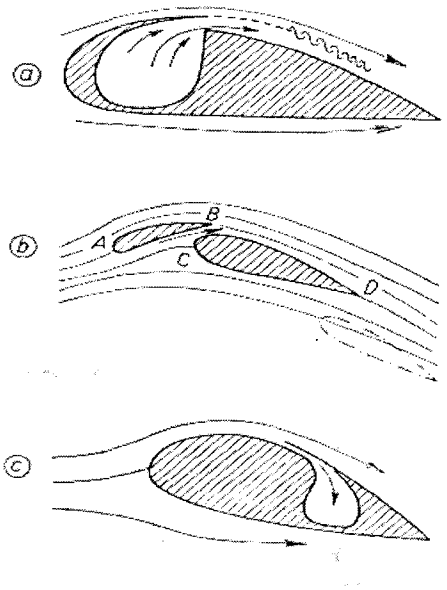

Figure 1.1 Different Arrangements for Boundary-Layer Control.
a) Discharge of Fluid, b) Slotted Wing, c) Suction

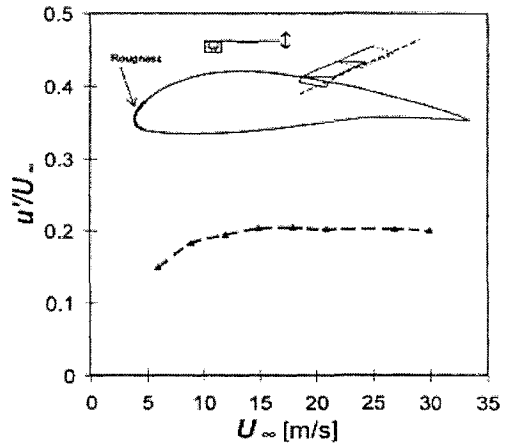

Figure 1.2 Excited Boundary-Layer Perturbation vs. Free-stream Velocity.

kinetic energy into an otherwise decelerating boundary layer to curtail separation, this technique also possibly increases the skin friction drag at the point where the device is installed. There is also an electrical power requirement that must be evaluated when examining the design of the entire aircraft. These powered control concepts definitely possess potential advantages and yet are still beset with challenging disadvantages. However, the aerodynamicist must not be daunted by these challenges but must continue to seek novel means to achieve high lift with minimal additions to weight and complexity and with minimal deleterious effects on drag.

1.2 Overview of the History of High-Lift Research

The area of high-lift aerodynamics has been the subject of a wealth of scientific inquiry. One of the more important reasons includes the need to meet safety requirements for take off and landing. With the high speeds attainable for modern commercial transports, the wing loading is normally high and, consequently, improved high-lift systems are required for low-speed operations, such as take off and landing. Another reason is the advantage of reduced angle-of-attack near minimum flying speeds, which would result in less drag as well as the delay of the stalled wing condition. With improved high lift systems, added savings of weight and cost are achieved because of a smaller wing plan form. Noise abatement would be an added environmental benefit because a lower engine thrust level would be needed to achieve the required amount of lift for takeoff.

Research in the development of high-lift devices came into prominence with the investigations performed by Prandtl [1904], who experimented with the idea of employing suction to remove portions of the boundary layer on a cylinder in a stream of flowing air. This procedure allowed the boundary layer to remain attached to the surface of the

cylinder, which not only reduced the size of the wake (hence less drag) but also generated an asymmetric flow field around the cylinder thereby increasing lift. In the 1920's, both Handley Page [1921] of England and G. V. Lachmann [1961] of Germany concurrently developed the concept of the slotted wing, which was able to achieve a C_{Lmax} that was markedly higher than that of the conventional wing at that time. Also during that time, some researchers [Harris, R. G., 1920] explored the use of variable-camber wings to improve lift performance. Throughout the early 20th century, researchers such as Klemin, Schrenk and Royer [Weyl, A. R., 1945] and Fowler [1931] focused on the design of flaps as a way to increment lift, which culminated in the development of the jet flap during the 1950s. These historical highlights emphasized the advantage of having an arrangement of more than one airfoil element to achieve greater lift. Additionally, research efforts in the area of either boundary-layer suction or blowing have demonstrated that boundary-layer control is a promising approach to improving the lifting capabilities of contemporary aircraft

In addition to flaps, innovations have been made in the design of leading edge devices to achieve high lift. Both Krueger flaps hinged at the wing leading edge and slats [Kermode, A. C., 1997] have been developed to keep the oncoming flow contoured to the wing to inhibit separation. Fixed and moveable slats have both been designed to achieve high lift. The fixed slats offer a less complicated design, whereas the movable slats have the advantage of allowing adjustments to be made for variations in flight conditions and they also exhibit less drag than the fixed slats at higher speeds.

The dynamics of vortex flow have been capitalized in the development of swept delta wings, which utilize the vortex system at the leading edge to induce an increased

velocity on the wing upper surface. This increased velocity translates into greater upper surface suction with sizable increments in lift coefficient.

The technology of vortex generators has been used to produce sizable increment in lift. The underlying principle is that the vortex generators increase the degree of turbulence in the boundary layer, which imparts enough energy to inhibit or delay separation. Klausmeyer [1997] has performed extensive research using this technology with favorable results.

More recently, some researchers [McLean, J. D. et al., 1999] have examined the feasibility of active control devices to reduce trailing edge separation. Their research has focused on improving high-lift systems, particularly for the High Speed Civil Transport (HSCT).

Theoretical approaches [Liebeck, R. H. and Ormsbee, A. I., 1970] have been devised to optimize the design of airfoils for the purpose of increasing aerodynamic lift. In one study [Stratford, B. S., 1959] a method was devised to ascertain the pressure distribution on the upper surface of an airfoil such that the boundary layer is on the verge of separating. To satisfy this criterion, the roof top region of the pressure distribution must be as long as possible and the pressure recovery should be gradual. This idealized pressure distribution was then used to design a wing with a contour that produces that distribution. This process is termed the "inverse problem" and in this application this strategy was used to design a wing that produces an increment in aerodynamic lift.

Progress has also been achieved in the area of Computational Fluid Dynamics research. However, several major stumbling blocks to obtaining accurate predictions remain, most notably in the area of turbulence modeling and the modeling of a separated

boundary layer. Another problem is determining the appropriate grid scheme for handling multiple components for a multi-element airfoil.

Various methods have been devised to obtain accurate solutions including, inviscid approaches, viscous/inviscid interaction approaches or methods using Navier-Stokes equations. In one study, a inviscid code was developed called VSAERO [Maskew, B., 1982], which used the panel method. In another study [Drela, M.] the code MSES was developed, which is categorized as a viscous/inviscid method using the Euler Equation. An entropy- conserved equation was used in place of the usual stream-wise momentum equation. The use of the Navier-Stokes equations is an appealing method since it seems to be a more natural approach to handling the intricate flow physics associated with multi-element airfoils. Some codes have been developed, which featured both structured [Vatsa, V. N., et al., 1994] and unstructured grids [Johnson, L. J., and Stolcis, L., 1993] as well as both multi-block patched [Schuster, D. M. and Birckelbaw, L. D., 1985] and chimera [Jasper, D., et al., 1993] schemes.

1.3 Flow Control Issues Related to High-Lift Aerodynamics

Flow control can be applied to achieve a variety of objectives. This dissertation is primarily concerned with flow control as it pertains to the enhancement of high lift for aircraft, specifically at subsonic speeds. Researchers have discovered that physical mechanisms associated with the dynamics of vortices have favorable consequences when it comes to the generation of high lift. Experiments have been conducted which have studied how vortex interactions in the shear layer of a separated boundary layer can contribute to the enhanced spreading rate of the shear layer. The research results have shown that this phenomenon promotes boundary layer reattachment. Previous researchers [Bhattacharjee,

S. et al., 1986] observed that the process of "vortex pairing" increases the shear-layer-spreading rate. This phenomenon associated with vortices can be described as the amalgamation of neighboring vortex lumps into larger ones. Figure 1.3 shows the flow visualization of vortex pairing [Winant, C. D., and Browand, F. K., 1974]. Notice how the eddies coalesce and their frequency decreases with downstream location.

Through this mechanism, the influence of vortex structures in terms of momentum and kinetic energy is diffused in a transverse direction. This dissertation describes how this turbulent kinetic energy can be diffused to the boundary layer of a wing to either increase lift or delay separation. Their research [Bhattacharjee, S. et al., 1986] has shown that this process can be controlled through the use of an acoustical energy source tuned at selected frequencies. Specifically, a sound source was mounted on the ceiling of a wind tunnel and directed acoustical energy onto a subsonic flow field of an aft-facing step. A drawing of their experimental setup is depicted in Figure 1.4. Hot-film measurements were made using single-sensor wires for multiple probe measurements and a cross-wire and pitot-static probe for single probe measurements. The hot-wire anemometers were used to obtain power spectra, time-history, and cross-correlation data.

Power spectra were obtained as a function of Strouhal number based on step height. Figures 1.5 through 1.7 show the effect of externally forcing the passage of vortices.

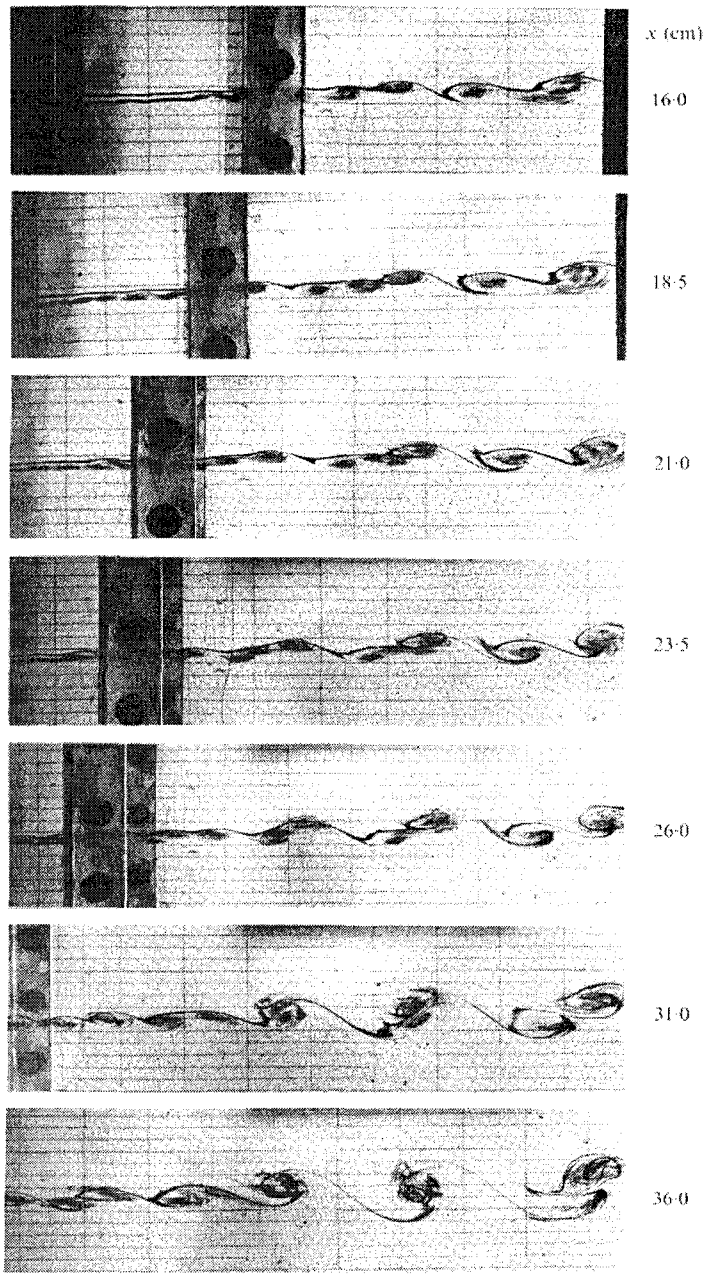

Figure 1.3 Flow Visualization of Vortex Pairing.
Copyright © 1974 J. Fluid Mech. – Reprinted with permission

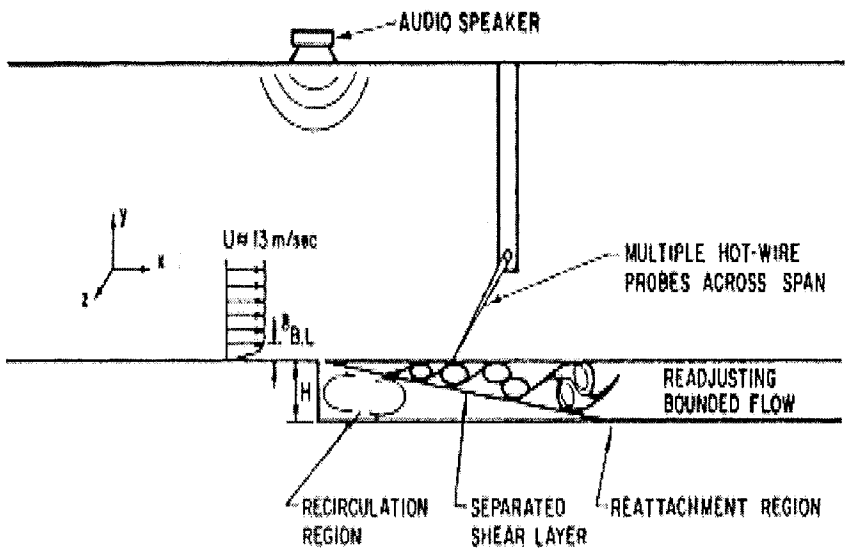

Figure 1.4 – Experimental Setup Using Loudspeaker to Force Reattachment.

Figure 1.5 shows the power spectrum for the natural case; note a broad peak at around a Strouhal number of 0.4. Bhattacharjee [1986] and his associates have noted that this broad peak is associated with the large-scale vortex passage frequency, also known as the natural frequency. Figures 1.6 and 1.7 show the power spectra for forcing at Strouhal numbers 0.2 and 1.2, respectively. The data show that forcing at a harmonic of the natural frequency has little effect on the power spectrum. However, forcing at a subharmonic creates a spike in the power spectrum, which indicates that the power spectrum has undergone a significant change. The spike in the power spectrum was an indication that the energy was enhanced in the naturally occurring frequency component of the flow when the acoustic signal was tuned to this subharmonic. This marked change in the power spectrum coincided with the occurrence of coherent vortex merging and the accelerated spreading rate of the

shear layer. Furthermore, the results demonstrated that forcing at a frequency equal to the vortex passage frequency tended to inhibit the vortex-merging process. Their investigation showed that the advantage of accelerating the spreading rate was to shift forward the location where boundary-layer reattachment occurred. The researchers theorized that the effect of the forcing upon the merging process would reveal itself through examination of the spanwise correlation of hot-wire measurements. The assumption is that, with increased merger or coupling of spanwise vortices, the cross correlation should increase. When the spanwise vortices are more three-dimensional the cross-correlation is expected to be low. It is this coupling which forces the vortices to act uniformly and to unite their collective energies to bring about an increased spreading rate of the shear layer. This assumption was verified by zero-time-delay cross-correlation data obtained from an array of hot-wire probes. The results for the natural and forced cases are shown in Figure 1.8, which presents the cross-correlation data versus spanwise separation at a particular Reynolds number based on step height.

Figure 1.9 shows the effect of normalized downstream location on the cross-correlation coefficient. Finally, Figure 1.10 shows the profiles of turbulent kinetic energy in the shear layer. The data show that a higher level of turbulent kinetic energy is transported closer to the floor surface under the condition of forced excitation. Thus, the data demonstrated that if properly controlled, vortices could be used as a mechanism to transport turbulent kinetic energy to delay or inhibit separation. The experiment described herein attempted to capitalize on the dynamics of vortices found naturally on multi-element airfoils to suppress boundary-layer separation, particularly on the trailing-edge flap.

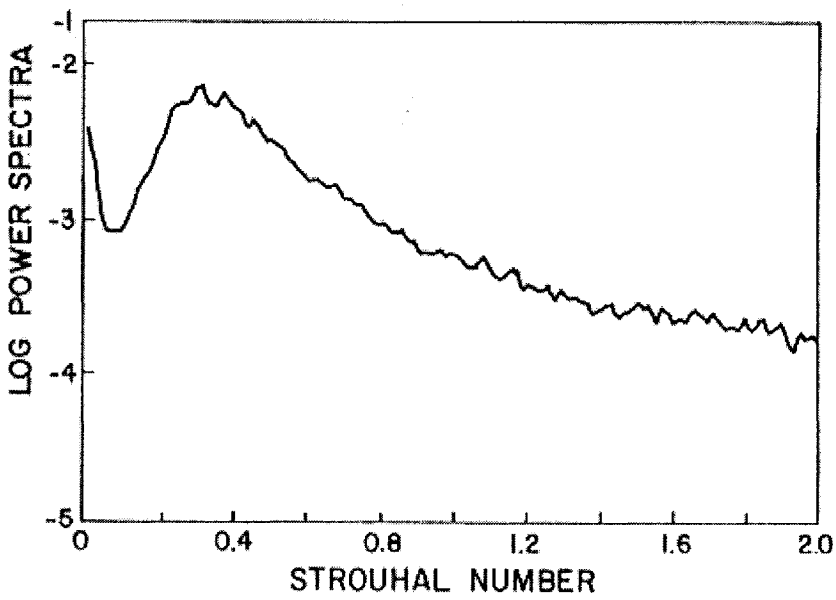

Figure 1.5 – Power Spectrum for Natural Case Behind Step.

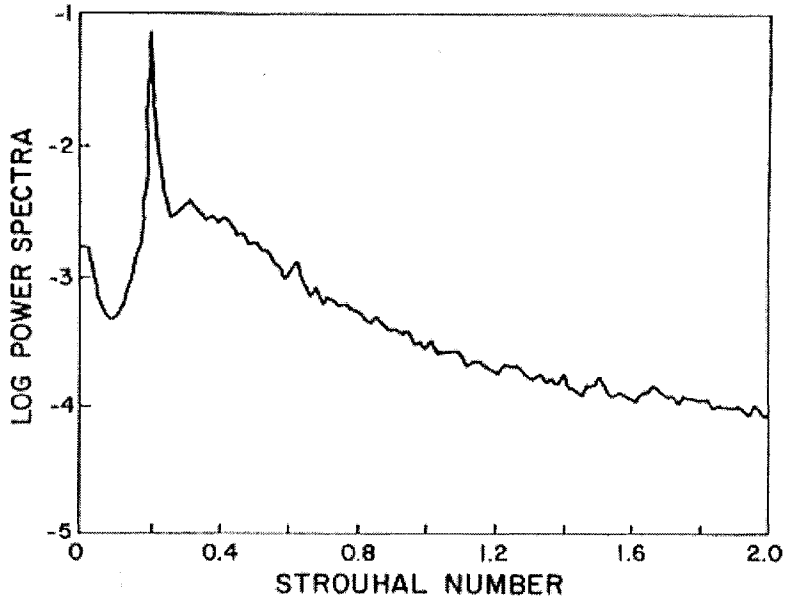

Figure 1.6 - Power Spectrum Behind Step with Forcing at St=0.2.

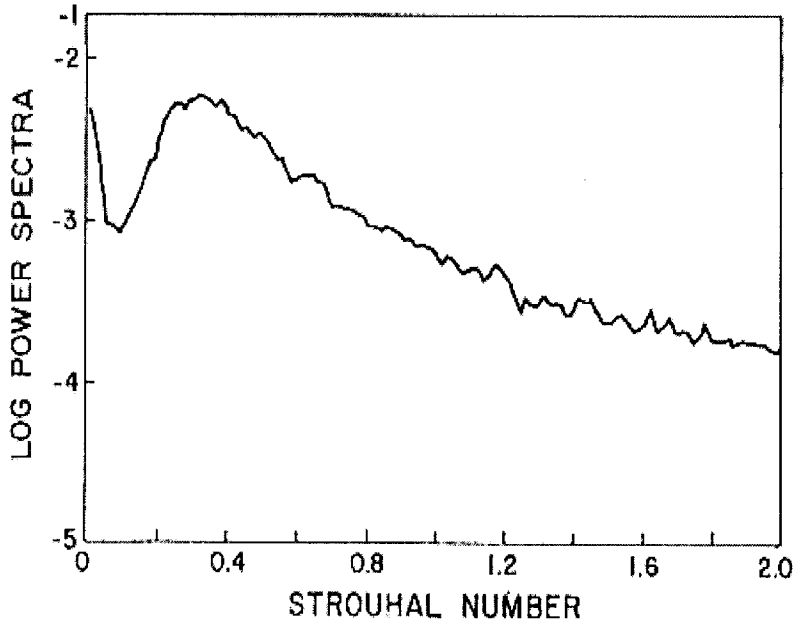

Figure 1.7 - Power Spectrum Behind Step with Forcing at St=1.2.

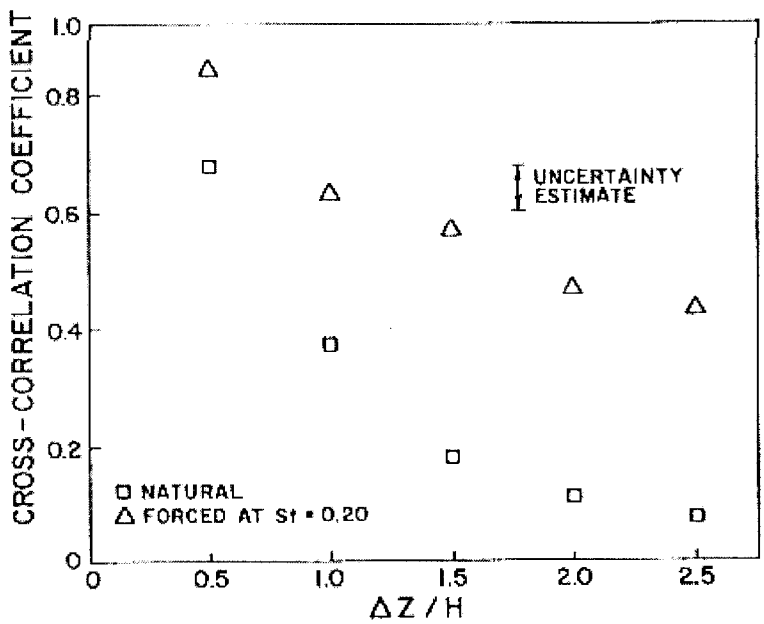

Figure 1.8 - Cross-Correlation Coefficient versus Spanwise Displacement; X/H = 4, R_H = 32,500.

The same mechanism can be used to increase the suction on the upper surface of the main wing. These results supported the findings of an investigation by Ahuja [1983], who also showed that separated flow could be modified using an acoustic source. Studies conducted by Troutt, [1984] Brown and Roshko [1974], and Browand and Troutt [1980] have all confirmed through experimental evidence that there is a positive correlation between the formations of large-scale vortex structures in the shear layer and the tendency for boundary layer reattachment. Other researchers have examined other modalities of flow field excitation to affect mixing of the shear layer. Oster and Wygnanski [1982] used the mechanical oscillation of a flap on the trailing edge of a splitter plate to modify the degree of mixing

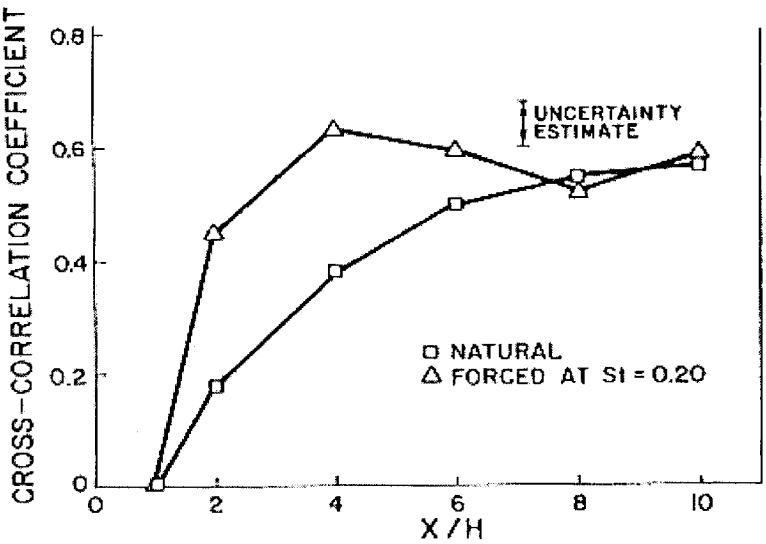

Figure 1.9 – Cross-Correlation Coefficient versus Streamwise Direction; $\Delta Z/H=1.0$, $R_H = 32{,}500$.

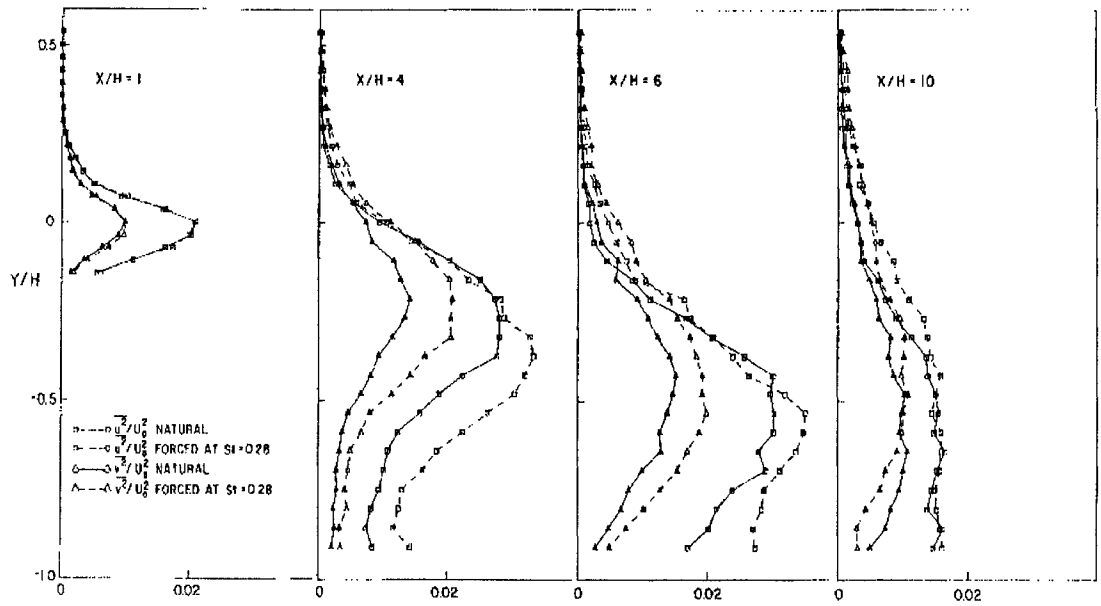

Figure 1.10 – Profiles of Turbulent Kinetic Energy Behind Step; $R_H = 45{,}000$.

of two parallel streams of air flowing at different velocities. In the aforementioned study by Oster and Wygnanski [1982], the researchers varied both the amplitude and frequency of the oscillating flap and took measurements downstream of the splitter plate. The momentum thickness was used as an indicator of the extent of the mixing width and hence of the spreading rate.

Tordella [Tordella D. and Christiansen, W. H., 1989] conducted a similar experiment and made detailed observations of the spectral content of a mixing layer downstream of a splitter plate with the result that energy was transported through the mechanical oscillations of a trailing-edge flap.

Dogval [1986] applied the theory of hydrodynamic instability by generating controlled disturbances in the boundary layer of a wing upstream of the point of separation. They were able to do this by placing a vibrating ribbon in the boundary layer or by inducing disturbances with a loudspeaker, which could be tuned at selected frequencies. They operated the vibrating ribbon at frequencies of 85, 116, 156, 176, and 196 Hz. Their results showed that these frequencies were strongly amplified in the region of separation and that they strongly affected the flow structure in the adverse pressure region of the wing. The data showed that when the boundary layer was excited, the mean velocity profile became fuller for transverse locations closer to the model surface. This would suggest that there would be a tendency for the boundary layer to attach because of higher velocities near the surface.

Dogval [1986] also obtained data when the wing was subjected to acoustic excitation from a loudspeaker. The acoustic excitation induced a system of two-dimensional vortices in the boundary layer. The frequency of the induced vortices was found to be equal to the frequency of the acoustic wave. As expected, the velocity near the surface became more full when in the presence of external excitation. This would suggest that because higher velocities occur near the surface, enough kinetic energy existed within the boundary layer to delay or prevent separation. The surface pressure distribution on the model was markedly altered under the influence of the sound field. For example, the data show that when the sound source was tuned at 412 Hz, the surface pressure distribution exhibited a favorable pressure recovery.

In a related study, Kourounis [1998] performed an experiment to enhance understanding of the nature of the interaction between a wake and a turbulent boundary

layer. Although their experiment did not involve the use of an actuator, their work confirmed the accepted theory of how vortices from an upstream airfoil can affect the boundary layer on a downstream surface. The motivation of their efforts was to generate a database to aid in the design of high-lift configurations. Previous studies were done to acquire data that could be used to construct theoretical codes to predict the characteristics of boundary layer flows and their attendant effects on the aerodynamic performance of high-lift airfoils. Their test set-up consisted of an airfoil (NACA 0015) mounted in a low-turbulence, indraft, open wind tunnel. The airfoil featured a trailing-edge flap that could be set at various angles of incidence. The wake from the airfoil was directed onto the floor boundary layer by setting the flap trailing edge downward (positive angle of incidence). Boundary-layer measurements were obtained near the floor of the test section by using a hot-wire sensor and anemometer. The hot-wire sensor was used to obtain measurements of various quantities (e.g., mean and turbulent velocities, vorticity, shear stress, and turbulent kinetic energy). To form a basis of comparison, the researchers looked at both disturbed and undisturbed boundary layers. In regards to the equation expressing the turbulent kinetic energy budget, they concluded that the two dominant terms are the production and dissipation terms. They found, that in the disturbed boundary-layer case, the production term of the turbulent kinetic energy was markedly higher than in the undisturbed case. However, the dissipation terms were about equal. They postulated that for the disturbed case, the increased production of kinetic energy was a consequence of increased shear stresses brought on by the impingement of the wake.

The results from these studies strongly suggest that vortices on an airfoil can be used to influence the distribution of important physical quantities in the boundary layer of a

device such as a wing or flap to affect the transport of kinetic energy. This phenomenon offers hope as a viable means for controlling boundary-layer separation on a lifting surface and, as a result, it shows the possibility of increasing aerodynamic lift.

The velocity profile near the wall must have certain characteristics that tend to inhibit boundary-layer separation. Figure 1.11 (a) shows the effect that the sign of the pressure gradient has on the profile, and Figure 1.11 (b) shows the evolution of a velocity profile adjacent to a wall for various streamwise locations. At the location corresponding to incipient separation, the derivative of the velocity along the normal direction is zero, and the second derivative is positive. This fact suggests, that to delay or eliminate boundary-layer separation, the velocity profile should be full, and the second derivative of the mean velocity with respect to the normal direction should be negative [Gad-el-Hak, M. and Bushnell, D., 1991]. Prandtl's momentum equation for a laminar boundary layer as is shown in Equation 1.3-1 [Currie, I. 1974] can be used to provide further understanding of some of the requirements for the prevention of boundary-layer separation.

$$u\frac{\partial u}{\partial x} + v\frac{\partial u}{\partial y} = -\frac{1}{\rho}\frac{\partial p}{\partial x} + \nu\frac{\partial^2 u}{\partial y^2} \qquad (1.3\text{-}1)$$

For application of this equation to the flow properties on the model surface, the left-most term vanishes because of the well-known no-slip boundary condition and the streamwise velocity u is zero. Ordinarily, the normal velocity v would also be zero,

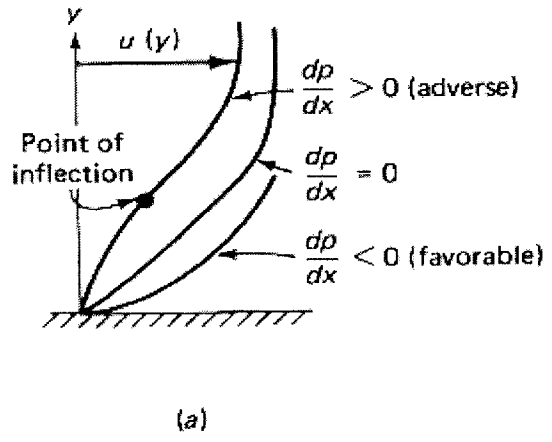

Figure 1.11a - Effect of Pressure Gradient on Velocity Profile.

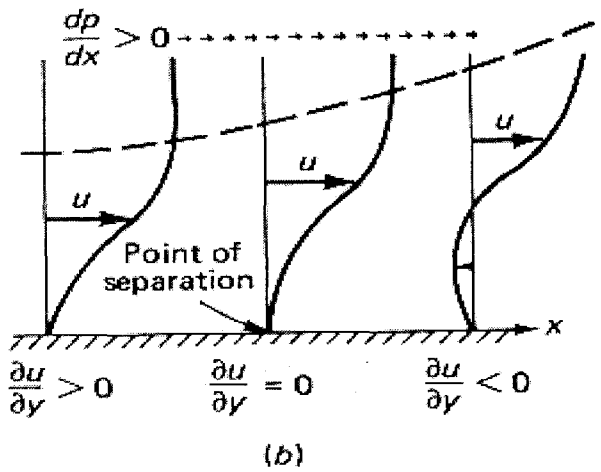

Figure1.11b - Evolution of Velocity Profile in an Adverse Pressure. Gradient

but in the case of transpiration through a porous wall where suction is being applied, the velocity v is not zero but has a negative value. In Equation 1.3 –1, this would tend to make the second derivative on the right more negative, which as previously stated, is a desirable effect. An explanation based more on physical reasoning is that the suction of boundary-layer air at the surface has the effect of removing the slower moving air in the near-wall region which increases the velocity gradient and causes the profile to be fuller.

In one study [Champagne, F. H., et al. 1976] there was an experimental investigation of the mixing that occurs in the wake of a splitter plate, wherein the flows above and below the plate were at two different velocities. To quantify the extent of the mixing region, the researchers identified the specific coordinates in the direction transverse and perpendicular to the plate where the velocity deviated by a given percentage from the velocity difference between the streams. That is, they found the location of $y_{0.1}$ corresponding to the location at which $U = U_1 + 0.1(U_2 - U_1)$ and $y_{0.95}$ corresponding to the location where $U = U_1 + 0.95(U_2 - U_1)$. In this referenced report, U was the free-stream velocity, U_1 was the velocity on the low-speed side and U_2 was the velocity on the high-speed side. The local width of the mixing layer was defined as $b = y_{0.1} - y_{0.95}$. The coordinates were plotted versus the longitudinal distance from the splitter plate trailing edge. For increasing downstream stations the width of the mixing layer grew linearly. Their resulting plots demonstrated that the locus of these coordinates was a straight line with a positive slope, which suggested that the flow-field properties possessed similarity.

Another idea, which can be used to create a more favorable velocity profile, is to make the longitudinal pressure distribution more negative, which after transposing the

pressure term to the left hand side of Equation 1.3-1, results in a more negative curvature or second derivative. One way to promote a negative pressure distribution is to contour the upper surface so that the static pressure decreases with increasing longitudinal position. Another way to do this is to blow air tangentially on the model surface in the streamwise direction. One interpretation of this effect is that forcing air along the surface of the model speeds up the air particles, which lowers the surface static pressure and results in a more negative streamwise pressure distribution. Another interpretation is that the newly energized air particles will become infused with enough momentum and kinetic energy that they can withstand the adverse pressure distribution and thus delay or even eliminate boundary-layer separation. It has been shown theoretically [Gad-el-Hak, M. and Bushnell, D., 1991] that by transferring heat from the air to the wall makes the curvature of the velocity profile more negative.

The fact that laminar boundary layers are more susceptible to separation than turbulent ones has been well established. This invites the probable solution of supplying the boundary layer with turbulence either by placing some passive miniature objects on the model surface to introduce disturbances into the airflow or by using active implements such as piezoelectric devices, which oscillate at some prescribed frequency. The passive approach involves the use of devices called turbulators, which are elements that are placed on the model wall and which increase the growth rate of naturally-occurring Tollmien-Schlichting waves. Other mechanical elements can be used to increase turbulence such as serrations, strips, bumps, or ridges [Gad-el-Hak, M. and Bushnell, D., 1991]. Vortex generators have been the subject of many wind tunnel experiments on flow control and show promise as a tool to augment aerodynamic lift. This is due to the well-established fact

that turbulent boundary layers are more resistant to separation. In the case of a turbulent boundary layer, the steady-state momentum equation and stress tensor (White, F. M, 1991) would be as is shown in Equation 1.3-2.

$$\bar{u}\frac{\partial \bar{u}}{\partial x} + \bar{v}\frac{\partial \bar{u}}{\partial y} = -\nabla \bar{p} + \nabla \cdot \tau_{ij} \qquad (1.3-2)$$

$$\tau_{ij} = \mu \left(\frac{\partial u_i}{\partial x_j} - \frac{\partial u_j}{\partial x_i}\right) - \rho \bar{u}_i \bar{u}_j \qquad (1.3-3)$$

In Equation (1.3-3) the second term on the right hand side is the turbulent-stress tensor, which increases with increased turbulence in the boundary layer. Mathematically, it can be seen that as this term increases, the total stress term becomes more negative. The divergence of this tensor in Equation (1.3-2) corresponds to a more negative second derivative of the mean streamwise velocity. As indicated previously, a more negative second derivative of the mean velocity translates into a profile where the boundary-layer velocity profile is fuller and less susceptible to separation.

Previous studies [Kourounis, 1998], [Nakayama, A., et al., 1990] have examined the interplay between turbulent wakes and boundary layers. Measurements of turbulence intensity have been obtained to gain further understanding of energy budgets in highly viscous regions. One of the major tasks is to determine the relative importance of the various terms in the well-known energy transport equation. These terms primarily consist of advection, production, diffusion, and dissipation. A primary motivation behind this research was the hope of developing reliable turbulence models to incorporate into CFD codes.

In one study [Bario, F. et al., 1982], the researchers investigated the aerodynamic characteristics of the flow field surrounding a two-dimensional airfoil embedded in a wake produced by another two-dimensional airfoil positioned upstream. The wall of the test section adjacent to the upper surface of the tandem airfoil arrangement was variable and was geometrically altered to ensure that boundary-layer separation occurred on the surface of the trailing airfoil. One of the fluid mechanical quantities examined was the velocity fluctuation on the aft airfoil, in both the longitudinal and transverse directions. Their results suggested that there was a transfer of energy from the mean velocity to the longitudinal fluctuation velocity in the streamwise direction. As expected, they observed that the fluctuating velocities near the surface of the model were highly anisotropic where the longitudinal turbulent velocity was always larger than the corresponding velocity in the transverse direction.

On the other hand, active devices can be used as a means of providing flow control. Not only can piezoelectric devices, oscillating trailing-edge flaps and loudspeakers be used to inject turbulence into airflow, but also some research has used such devices to force the coupling of naturally occurring vortices. Evidence supports the belief that engineers can utilize the amalgamation of these vortices to induce mixing of a shear layer and a separated boundary layer and diffuse momentum from regions in the flow field where it is high to regions where it is low. This is appealing because the test article itself naturally provides a significant part of the momentum and it awaits the engineer to capitalize on this available source of energy to increase the aerodynamic performance of the airfoil.

1.4 Previous Studies involving Flow Control

In a classic experiment from the post-war era [Schubauer, G.and Skramstad, H., 1947] the researchers obtained measurements along a flat plat in an attempt to better understand the role played by oscillations on the transition process from laminar to turbulent boundary-layer flow. The experimenters in this study were able to conduct their investigation in a facility that was characterized by a very smooth and low-turbulent stream of air. Their goal was to verify that the transition to turbulence is mainly triggered by the presence of disturbance wavelengths within a certain critical range even when disturbances are present with very low amplitudes. Thus, this experiment greatly enhanced the viability and esteem of Stability Theory. They used a pitot-static probe to acquire mean values of total and static pressures and a hot-wire sensor to obtain measurements of turbulence.

In their experiment, a 25-watt loudspeaker was mounted on the ceiling of the wind tunnel directly above the leading edge of the plate. An oscillator drove the loudspeaker through an amplifier. Their results showed that they were able to exercise considerable control over the characteristics of the boundary layer. In particular, they could easily induce oscillations in the boundary layer and could shift the transition point by as much as 1 or 2 feet by using the proper combination of sound intensity and audio frequency. These results opened up a vista of ideas regarding the potential use of sound as a means for controlling boundary-layer characteristics.

A wind tunnel experiment [Seifert, A., et al., 1998] was conducted using piezoelectric devices on an Israel Aircraft Industries (IAI) Pr8-40-SE multi-element airfoil. The purpose of the test was to add cyclic vortical perturbations to a boundary layer in an attempt to delay separation. The model was also instrumented with surface static pressure

orifices to measure the lift, moment, and form drag. A channel was machined into the upper surface of the wing and contained ten piezoelectric actuators that were mounted flush to prevent any interference effects due to the actuators themselves. The researchers in this experiment operated the devices in two different modes: (1) each device attained the same amplitude and was in phase with respect to each other, and (2) the phase of the devices were reversed between each adjacent device. These modes were designated as being two-dimensional and three-dimensional, respectively. The model was placed at various angles of attack and the Reynolds number was $R_e = 0.55$ E+06. A transition strip was placed at the leading edge of the airfoil. A sinusoidal voltage drove the devices. The data showing C_L versus angle of attack is shown in Figure 1.12.

The data showed, that for the baseline configuration, the maximum lift coefficient was 1.26, whereas for the two-dimensional and three-dimensional cases, the maximum lift coefficients were 1.51 and 1.54, respectively. The data also showed that at 15° angle of attack there was a 35% increment in C_L between the baseline configuration without excitation and the measurements obtained with piezoelectric excitation for the 2D mode. This improvement in maximum lift is significant in view of previous research, which suggested that a 5% improvement in maximum lift coefficient translates into a 25 % payload increase [Gad-el-Hak, M. and Bushnell, D., 1991]. Concerning power consumption, the data indicated that, when the devices were driven in the three-dimensional mode the efficiency was superior.

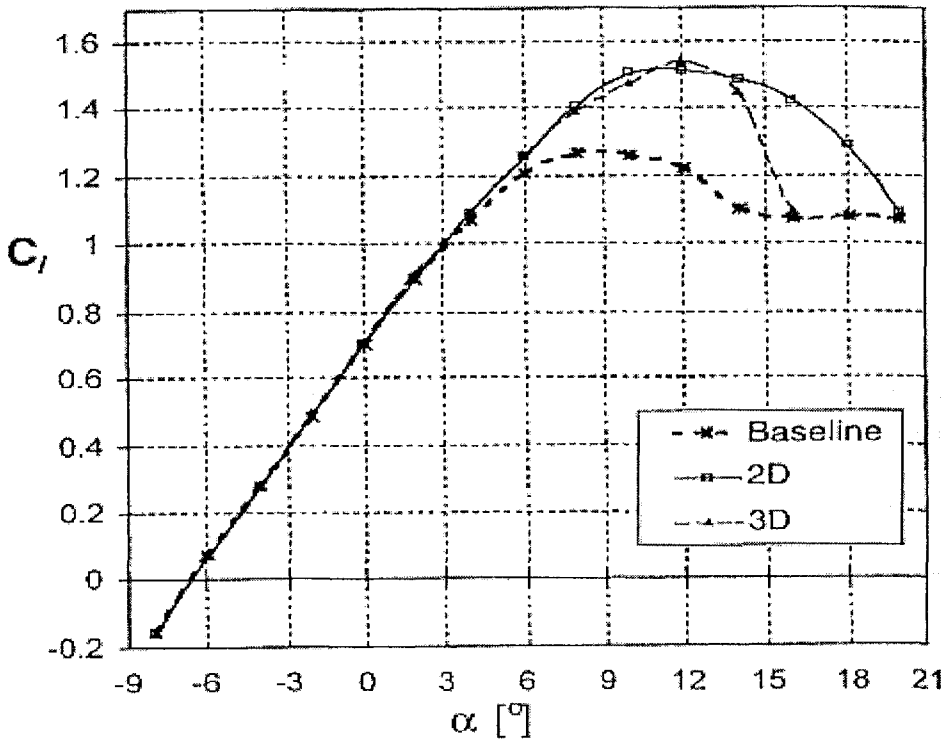

Figure 1.12 – Effect of Piezoelectric Excitation on Lift Coefficient.

In one investigation [Tam C. K. W. and Pastouchenko, N., 2001] the authors used CFD to identify the source of noise on a multi-element airfoil. They concluded that the noise originated from the region in the vicinity of the slat where there exists a system of vortices that are shed from the trailing edge of the slat. The difference in velocity between the upper surface and lower surface flows is responsible for the vortices. They modeled the interaction between the slat and the wing with a zero-thickness plate suspended above a flat wall. The flow between the plate and the wall formed a plane jet that has similarities with the flow through the slat of a multi-element airfoil. A sketch of their theoretical model is shown in Figure 1.13.

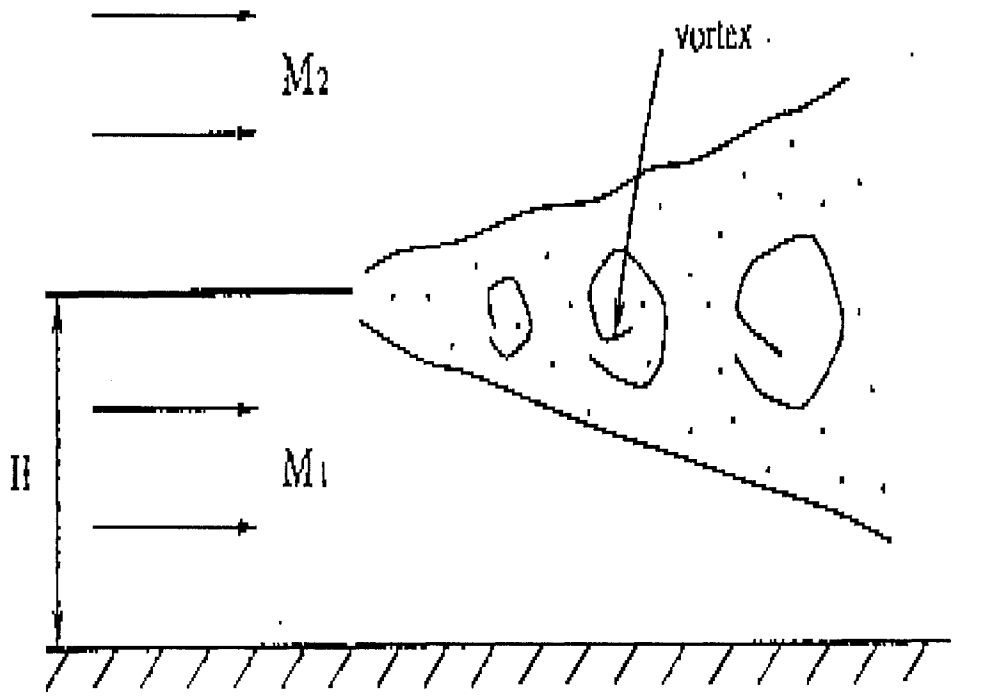

Figure 1.13 - Generic Wall Jet Model.

Several researchers [Strange, P.J.R. and Crighton, D.G., 1983], [Paschereit, C. O. et al., 1995] have studied the behavior of circular jets when subjected to various types of artificial perturbation, such as acoustic energy generated by a loudspeaker or by piezoelectric devices. Their results demonstrated that by selecting specific frequencies of external excitation, the jet was found to spread. A previous wind tunnel experiment [Crow, S. C. and Champange, F. H., 1971] involved the study of orderly structures in jet turbulence.

They also used a loudspeaker to excite the modes in the jet and found that optimal spreading of the jet occurred at around a Strouhal number of 0.3. Their Strouhal number was defined using the diameter of the jet as the reference length and the jet speed as the reference velocity.

Several researchers have studied the interaction of external excitation on vortex pairing, particularly with regards to axisymmetric jets. An important reason for this is to study the dynamics of vortices and their effect upon the mixing rate of fuel and air in aircraft combustion chambers. In one study [Cho, S. K., et al., 1998], the researchers examined the phenomenon of vortex pairing in an axisymmetric jet using two-frequency acoustic forcing. The main objective of their experiment was to try to control the amount of vortex pairing by modulating an acoustic source tuned at the fundamental frequency of the main flow with its subharmonic. The data showed that varying the initial phase difference between the fundamental and its subharmonic could control the extent of vortex pairing. Their results indicated that control was best achieved for Strouhal numbers between 0.3 and 0.6. The reference length was based on jet diameter. The authors [Cho, S. K., et al., 1998] state that after the fundamental grows exponentially, the amplitude of the subharmonic also grows and interacts with the fundamental until its energy reaches a maximum at the location of their merger. Their study consisted of an air jet facility, acoustic forcing system, data acquisition system and a flow visualization system. Velocity measurements in the jet were obtained using a hot-wire anemometer. Acoustic forcing was achieved by using a 4 in. diameter speaker that was mounted on the section of the facility just preceding the diffuser. For flow visualization, the authors used multi-smoke wires and

a camera to record still photographs of the smoke trail behind the nozzle. The experimental setup is shown in Figure 1.14.

When the fundamental acoustic signal was mixed with its subharmonic with phase differences of 23° and 272°, the smoke visualization revealed the presence of the most intense vortex pairing. However, when the phase difference was 120°, they observed that vortex pairing was suppressed. Figure 1.15 shows a time sequence of photographs of the jet exiting from the nozzle, showing the effect of acoustic forcing. Photographs (a)-(e) show vortex pairing that has occurred as a result of modulating the fundamental acoustic source with its subharmonic. Photograph (f) was for the case of no forcing and does not show any evidence of vortex pairing. The authors examined the longitudinal evolutions of both fluctuating and mean velocities. In this experiment by Cho [1998], a hot-wire sensor was used to take measurements of both mean and fluctuating velocities. Their findings are shown in Figure 1.16. Two ratios were defined, namely, the ratio of the fundamental fluctuating velocity to the jet center velocity, i.e. a_f, and the ratio of the subharmonic fluctuating velocity to the jet center velocity, i.e., a_s. The results in Figure 1.16 show that when the phase difference between the fundamental and the subharmonic was 272° the amplitude of the total fluctuating velocity grows most rapidly with longitudinal position. Figure 1.17 shows the evolution of the mean velocity and indicated a trend that was the reverse of the fluctuating velocity. That is, for the case of most intense vortex pairing the mean velocity decreases most. At the longitudinal location where the fluctuating velocity shows an increase there is a corresponding decrease in the mean velocity. Cho et al. [1998] explained this phenomenon as arising from an energy exchange between the fluctuating velocity and the mean velocity. This is due to the transfer of kinetic energy from the mean

to the turbulent flow. Paschereit et al. [1995] also investigated and reported on this mode of energy exchange.

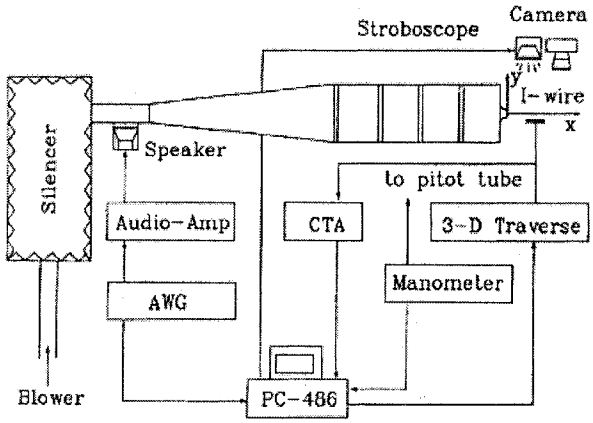

Figure 1.14 – Experimental Setup of Facility for Axisymmetric Jet Study.

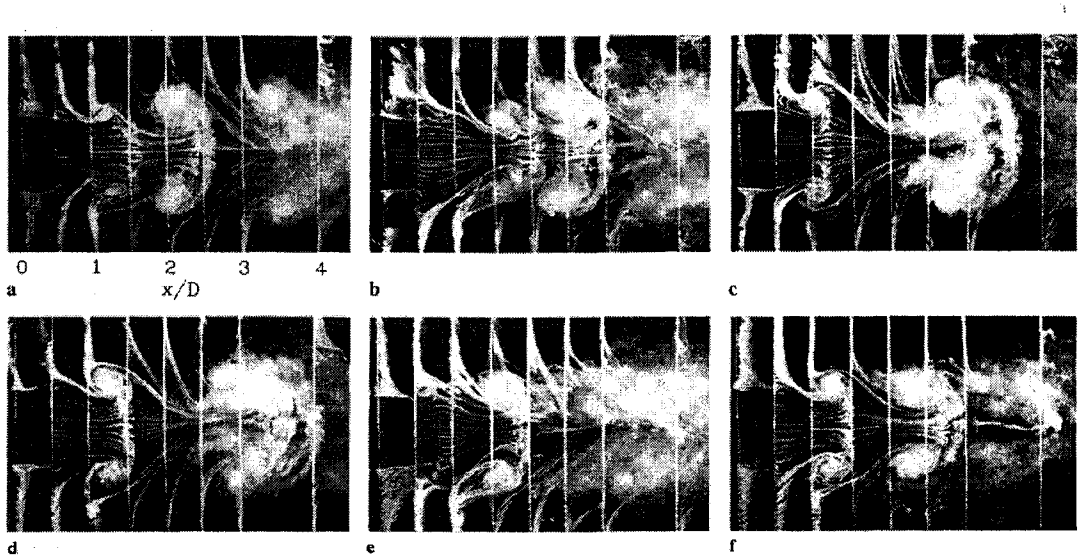

Figure 1.15 - Smoke Visualization of Axisymmetric Jet showing Time Sequence of Vortex Pairing.

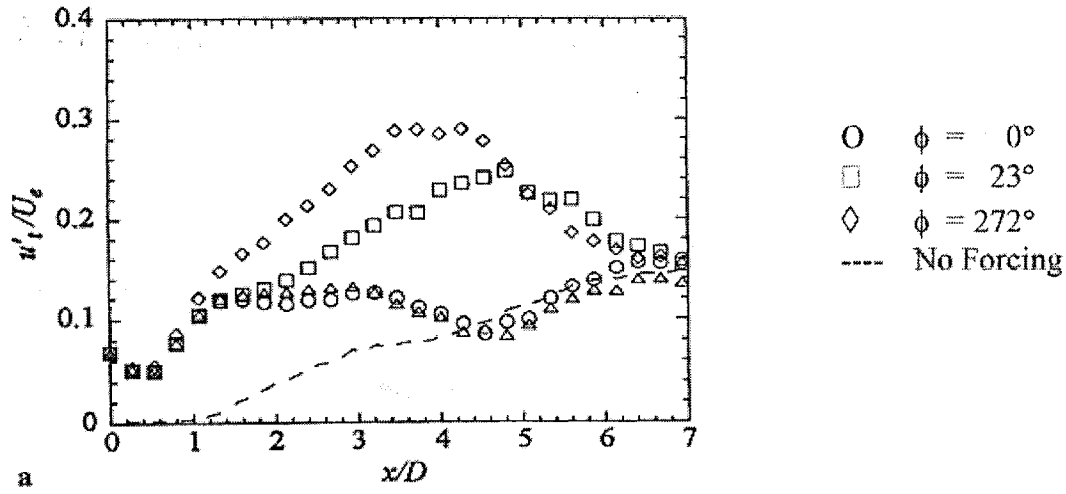

Figure 1.16 – Longitudinal Evolution of Fluctuating Velocity with Forcing and No Forcing.

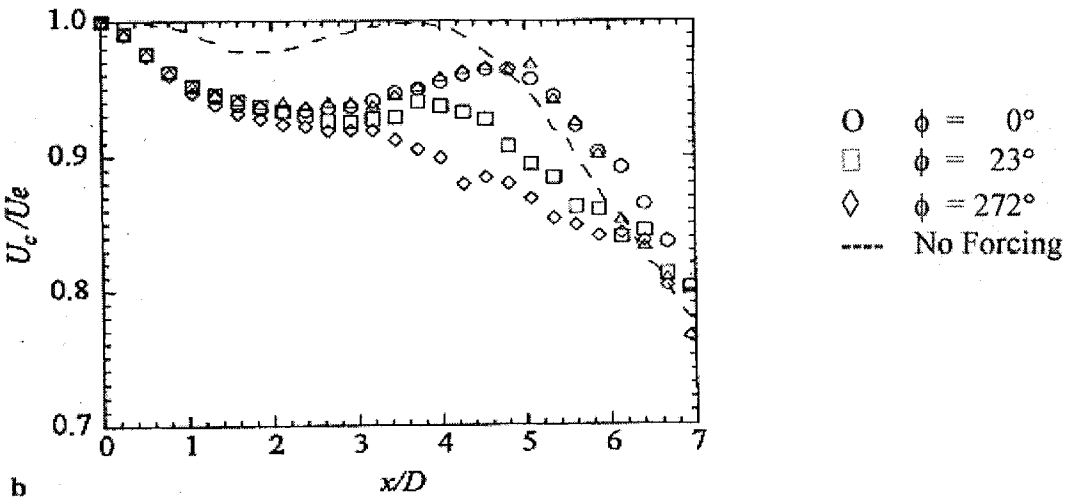

Figure 1.17 – Longitudinal Evolution of Mean Velocity with Forcing and no Forcing.

Whereas in the study just reviewed, only the first subharmonic was used to control vortex pairing, in another experimental study [Ho, C. and Huang, L., 1982] several subharmonics were used to ascertain their effect upon the amalgamation of vortices. The main objective of the experiment was to study the spreading rate of a mixing layer. The fluid medium in this study was water and was performed in a water channel as shown in Figure 1.18. A splitter plate was installed in the chamber upstream of the test section. The fluid velocities differed on both sides of the splitter plate. The high-speed side of the flow was kept at 9.5 cm/s and the low-speed side was kept at a velocity of 5.0 cm/s. The disparity of velocity ensured the formation of vortices at the trailing edge of the splitter plate. A hot-film probe was inserted in the flow in the test section to obtain measurements of velocity and spectra. The peak frequency of the unforced mixing layer f_m was around 5.06 Hz, which was close to the theoretical most-amplified frequency f_o. Perturbations were supplied to the flow by two butterfly valves, which were driven by a DC motor. The amplitude and frequency of the velocity perturbations were varied by adjustments to both the flowmeter and DC motor. The most-amplified frequency of the forced mixing layer f_r was called the response frequency and was determined by visualizing the passage of vortices and by hot-film measurements. Dye trace was used to visualize the evolution of vortices downstream of the splitter plate. Their data showed that for the case of no forcing the vortices merged randomly in space and time. However, at various subharmonics of the frequency f_m, vortex pairing occurred systematically and not randomly. The authors identified four distinct modes of vortex amalgamation, where each mode was defined by intervals of subharmonics of the frequency f_m. With each succeeding mode number the forcing frequency f_f was a lower subharmonic of the frequency f_m. In mode I, vortex

merging was suppressed until some significant distance downstream of the splitter plate and the spreading of the mixing layer was minimal. In mode II, every two vortices merged with the result that the extent of the mixing layer had grown substantially. In mode III, every three vortices merged and in mode IV every four vortices merged in to one amalgamated vortex. The frequency of forcing was decreased to the case when the frequency ration f_f/f_m was equal to 0.17, that is, the forcing frequency was 17% of the fundamental frequency.

The results from this experiment [Ho, C. and Huang, L., 1982] were summarized in the mode diagram shown in Figure 1.19. Each horizontal line on the graph represents one of the four modes described earlier. Ho and Huang [1982] explained the merging process by stating that a small amount of energy at the forcing frequency, which is the Mth subharmonic of the fundamental frequency, is fed into the mixing layer and continues to grow downstream. The researchers found that M number of vortices will experience a gradient of lateral velocity until they merge to form a single structure. Furthermore, they found that the presence of the fundamental and the subharmonic are very important in the vortex merging process. If only the subharmonic appears large vortices will form but no merging will occur. The merging process for three vortices is shown in Figure 1.20. The merging of the vortices is the process, which is most essential for increasing the spreading rate of the mixing layer in the region of confluence. According to Ho and Huang [1982], the subharmonic component begins to amplify at the location where the phase speed of the subharminc equals that of the fundamental frequency. The location where the subharmonic reaches its peak amplitude is where the coherent merging of the vortices begins.

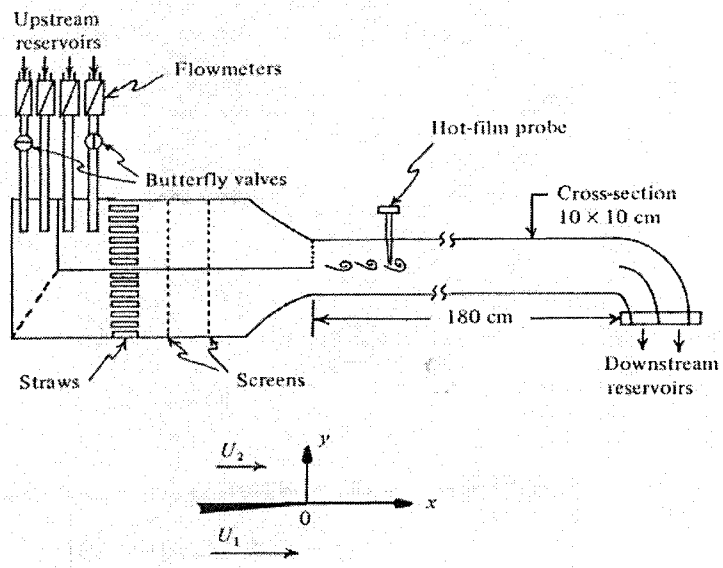

Figure 1.18 – Experimental Setup of Splitter Plate in Water Chamber.

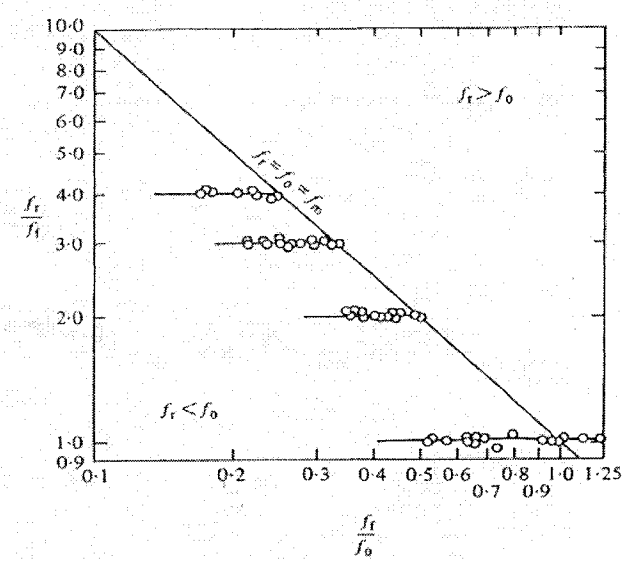

Figure 1.19 – The Mode Diagram for Vortex Pairing.

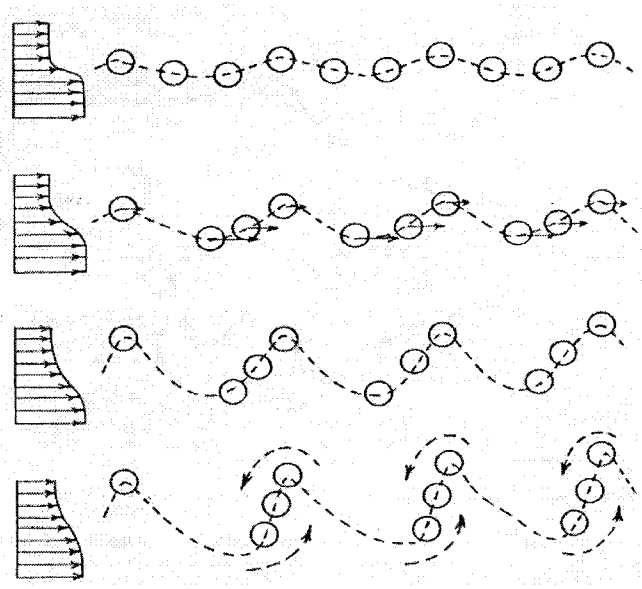

Figure 1.20 – Sketch of Multiple-Vortex Merging.

An important relationship was found between the forcing frequency and the response frequency, f_r as is shown in Equation 1.4.

$$f_f = \frac{1}{M} \times f_r \qquad (1.4)$$

In this equation M is the mode number and M =1, 2, 3, 4 for modes = I, II, III, and IV, respectively. This result shows that the forcing frequency is the Mth subharmonic of the response frequency at which the vortices develop initially in the mixing layer. Under some conditions, the response frequency is very nearly equal to what the authors call the most-amplified frequency, which corresponds to the fundamental or natural frequency.

Various innovative techniques have been devised to delay boundary layer separation, but all these techniques are predicated on the objective of accelerating the flow around an airfoil to overcome an adverse pressure gradient. One such method under investigation was the use of a magnetohydrodynamic (MHD) Lorentz force to increase the velocity of flow around a test article. In one study [Gailitis, A. and Lielausis, O., 1961] the researchers had proposed a test article composed of an arrangement of electrodes and permanent magnets of alternating polarity and magnetization, which interacted with an electrolytic fluid with velocity U of sufficient electrical conductivity σ such that a Lorentz force f was induced in the direction of the flow. Experimental results employing this technique [Weier, T., et al., 2001] showed that it was possible to generate increment in lift over a hydrofoil. The researchers used a NACA-0017-like hydrofoil immersed in an electrolytic liquid and obtained measurements of lift from a force balance. They observed that when active control was implemented, the momentum thickness of the boundary layer had decreased compared with the unforced or natural test case. The researchers also observed that at small angles of attack, a moderate increase in lift occurred due to the additional circulation.

Although these results were for a liquid working fluid, the underlying principle of operation has relevance to boundary-layer separation for airfoils. Researchers [Nosenchuck, D. M., et al., 1995] have used MHD technology to engender favorable aerodynamic results. As has been reported [Roth, J. and Sherman, D., 1998] although MHD has been used with some success, an alternative approach is to use electrohydrodynamic (EHD) control. This field of boundary layer research involves use of the electric field alone to accelerate boundary layer velocity. In this approach, an external electric gradient is used

to accelerate an ionized gas. The advantage of this approach is that the electrostatic force on a charged particle can be markedly greater than the magnetic force on the same moving charge [Roth, J. and Sherman, D., 1998]. The results of the study [Roth, J. and Sherman, D., 1998] showed that significant favorable changes in the momentum thickness were observed when active control using EHD technology was implemented.

As has been previously mentioned, vortex generators have shown promising effects in the area of flow control. An extension of this technology has been the development of vortex generator jets (VGJs) as a means for controlling boundary layer separation. VGJ devices produce a jet of air injected into the boundary layer through the surface, but which also generates a dominant streamwise vortex. An experiment [Johnston, J., 1999] was conducted using VGJs on an airfoil to control boundary layer separation. The vortical jets add momentum to the boundary layer, which enables the flow to better withstand the adverse pressure gradient. For some cases, these devices were able to almost completely suppress separation and in other cases reduced the size of a stall bubble. Increasing the jet speed of the air discharged from these devices produced favorable boundary-layer effects. In another experiment [Hwang, K. S., et al., 2001], the researchers investigated the effect of pulsating the flow on the location of the reattachment line on a flat plat. The results from this experiment showed that by introducing a periodic component into the flow the extent of boundary-layer separation could be significantly reduced. Reattachment is characterized by the rolling-up and growing-up of large-scale vortices in the shear layer, which is subsequently shed from the separated region [Hwang, K. S., et al., 2001]. The external excitation was produced by a loudspeaker that was attached to the inside of the settling

chamber of the wind tunnel. The pulsating frequency of the loudspeaker was varied and the resulting location of the reattachment line was subsequently determined using a split-film

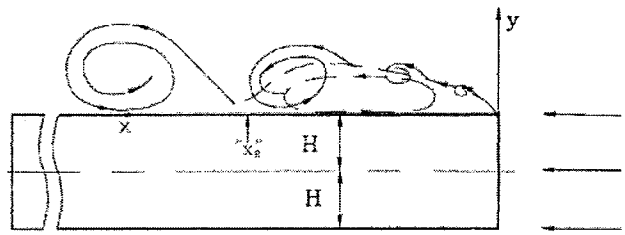

$$U = U_o (1 + A_o \cos 2\pi f_p t)$$

Figure 1.21 – Sketch of Flat Plate Experiment in Pulsating Flow.

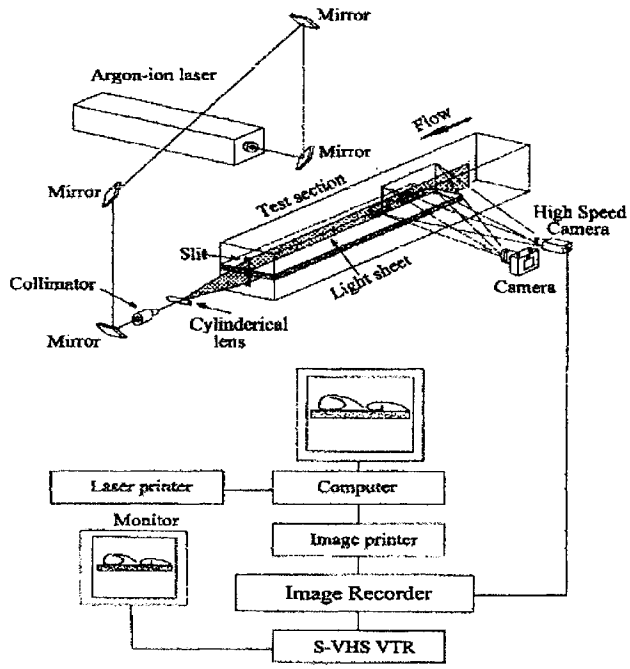

Figure 1.22 – Schematic Diagram of Experimental Apparatus for Flow Visualization of Flat Plate in Pulsating Flow.

sensor. Figure 1.21 shows a sketch of the flat plate model with its attendant flow field. The separated shear layer exhibits a roll up and reattachment at the location x_R.

The experiment was performed in an open circuit blower-type tunnel. The free stream velocity varied from 1.2 to 12 m/s. The flat plate was constructed of acrylic resin with a precision-machined leading edge. The dimensions of the flat plate were 12.1 by 250 by 1000 mm in thickness, width and length, respectively. The acoustic excitation was produced by the loudspeaker, which was driven by a function generator signal that passed through an audio amplifier. A hot wire anemometer was used to obtain power spectra of the pulsating free stream. The test article was instrumented with a total of 42 pressure taps along the centerline to obtain distributions of pressure coefficients. The smoke-wire technique was used for flow visualization. The schematic for the flow visualization is shown in Figure 1.22.

In this experiment [Hwang, S. K., et al., 2001], the time-mean length of the reattachment region for pulsating flow, x_R was gauged by the forward-flow time fraction (γ_p), which is measured by using the split-film sensor near the surface of the flat plate. The location of the reattachment line without pulsating flow was x_{RO}

Figure 1.23 shows the ratio x_R/x_{RO} as a function of the Strouhal number of the pulsating flow for various pulsating amplitudes, A_o. The data show that there is a Strouhal number where the ratio exhibits a minimum. The location of the minimum is slightly dependent upon the amplitude. These results demonstrate that a significant amount of control can be used to shift the location of the reattachment line. This dissertation seeks to expand on the knowledge about flow control of boundary layers by applying these well-established principles to a multi-element airfoil.

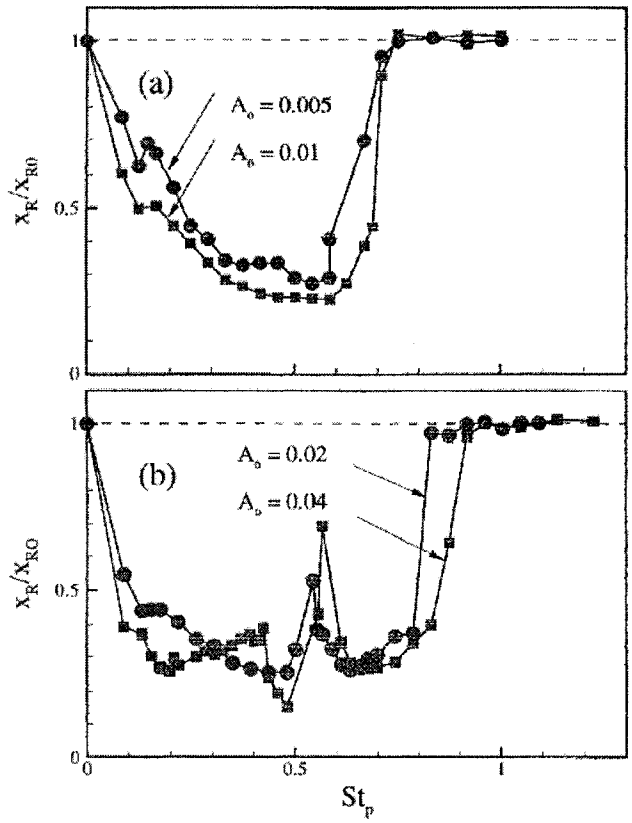

Figure 1.23 - Variations of x_R versus St for Different Amplitudes, Re = 560.

The studies described in this section are only an infinitesimally small sample of the plethora of experiments that have been conducted which demonstrate the utility of active excitation of boundary layers. The present database of research on this topic, leaves no doubt that such technology can play a prominent role in the area of high-lift aerodynamics. The engineer must continue to work to overcome some of the practical challenges that persist. The author hopes that the results reported in this study will provide some contribution, albeit a small one, to this interesting field of research.

1.5 Viscous Linear Stability Theory

In this study, Linear Stability Analysis was used to estimate the fundamental frequency for the free-stream velocity of 10 m/s at 0° angle of attack. The data for the Linear Stability Analysis was obtained at such a low free-stream velocity to avoid the large amount of sensor vibration at the higher speeds. A major objective was to determine the applicability of Linear Stability Analysis for the complex geometry of a multi-element airfoil. As a result, the flow conditions and model attitude were selected for the sake of simplicity. The approach taken was similar to that chosen by Ho and Huerre [1984]. They determined the fundamental frequency by using Linear Stability Analysis to produce an empirical curve showing the normalized amplification rate of various perturbed disturbances as a function of Strouhal number. The fundamental or natural frequency was determined from the Strouhal number corresponding to the maximum normalized amplification rate. A computer program in Fortran was written to implement this procedure. A velocity profile was generated and its first and second derivatives were calculated in the direction normal to the model as close as possible to the trailing edge of the slat. Because of the highly viscous interactions in this region, the Navier-Stokes equations are used for viscous incompressible flow. The governing equations are the continuity Equation 1.5-1 and the momentum Equations 1.5-2 through 1.5-4.

$$\frac{\partial u}{\partial x}+\frac{\partial v}{\partial v}+\frac{\partial w}{\partial z}=0 \qquad (1.5\text{-}1)$$

$$\frac{\partial u}{\partial t}+\frac{u\partial u}{\partial x}+\frac{v\partial u}{\partial y}+\frac{w\partial u}{\partial z}=-\frac{\partial p}{\partial x}+\frac{1}{R}\nabla^2 u \qquad (1.5\text{-}2)$$

$$\frac{\partial v}{\partial t}+\frac{u\partial v}{\partial x}+\frac{v\partial v}{\partial y}+\frac{w\partial v}{\partial z}=-\frac{\partial p}{\partial y}+\frac{1}{R}\nabla^2 v \qquad (1.5\text{-}3)$$

$$\frac{\partial w}{\partial t} + \frac{u\partial w}{\partial x} + \frac{v\partial w}{\partial y} + \frac{w\partial w}{\partial z} = -\frac{\partial p}{\partial z} + \frac{1}{R}\nabla^2 w \qquad (1.5-4)$$

These are the continuity equation, x, y, and z momentum equations and respectively. The nondimensional Reynolds number is denoted in Equation 1.5-5.

$$R_e = \frac{\rho U_\infty l}{\mu} \qquad (1.5-5)$$

According to the stability theory, a sinusoidal disturbance is introduced into the above equations by superimposing a fluctuating term onto the mean flow quantities, as shown in Equation 1.5-6.

$$u = \bar{u} + u' \qquad v = v' \qquad w = w' \qquad p = \bar{p} + p' \qquad (1.5-6)$$

Note that the mean flow is only assumed in the x direction. The relationships in Equation 1.5-6 are substituted into the equations 1.5-1 through 1.5-4 with second order terms eliminated because of the assumption of linearity. The assumption of linearity assumes that the terms in the equations 1.5-1 through 1.5-4 containing products of the fluctuating quantities are negligible. This procedure results in the derivation of the Equations 1.5-7

$$\frac{\partial u'}{\partial x} + \frac{\partial v'}{\partial y} + \frac{\partial w'}{\partial z} = 0 \qquad (1.5-7)$$

$$\frac{\partial u'}{\partial t} + \frac{\bar{u}\partial u'}{\partial x} + \frac{w'\partial \bar{u}}{\partial z} = -\frac{\partial p'}{\partial x} + \frac{1}{R_e}\nabla^2 u' \qquad (1.5-8)$$

$$\frac{\partial v'}{\partial t} + \frac{\bar{u}\partial v'}{\partial x} = -\frac{\partial p}{\partial y} + \frac{1}{R_e}\nabla^2 v' \qquad (1.5-9)$$

$$\frac{\partial w'}{\partial t} + \frac{\bar{u}\partial w'}{\partial x} = -\frac{\partial p}{\partial z} + \frac{1}{R_e}\nabla^2 w' \qquad (1.5-10)$$

through 1.5-10.

Normal Mode Analysis was then used with the assumption that each mode of the disturbance can be represented by an expression involving the complex exponential forms shown in Equations 1.5-11 – 1.5-14.

$$u' = \hat{u}e^{i(\alpha x + \beta y - \alpha ct)} \tag{1.5-11}$$

$$v' = \hat{v}e^{i(\alpha x + \beta y - \alpha ct)} \tag{1.5-12}$$

$$w' = \hat{w}e^{i(\alpha x + \beta y - \alpha ct)} \tag{1.5-13}$$

$$p' = \hat{p}e^{i(\alpha x + \beta y - \alpha ct)} \tag{1.5-14}$$

The amplitudes of the exponentials as shown in the Equations 1.5-11 through 1.5-14 are functions of the z component only. These are the normal mode expressions for the disturbance and are substituted into Equations 1.5-7 – 1.5-10 to get the finalized form of the linear differential Equations 1.5-15 – 1.5-18 governing the fluctuating flow quantities.

$$\frac{d\hat{w}}{dz} + i(\alpha \hat{u} + \beta \hat{v}) = 0 \tag{1.5-15}$$

$$\frac{d^2\hat{u}}{dz^2} - [(\alpha^2 + \beta^2) + i\alpha R_e(\bar{u} - c)]\hat{u} - R_e\hat{w}\frac{d\bar{u}}{dz} - i\alpha R_e\hat{p} = 0 \tag{1.5-16}$$

$$\frac{d^2\hat{v}}{dz^2} - [(\alpha^2 + \beta^2) + i\alpha R_e(\bar{u} - c)]\hat{v} - i\beta R_e\hat{p} = 0 \tag{1.5-17}$$

$$\frac{d^2\hat{w}}{dz^2} - [(\alpha^2 + \beta^2) + i\alpha R_e(\bar{u} - c)]\hat{w} - R_e\frac{d\hat{p}}{dz} = 0 \tag{1.5-18}$$

With the assumption of spatially growing disturbances, the normalized wave numbers α and β are complex, and the angular phase velocity αc is real. After obtaining eigensolutions of Equations 1.5-15 through 1.5-18, the distribution of amplification rates for various Reynolds numbers was obtained. A fourth order accurate scheme used the Euler-Maclaurin formula as shown in Equation 1.5-19 below.

$$\psi^k - \psi^{k-1} = \frac{h_k}{2}\left(\frac{d\psi^k}{dz} + \frac{d\psi^{k-1}}{dz}\right) - \frac{h_k}{12}\left(\frac{d^2\psi^k}{dz^2} - \frac{d^2\psi^{k-1}}{dz^2}\right) \qquad (1.5\text{-}19)$$

This scheme leads to a tridiagonal block matrix, which when solved, admits solutions of the eigenvalues or in this case the amplification rates for spatially growing disturbances.

The dependent variable ψ and its derivative will be represented by the following column vectors as shown in Equations 1.5-20 and 1.5-21.

$$\psi^T = \left[\hat{u}, \hat{v}, \hat{w}, \hat{p}, \frac{d\hat{u}}{dz}, \frac{d\hat{v}}{dz}\right]^T \qquad (1.5\text{-}20)$$

$$\left(\frac{d\psi}{dz}\right)^T = \left[\frac{d\hat{u}}{dz}, \frac{d\hat{v}}{dz}, \frac{d\hat{w}}{dz}, \frac{d\hat{p}}{dz}, \frac{d^2\hat{u}}{dz^2}, \frac{d^2\hat{v}}{dz^2}\right]^T \qquad (1.5\text{-}21)$$

A matrix is defined which operates on the column vector in Equation 1.5-20 to result in the column vector represented by Equation 1.5-21.

$$\frac{d\psi}{dz} = A\psi \qquad (1.5\text{-}22)$$

The elements of the two-dimensional array on the right-hand side are as indicated in Equations 1.5-23 through 1.5-29.

$$\frac{d\hat{u}}{dz}=\sum_{j=1}^{6}a_{ij}\psi_j \qquad a_{15}=1 \qquad a_{11}=a_{12}=a_{13}=a_{14}=a_{16}=0 \tag{1.5-23}$$

$$\frac{d\hat{v}}{dz}=\sum_{j=1}^{6}a_{2j}\psi_j \qquad a_{26}=1 \qquad a_{21}=a_{22}=a_{23}=a_{24}=a_{25}=0 \tag{1.5-24}$$

$$\frac{d\hat{w}}{dz}=\sum_{j=1}^{6}a_{3j}\psi_j \qquad a_{31}=-i\alpha \quad a_{32}=-i\beta \quad a_{33}=a_{34}=a_{35}=a_{36}=0 \tag{1.5-25}$$

$$\frac{d\hat{p}}{dz}=\sum_{j=1}^{6}a_{4j}\psi_j \qquad a_{43}=\frac{-(\alpha^2+\beta^2)}{R_e}-i\alpha(u-c)\ ;\ a_{45}=\frac{-i\alpha}{R_e}\ ;\ a_{46}=\frac{-i\beta}{R_e} \tag{1.5-26}$$

$$a_{41}=a_{42}=a_{44}=0 \tag{1.5-27}$$

$$\frac{d^2\hat{u}}{dz^2}=\sum_{j=1}^{6}a_{5j}\psi_j \qquad a_{51}=(\alpha^2+\beta^2)+i\alpha R_e(u-c)\ ;\ a_{53}=R_e\frac{du}{dz}\ ;\ a_{54}=i\alpha R_e$$
$$a_{52}=a_{55}=a_{56}=0 \tag{1.5-28}$$

$$\frac{d^2\hat{v}}{dz^2}=\sum_{j=1}^{6}a_{6j}\psi_j \qquad a_{62}=\alpha^2+\beta^2+i\alpha R_e(u-c)\ ;\ a_{64}=i\beta R_e$$
$$a_{61}=a_{65}=a_{66}=0 \tag{1.5-29}$$

The derivative of equation 1.5-22 is taken to give the identity in Equation 1.5-30.

$$\frac{d^2\psi}{dz^2} = \frac{dA}{dz}\psi + A^2\psi \qquad (1.5\text{-}30)$$

The second term on the right-hand side of Equation 1.5-30 indicates the inner product of the matrix A with itself. The right-hand side is then represented as a matrix operator which operates on the column vector ψ. The new matrix is given the designation B and is defined as below:

$$b_{ij} = \frac{da_{ij}}{dz} + \sum_{k=1}^{6} a_{ik}a_{kj} \qquad (1.5\text{-}31)$$

To obtain eigensolutions a velocity profile of the region immediately downstream of the leading edge slat must be provided. First and second derivatives of the velocity are needed as well.

A cubic-spline fit was applied to the velocity measurements obtained from hot-wire data taken at several positions normal to the model surface. Each hot-film measurement represented a node point in the cubic-spline-fit analysis. In the subinterval $[z_{k-1} - z_k]$ between two nodes or measurement locations, the cubic-spline fit would be calculated using Equations 1.5-32 and 1.5-33.

$$v(z) = \left[\frac{h_k - (z - z_{k-1})}{h_k}\right]v_{k-1} + \frac{[(z_k - z)^3 + h_k^2(z - z_{k-1}) - h_k^3]}{6h_k}v''_{k-1}$$

$$+\left[\frac{z - z_{k-1}}{h_k}\right]v_k + \frac{[(z - z_{k-1})^3 - h_k^2(z - z_{k-1})]}{6h_k}v''_k \qquad (1.5\text{-}32)$$

$$h_k = z_k - z_{k-1} \qquad (1.5-33)$$

The procedure for using a spline fit requires that there exists a smooth continuous transition from one subinterval to the adjoining one. Therefore, from one subinterval to the subsequent subinterval, the second derivative must be the same from one side of the node to the other. When this condition is evoked, then the tridiagonal system equation 1.5-34 is generated.

$$\frac{h_k}{6} v''_{k-1} + \frac{(h_k + h_{k+1})}{3} v''_k + \frac{h_{k+1}}{6} v''_{k+1} = \frac{v_{k+1} - v_k}{h_{k+1}} - \frac{v_k - v_{k-1}}{h_k} \qquad (1.5-34)$$

In this analysis, Equation 1.5-34 was used to construct the tridiagonal system of equations to obtain solutions of the second derivative at each node point. These second derivatives were then substituted into Equation 1.5-32 to solve for the velocity profile at any normalized distance from the model surface. Equation 1.5-32 was then differentiated once and twice to obtain both the first and second derivatives of the normalized velocity as a function of normalized distance from the model wall.

Once the first and second derivatives of the velocity profile are computed at each node point, these values are used in a linear interpolation table to compute both derivatives at predetermined computational grid lines. This grid originates at the wall of the model and extends beyond the viscous shear layer into the region of potential flow. These derivatives are then used to modify those elements of the matrix A, which vary as a function of velocity and its derivatives. This means that at each grid line, a velocity and its derivatives must be computed based on the linear interpolation scheme of Equation 1.5-34. Those

matrix elements that are affected are then recomputed for that unique grid line. After the proper substitutions are made equation 1.5-19 then becomes

$$\psi_i^{\,k} - \frac{h_k}{2}\sum_{j=1}^{6} a_{ij}^{\,k}\psi_j^{\,k} + \frac{h^2{}_k}{12}\sum_{j=1}^{6} b_{ij}^{\,k}\psi_j^{\,k} - [\psi_i^{\,k-1} + \frac{h_k}{2}\sum_{j=1}^{6} a_{ij}^{\,k-1}\psi_j^{\,k-1} + \frac{h^2{}_k}{12}\sum_{j=1}^{6} b_{ij}^{\,k-1}\psi_j^{\,k-1}] = 0 \quad (1.5\text{-}35)$$

Equation 1.5-35 forms a block tridiagonal system, which was then solved with the appropriate boundary equations and far-field conditions. The eigenvalues of normalized wave number and angular frequency are then computed and plotted for a specified Reynolds number.

To verify the accuracy of the computer program, it was first used to compute the eigenvalues for the classical Blasius velocity profile. The velocity profile for this case was derived using a Runge-Kutta algorithm to integrate numerically the well-known nonlinear differential equation. Solutions were obtained for a Reynolds number of 1414. Figure 1.24 shows the expected peak of normalized wave number at some normalized frequency or Strouhal number, which is also being called the fundamental frequency. This frequency is important because it is equivalent to the vortex passage frequency that occurs naturally on the model. It is also important because it can be used to determine which frequency plays the most dominant role in terms of producing turbulence. This would be advantageous if the aim is to deliberately induce turbulence to facilitate boundary-layer reattachment. As will be later explained in greater detail, forcing of the flow field using a subharmonic of the fundamental frequency is responsible for producing vortex pairing, which generates a

coherent system of rapidly spreading vortices. This facilitates the transport of turbulent kinetic energy into the boundary layer.

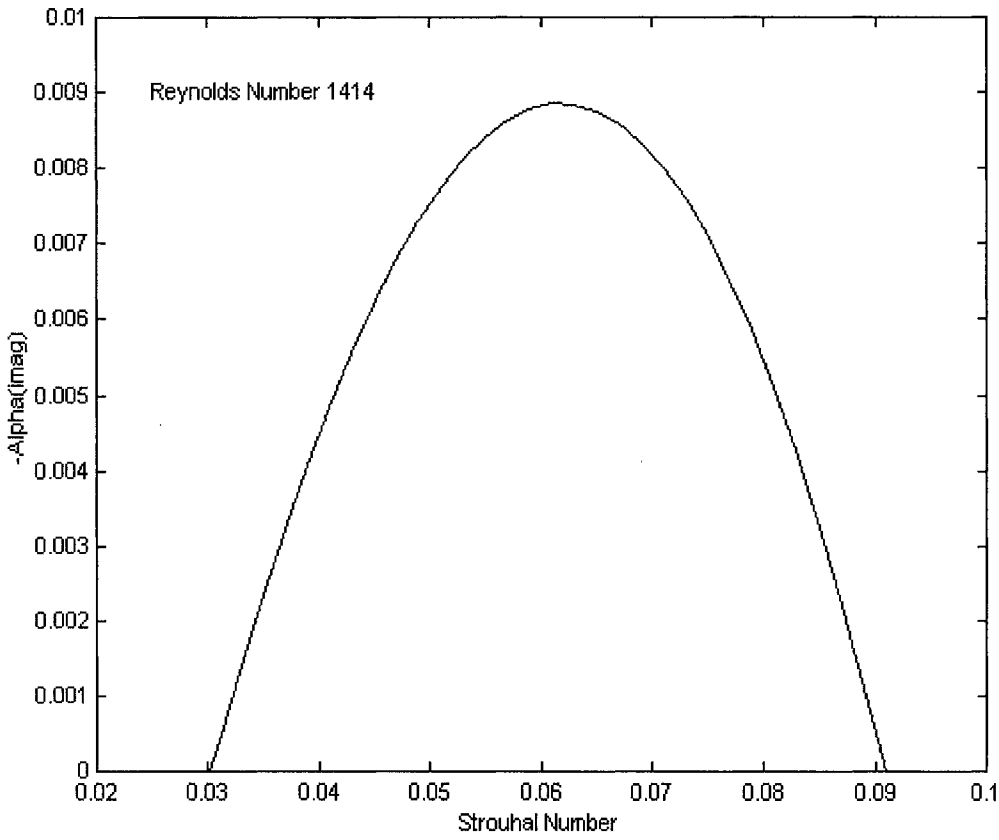

Figure 1.24 – Distribution of Eigenvalues for Blasius Profile on Flat Plate.

The distribution shows the imaginary part of the wave number on the vertical axis and the Strouhal number on the horizontal axis. The Strouhal number in this case is actually a non-dimensional angular frequency. The peak wave number identifies the frequency of the disturbance associated with the largest amplification rate. This corresponds to the disturbance caused by the downstream transport of vortices.

In this dissertation, Linear Stability Theory was applied at Reynolds numbers 290,000 and 9,000,000. The theoretical results showing the relationship between

normalized frequency and Reynolds number for Blasius flow are displayed in Figure 1.25. The vertical axis on the left shows the normalized disturbance frequency and the vertical axis on the right shows the normalized wave velocity. The horizontal axis shows the Reynolds number. The curves indicate the coordinates for neutral stability. The region enclosed within the lower curve is a mapping of those normalized frequencies and Reynolds numbers where the boundary layer is unstable. A vertical line sliced through this curve at a specified Reynolds number indicates the range of normalized frequencies over which there exists boundary-layer instability. The theory demonstrates that both the range and the magnitude of the normalized frequency decrease with increasing Reynolds number.

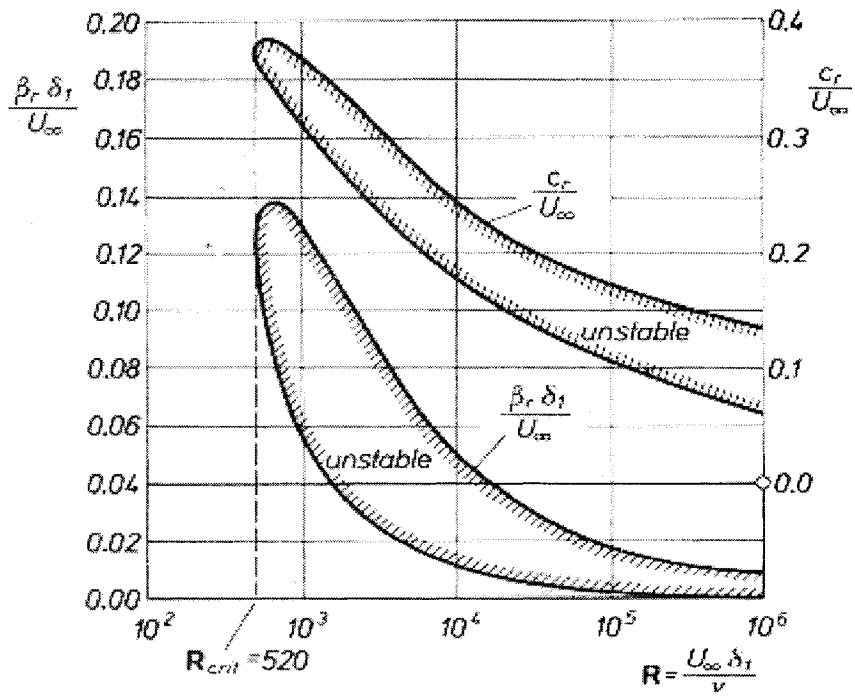

Figure 1.25 – Neutral Stability Curves for Disturbance Frequency and Wave Number.

For the test model used in this experiment, similar solutions were obtained to identify the fundamental frequencies at two selected flow speeds. Based on previous studies, the hypothesis in this experiment was that the fundamental frequency predicted from Linear Stability Theory is the same as the vortex passing frequency. Tordella and Christiansen [1989] used a very similar approach based on linear inviscid stability theory, whereby the fundamental frequency of a disturbance aft of splitter plate was found to be 0.032 and corresponded to the most-amplified disturbance. The forcing frequency of the proposed actuator in this study is predicated on the fundamental frequency of the traveling vortices in the case of no external forcing.

Oscillations in an air stream are known to be caused by the presence of a convecting system of vortices. Taneda [1958] performed an experiment in a water tank and examined the oscillations that are produced in the wake of a flat plate model. He observed that there appeared a system of vortices in the wake for high enough Reynolds numbers and that their presence was detected using a hot-wire probe. His research found that the passage or natural frequency was nearly proportional to 3/2 power of the flow velocity. For this experiment the vortices in question are the ones that emanate from the trailing edge of the slat. These oscillations originate from the difference between the velocities on the upper and lower surfaces of the slat. The dynamic characteristics of these vortices have been reported by Paschal [2000] who observed some unsteadiness in these vortices under certain model orientations and flow conditions.

When first proposed, the object of this experiment was to correlate the correct operating frequency of the external modes of excitation with the vortex frequency of the naturally occurring vortices emanating from the slat wake. Therefore, the determination of

that frequency for various flow conditions was considered paramount to the successful completion of this experiment. The original intention was to place the piezoelectric devices near the leading-edge cove to control this system of vortices in an attempt to influence downstream the airflow over the trailing edge flap. Because early test data showed that no favorable changes were induced in the surface static pressure distribution on the flap, this scheme was abandoned in favor of installing the devices in closer proximity to the rearward cove and the flap. By positioning the devices closer to the area of interest on the model, more significant effects were anticipated in the flow field surrounding the flap. In retrospect, the original concept might have shown merit and further experimentation along those lines could be the subject of future and more in-depth research. However, the investigation of the characteristics of these vortices had merit in its own right. A particularly interesting aspect of this experiment would be to determine if Linear Stability Analysis could be used to predict properties of the propagating disturbances. This was the reason for the inclusion of Linear Stability Analysis into this dissertation.

1.6 Skin Friction Calculations

A method was employed to verify the effectiveness of the piezoelectric devices with regards to the abatement of boundary-layer separation. This method is predicated on the well-known fact that skin friction tends to zero at the location of incipient boundary-layer separation. Accordingly, the skin friction coefficient will approach zero as the extent of boundary layer separation decreases.

The approach for this method of analysis begins with the empirically derived equations, which govern the velocity distribution in a boundary layer. The details of the derivations of these equations are more thoroughly outlined by White [1991]. Extensive

experimentation has demonstrated that the boundary layer is subdivided into three separate regions. The region closest to the surface is an inner viscous sublayer near the surface, where turbulence eddies are damped. The flow phenomena in this layer are governed by the celebrated "law of the wall." [White, F., 1991]. In this region, the normalized velocity profile is generally linear with respect to a normalized distance from the wall. This is followed by an overlap layer characterized by a logarithmic relationship between normalized velocity and a dimensionless distance that is normal to the wall. Finally, there is an outer layer that is characterized by the well-known "velocity defect law." The flow properties occurring in the region of overlap are specified by sets of variables associated with the inner and outer layers. Again, these variables are described [White, F. M., 1991] in Equations 1.6-1 and 1.6-2.

$$\frac{\bar{u}}{v^*} = \frac{1}{\kappa}\ln\frac{yv^*}{\nu} + B \qquad (1.6\text{-}1)$$

$$\frac{U_e - \bar{u}}{v^*} = -\frac{1}{\kappa}\ln\frac{y}{\delta} + A \qquad (1.6\text{-}2)$$

Work done by Coles and Hirst [1968] produced values of 0.41 and 5.0 for the universal constants κ and B, respectively. The value of A was found to depend largely on the pressure gradient. Although these equations supremely predict the flow properties in the region of overlap, they underpredict in the so-called outer layer. To compensate for this discrepancy, Cole's law of the wake is added to the logarithmic equation for the overlap region as is shown in Equation 1.6-3.

$$u^+ = \frac{1}{\kappa}\ln(y^+) + B + \frac{2\Pi}{\kappa} f\left(\frac{y}{\delta}\right) \qquad (1.6\text{-}3)$$

The quantity Π is called the Cole's wake parameter. The normalized variables u^+ and y^+ are defined in Equations 1.6-4 and 1.6-5

$$u^+ = \frac{\bar{u}}{v^*} \qquad (1.6-4)$$

$$y^+ = \frac{yv^*}{\nu} \qquad (1.6-5)$$

The variable v^* is called the wall-friction velocity, which is defined by Equation 1.6-7.

$$v^* = \left(\frac{\tau_w}{\rho}\right)^{1/2} \qquad (1.6-7)$$

After some lengthy algebraic manipulation of the above equations along with the well-known Karman integral relation, a unique relationship can be established between the skin friction coefficient C_f, the Reynolds number based on momentum thickness R_θ, and the shape factor H. The shape factor H is defined by Equation 1.6-8

$$H = \frac{\delta^*}{\theta} \qquad (1.6-8)$$

A curve fit is produced correlating the skin friction coefficient and the Reynolds number, where H is used as a parameter. The result is the relation shown in Equation 1.6-9.

$$C_f = \frac{0.3e^{-1.33H}}{(\log_{10}R_\theta)^{1.74 + 0.31H}} \qquad (1.6-9)$$

The accuracy of this formula is reported to be ±3 percent.

CHAPTER 2

MULTI-ELEMENT AIRFOILS

The test article used in this experiment belongs to a class of lifting surfaces called multi-element airfoils. Because of its capability to provide greater lift and to also extend the angle of attack at which stall occurs, this type of airfoil is the frequent subject of research centered on high-lift aerodynamics. As its name implies, these are lifting surfaces, comprising a main wing with additional high-lift devices such as slats and flaps. As air passes through the slot between the leading-edge slat and the main wing, it has a tendency to conform to the model surface and to stay attached to the wing, thus avoiding form drag and also increasing lift [Kermode, A., 1972]. The purpose of the trailing-edge flap is to provide additional plan form area and to modify the overall camber. A downward deflection of the trailing-edge flap increases the effective angle of attack of the main wing without pitching the airplane [Shevell, R. S., 1983]. This increases the maximum lift coefficient [Shevell, R. S., 1983]. Some configurations feature multiple articulated flaps to improve the lifting performance even further. This experiment seeks to enhance the lifting capability of this airfoil even more by applying flow control techniques to either inhibit boundary-layer separation on the flap or to induce a favorable pressure distribution on the main wing.

2.1 Aerodynamics of Multi-Element Airfoils

Much work has been done, both computationally and experimentally, to understand the underlying physics and to develop the proper design criteria for multi-element airfoils. By way of example, previous researchers [Jones, K. M., et al, 1995] investigated the use of a Reynolds Averaged Navier-Stokes code (CFL3D) for both two-dimensional and three-

dimensional multi-element high-lift systems. Their research employed multi-zonal structured grid techniques to accurately model the complex geometry. Although they were unable to accurately predict the absolute values for lift, they were able to reasonably predict the trends for variations with Reynolds number and flap position. CFD offers distinct advantages over experimental studies, but falls short of accurately predicting flow-field values over multi-element airfoils because of the inherent complexities of the viscous flow field arising from the interactions between the wakes and boundary layers formed from the different model components. At least for now, the expertise of the experimentalist will be relied upon until a comprehensive body of knowledge can be obtained to refine the CFD models.

The main elements of the flow field are shown in Figure 2.1. The challenge for the aerodynamicist is to understand the interactions between the slat wake and the main wing boundary layer, the interplay between the trailing edge flap and the upstream wakes, the influence of the separated flows in the fore and aft cove regions as well as the usual issues associated with shear-layer separation (both on-body and off-body) and transition to turbulence. The region where these multiple viscous-layer interactions occur is called the confluent boundary layer (CBL). Many experiments have been done to obtain a clearer understanding of the complex flow that exists in this region, however very few of these experiments provide a complete set of detailed data [Ying, S. X., et al., 1999]. The flow around a multi-element airfoil is characterized by the strong interactions of the main element boundary layer with both the core of the potential flow through the slot and the wake shed from the slat. This region of confluence grows on the main wing and flap producing a complex velocity profile that extends well into the flow field. Ying et al.

[1999] reported that because of these strong interactions, the CBL can more effectively withstand a much higher overall pressure rise without separation. They also stated that the wake of the slat and main element are able to penetrate regions of high adverse pressure gradient to favorably influence the pressure profile on a lifting surface element. The design of high-lift systems could be greatly hastened by using CFD, but experimental studies are still needed to provide critical information about the complicated flow physics in the CBL. Since the shed vortices embedded in the slat wake play a prominent role in the physics of the overall flow field, the results of this dissertation are important since the dynamics of the vortex field were used as the primary mechanism of energy transport.

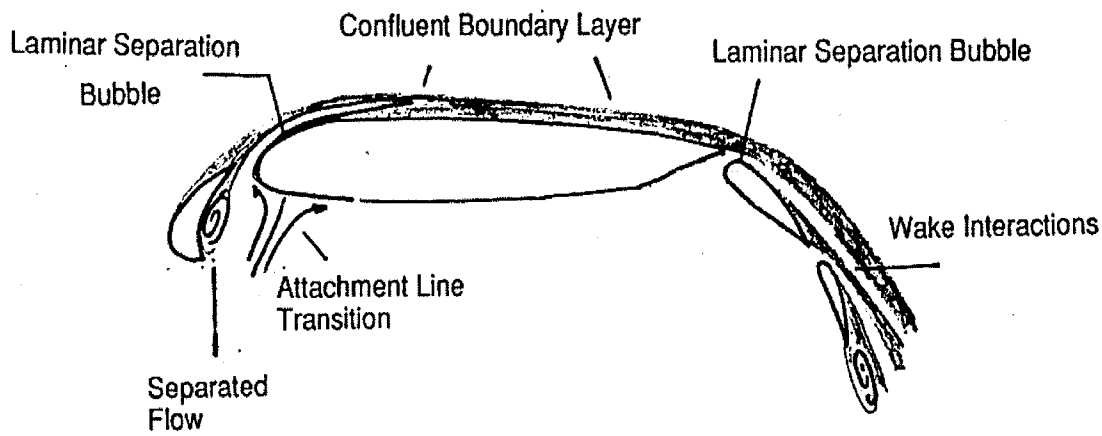

Figure 2.1 – Primary Regions of Flow Around a Multi-Element Airfoil.

Off-body separation occurs on multi-element airfoils when the wake from an upstream element experiences flow reversal. This results from the fact that the deficient velocities in the wake cannot overcome the off-body adverse pressure gradient, which occurs along the rear of the model. Another concern is the effect that unsteadiness,

particularly in the cove region between the slat and main wing, has on the aerodynamic characteristics. The resolution of these issues is worth the effort because of the tremendous advantages offered by multi-element airfoils. Figures 2.2a and 2.2b demonstrate the substantial increment in lift that results from both the trailing-edge flap and the leading-edge slat. These results show that the lift is substantially increased for higher flap deflection angles. The increased C_{Lmax} is very beneficial especially during the takeoff and landing stages of the flight since it is inversely proportional to the takeoff and landing speeds. For example, if during takeoff the C_{Lmax} is larger due to efficient flap design then the speed at lift off can be decreased and the runway can be made shorter. Furthermore, when the lift has been augmented by suitable flap deflection the landing speed can be diminished, which is desirable for safety reasons. However, the data show that one undesirable effect of increased flap deflection is the decreased angle of attack at stall.

The data also show that the effect of the slat is to extend the angle of attack before the wing is stalled. Moreover, the data show that sizable increments in lift can be achieved at higher angles of attack. At the higher angles of attack, the aircraft must be designed such that the view of the pilot is not obstructed by the nose of the plane and that the tail is designed so that it does not make contact with the ground during landing.

These results suggest that the undesirable effects of the flap and slat can be remedied if some other technique could be used to provide the additional lift. The techniques discussed in this dissertation aim to enhance the lift of the airfoil without the deleterious effects of decreased stall angle and the required structural accommodations. These techniques offer the designer more flexibility and increase the number of options to achieve adequate lift for the various stages of flight. The designer would have at

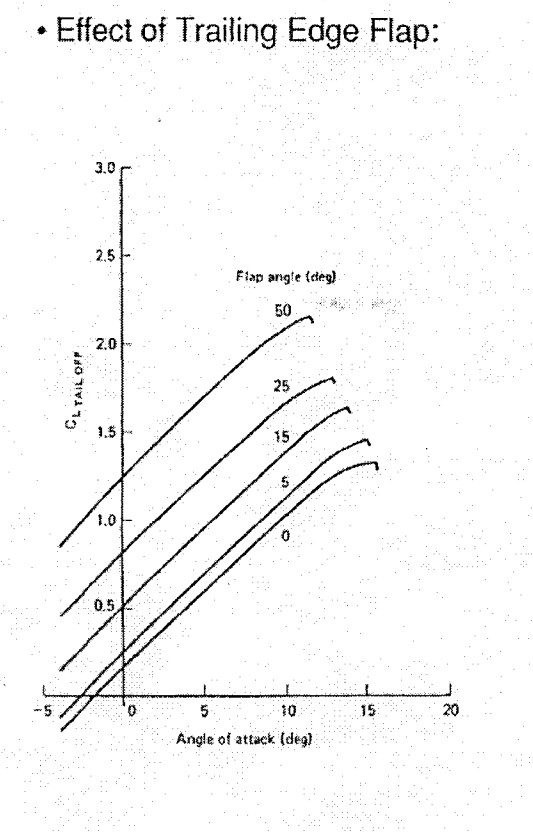

Figure 2.2a – Effect of Trailing Edge Flap Angle on Lift Coefficient
Reprinted by permission of Douglas Aircraft Company

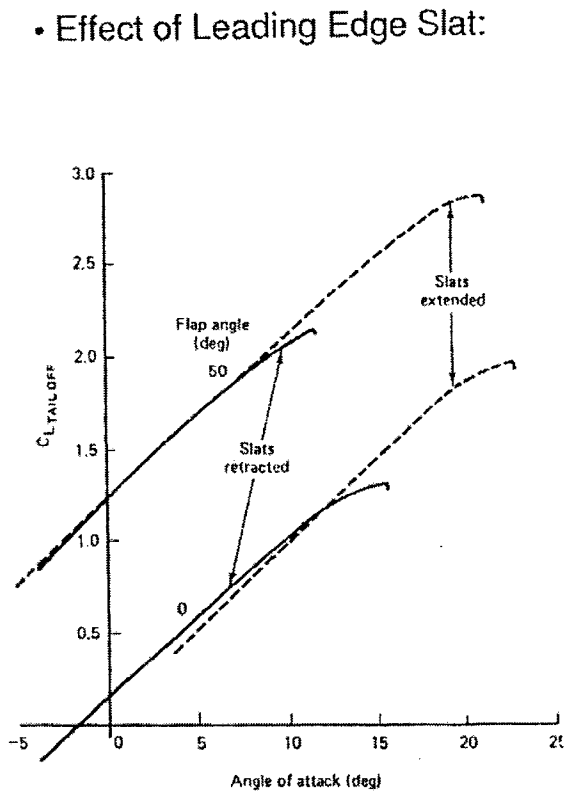

Figure 2.2b Effect of Leading Edge Slat Angle on Lift Coefficient
Reprinted by permission of Douglas Aircraft Company

his/her disposal the slat and flap setting and possibly a technique as discussed in this dissertation. The techniques tested in this experiment could assist the slat and flap by being made part of a feed-back loop design to provide increments in lift for variations of flow field conditions.

Attention will now be given to the qualitative description of the mechanisms that give rise to the aforementioned characteristics. According to Smith [1975], five primary

effects govern the flow field around multi-element airfoils. These effects are the slat effect, the circulation effect, the dumping effect, off-surface pressure recovery, and the fresh boundary-layer effect.

2.1.1 The Slat Effect

Reasons given as to why the slat provides the aerodynamic advantages that it does have been controversial. Smith [1975] reports that the most prevailing misconception has been that the air originating from the slot is high-energy air that energizes the boundary layer on the main wing to moderate separation. He traces this idea to no less an authority than Ludwig Prandtl [1904] who stated that:

> "The air coming out of a slot blows into the boundary layer on the top of the wing and imparts fresh momentum to the particles in it, which have been slowed down by the action of viscosity. Owing to this help the particles are able to reach the sharp rear edge without breaking away."

Other researchers have followed the model proposed by Prandtl [1904] by exclaiming that the slot increases the local velocity so that the boundary layer flow can prevail against the adverse pressure gradient. Smith [1975] continues by saying that the flow is actually slowed down as it passes through the slot because the circulation caused by the slat runs counter to the main wing circulation. Figure 2.3 shows the effect of an idealized leading-edge vortex on the main wing. The figure depicts the local velocity versus the arc length along the wing. The effect of the vortex is to lessen the velocity peak on the wing, which in some cases would mitigate a strong suction peak at the leading edge. This can be beneficial because sharp suction peaks often give rise to separation and/or transition, due to the strong adverse pressure gradients downstream of the suction peak. Another advantage of decreasing the strong suction peak at the leading edge is the fact that it is more beneficial to distribute the surface pressure along as much of the wing plan form

area as possible to increase the total lift. Thus, the role of the leading edge slat in terms of enhancing the total lift is multifaceted. Not only does the slat help to maintain a streamlined flow over the wing but it also reduces the undesirable leading edge pressure peak.

The plot in Figure 2.3 demonstrates that when the airfoil is placed downstream of a leading edge slat, the velocity ratio on the upper surface does not exhibit the notably sharp and high peak that occurs in the absence of the slat. The velocity ratio in this case was the velocity at the edge of the boundary layer normalized by the free stream velocity. This shows that, contrary to popular belief, the effect of the slat is to suppress the magnitude of the peak velocity ratio.

2.1.2 The Circulation Effect

The circulation effect pertains to the influence of a downstream element on the circulation of an adjoining element positioned upstream. In this discussion, the circulation of the wing induces a greater circulation about the leading-edge slat and of an airfoil, this phenomenon can be described in terms of potential theory. As shown in Figure 2.4, the vortex at the trailing edge has the effect of deflecting the local velocity at the wing trailing edge. As shown in Figure 2.4, the effect of the downstream element (flap) is to increase the circulation of the forward element. This increased circulation causes the air particles on the upstream element to move with a higher velocity. This results in lower static pressures on the upper surface with the attendant greater suction and higher lift. These results demonstrate the strong interactions that exist between the various elements that make up the multi-element airfoil.

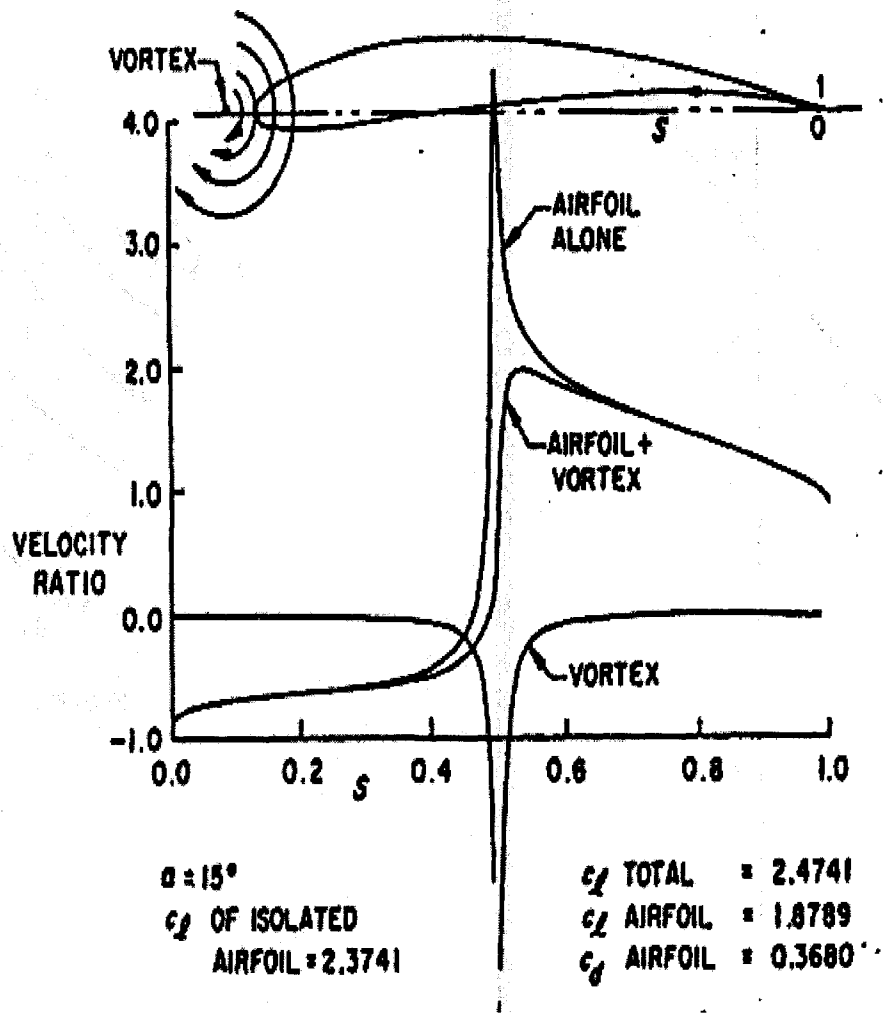

Figure 2.3 – Velocity Distribution on Wing due to Upstream Circulation.

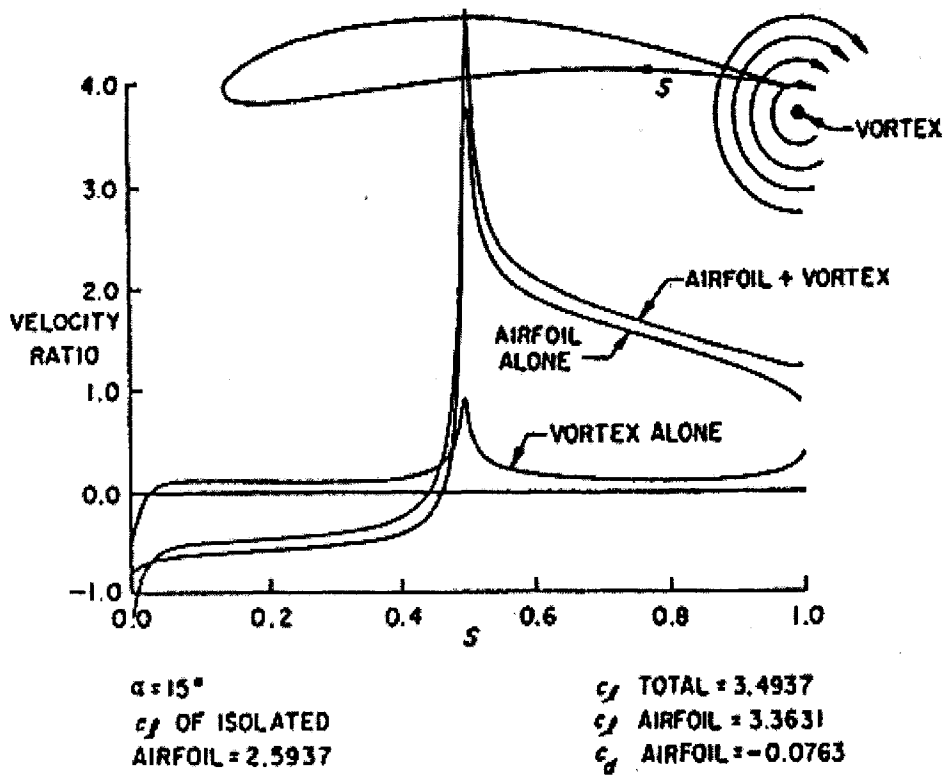

Figure 2.4 – Velocity Distribution on Wing due to Downstream Circulation.

2.1.3 The Dumping Effect

The dumping effect is closely associated with the circulation effect, previously described. Because the velocity on the upper surface of the upstream element is increased, its boundary layer is "dumped' at a higher discharge velocity onto the downstream element, which relieves the pressure rise developing on the subsequent element. This coupling

between the two elements results in the elimination of boundary-layer separation on the second element hence produces a lift increment.

2.1.4 Off-The-Surface Pressure Recovery

Boundary-layer separation occurs primarily when the surface flow has decelerated to such an extent that it cannot penetrate a region of reversed flow caused by an adverse pressure gradient. However, for multi-element airfoils, a large part of the deceleration occurs off the body, resulting in the boundary layer being able to more adequately meet the pressure-rise demands on the surface.

2.1.5 Fresh Boundary-Layer Effect

As the oncoming flow approaches each element, a fresh boundary layer forms at the leading edge. Thin boundary layers are known to be able to withstand adverse pressure gradients better than thicker ones. This fact would imply that because thinner boundary layers exist at higher Reynolds numbers, the ground-based estimates of lift coefficient would serve as conservative estimates. However, full-scale flight tests have confirmed that in some cases the lifting capabilities of aircraft degrade at the higher Reynolds numbers. Mack and McMasters [1992] have presented these results. The relevant data are shown in Figure 2.5.

Bourassa, et al. [2000] and Yip et al. [1995] have suggested that the inverse Reynolds number effect is caused by the transition to turbulence of the flow at the reattachment line near the leading edge of a main wing. At realistic flight Reynolds numbers, the flow can become turbulent at the reattachment line, which shifts forward the location on the main wing where turbulence commences. Since the turbulent boundary layer has more distance to grow, this forward advancement of the transition point has the

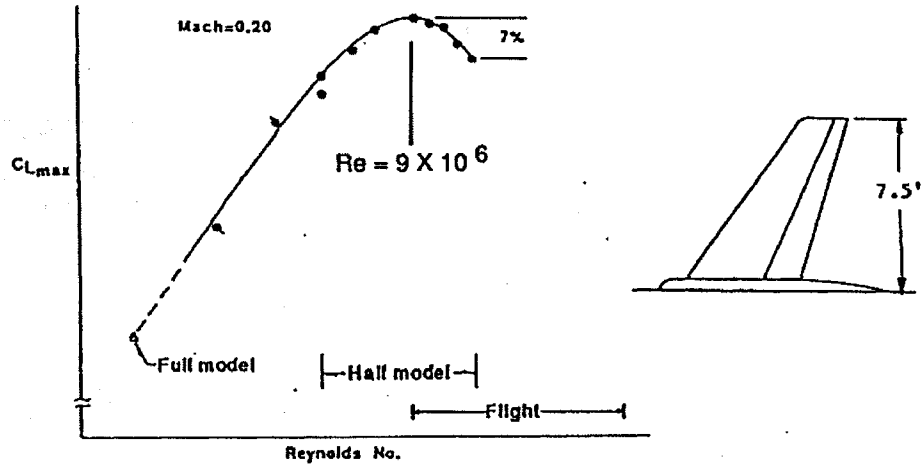

Figure 2.5 – Degradation of C_{Lmax} due to Inverse Reynolds Number Effect.

effect of also shifting forward the flow separation point. A result of this occurrence is that the percentage of the wing upper surface subjected to a separated boundary layer has increased, which decreases the lift coefficient.

2.2 Previous Studies Involving Multi-Element Airfoils

Bario [1982] conducted a wind tunnel test, which was designed to study the confluence of a wake with a boundary layer. In this experiment, two separate airfoils were suspended from the ceiling of the tunnel using jacks and piano wire. The shorter airfoil was located upstream of the second airfoil and simulated the presence of a slat. Again, the primary motivation was to ascertain the effect and degree of interaction between the wake of the first airfoil and the boundary layer of the second. The floor of the test section was capable of having a variable contour to produce the needed adverse pressure gradient to force separation. The data showing the velocity fluctuations u′ and v′ indicated that the longitudinal component is always larger than the normal component. Furthermore, the

kinetic energy originating from the mean flow is transferred mainly to the longitudinal fluctuating velocity, which eventually gets redistributed through the pressure field in both the normal and traverse directions. Their conclusions included the fact that the "law of the wall" and the 'law of the wake" provide valid descriptions of the velocity profile observed in the region characterized by an adverse pressure gradient. The researchers also used a Preston tube and plots by Clauser to obtain skin friction measurements. In that regard, they found that the location of zero shear stress did not correspond to the position of zero velocity gradient in the normal direction. This result has been duplicated in several experiments and indicates that, at least for some flow conditions, the Boussinesq assumption for turbulence modeling is invalid. Researchers in the field of fluid mechanics have assumed that the turbulent stress is directly proportional to the product of the eddy viscosity and the gradient of the mean velocity in the direction normal to the wall. This relationship is shown in Equation 2.1

$$-\overline{u'v'} = \varepsilon \frac{\partial U_\infty}{\partial y} \qquad (2.1)$$

The turbulent stress is shown to be equal to the negative of the cross-correlation of the fluctuating velocities in the longitudinal and normal directions. Normally, if the mean velocity gradient is positive, then momentum is transferred downward to the wall, which corresponds to a negative value for the fluctuating velocity v'. The result is that both sides of Equation 2.1 are positive. However, some researchers [Hinze, J. O., 1970] have experimentally found that sometimes the terms on both sides of Equation 2.1 are not equal to zero at the same location in the boundary layer. In the region between the two different

locations where the terms are zero, they have opposite signs, which would imply a negative eddy viscosity [Hinze, J. O., 1970]. Hinze [1970] circumvented this dilemma by proposing that the exchange of momentum between adjoining planes in the boundary layer is governed by an additional term not associated with the gradient of the mean velocity. He proposed the relationship shown in Equation 2.2.

$$-\overline{u'v'} = \varepsilon \frac{\partial U_\infty}{\partial y} - \frac{1}{2}\overline{v'(0)y^2}\frac{d^2U_\infty}{dy^2} \qquad (2.2)$$

In one particular study [Nakayama, A., et al., 1990], detailed measurements of the mean velocity profiles and turbulence quantities were made around a multi-element airfoil using hot-wire probes. These measurements were obtained in the NASA Langley Research Center Low Turbulence Pressure Tunnel (LTPT). Data were taken at a chord Reynolds number of 3×10^6 and a free-stream Mach number of 0.2. The purpose of the test was to provide experimental data that could be used to refine numerical codes by supplying a more realistic representation of complex shear flows. The model used in the study [Nakayama, A., et al., 1990] was a geometry that was grit-free with a slat, wing and trailing-edge flap with a stowed chord length of 22 in. To cross check the mean velocity profiles, a five hole pressure probe was also used. The results of the study were shown by plotting the mean velocity vectors and turbulent stresses around a computerized drawing of the model. Of particular interest were the profiles of turbulent stress because this can be used an indicator of the degree of mixing that has occurred in the confluent region around a multi-element airfoil. It is hypothesized that the mixing that occurs in the region of confluence serves as a mechanism for the transfer of turbulent kinetic energy and

momentum into an otherwise low-energy boundary layer. Figure 2.6 shows the profiles of the turbulent stress at specific normalized chord locations on the main wing, flap and in the wake. Figure 2.7 shows the global variation of fluctuating properties for several stream-wise locations.

The turbulence on multi-element airfoils is important because of the interaction of the wake of upstream surfaces with the boundary layers of downstream elements. The flow field on a multi-element airfoil is characterized by thicker wakes in the near field region due to the wake/boundary layer confluence.

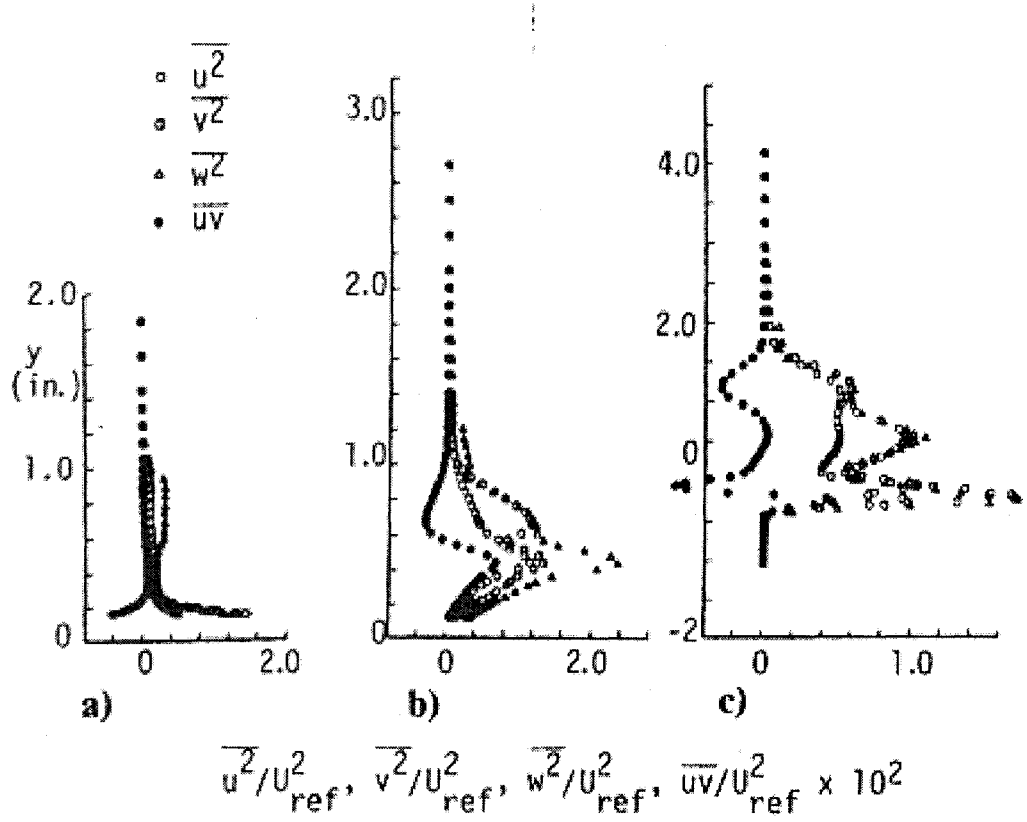

Figure 2.6 - Fluctuating Flow Properties on a Multi-Element Airfoil; Reynolds Number 3 Million (a) Main Wing, (b) Flap (c) Wake.

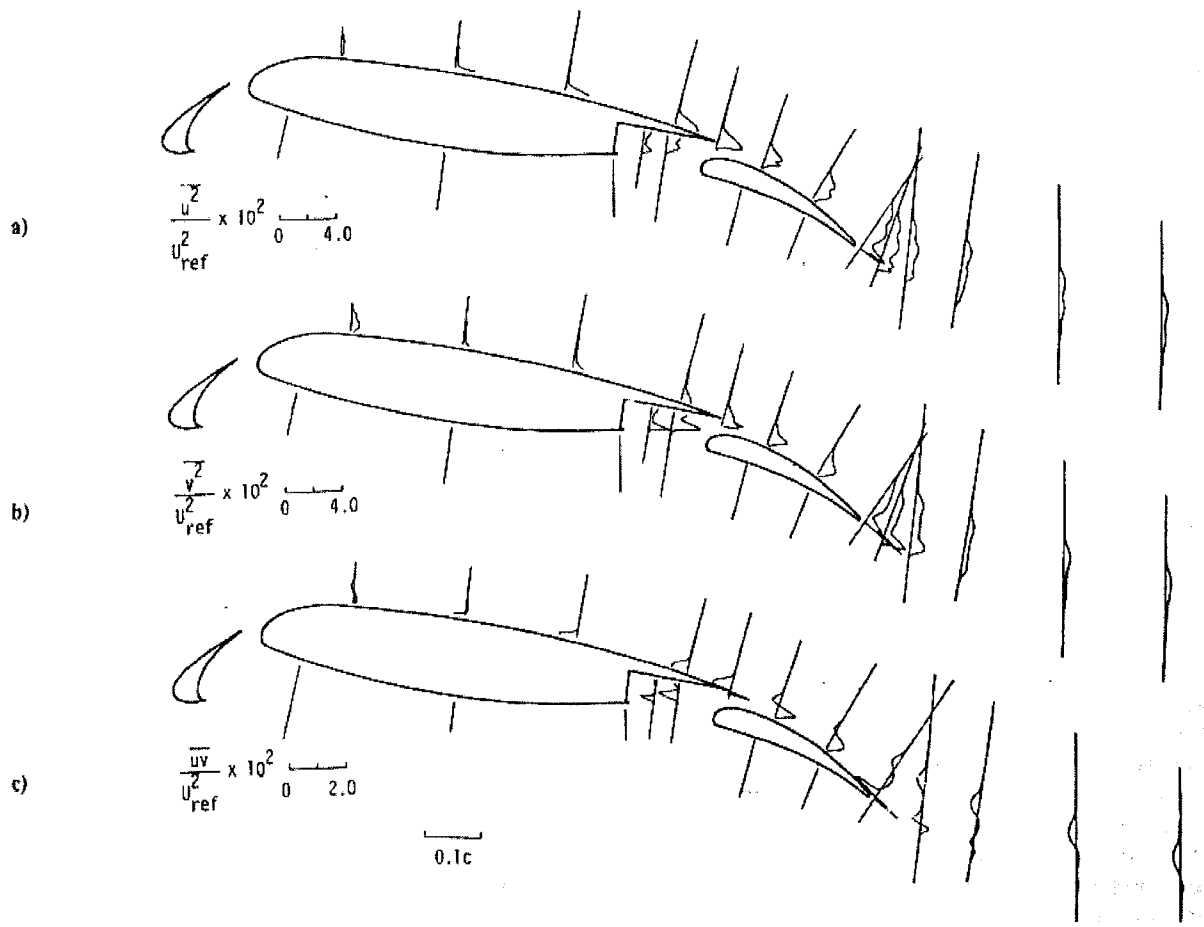

Figure 2.7 - Global Variation of Fluctuating Flow Properties on a Multi-Element Airfoil, Reynolds Number 3 Million.

Flow field measurements were obtained using the McDonnell Douglas three-element airfoil again by Chin et al. [1993], in the LTPT at NASA LaRC. In similar fashion to earlier reported investigations, the purpose of this experiment was to enhance the understanding of the slat wake/main element boundary-layer interaction. The test condition variables were Reynolds number, angle of attack, and slat and flap gap riggings. Both a

flat-tube probe and a hemispherical probe were used to obtain boundary-layer and off-body flow field pressure measurements, respectively. Velocity profiles were obtained at an angle of attack of 8°. The most forward longitudinal model station was located at x/c = 0.45. At this model station for a Reynolds number of 9 million, the main element boundary-layer profile appears to be full and monotonic and shows no vestiges of the slat wake. On the contrary, the profiles of the flap indicated that the boundary layer was on the verge of separation. At the higher angles of attack of 16° and 21°, the velocity profiles at the most forward model station showed the influence of the slat wake, and the flap boundary layer is more full than at the 8° angle of attack. They also observed that at the higher angles of attack the centerline of the main-element wake has markedly diverged from the flap upper surface, so much so that their probe traversing system was unable to capture the full extent of the wake. They also observed some unsteadiness in the aft profiles at the 21° angle of attack. To gage the effect of model scale, data were taken at different Reynolds numbers. Data were collected at a Mach number of 0.2 at Reynolds numbers of 5 and 9 million. The data showed that the integrated lift was greater at the higher Reynolds number with the increment increasing as the angle of attack increases. Slightly more negative suction peaks were observed on the flap at the higher Reynolds number over the range of selected angles of attack. In agreement with other tests reported, the C_{lmax} was improved by increasing the flap gap and the angle of attack at stall increased by 1° at the wider gap setting. Moreover, they found that for the larger flap gap the wake deficit is smaller at the downstream stations for all angles of attack and that there is less wake spreading at the angle of attack producing the maximum lift coefficient. They also found that the main-element wake and the flap

boundary layer demonstrated less of a tendency to merge and that there was less off-body flow reversal.

Klausmeyer [1996] performed an experimental study involving the use of vortex generators (VG) placed on the flap to increase the maximum lift. They utilized a Laser Doppler Velocimeter (LDV) to obtain images of the velocity field on the multi-element airfoil. Measurements were obtained in the Shear Layer Research Wind Tunnel at NASA LaRC. The flow velocity was set at a Mach number of 0.15 at a Reynolds number of 1.2 million. The angle of attack selected for this study was 8°, which was considered to be the typical angle of approach. Their intent was to gain a better understanding of the flow physics involved in the interaction between vortices and the confluent boundary layer over the flap. This was done by characterizing vortex structures, examining vortex paths, and analyzing the streamwise decay of vortices shed from these vortex generators. They also took measurements of the velocities in all three directions as well as the various turbulent stress quantities.

Their findings showed that separation could be markedly alleviated on the flap. Without the vortex generators, the researchers found that the surface static pressure on the leeward side of the flap exhibited a flat distribution. This absence of the usual pressure recovery was indicative of boundary-layer separation. When the model was equipped with vortex generators, the pressure distribution showed an improved recovery, which indicated the absence of separation. They found that with the vortex generators, the lift coefficient was increased by 4.5%.

Spaid [1996] also tested the basic three-element airfoil in the NASA LaRC LTPT to obtain flowfield measurements at flow conditions meant to be comparable to full-scale

flight conditions. Their objective was to shed more light on the underlying physics of the complex flow interactions about multi-element airfoils. The instrumentation employed for this study included electronic scanning pressure (ESP) modules, which were used for measuring surface static pressures on the model. They also used a flattened pitot probe and a hemispherical five-hole probe. The former was used for making boundary-layer measurements and the latter was used to make measurements in the flow field such as total pressure, static pressure, velocity, and flow angularity. The researchers examined the effect that various slat and flap riggings had on the aerodynamic characteristics of the multi-element airfoil. Their findings indicated that small increases in flap gap (e.g., 0.23%) resulted in improved lift. Additionally, they found that the C_{lmax} increased by an increment of 0.05 when the gap size was increased as noted. For the range of flow variables and model attitudes used in this test, there were no significant changes to the flow field over the main wing. The researchers in this study examined the effect of slat gap on the flow field about the main wing as well as the global effects. At the 21° angle of attack, corresponding to maximum lift they found that the suction peak on the main wing showed a slight increase for the configuration where the slat gap was narrower. They also found that values of C_p were higher near the slat trailing edge at the narrower slat gap setting. This they concluded was due to the closer proximity of the slat to the stagnation point on the main wing. They also took velocity profiles of the region of confluence and observed that the greater gap size caused the velocity deficit in the outer wake to occur at a location farther away from the model surface. The increase in slat gap did not reach the point at which there was a concern with the phenomenon of slat-wake spreading and merging. This would have significant repercussions on the displacement of streamlines on the flap resulting in

the unloading of the flap as well as the aft portion of the main wing. Their flow field measurements about the slat also showed that, as the angle of attack increased, the total pressure deficit in the wake became more severe and that this correlated with the forward shift of the point of boundary layer transition on the slat. They also varied the flap deflection angle and observed that, at the angle of attack near maximum lift, increasing the flap deflection increased the displacement above the flap. That is, the flow did not follow the flap deflection. This displacement results in a lessened lift capability for the flap. In general, they concluded that flap riggings needed to be selected which minimize the merging and spreading of the wakes from upstream elements and the flap wake. This must be done to ensure the required amount of loading on the flap for optimal performance.

An experimental wind tunnel test was conducted by Thomas et al. [1998], to study the unsteadiness of flow in the confluent region and its effects on the aerodynamic performance of a multi-element airfoil. They concluded that the unsteadiness resulted from the aggressive mixing between the slat wake and main wing boundary layer. Moreover, they postulated that, because of the unsteadiness, enhanced mixing of the slat wake and the main wing boundary layer occurred. This resulted in a thicker viscous layer near the model wall, which was therefore more susceptible to separation when subjected to the downstream adverse pressure gradient. However, the research reported in this dissertation attempted to show that external excitation at specific frequencies can cause the vortices in the flow-field to become coherent. It is being hypothesized that these organized structures become a more efficient mechanism for transferring turbulent kinetic energy into the boundary layer. When operating in this mode, the increased mixing in the flow field and boundary layer becomes an advantage that tends to mitigate separation of the boundary

layer. The study reported in this dissertation used smart skin actuators and a loudspeaker to harness the energy in the system of vortices emanating from the slat via the mechanism of vortex pairing. In the study reported by Thomas [1998], LDV surveys were performed for several slat gap and overhang settings. Their multi-element test article was tested in the Hessert Center for Aerospace Research at the University of Notre Dame. The nominal Reynolds number was 1.1 million. The data indicated that the velocity profiles exhibited scatter, which is indicative of the unsteadiness in the slat wake region. Using hot-wire anemometry, they observed that the largest velocity fluctuations were found around the lower slat surface and approached levels of 23%. One of their conclusions was that some of the disparity between the results from theoretical codes and experimental results could be due to the fact that the observed unsteadiness is not accounted for in these codes.

An experimental study was performed by McGinley [1998] with a "McDonnell Douglas model" similar to the test article that was used in this experiment. Their investigation was motivated by the fact that current theoretical codes are unable to adequately predict the location of transition on a multi-element airfoil. The fault is thought to result from imperfections in the turbulence modeling and the extent to which imperfections can be determined by comparing the predicted values of Reynolds stress with the experimentally determined values. Measurements were obtained in the NASA LaRC LTPT at a free stream Mach number of 0.2. Surveys of the Reynolds stress were made using both single axis and cross-axis hot-wire probes. The data obtained in the slat wake region showed unsteadiness in the flow-field, and this unsteadiness was thought to originate in the slat cove region. The reason could be that the recirculation region in the cove is breaking down and reforming. They reasoned that this ultimately led to the velocity

deficit in the slat wake region being rather diffused. This effect was most pronounced at lower angles of attack, particularly at 4° and at 8°.

Ying [1999] conducted an investigation comparing the experimentally determined flow field trends exhibited on a multi-element high-lift airfoil with predictions from a thin-layer Reynolds Averaged Navier-Stokes computer code called CFL3D. The test article they used was identical to the one featured in this study and was installed in the LTPT at the NASA Langley Research Center (LaRC) in Hampton VA. Their study was conducted at a Mach number of 0.2 with a Reynolds number range between 5 to 16 million, based on the stowed-chord length. They subdivided the confluent boundary layer (CBL) into three regions: the wall layer, the inner half wake, and the outer half wake. They concluded that for the predictive method, the rate of convergence was strongly dependent upon the correct modeling of the slat wake. They also found that the larger the wake deficit, the more the flow over the main wing was displaced, resulting in overall loss of lift. Thus, the slat wake had the effect of decambering the main wing. Increasing the Reynolds number is known to result in a thinner slat boundary layer. The effect of increased Reynolds number is to result in a wake deficit less severe, reducing the flow-field displacement over the main wing and resulting in improved lift.

The data demonstrated the fact that the same trend showing a direct positive relationship between lift and Reynolds number could be replicated by increasing the amount of flap overhang (horizontal distance from the main wing trailing edge). Indeed they found that they could increase the lift coefficient by 0.043 when the flap overhang was increased by 0.23% of the chord length. In their experiment the maximum lift coefficient was 4.5624 based on all three elements at 21° angle of attack.

Paschal et al. [2000], also studied the flow field characteristics of the same model. Their experimental study was conducted in the Basic Aerodynamics Research Tunnel (BART) at NASA LaRC. Measurements were made at a Mach number of 0.15 and a Reynolds number of 1.5 million based on the stowed-chord length of the model. Again, their study was also motivated by the need to improve the modeling of the slat and wake at relevant flight angles of attack. Without this capability, computational codes will continue to fall short of accurately predicting the aerodynamic performance of multi-element airfoils. Their investigation utilized a Particle Image Velocimeter (PIV) system to obtain mappings of the velocity vector fields for 4°, 8°, and 10° angles of attack. Supporting the results reported previously, their findings reveal significant unsteadiness associated with the slat wake, especially at lower angles of attack. They also found that the slat wake was diffuse and contained disorganized structures. They concluded that this unsteadiness in the slat wake must be addressed before accurate predictions can be computed of slat and main wing transition locations.

2.3 Dissertation Objective

The proposed research will focus on a well-known, three-element airfoil for which an extensive experimental and computational database already exists. The hypothesis was that the aerodynamic performance of this test article could be improved by the application of flow control techniques. Earlier studies have suggested that forced excitation of the flow around an airfoil serves as a viable means towards favorably affecting its aerodynamic performance. Boundary-layer separation can be delayed by introducing energy into the boundary layer (e.g., so-called smart skin actuators). The devices chosen for this study are piezoelectric actuators developed by THUNDER™ technology that mechanically oscillate

in response to a drive voltage. The frequency of oscillation is equal to the frequency of the drive signal. This external excitation is proposed to enhance spanwise vortex pairing in the wall shear layer. As a result of this phenomenon, the spreading rate of the mixing layer in the confluent region will grow more rapidly and become more coherent. With increased mixing the turbulent kinetic energy from the confluent wake will diffuse towards the wall of the model. Thus energized, the boundary layer will be better able to withstand the adverse pressure gradient existing on the rearward portion of the multi-element airfoil. This process will tend to either delay separation or facilitate boundary-layer reattachment.

An alternative control technique that will be used to test the same hypothesis is the utilization of sound energy from a loudspeaker to either affect the amount of turbulent kinetic energy in the flow field or by using the acoustic waves to influence the phase relationship between adjoining vortices, which propagate downstream from the slat region to the flap. As with the part of the test involving the piezoelectric devices, the main interest is with the performance of the surface pressure distribution on the flap. The objective is to drive the loudspeaker with different frequencies to ascertain the dependence of the flap surface static pressure upon operating frequency. Of course, the ideal objective is to find a practical way using the two methods outlined above to prevent or delay boundary-layer separation. However, some measure of success will be attributed to either methodology if the flow field boundary-layer profile exhibits more favorable characteristics because external excitation was implemented.

To establish a set of reference data, the first step is to conduct an investigation of the flow physics on the multi-element airfoil without the external forcing of the actuators. The types of data to be obtained include surface static pressure; smoke flow visualization;

spectral data and cross-correlation analysis. A very crucial set of test runs include the determination of the passing frequencies of the system of vortices emanating from the leading-edge slat. These frequencies at various flow conditions will be determined through hot-film measurements and smoke visualization. These frequencies will, henceforth, be called the natural frequencies. The smart skin actuators will then be placed on the model and driven electronically by a signal generator tuned at various harmonics and subharmonics of the natural frequencies.

CHAPTER 3

EXPERIMENTAL COMPONENTS

This section outlines the basic hardware and software components used in this study. Generally, this section provides a description of the basic tools employed in this experiment but not a detailed account of the actual test procedures and analyses that were conducted to obtain data. Chapter 4 will give a description of how these hardware and software tools were implemented to acquire experimental results.

3.1 Hardware Considerations

The hardware used in this experiment consisted of three main groups; first the multi-element airfoil, second all data gathering instrumentation including the wind tunnel, hot-film sensors, anemometer and pressure transducers and lastly the external excitation devices, including the piezoelectric devices and the loudspeaker. The following sections outline these various hardware components.

3.1.1 Model Geometry

The test article used in this investigation was a three-element airfoil that consisted of a leading-edge slat, a main wing and a trailing-edge flap. Landman [1998] describes the details of its geometry and presented the entire attendant set of mechanical drawings. The model was designed by Landman [1998] to possess characteristics that typify a modern civil transport. It was provided to a host of researchers by the Douglas Aircraft Company and has served as a test article for CFD code validation studies [Klausmeyer, S. M. and Lin, J. C., 1997].

When the model is configured in the stowed position, the chord length is 18 in and the span is 36 in. The aspect ratio was designed to establish a two-dimensional flow field

over the model. The slat and the main wing were machined from aluminum, whereas the trailing flap was made from stainless steel. The model was machined to a tolerance of 0.0005 inches with reference to its theoretical contour specifications.

The slat was affixed to the main wing by four stainless steel brackets and was designed so that the incident angle was 30°. The vertical displacement of the slat can be changed by inserting the appropriate number of shims at the points where the slat is mated with the wing brackets. The slat can be moved either fore or aft along screw slots, which are located in the wing brackets. Different mounting brackets were designed to modify the incident angle for the slat. The flap was capable of being driven by four servomotors that were housed in the interior cavity of the main wing. This capability allowed the flap to be deflected at selected angles. For this experiment, incidence angle of the flap was maintained at a fixed angle of 30°. The flap was designed to travel on two brackets, which were capable of a vertical translation on dual pins and horizontally on machined dovetails. The brackets were designed with the required rigidity to assure that the gap between the flap and the main element remained constant.

The multi-element model was instrumented with pressure orifices to obtain surface static pressure measurements, which are used to compute the lift coefficient. The pressure orifices had a diameter of 0.02 in and were plumbed to stainless steel tubing with an outside diameter of 0.04 in.

The main wing was instrumented as well as with a row of off-centerline orifices to check for the two-dimensionality of the surface static pressures. Additionally, some pressure orifices are placed spanwise on the trailing edge flap.

The trailing edge flap had 25 pressure tap locations, 19 of which were placed along the chord midspan. A total of 6 pressure taps were located spanwise near the trailing edge. A total of 7 pressure taps were located along the centerline of the slat.

The pressure tubing was routed from the model through a slotted aluminum disk that was abutted to the bottom of the test section sealed over a hole in the tunnel floor. From there, the tubing went to pressure instrumentation located outside the wind tunnel. More details about the pressure measurement system are outlined in a subsequent section.

As was mentioned earlier, two methods were explored as a way to externally excite the boundary layer on a multi-element airfoil. One method used the THUNDER™ piezoelectric actuators and the other method used a loudspeaker, rated at 75 watts. An oscillator that could be tuned at various output frequencies delivered a signal that was amplified by a voltage amplifier, which drove each device. All measurements were obtained with a pair of 3/16 in thick Plexiglas® sidewalls placed on the model to ensure that the observed flow field was two-dimensional. The sidewalls were held in place by 1/4-in-diameter Plexiglas® rods, which were fastened to both the tunnel ceiling and floor. The clearances between the model surface and the sidewalls were filled with silicon rubber to avoid leakage. The sidewalls helped to ensure that that the flow over the model was two-dimensional.

Figure 3.1 shows the rigging nomenclature for the slat and flap on a multi-element airfoil. Figure 3.2 shows the typical slat and flap settings for the stages of flight, namely, cruise, take-off, and landing. For this test, the various slat and flap settings were as follows:

δ_s (slat deflection) = 30 °

G_s (slat gap) = 2.7%

Os (slat overhang) = -0.7%

δ_F (flap deflection) = 30°

G_F (flap gap) = 2.7%

O_F (flap overhang) = 0.7%

The rigging settings were based on the nested chord length of 18 in. This particular configuration was unaltered throughout the duration of the experiment.

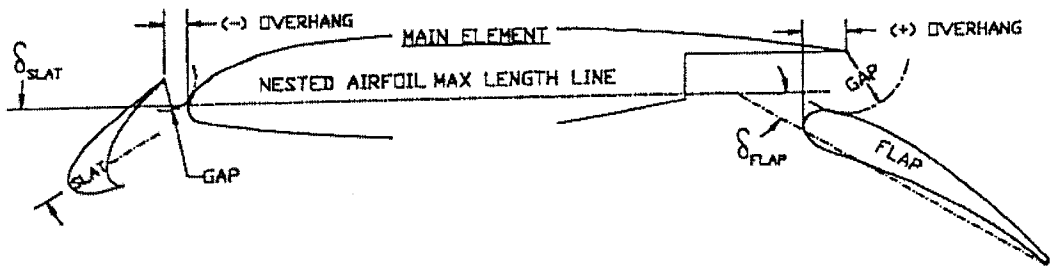

Figure 3.1 – Nomenclature of Rigging Settings for Multi-Element Airfoil
From Landman, D. 1998 – Reprinted with permission from author

These slat and flap riggings as shown above were tested at low Reynolds numbers. One of the most troublesome tasks of the aerodynamics engineer is to extrapolate the high lift characteristics of configurations with their various slat and flap settings from wind

tunnel data to full-scale high Reynolds number performance parameters. Historically, the assumption has been made that the aerodynamic characteristics of a particular configuration follow a linear trend as a function of Reynolds number [Mack, M. D. and McMasters, J. H., 1992]. Linear extrapolation was then used to predict flight aerodynamic characteristics.

Both the flap and slat deflection angles of 30° were selected for the purpose of comparison with previous experiments that tested multi-element airfoils [Spaid, F. W. and Lynch, F. T., 1996, Chin, V. D., et al., 1993, Landman, D., 1998] using these same slat and flap deflection angles. Landman [1998] performed a slat optimization procedure for this same model and found that the maximum lift coefficient occurred at a slat deflection angle of 30°.

In the study conducted by Spaid [1996], the results indicated that for angles of attack between 12° and 16°, the total lift of the airfoil was reduced for the case when the flap gap was increased (0.23%). However, for angles of attack greater than 16° the total lift was increased for the case of the larger flap gap. The largest flap gap that was tested by Spaid [1996] was 1.50 % chord. The model in this experiment was fixed at 19° angle of attack and the flap gap in this experiment was set to 2.7% to configure the wing for a high lift condition. An experiment was performed on a 2D NACA 2419 airfoil with a 30% Fowler flap [Hoerner, S. F., 1985] and the optimum flap gap was found to be 2.7% at a Reynolds number of 9 million. Additionally, that same study found that the optimum configuration for high lift was for the flap to have a small positive overhang. A photograph of the test article mounted in the Old Dominion University Low-Speed Wind Tunnel (ODU LSWT) is shown in Figure 3.3.

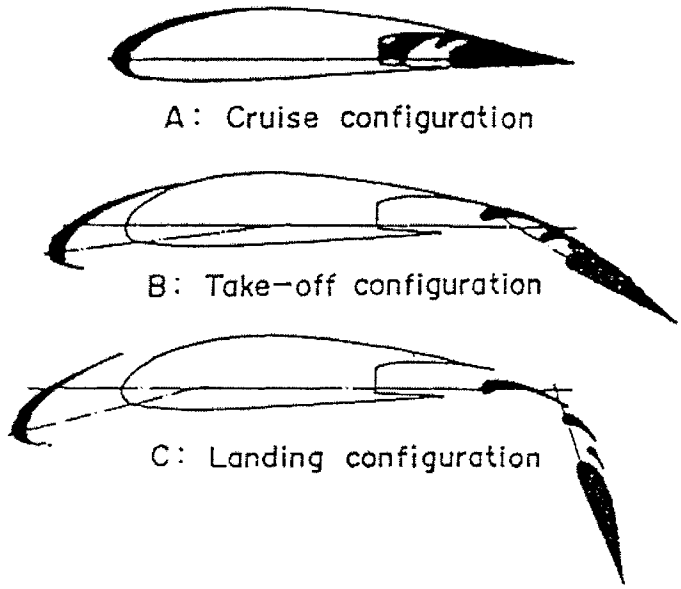

Figure 3.2 – Configurations of Multi-Element Airfoil for Various Stages Of Flight.
From Landman, D. 1998 – Reprinted by permission from author

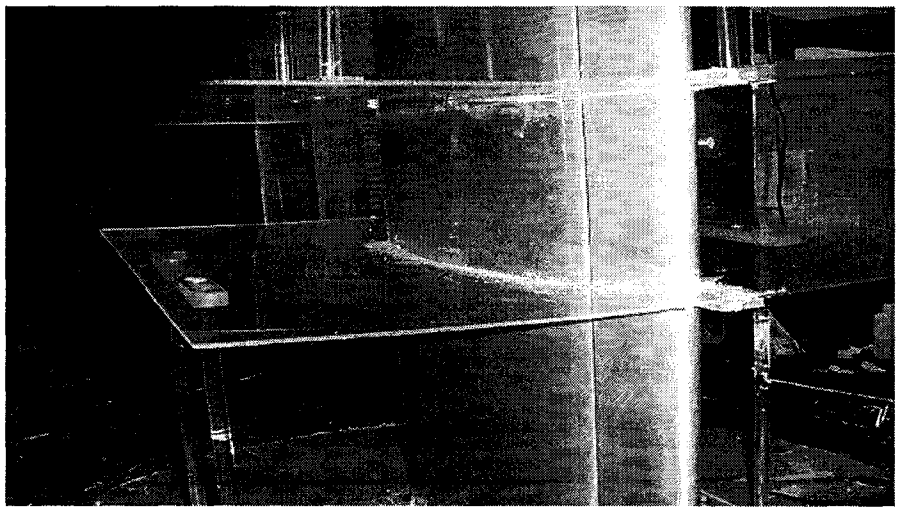

Figure 3.3 – Model Mounted in Test Section of ODU LSWT with Sidewalls.

3.1.2 Piezoelectric Actuators

The primary mode of flow-field excitation in this study was derived from the oscillatory motion of piezoelectric actuators. These devices were manufactured by the FACE International Corporation and have been given the designation of THUNDER™ devices. Research [Mossi, K. M., and Bishop, R. P., 2000] has been done to characterize these actuators for a variety of engineering applications. These actuators are formed from a composite of materials consisting of an aluminum outer layer and a stainless steel substrate sandwiched in-between by a PZT material (lead zirconate titanate) They are manufactured by first heating the composite to 325 °C and then cooling to room temperature. This results in a device that is prestressed into a curved shape and that provides ruggedness and displacement and force capabilities superior to a single ceramic wafer.

The THUNDER™ actuators come in two standard shapes, circular and rectangular. The devices used in this study were of the latter type. Specifically, the model used was TH-7R with the overall dimensions of 96.52 mm x 71.12 mm x 0.584 mm. Two mounting configurations were possible simply supported and cantilevered. In this study, the devices were simply supported with aluminum tape applied to both ends of the stainless steel substrate. The amount of displacement depends on several factors, namely: the driving frequency, the amplitude of the driving voltage, and the mounting configuration. Generally, the displacement changes directly with voltage and inversely with frequency. The typical displacement for the TH-7R device is 7.62 mm at a frequency of 1 Hz and a drive voltage of 595 volts peak-to-peak.

The devices were driven by a voltage oscillator, which was connected to a high-impedance, low-current voltage amplifier. The equipment that was used was the TREK

model 50/750 high-voltage amplifier. The output from the amplifier was connected to two pairs of leads, which passed through the floor of the test section and were soldered to the two devices mounted onto the model.

3.1.3 Acoustic Instrumentation

As reported in other studies, acoustic energy can be used to affect the transport of turbulent kinetic energy boundary into a boundary layer. In this study, the 75-watt loudspeaker was inserted into a plywood door, which was mounted into the wall of the test section. The centerline of the speaker was positioned as close as possible to the trailing-edge flap. A sinusoidal signal was generated by an oscillator, which was then input to an audio power amplifier. The output from the amplifier was then used to drive the loudspeaker. So that the flange of the speaker might not cause an unwanted disturbance to the flow field duct tape was used to produce a faired surface.

3.1.4 Description of ODU Low-Speed Wind Tunnel

All measurements were obtained by using the Old Dominion University Low-Speed Wind Tunnel. Aerolab, Inc. manufactured the tunnel, which is a closed-return, fan-driven model with an operating total pressure of one atmosphere. The test section is 4 ft wide, 3 ft high and 8 ft long. Figure 3.3 shows the front view of the multi-element airfoil installed in the test section with Plexiglas® sidewalls to maintain a two-dimensional flow field over the center portion of the wing. The fan is driven by a 125-hp ac motor to deliver air speeds from 10 m/s to 55 m/s. A Westinghouse variable frequency drive was used to reduce fluctuations in air speed controlled the motor. The flow field was characterized by a nominal turbulence of around 0.2% at normal velocities, slightly less at the lower speeds. The air speed was calculated by determining the total pressure and static pressure, using a

pitot pressure probe and two static pressure rings respectively. The static pressure orifice was located on the ceiling of the tunnel near the interface of the contraction section and the working test section. These pressures were read into a PC-based application program, using LabVIEW by National Instruments, which is a graphics-based programming language. A sketch of the ODU Low Speed Wind Tunnel and its coordinate system is shown in Figure 3.4.

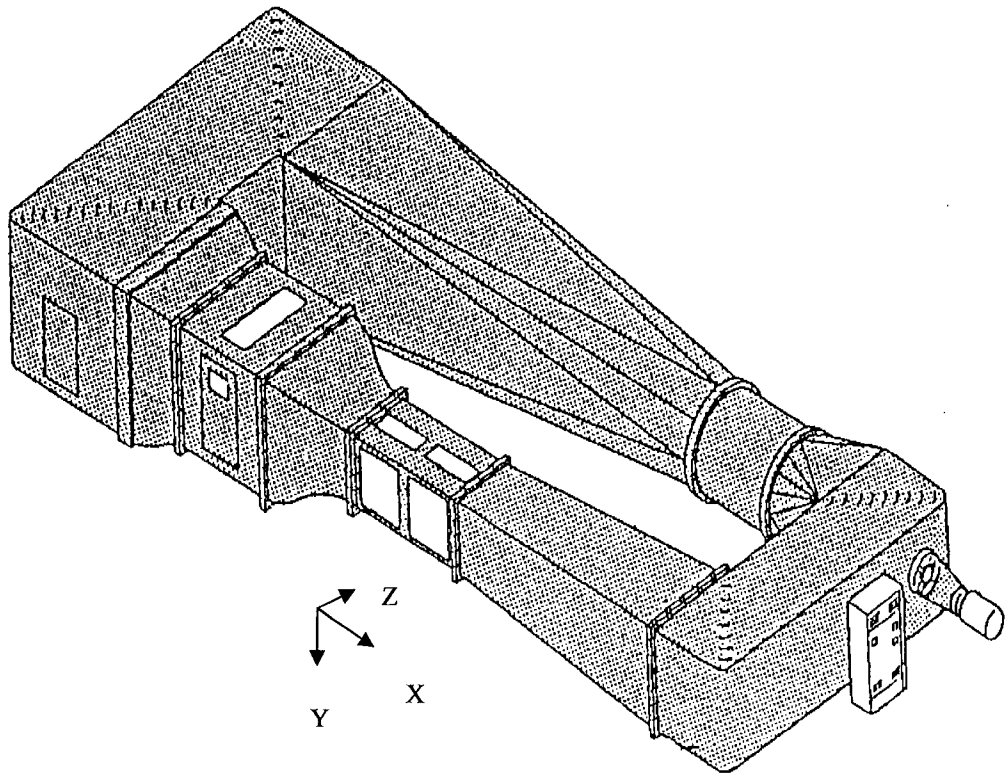

Figure 3.4 – Sketch of ODU LSWT and Coordinate System
From Landman, D. 1998 – Reprinted with permission from author

3.1.5 Data Acquisition System

One component of the data acquisition system for this experimental study was the 3497A Hewlett-Packard Data Acquisition/Control Unit, which was used to process measurements of both temperature and voltage. A thermocouple was placed inside the wall of the tunnel at the entrance to the diffuser section to acquire measurements of ambient temperature at the same time that the hot-film measurements were obtained. This was necessary in order to make the proper temperature corrections to the velocity measurements. A 100-torr high-accuracy Baratron diaphragm pressure transducer was used to measure the differential pressure between the test section static and total pressures. This was required to compute the test section free-stream velocity for both sensor calibrations and velocity measurements. The outputs from the thermocouple and the pressure transducer were first sent to amplifiers, whose outputs were then sent to a 20-channel multiplexer. These data were then communicated to a personal computer via a standard HP-IB parallel interface bus.

3.1.6 Hot-Film Anemometer System

The velocity measurements were acquired by using the TSI model 1201 hot-film cylindrical single-axis sensor. These sensors are disposable and more durable than the traditional hot-wire type sensors. The most salient characteristic of this measurement technique is the superior frequency response when compared with other systems for measuring velocity in a gas flow.

The operating principle underlying hot-film anemometers is that flow velocity in a gas can be correlated to the heat transfer rate of the sensor. More details governing the

operating principles of hot-film anemometry can be found in many references [Goldstein, 1983].

The anemometry assembly used in this experiment was the TSI Intelligent Flow Analyzer (IFA) 100 system. It incorporated four input channels, although only one channel was used for the velocity profile data when one probe was used and two channels were activated for the cross-correlation data when two probes were used. The fourth channel was used for monitoring temperature. At the beginning of each day of testing, the system was readied for use by recording the probe resistance using a shorting probe, and a control was adjusted to attain the required heated operating resistance. The so-called "overheat ratio (OHR)" is defined as the ratio of the heated sensor resistance to the cold sensor resistance. The manufacturer specified the OHR for the particular sensor that was used. At the time that the sensor was calibrated, the proper frequency compensation setting was established to optimize the frequency response. An Intelligent Flow Analysis (IFA) 200 digital digitizer was used with the anemometer. For this experiment, the sampling rate of the digitizer was set at 20,000 samples per second for 20,000 data points. Both units communicated with a host computer on which the TSI Thermal Anemometry Software Package was installed. This software was also called the IFA Software Package.

3.1.7 Electronic Scanning Pressure Transducers

The surface pressure measurements on the test article were obtained by using the electronic scanning pressure transducers manufactured by Pressure Systems Inc. The particular pressure model that was used in this study was the 9010 Pneumatic Intelligent Pressure Scanner. A total of five modules were used during the pressure testing, and were interconnected in tandem fashion, with each module containing sixteen pressure ports. The

voltage outputs from the pressure ports were sent to a digitally addressed analog multiplexer that allows scanning of the ports at a rate of 20,000 ports per second. The accuracy of the transducer is rated at ±0.05 % full scale over a temperature range of –25 to 80° C with a measurement range from ±10 inches of water to 750 psid.

The reference port on each module was connected to the free-stream static pressure in the test section to facilitate the calculation of pressure coefficient. The dynamic pressure for this calculation was computed by using the output from the 100-torr Baratron pressure transducer. The output from the electronic scanning pressure transducers was communicated to a personal computer via an Optomux®-style serial interface. The hardware interface was the RS-422 converter that was connected to the serial input port of the host computer. Surface static pressures were transmitted to the scanning instruments using flexible plastic tubes that ran from an opening in the floor of the test section.

3.1.8 Three-Axes Traversing Mechanism

The wind tunnel at Old Dominion University featured a translatable strut that was capable of three-dimensional motion. The strut was aerodynamically contoured to minimize drag and test section blockage. A motorized lead screw was installed along the spanwise direction of the strut. An aluminum table was attached to this lead screw and was used for mounting and translating the hot-film sensor in the vertical direction for flow-field surveys. The strut itself was attached to two additional lead screws that were fastened to the ceiling of the test section. These motorized lead screws allowed movements along both the longitudinal and lateral directions in the test section. An electrical controller that was remotely operated outside of the tunnel directed the movement of the strut.

Magnetostrictive position transducers were incorporated in the traversing system and transmitted the X, Y and Z coordinates of the strut to a LED display unit.

3.1.9 Measurement Uncertainty Considerations

The discussion in this section describes and quantifies the amount of measurement uncertainty associated with all data obtained in this experiment. First, the sources of measurement uncertainty are identified and then well-established formulas are used to estimate the error associated with the data. These methods for uncertainty measurement have been published by Kline and McClintock [1953].

With regards to the hot-wire anemometer data, errors originate largely from uncertainty associated with the bridge voltage, inherent calibration variability, and deviations from exact measurements attributed to temperature variations. According to TSI specifications, the variation of the operating resistance in the IFA 100 anemometer is ± 0.002 ohm and the maximum probe current is 1.2 amps. Applying Ohms Law, the most cautious estimate of the uncertainty attributed to bridge voltage is shown in Equation 3.1.9-1

$$\Delta E_b = 0.002 \text{ ohms} \times 1.2 \text{ amps} = 0.0024 \text{ volts} \qquad (3.1.9\text{-}1)$$

The uncertainty due to the probe calibration was determined by using the 4^{th} order polynomial fit of the calibration velocities versus the bridge voltage. The curve fit is represented in Equation 3.1.9-2.

$$V(E) = GE_b^4 + FE_b^3 + EE_b^2 + DE_b + K \qquad (3.1.9\text{-}2)$$

The uncertainty of the velocity was the partial derivative calculated with Equation 3.1.9-3.

$$\Delta V(E) = \frac{\partial V}{\partial E_b}\Delta E_b \qquad (3.1.9-3)$$

Therefore, the uncertainty of the hot-film velocity data was computed by combining the two previous equations as in Equation 3.1.9–4.

$$\Delta V(E) = (4GE_b^3 + 3FE_b^2 + 2EE_b + D)\times \Delta E_b \qquad (3.1.9-4)$$

The uncertainty is a function of the probe calibration constants as well as the nominal bridge voltage, which varies depending on the tunnel free-stream velocity. The probe calibration constants for both sensors number 1 and 2 are shown in Table 3.1.

Calibration Constant	Sensor 1	Sensor 2
K	3948.6733	3944.9184
D	-6894.8632	-6858.9213
E	4493.3896	4451.1235
F	-1279.2324	-1279.6468
G	140.9319	138.4511

Table 3.1 – Calibration Coefficients for Hot-Film Sensors.

The nominal output voltage for a free-stream velocity of 20 m/s is 2.23 volts. The appropriate constants are then substituted into Equation 3.1.7 – 4 that calculates the uncertainty. For sensor number 1, the result is as follows:

$\Delta V_b = 4(100.7082)(2.23)^3 + 3(-903.2609)(2.23)^2 + 2(3059.2023)(2.23) - 4589.1860$

$\Delta V_b = \pm 0.11$ m/s (3.1.9-5)

Doing a similar calculation for sensor number 2, the result was as follows:

$\Delta V_b = 4(-3.7491)(2.23)3 + 3(51.9862)(2.23)2 + 2(-204.924)(2.23) + 349.6921$

$\Delta V_b = \pm 0.11$ m/s (3.1.9-6)

These results show that the uncertainty attributed to the variability of the bridge circuitry is relatively small and is the same for both sensors. In fact, the uncertainty is only 0.55 % of the free stream velocity.

Calibration errors were a second source of uncertainty for the hot-film anemometer, that is, discrepancies between the calibration velocities and their corresponding predicted values. For sensor numbers 1 and 2, the calibration error analysis is shown in Tables 3.2 and 3.3.

Predicted Velocity (m/s)	Calibration Velocity (m/s)	Error
10.10	10.07956	-0.02044
14.34	14.46117	0.12117
16.64	16.55762	-0.08238
19.63	19.56169	-0.06831
26.53	26.57252	0.04152
30.07	30.12151	0.05151
38.33	38.26546	-0.06454
46.77	46.79928	0.02928
48.80	48.79126	-0.00874

Table 3.2 – Comparison of Predicted and Calibration Velocities for Sensor Number 1.

Predicted Velocity (m/s)	Calibration Velocity (m/s)	Error
10.03	10.08932	0.05932
11.55	11.52731	-0.02269
13.85	13.74135	-0.10865
16.90	16.80246	-0.09754
19.76	19.94994	0.18994
24.68	24.72922	0.04922
26.61	26.78265	0.17265
29.93	29.86406	-0.06594
33.52	33.15668	-0.36332
37.29	37.26805	-0.02195
39.53	39.43834	-0.09166

Table 3.3 – Comparison of Predicted and Calibration Velocities for Sensor Number 2.

A suitable estimate of the calibration uncertainty for sensor number 1 is the root mean square of the above errors. Equation 3.1.9-7 was used for this calculation.

$$\Delta V_c = \left[\frac{\sum (\text{error}_i)^2}{N}\right]^{\frac{1}{2}} \text{ where } \quad N = 9 \qquad (3.1.9\text{-}7)$$

The result of this calculation was that

$$\Delta V_c = \pm 0.06 \text{ m/s} \qquad (3.1.9\text{-}8)$$

Now to ascertain the total uncertainty of the hot-film measurements, both components are combined as follows:

$$\Delta V_T = [\,(\Delta V_b)^2 + (\Delta V_c)^2\,]^{.5} = [\,(0.11)^2 + (0.06)^2\,]^{.5} = \pm 0.13 \text{ m/s} \qquad (3.1.9\text{-}9)$$

It can be concluded that this uncertainty can be considered relatively insignificant. Uncertainty in the hot-wire anemometry data occurs because the temperature of the jet of air flowing through the test section generally increases with time. The temperature of the air during the experiment thus is different from the temperature during calibration. To compensate for this change, the bridge voltage is corrected to be what it would have been at the calibration temperature T_c.

Equation 3.1.9-10 was used to correct the bridge voltage, where Ts is the operating temperature of the sensor, T_e is the temperature of the fluid during the experiment, and T_c is the temperature during calibration. V_t is the corrected voltage and V_s is the voltage of the sensor.

$$V_t = V_s \times \sqrt{\frac{(T_s - T_c)}{(T_s - T_e)}} \qquad (3.1.9\text{-}10)$$

Equation 3.1.9-10 was derived by forming the ratio of the power emanating from the sensor for the two different fluid temperatures (i.e., T_c and T_s). The equation for power as a function of the Nusselt number can be found in many references that describe the operation

of hot-wire anemometers. Because the bridge voltage was corrected for temperature, an uncertainty assessment was not required because of the increments in temperature.

Other sources of uncertainty associated with the anemometer measurements included nonuniformity of the heat convection along the axial axis of the sensing element, the aerodynamic interference of the sensor and probe, and the uncertainty associated with the X and Y coordinates of the probe. The other major source of uncertainty is involved with the calculation of the pressure coefficient. As usual, the pressure coefficient was computed using Equation 3.19-11.

$$C_p = \frac{\delta p}{q_\infty} \text{ where } \quad \delta p = p - p_\infty \qquad (3.1.9\text{-}11)$$

From Equation 3.1.9-11 note that the pressure coefficient is a function of both δp and q_∞, as previously treated, the uncertainty was found from Equation 3.1.9–12.

$$\Delta C_p = [(\frac{\partial C_p}{\partial(\delta p)}\Delta(\delta p))^2 + (\frac{\partial C_p}{\partial q_\infty}\Delta q_\infty)^2]^{.5} \qquad (3.1.9\text{-}12)$$

The differentiation was performed with Equation 3.1.9–13.

$$\Delta C_p = [((\frac{1}{q_\infty})\Delta(\delta p))^2 + ((-\frac{\delta p}{q_\infty^2})\Delta q_\infty)^2]^{.5} \qquad (3.1.9 - 13)$$

The uncertainty $\Delta(\delta p)$ of .05% full scale reading was based on the specifications for accuracy published by Pressure Systems, Inc for their 9000 series scanning pressure transducers. The pressure transducer had a full-scale reading of 20 in H_2O. The uncertainty of Δq_∞ was based on the accuracy published by MKS Instruments for their 100 Torr pressure transducer. They state that the accuracy is 0.08% of the full-scale reading. The

above development indicated that the overall uncertainty of the measured pressure coefficient, by the presence of both instruments, was a function of the free-stream velocity. The uncertainty of the pressure coefficient was calculated based on nominal test conditions.

$\rho = 1.1766\,\text{kg/m}^3$

$V_\infty = 20\,\text{m/s}$

$$q_\infty = \frac{1}{2} \times 1.1766\,\text{kg/m}^3 \times 400\,\text{m}^2/\text{s}^2 = 235.32\,\text{Pa}$$

$$\Delta q_\infty = 0.0008 \times 100\,\text{Torr} \times \frac{101300\,\text{Pa}}{760\,\text{Torr}} = 10.66\,\text{Pa}$$

$$\Delta(\delta p) = 0.0005 \times 20\,\text{in}\,H_2O \times \frac{1\,\text{atm}}{406.8\,\text{in}\,H_2O} \times \frac{101300\,\text{Pa}}{1\,\text{atm}} = 2.49\,\text{Pa}$$

$$\Delta C_p = [\,(\frac{1}{235.32} \times 2.49)^2 + (-\frac{2.49}{(235.32)^2} \times 10.66)^2\,]^{\frac{1}{2}} = 0.01059$$

3.2 Software Considerations

All of the data analysis performed in this experimental study was performed with either existing software or software that this author had developed. The analysis done in real time was performed using existing LabVIEW programs [Landman, D., 1998] that were modified to custom-fit the requirements of this study. The bulk of the post-processing analysis was performed either using FORTRAN programming or MATLAB utilities.

3.2.1 LabVIEW Application Programs

Most of the software development that was used for this experiment was pre-existing. However, for the case of the application programs known as Virtual Instruments (VI's) some modifications were performed to satisfy some of the requirements specific to

this study. In order to perform the calibrations of the hot-film sensors, it was necessary to determine the jet free-stream velocity in the test section at the time of calibration. A LabVIEW program read in as input the total pressure and static pressure in the test section as well as the temperature, which was measured using a thermocouple that was inserted in the tunnel just at the junction between the test section and the diffuser. The two pressures were used to compute the dynamic pressure of the jet flow and the temperature data was used to correct for density. The jet velocity was then calculated by using the corrected dynamic pressure.

Modifications to an existing program were done to obtain surface pressure measurements from the model for all three components. An original LabVIEW program was developed to accommodate only three scanning pressure modules. For this experiment, that capability was expanded to accommodate a total of five pressure modules. The pressure data represents averages of a sample of data acquired at a rate of 20,000 measurements per second. Programming was created to convert the raw pressure measurements to pressure coefficients using the free-stream static pressure obtained from a pressure port located in the test section at the end of the contraction region. This static pressure port was connected via flexible plastic tubing to an unused pressure port on one of the scanning pressure modules. A formatted text file was created that contained a listing of the pressure coefficients for each of the three model components.

3.2.2 TSI® Data Acquisition Program

The analysis of the hot-film anemometry data was done by implementing the IFA Thermal Anemometry Software Package, which was an interactive program developed by TSI®. The fluid dynamic properties of the flow during the test runs were determined by

processing the analog thermal output from the bridge circuitry of the anemometer containing the hot-film sensor as one resistance element of a Wheatstone electrical bridge. This data is then passed onto a signal conditioner, which applied an offset, gain and filter. The resulting digital data were then processed by a personal computer, which deconditioned the data and performs a correction since the ambient temperature of the flow invariably changed from the value at the time the sensor was calibrated. The ambient temperature was recorded at the beginning of each test run. The anemometer software package contained a suite of programs to perform a variety of functions. The programs used in this study were for sensor calibration, data calibration, statistical analysis, spectral analysis and cross-correlation.

The calibrations of the hot-film sensors were performed by placing them in the empty test section to obtain measurements at selected air speeds. The test section air speed was calculated from the dynamic pressure, which was determined by using the Baratron 100-torr pressure transducer. A LabVIEW program was used to perform the actual calculation of the test section air speed based on the dynamic pressure. The calibration program was then implemented to construct a 4th order polynomial fit through the measured data. The resulting coefficients were subsequently used in the measurement of velocity during the actual test runs.

After the calibrations were performed, the data acquisition program was then used to initiate the acquisition of bridge voltages and to create raw data files. Groups of related test runs were systematically categorized by assigning a common prefix name to the raw data files. Up to 99 files could be assigned the same prefix file name. Each file could be distinguished by its own two-digit file name extension.

The raw data files were converted to files containing velocity in meters per second by applying the coefficients computed in the calibration program. These velocity data files had the same prefix file name as the companion raw data files but had a different extension.

The cross-correlation program computed the power spectrum, the cross-correlation of the velocities in the case of two different sensors, and the auto-correlation of a single sensor. These data were built using the Fast Fourier Transform (FFT) technique. This program had the capability of writing the power spectrum data to a formatted file, which was later used for processing.

3.2.3 FORTRAN Application Programs

A FORTRAN computer program, WAKEIGN, was developed by this author to execute the Linear Stability Analysis. The computational analysis was done for the boundary layer region on the main wing within the proximity of the leading-edge slat. The main input to the program was the velocity profile obtained from the hot-film measurements near the surface of the model. The free-stream velocity normalized these velocities. The distance from the model surface was normalized by the reference length, which was the stowed chord length of 18 in. Velocities at intermediate heights between selected probe locations were interpolated using a cubic-spline fit. Since the hot-film sensor was incapable of obtaining measurements too close to the model surface (to avoid sensor damage), a method was devised to interpolate velocities from the model surface to the first transverse location where hot-film data were obtained. See section 5.1.1 for more details on how the velocity profile was synthesized for the stability analysis.

The main output from the program were the eigenvalues associated with the propagation of vortex-induced disturbances that originate from the slat-wake region. These

eigenvalues included both real and imaginary parts of the wave number and angular frequency of the disturbance. An initial guess for the wave number was selected for an initial angular frequency. These eigenvalues were then used in the body of the analysis with the appropriate far-field boundary conditions applied. The details of the program were in accordance with the algorithm as described in Chapter 4.1. A shooting method was employed as a basis for the computer algorithm. The velocity computed at the wall was compared with the usual no-slip boundary condition to validate the initial guess of the eigenvalues. If the computed velocity was not within a specified tolerance of the expected value, then a Newton-Raphson iterative algorithm was employed to make a correction to the wave number. The process is then repeated until the wall boundary condition was satisfied. The result was a wave number at a corresponding angular frequency. The initial angular frequency was then reduced by a fixed decrement, and the entire process of finding the associated wave number was repeated.

The program WAKEIGN generated a computational grid with node points in the direction normal to the wall. A system of differential equations was developed for the node points starting from the wall boundary to the edge of the velocity profile. These equations were subsequently discretized and were incorporated into a tridiagonal matrix, which is then solved using a variation of Crout Reduction [Hilderbrand, F. B., 1956]. The solution array for this system of equations includes the computed wall velocity.

Another FORTRAN program, FUNFREQ was developed to read a formatted file of the hot-film raw data containing the frequencies and their corresponding power spectrum amplitudes. This data was then written to a binary file that was suitable as input to a MATLAB program.

The THETAY program was developed to compute the momentum thickness across the shear layer directly above the model, particularly at the trailing-edge flap. The velocity profiles were stored in the program using a DATA statement and were normalized by the velocity at the edge of the shear layer. Normalization of the distances from the model surface was performed by using the aforementioned reference length. The momentum thickness was then computed using Equation F.2-1, where the integration was performed as a simple sum. The differential length in the integral was computed as the increment between successive normalized distances.

A FORTRAN computer program named SKINFRC was written to compute the skin friction at a single location of the model based on the local momentum thickness, and local shape factor. These two quantities were numerically integrated by summing the products that normally make up their integrands. This numerical integration method was considered sufficient since the differential increments in the traverse direction were small. The momentum thickness and the shape factor were used in a formula that was based on the "law of the wake" by Coles [White, F. M., 1991].

Another important FORTRAN program was called LIFT, which computed the total lift of the main wing. This was done by performing the numerical integration of the surface pressure coefficients on both the upper and lower surfaces of the main wing. When performing the integration, the differential arc length along the surface was projected into the plane of the main-wing chord. The trapezoidal rule was employed to do the actual numerical integration.

CHAPTER 4

EXPERIMENTAL DETAILS

This section describes in detail the experimental procedures and analyses that were performed for the experiment at hand. A description will first be given of the procedures performed in the test section before the model was installed (e.g., such as calibration of the hot-film sensors and the acquisition of preliminary baseline measurements). This will be followed by an exposition of the procedures and analysis associated with obtaining measurements on the test article. Most notably, this section includes detailed information about the piezoelectric sensors and the loudspeaker used throughout the study.

4.1 Calibration of Hot-Film Sensors

Two hot-film sensors were used for this experiment. They were used primarily to obtain measurements of mean velocity and turbulence intensity. The hot-film data were used to develop spectral data for computation of the power spectra and cross-correlation in the case when two probes were simultaneously being used.

The sensors were calibrated by mounting them individually in the center of the test section for free-stream velocities ranging from 10 m/s to 40 m/s. The calibration velocities were determined by using a LabVIEW program to calculate the air speed based on the measured static and dynamic pressures in the test section.

The TSI® IFA 100 anemometer produced the bridge voltage corresponding to the rate of heat transfer from the sensor, and the TSI® IFA 200 performed the digitization of this analog data so that it could be processed by a personal computer. Signal conditioning was accomplished by performing low-pass filtering and by imposing both an offset and gain to the analog data before digitization.

The sensor resistance was determined by placing an electrical shunt in the probe, which then became one leg of the internal Wheatsone bridge circuit. The resistance was measured by the anemometer and stored into memory to be ultimately subtracted out of subsequent measurements.

After the sensor resistance had been measured and stored, the controls on the front panel of the IFA 100 were adjusted to arrive at the over-heat ratios (OHR) for both sensors. The OHR is calculated according to the following equation:

$$OHR = \frac{\text{heated sensor resistance}}{\text{cold sensor resistance}}$$

Based on the specifications provided by the manufacturer, the over-heat ratios for the sensors was 1.8. The denominator in the above relationship is the resistance before current is passed through the sensor to elevate its temperature. During actual operation, more current is passed through the sensor in an attempt to heat it and raise its temperature. The air, which passes over the sensor during a test run will cool it, and therefore, the amount of current necessary to restore it to its heated value is correlated with the velocity of the air flow.

Additional adjustments were made from the control panel of the IFA 100 to optimize the frequency response of the system to handle highly fluctuating airflow. The tunnel was run at approximately 45 m/s and a test square wave was applied across the Wheatstone bridge to simulate an input composed of high frequencies. Adjustments were made to the internal control circuitry so that the response to the square wave input did not demonstrate an unacceptable amount of oscillations or ringing when the input signal transitioned from a low value to a high value or vice versa.

The calibration velocities and their associated bridge voltages were stored and the coefficients of a 4th order polynomial fit were calculated and subsequently used to obtain measurements of velocity during the actual test. The calibration data for sensors 1 and 2 have already been presented in Tables 3.2 and 3.3.

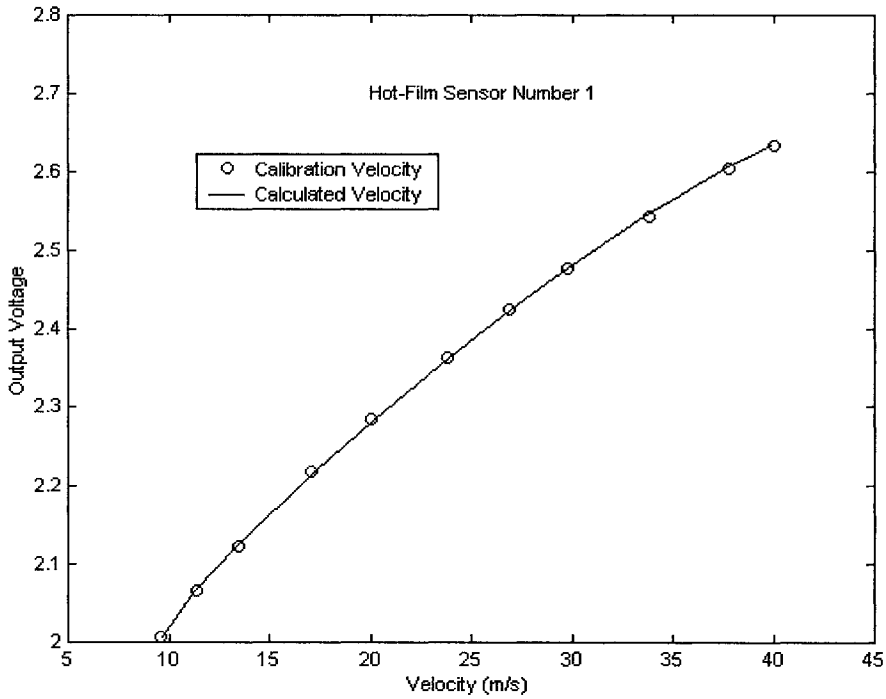

Figure 4.1 - Calibration Curve for Hot-Film Sensor Number 1.

The fourth order polynomial that was used to fit the data is shown in Equation 4.1-1.

$$V_{Cal} = K + DE_b + EE_b^2 + FE_b^3 + GE_b^4 \qquad (4.1)$$

The coefficients were calculated automatically by the TSI® IFA Thermal Anemometer Software Package. The calibration curves for the two sensors used in this study are shown in Figures 4.1 and 4.2. The coefficients for the two sensors used in this study are shown in Table 3.1.

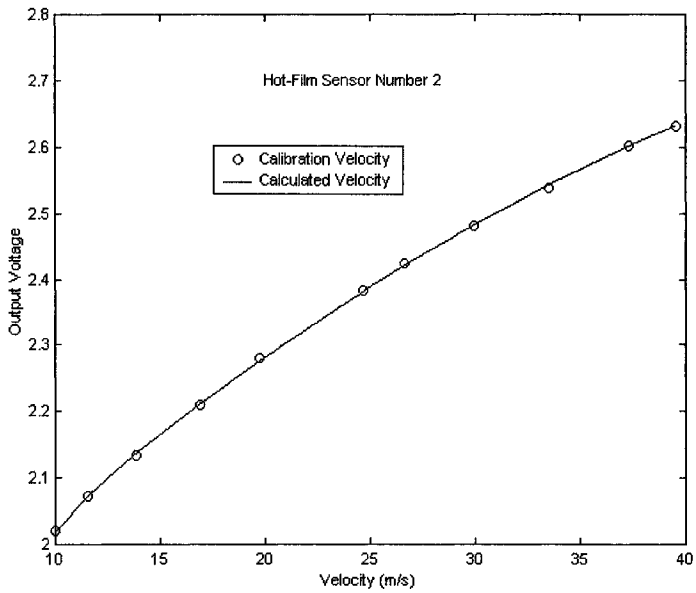

Figure 4.2 - Calibration Curve for Hot-Film Sensor Number 2.

4.2 Flow Field Survey of Empty Test Section

Before the main bulk of the data acquisition was performed, preliminary testing in an empty tunnel test section was necessary to establish a background set of data for reference. These results were compared with data acquired when the test article was installed to determine some of its attendant effects on the flow field. The TSI® hot-wire sensor and anemometer system were used to measure the velocity of the flow field. Two types of preliminary tests were conducted. The first test consisted of a survey of the freestream velocity in the test section as a function of longitudinal, lateral, and vertical position of the hot-film probe for different free stream velocities. The second test involved determining the spectral signatures of the airflow for different flow velocities. The last procedure was especially important because subsequent testing required the accurate establishment of the correlation between the spectral data and the flow-field characteristics

in the presence of the model. Prominent frequency amplitudes induced by the model will have to be distinguished from any background spectral characteristics that were present in an empty test section. The hot-film sensor was mounted onto a streamlined strut that was fixed to a three-dimensional traversing mechanism. Data were obtained at the free-stream velocities from about 10m/s to 40m/s in increments of 10m/s. In the streamwise or X direction, measurements of the velocity were taken every 6 in. In the vertical or Y direction, measurements were taken every 3 in. Finally, along the lateral or Z direction, measurements were also taken every 3 in. Figures 4.3 through 4.5 show the velocity surveys and reveal, that generally, the flow was uniform, which suggests that the wall interference due to boundary layer growth is minimal. The test section is diverged to offset any boundary-layer growth on the walls.

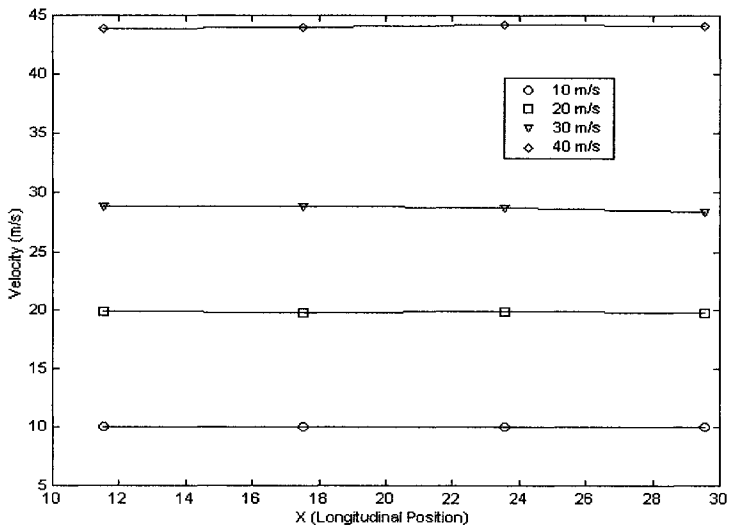

Figure 4.3 - Longitudinal Survey of Empty Test Section at Selected Speeds.

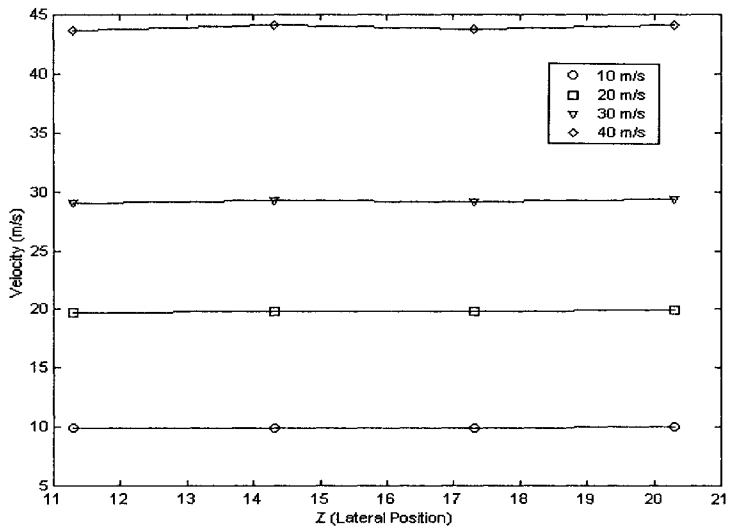

Figure 4.4 - Lateral Survey of Empty Test Section at Selected Speeds.

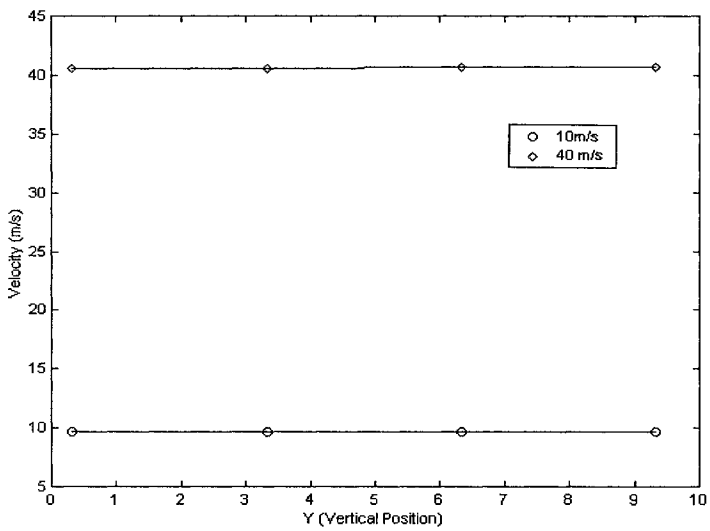

Figure 4.5 - Vertical Survey of Empty Test Section at Selected Speeds.

4.3 Spectral Analysis of Empty Test Section

Power spectra were obtained in an empty test section at the free-stream velocities of 10 and 20 m/s, which corresponded to Reynolds numbers 290,000 and 580,000 based on the stowed chord length of 18 in. The spectral calculations were performed by a software package developed by TSI® for their hot-wire anemometry system. The software consisted of an algorithm to do a Fast Fourier Transform (FFT) of the sequence of data that resulted from sampling the analog root-mean-square bridge voltage at a rate of 20kHz. The data show the power of each frequency component as a function of Strouhal number. The Strouhal number was based on the reference length equal to 18 in. (chord length of nested wing) and the free-stream velocity. The results of this test are shown in Figures 4.6 and 4.7 and show the existence of a prominent spike at Strouhal numbers of 48 and 49, respectively. Based on the reference length of 18 in this corresponded to peak frequencies of 1,054.7 and 1,074.2 Hz. Additionally, some very pronounced and more rounded component amplitudes are shown to exist at the lower frequencies. The sources of these peaks are not thoroughly understood, but they could possibly be attributed to extraneous alternating current noise, the drive motor fan blade passing frequency, or various acoustical sources such as structures inside the tunnel or apertures in the tunnel walls. As will be shown later, an excitation frequency of 320 Hz was found to be critical to the formation of vortex pairing. This corresponded to a Strouhal Number of 7.3, based on the stowed chord length of 18 in. The results from this experiment would have been compromised if the background spectrum amplitude at 320 Hz had been significant.

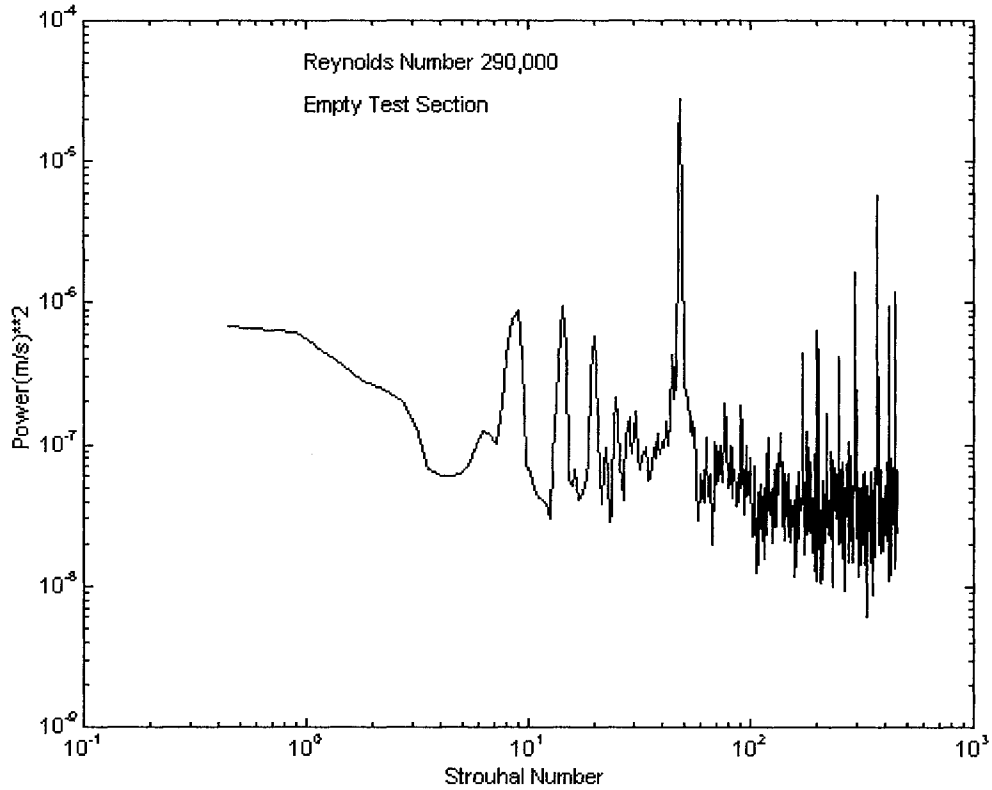

Figure 4.6 - Power Spectrum in an Empty Test Section at 10 m/s.

This data needed to be compared with the spectral data when the model was installed in the test section to determine the passage frequency of the vortices emanating from the region of the slat. The empty tunnel data was used to identify some of the background prominent amplitude peaks, which may also appear when trying to determine the vortex passage frequency at different free stream conditions. An important consideration is whether a harmonic of the most prominent frequency component in an empty test section is near the vortex passage or fundamental frequency for the test article at the selected free stream velocity.

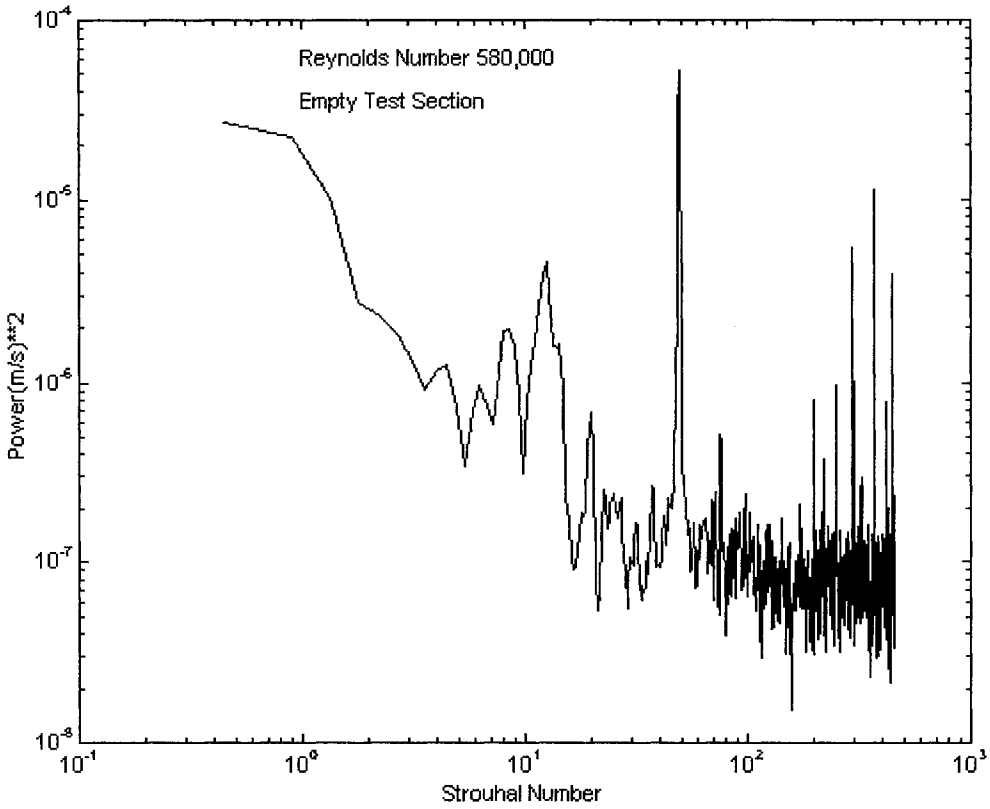

Figure 4.7 - Power Spectrum in an Empty Test Section at 20 m/s.

Also of importance, the level of background turbulence that exists in an empty test section was ascertained. This was accomplished by using a hot-film sensor to measure the root-mean-square values of the velocity in all three directions, normalized by the free stream velocity. The important quantities for this type of experimental study are shown in equation 4.3-1.

$$\frac{u'}{U_\infty} << 1 \qquad \frac{v'}{U_\infty} << 1 \qquad \frac{w'}{U_\infty} << 1 \qquad (4.3\text{-}1)$$

Since the hot-film sensors in this study were of the single axis type, only velocity fluctuations in the longitudinal directions could be measured. These measurements in this study were taken approximately at the same location as anticipated for the actual test runs when the model would be installed in the test section. If the level of free-stream turbulence is above a certain threshold, then all measurements will have to be corrected to compensate for the excessive turbulence to insure the accuracy of the measurements.

Using the single axis sensor as previously discussed, the spreading rate of the confluent mixing layer was deduced, as done by Tordella and Christiansen [1989], from static pressure profiles and by the computation of the momentum thickness at various chordwise locations along the main wing as computed in Equation F.2-1.

4.4 Surface Pressure Measurements

Before the model was connected to the pressure measuring system, the model was checked for leaks to determine which pressure ports, if any, might be defective. The surface static pressures of all three model components were obtained using the 9000 series PSI Intelligent Pressure Scanners measuring system as described in detail in the manual published by PSI. The stated accuracy of the transducer was ±0.15% full scale. Plastic tubing was used to connect the model stainless steel tubes to the pressure transducers. The measurements were first acquired without the electroactive actuators being attached to the model. Surface pressure coefficient data were obtained at 0°, 5° and 10° angles of attack. In this study the free-stream velocities were 10, 20, and 30 m/s. However, for the bulk of the data the free-stream velocity was 20 m/s. This choice of free-stream velocity was made to avoid excessive vibration of the Plexiglas ® sidewalls. When the model was tested at a velocity above 23 m/s the sidewalls began to vibrate and it was thought that the oscillations

of the sidewalls might affect the surface pressure measurements. The pressure coefficient was computed using measurements from the pressure transducer. In particular, the three required quantities are the local surface static pressure p_s, the free-stream static pressure p_∞, and the free-stream dynamic pressure q_∞. The pressure coefficient was computed according to Equation 3.1.9-11. The dynamic pressure was determined by measuring the difference between the total pressure and the static pressure as determined by pressure orifices located upstream of the test section. The 100-torr Baratron pressure transducer measured the difference between the total and static pressures in the test section and existing LabVIEW software did processing of the raw data. The pressure coefficient distributions for various flow conditions and model attitudes were plotted using off-the-shelf MATLAB utilities. In general, the contours of the various pressure distributions agree with those as reported in the work by Landman [1998] using the identical model.

4.5 Hot-Film Flow Field Surveys

The hot-film sensors were used primarily to conduct surveys of the velocity profile on both the main wing and the trailing-edge flap. The data from the upper surface of the main wing was, for the most part, obtained to validate the applicability of Linear Stability Analysis to multi-element airfoils. For this study, velocity profile measurements were obtained from both the trailing-edge flap and the main wing. The model was placed at a 19° angle of attack and the free-stream velocity was set at 20 m/s. These conditions were selected because, under these conditions, the flap boundary layer was found to be separated and on the verge of reattaching. The test of the model with these marginal flow conditions was important to determine the minimum amount of excitation required for the flow to reattach.

At the beginning of each profile, it was desirable to position the hot-film sensor as close to the model surface as possible to measure velocities very near the lower extremities of the boundary layer. The sensor was located 0.50 cm above the surface of the flap. This height was measured using a precision ruler and a magnifying glass. Because the probe holder was long and could be subjected to adverse buffeting, the sensor was not located any closer to the model surface to minimize the chance of damaging the sensor. The sensor was located directly above pressure tap number 14, which corresponded to the model X and Y coordinates of 1.7919 in and 0.3334 in, respectively. For more details, see the dissertation by Landman [1998]. At the beginning of each survey, the probe was located at X = 26.74, Y = 9.322 and Z = 13.99 in the test section frame of reference. Because the model was installed with the wing tips in the direction from top to bottom, the probe was traversed in the Z direction during the survey.

The step size of the probe displacement from the model surface varied depending on the probe location. From Z = 13.99 to Z = 13.90 the step size was 0.01 and from Z = 13.90 to Z = 13.30 the step size was 0.10. For distances between Z = 13.30 and Z = 12.72, the measurements displayed marked oscillations, so that data for this range were not obtained. This was indicated by the appearance of the oscillation light on the anemometer display panel. Data acquisition resumed at Z = 12.74 when the warning light disappeared.

At the start of each day of data acquisition, the sensor resistance was measured, and the overheat setting was adjusted to match the TSI® specifications. A total of ten data records were taken for each probe position. The ten measured mean velocities were inserted into a spreadsheet program and then averaged to get a representative velocity for each data point. The data acquisition software used was the TSI® program, which

computed both the mean velocity and the local shear stress. Both of these quantities were used to quantify the effect of external excitation, with the piezoelectric devices and the loudspeaker.

4.6 Flow Visualization

Smoke flow visualization was obtained to provide added verification of the vortex passage frequencies acquired independently from the other corroborative approaches used in this study. This was done because accurate knowledge of these frequencies was initially considered crucial to the outcome of this experimental investigation.

The smoke generator used in this study was manufactured by the Aerotech Corporation of Great Britain. Basically, the instrument consisted of a pump, which delivered smoke generator oil to the nozzle that was fitted with an electrical resistive element powered by a voltage source contained within the unit. By a proper setting of both the oil delivery rate and the source voltage, a fairly smooth stream of smoke was issued from the nozzle to obtain visualization of ambient airflow characteristics. As shown in Figure 5.11, the smoke generator wand with the nozzle at its tip was inserted into the test section through the floor and attached to an aluminum beam that was cantilevered to an angled bracket that was fastened to the floor. The entire wand assembly was located on the windward side of the model. The nozzle was positioned well within the cove region between the leading-edge slat and the main wing to ensure that streams of smoke would be accelerated around the leading edge of the main wing and flow downstream through the gap separating the first two elements. The camera observations were taken through a Plexiglas® door located on the leeward side of the model. The observed side of the model was partially covered with black masking tape to reduce the amount of reflection

emanating from the smooth aluminum surface of the model. A stroboscope was located on the top of the test section that allowed light to penetrate a Plexiglas® window that was fitted into the ceiling of the test section. The stroboscope was set with its frequency as high as possible to provide a virtual continuous source of white light. The smoke visualization study was conducted with the model oriented at a 0° angle of attack and data were collected at the three free stream velocities of 10, 20, and 30 m/s. However, the quality of the smoke visualization data for the two higher free-stream conditions was ambiguous. Hence, the following analysis excluded any consideration of the two higher test speeds and the data. Comparison with the linear instability computations was done only for the case of 10 m/s.

The smoke generating apparatus (not shown in Figure 5.11) was located outside of the tunnel beneath the test section floor. The oil was pumped upwards through plastic tubing and delivered to the smoke wand that was instrumented with a built-in heater. As the air flowed from left to right, it passed through the slat and entrained the smoke emanating from the wand, which was facing upstream within the cove region between the slat and the leading edge of the main wing.

One problem inherent with this smoke visualization technique was the fact that that at higher Reynolds numbers the smoke tended to quickly dissipate before it encountered the upper surface of the wing. At the lower Reynolds number of 290,000 this was not particularly a problem and visualization of the smoke trail was still possible. Although the primary Reynolds number throughout the test was 580,000, the primary objective for this part of the experiment was to verify the applicability of Linear Stability Analysis as a tool for predicting the passage frequency of the vorticies embedded in the wake of the slat.

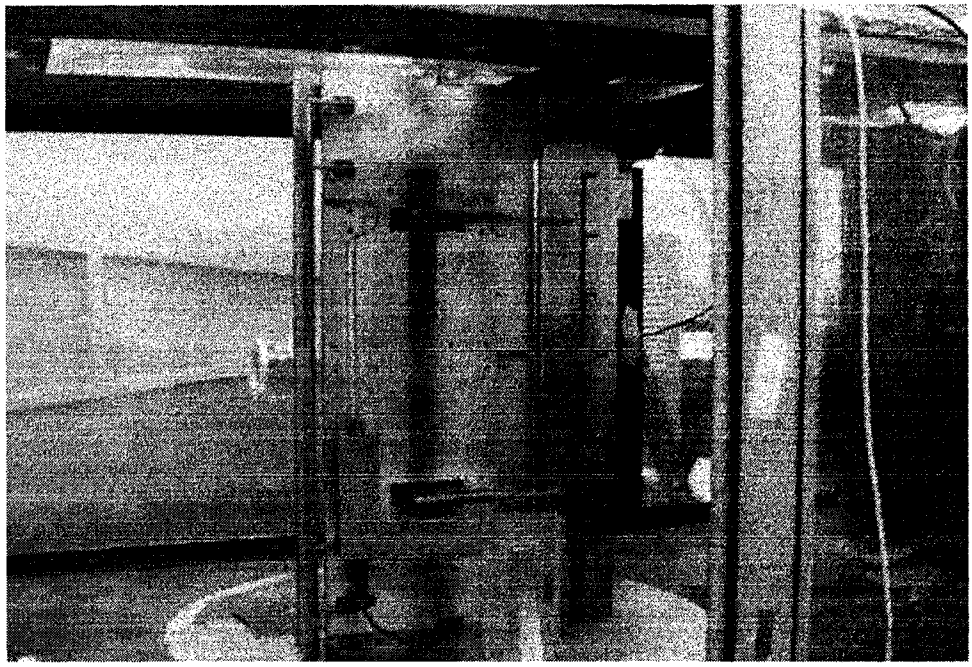

Figure 4.8 – Set-Up for Smoke Visualization in ODU LSWT

A motion film picture of the three test runs was produced with technical assistance from the Advanced Technology Department of Old Dominion University. The original movie was captured on analog tape and selected frames were digitized and stored on diskettes for subsequent analysis.

4.7 External Excitation Of Flow-Field

Two methodologies were tested to determine their effect on the flow-field mainly surrounding the trailing edge flap. First, a pair of piezoelectric devices were mounted on the model and made to oscillate at various operating frequencies. A moderate range of frequencies from 0 Hz to 120 Hz was tested to identify any possible trends in the surface static pressure and flow-field characteristics. Both the mean velocity profiles and

turbulence intensity profiles were measured using the hot-film sensor. The second method involved the use of a loudspeaker, which was mounted to the wall of the test section and was operated at 0, 80 and 120 Hz. Surface pressures, mean velocity profiles and turbulence intensities were also measured using this technique. Surface pressure measurements were also examined on the upper surface of the main wing. Although the boundary layer was attached on the main wing, surface pressure distributions were taken to observe possible increments in lift.

CHAPTER 5

RESULTS

This chapter outlines the data, which actually tested the hypotheses that forms the foundation of this study. First the results of the Linear Stability Analysis are presented to predict the vortex passage frequency of the model at 0° angle of attack. More importantly, this analysis seeks to identify the perturbation frequency, which corresponds to the highest rate of spatial amplification. This test has merit in that it validates the use of stability theory to make predictions in a flow region that is characterized by highly viscous effects. Since there is much uncertainty about the flow physics in this region, it was paramount that as much knowledge as possible should be brought to light about the flow characteristics. The results of theory were then compared with actual hot-film measurements, which were comprised of power spectra. These spectra were compared with results from previous studies and implications were inferred from the peak spectral components. For further corroboration smoke visualization was performed to determine qualitatively the natural or vortex passage frequency. Studies [Bhatteracharjee, S. et al, 1986], [Oster, D. and Wynanski, I., 1982], [Tordella, D. and Christiansen, W. H., 1989] have shown that a sizable amplification of disturbances inherent in the flow field occurs at subharmonics of the natural frequency. Finally, a summary was presented to compare the results from the theory, power spectra and smoke visualization.

To better understand the overall aerodynamic characteristics of this model, surface pressure measurements were obtained at various test speeds and model angle of attack. Although these results have no direct relevance to the objective of this experiment, they do

provide some insight into its aerodynamic performance that might serve as a frame of reference for the primary measurements obtained.

The next section contains the data that speaks to the central issues pertaining to this dissertation, i.e., the verification that external excitation can serve as a viable technique to increase the lifting capability of a multi-element airfoil. This was achieved by obtaining the mean velocity profiles, the turbulence intensity profiles and the surface static pressure coefficients as the flow field surrounding the model was externally excited using a pair of piezoelectric devices and a loudspeaker. Additionally, calculations of skin friction were also done using well-known analysis from boundary-layer theory.

Although the results from measurements obtained from the trailing-edge flap showed some interesting trends, data were also taken of the static surface measurements on the upper surface of the wing with periodic forcing of the flow field. For this configuration, it is known that boundary-layer separation occurs on the trailing edge flap for specific test conditions. However, it is important to determine if a more favorable surface pressure distribution can occur on the main wing under conditions of external periodic excitation.

The last task performed was to obtain measurements of cross-correlation coefficients using a pair of hot-film sensors that were placed at varying separations distances within the flow field. An earlier test [Bhattacharjee, S., et al., 1986] revealed that this technique could be used to determine if the system of vortices propagating downstream were two-dimensional. When the vortices are coherent and two-dimensional, their energy can be more effectively transferred to the boundary layer on the model surface.

5.1 Stability Analysis at Low Reynolds Number

Linear viscous stability analysis was performed using a velocity profile measured by the hot-film sensor placed immediately behind the trailing edge of the slat. The resolution of the survey in the vertical direction was 0.10 in. starting near the model surface to a position where the measured local velocity approximated the velocity at the edge of the potential core. For higher vertical distances, the velocity experiences a deficit due to the interference of the slat wake.

The profile was fitted to a cubic-spline function and used in the computer program called WAKEIGN as described earlier. The most challenging aspect of obtaining this solution was to construct a suitable boundary-layer profile for the wake region of the slat. Because the vortices are confined to a layer close to the model surface, a velocity profile was measured within a distance of roughly 1.05 in. from the main wing. This distance was not the reference length, but rather the nested chord length of 18 in. The velocity was normalized by using the velocity measured with the hot-film sensor at the reference distance from the model. The Reynolds number was calculated using the above reference values and a kinematic viscosity of 15.75×10^{-6} m^2/s, based on a mean air temperature of 300 K as reported in reference 18. The hot-film data were used to obtain measurements down to roughly 0.25 in from the model surface. The hot-film sensor was not placed closer to the model to avoid repeated buffeting against the surface, which would have possibly damaged the sensor. The velocity profile near the model surface was modeled using a cubic spline interpolation of the measured profile data. A MATLAB utility called SPLINE was executed to perform the interpolation using as input the normalized velocities and distances from the model surface. The reference chord length of 18 in normalized the distance from

the model surface. The free-stream velocity of 10 m/s normalized the velocity. Interpolation was done over equally spaced distances normal to the model surface. The normalized velocity profile that was used for the stability analysis is shown in Figure 5.1.

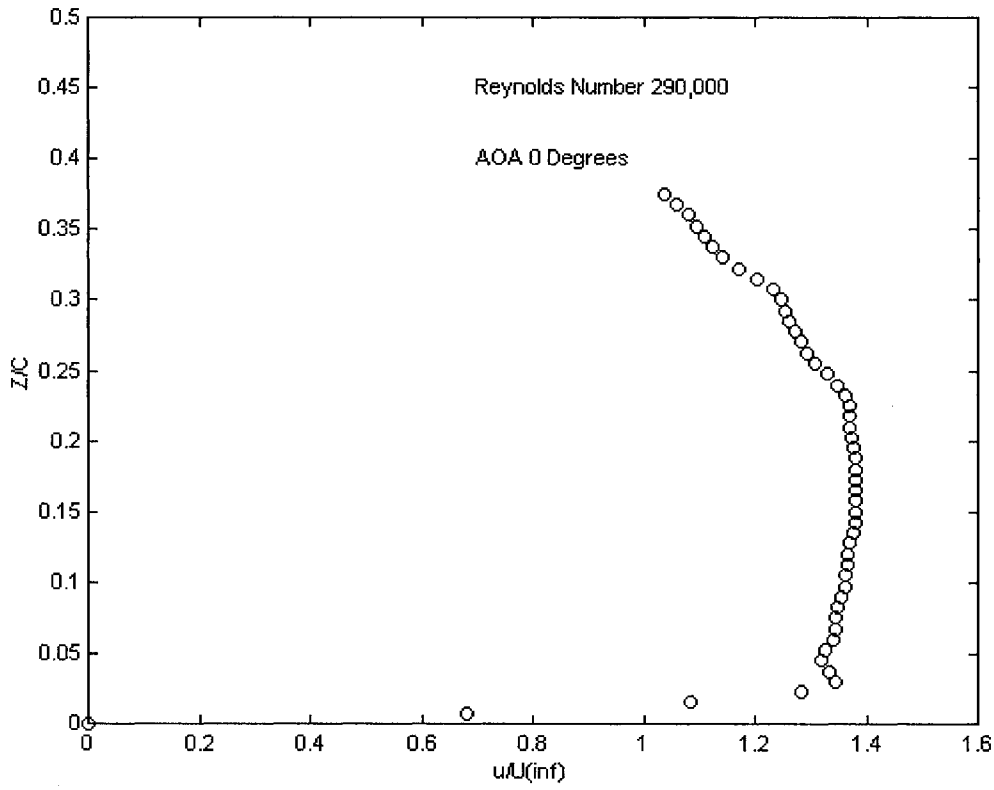

Figure 5.1 - Velocity Profile in Slat Wake, V_∞ = 10 m/s; 0° AOA.

Care was taken to ensure that the velocity profile was smooth when the cubic-spline utility was used to combine both data segments. The measured velocities were higher than the free stream velocity of 10 m/s due to the acceleration of the flow around the airfoil induced by the curvature of the main wing upper surface.

Z (in)	V (m/s)
0.0000	0.00000
0.250	13.0052
0.350	13.0819
0.450	13.1581
0.550	13.1106
0.650	13.2177
0.750	13.2185
0.850	13.3177
0.950	13.2748
1.050	13.3765
1.150	13.3126
1.250	13.3985
1.350	13.4383
1.450	13.3329
1.550	13.5125
1.650	13.5722
1.750	13.6128
1.850	13.5864
1.950	13.6461
2.050	13.6149
2.150	13.7387
2.250	13.6903
2.350	13.8041
2.450	13.7815
2.550	13.8143
2.650	13.7799
2.750	13.8020
2.850	13.7962
2.950	13.8534
3.050	13.8318
3.150	13.8116
3.250	13.7574
3.350	13.7899
3.450	13.7844
3.550	13.7061
3.650	13.7073
3.750	13.7055
3.850	13.6975
3.950	13.6934
4.050	13.7004

Table 5.1 – Velocity Profile Behind Slat Wake at V_∞ = 10 m/s; 0° AOA.

The other major inputs to the program included the initial values for the real and imaginary wave number and the angular frequency. Once the non-dimensional angular frequency is determined by the analysis, it must be divided by 2π in order to compute the non-dimensional frequency or Strouhal number. The results from the Fourier spectral analysis were presented in terms of a dimensional frequency in cycles per second. To compare the results from the linear stability analysis with the results from the Fourier spectral analysis, the frequencies generated by the latter were converted to Strouhal number using the free-stream velocity and the reference length of 18 in (nested chord length).

The required eigenvalues of wave number and angular frequency were normalized using Equation 5.1.1-1.

$$\delta = \frac{2\pi}{\lambda^*}\ell^* \qquad \omega = \frac{2\pi f_N \nu}{U_\infty^{\,2}} \qquad (5.1.1\text{-}1)$$

In Equation 5.1-36 λ^* is the dimensional wavelength of the vortical disturbance, ℓ^* is the reference length, and ω is the non-dimensional angular frequency. The portion of the velocity profile that was used for the linear stability analysis extended from the point 0.25 in. from the model surface to the vertical location where the mean velocity profile was uniform in the normal direction. The Reynolds number of 290,000 was also based on the reference length of the model.

Linear Stability Analysis was performed for the case of a spatially growing disturbance. In this case, the complex wave number δ is comprised of both a real and imaginary part, whereas the angular frequency is purely real. The real part of the wave

number δ_r provided information about the wavelength of the disturbance as observed by an observer traveling along with the disturbance. The imaginary part of the wave number δ_i is the amplification rate, whereas ω_r is the angular frequency of the disturbance as seen by a fixed observer in the test section. There should be correlation between the distribution of amplification factors and the distribution of power spectra as measured with the hot-film sensor. The peak amplification factor should occur near the first subharmonic of the natural frequency as identified by the hot-film sensor. If the perturbation component in the flow field with the highest amplification factor is externally excited, then vortex pairing is enhanced. When this happens, the system of vortices becomes more coherent and is more capable of transferring turbulent kinetic energy to the boundary layer. Figure 5.2 shows the results of the Linear Stability Analysis. Specifically, for the case of flow velocity of 10 m/s, the maximum disturbance amplification rate occurs at a normalized frequency of 15. This was determined by using a MATLAB utility called MAX, which not only selects the maximum number from a set of numbers stored as a vector, but also returns its index location in the vector. The velocity profile was taken with the hot-film sensor located as close to the slat as possible with the traversing strut being abutted to the trailing edge of the flap. The longitudinal position counter indicated a reading near 12.84, which was approximately the same longitudinal setting where spectral data were measured. This was to ensure that acquisition of both the spectral data and the velocity profile occurred at the same location and Reynolds number. This was necessary to independently compare the determinations of salient flow-field frequencies from both methods.

The eigensolutions algorithm developed using the Linear Stability Analysis code was programmed to generate a distribution within a prescribed bandwidth. It was not

considered necessary to locate where the curve crossed zero on the horizontal axis since the primary goal was to identify the critical frequency that had the greatest amplification rate.

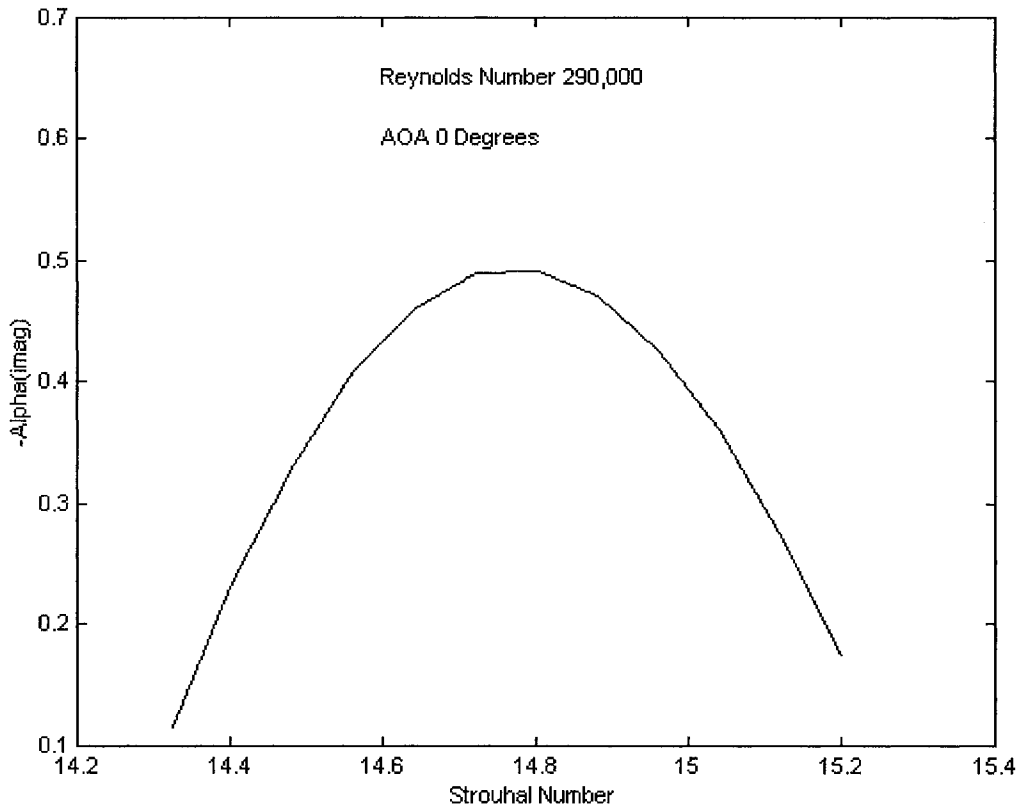

Figure 5.2 - Distribution of Eigenvalues in Slat Wake at V_∞ = 10 m/s and at 0° AOA

Figure 5.2 shows the typical rounded distribution of the normalized imaginary wave number versus the normalized angular frequency. The normalized angular frequency corresponding to the peak of the distribution is the frequency at the largest rate of amplification expressed in angular form. A MATLAB utility MAX, was used to determine the angular frequency corresponding to the maximum value of the wave number. Since the

maximum Strouhal number was found to be approximately 15, the corresponding frequency was computed in engineering units by using Equation 5.1.1-2.

$$f_n = \frac{St \times U_\infty}{\ell} \qquad (5.1.1-2)$$

When the appropriate values was substituted into this equation the frequency at the maximum rate of amplification is found in Equation 5.1.1-3

$$f_{max} = \frac{15 \times 10\ m/s}{0.4572\ m} = 328.08\ Hz \qquad (5.1.1-3)$$

Since the frequency, which dominates the vortex pairing process as been shown from previous studies [Bhattacharjee, S., et al, 1986], [Oster, D. and Wygnanski, I, 1982] to be a subharmonic of the vortex passage frequency, this would suggest that the vortex passage frequency is likely to be roughly twice the frequency corresponding to the peak amplification rate. Accordingly, based on Linear Stability Analysis, the natural frequency of the system of vortices emanating from the slat was approximately 656 Hz.

5.2 Stability Analysis at High Reynolds Number

The results of the linear stability analysis already reported is important because it demonstrated the potential of using this theory to predict the frequency distribution of flow-field disturbances. Since the region of confluence is a flow regime that is the subject of much recent inquiry, the frequency distribution of disturbances may open up an added window of knowledge concerning the inherent viscous slat/boundary-layer interactions.

However, because the data was for a relatively low Reynolds number, the results have limited applicability to full-scale aircraft. The following discussion focuses on the application of linear stability analysis to a data set derived from a multi-element airfoil tested at a higher Reynolds number that more closely approaches actual flight conditions. This objective is desirable due to the inherent uncertainty involved with using relatively low Reynolds number land-based data to extrapolate measured aerodynamic characteristics to flight conditions. An investigation of in-flight performance of a high-lift wing section [Long, P. Yip, et al., 1995] was performed using a Boeing B737-100 twin jet transport. The lifting surface consisted of a slat, main wing and a triple-slotted Fowler flap. The data was collected for Reynolds numbers ranging from 10.2 to 21 million, based on the mean aerodynamic chord. The results reported herein can be used to more directly infer information about the flow field stability characteristics of full-scale subsonic transports. The distribution of disturbances in the flow field has an effect upon the mechanisms responsible for the development of a turbulent boundary layer. Although the connection between stability analysis and the physics governing boundary layer transition to turbulence has not been satisfactorily resolved, it is undeniable that these two important topics are in some way intertwined. The effect of separation on the high-lift capability of an airfoil has also been well established. Moreover, because of the interplay between boundary-layer transition and separation, stability analysis should play a meaningful role in any discussion of aerodynamic lift.

The data reported in this section was for a similar geometry at an angle of attack of 8.1 degrees and a Reynolds number of 9 million at station number 0.45. The data is derived from [Chin, V. D. et al. 1993] and [Klausmeyer, S. M. et al., 1997]. A normalized velocity

profile from the data was used as input to the stability analysis program and the eigenvalues were calculated as previously done for the lower Reynolds number case. The velocity profile for these test conditions is shown in Figure 5.3. The velocity profile near the model surface was modeled as before using cubic-spline interpolation. This velocity profile is shown in Figure 5.4 and is presented in Table 5.2. The results of the stability analysis are depicted in Figure 5.5.

The original data [Chin, V. D. et al. 1993] and [Klausmeyer, S. M. et al., 1997] normalized the velocity using the experimental free stream velocity. For the stability analysis reported in this dissertation, the velocities were normalized by the velocity at the point coinciding to incipient interaction of the slat wake and main wing boundary layer. The purpose of this study is to understand the physical mechanisms occurring within the The results of the Linear Stability Analysis at the higher Reynolds number showed in Figure 5.5 that the peak amplification rate occurred at a Strouhal number of 0.058. The stability analysis program expresses the frequency in terms of a normalized angular frequency. To compute the Strouhal number, the angular frequency was divided by 2π. To capture the effect of the vortices in the slat wake it was necessary to include the wake in the velocity profile. This necessitated using the entire velocity profile from the surface of the model to the far-field flow field.

Through experience it was determined that the Linear Stability Analysis code worked best when the velocity profile was as smooth as possible, that is, without many irregularities. The required amount of smoothness could be achieved by using a polynomial fit through the data. Fortunately, this was not found to be necessary for the data at the higher Reynolds number.

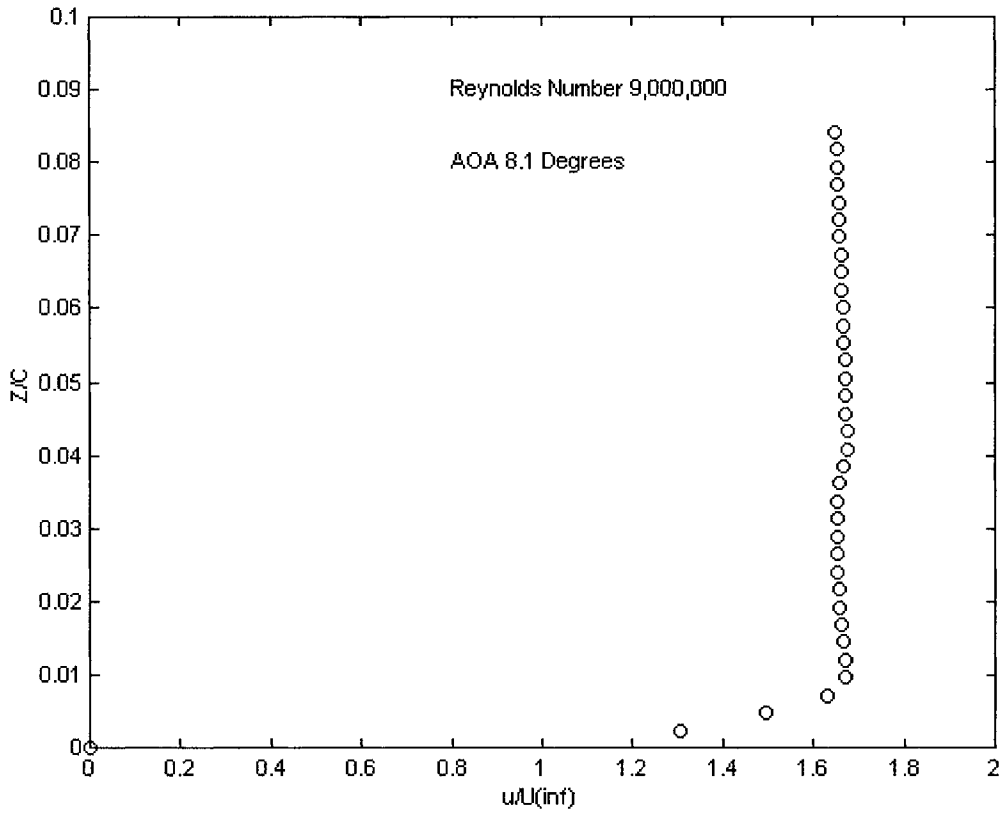

Figure 5.3 Velocity Profile Over Main Wing at 8.1° AOA, R=9,000,000,x/c=0.45

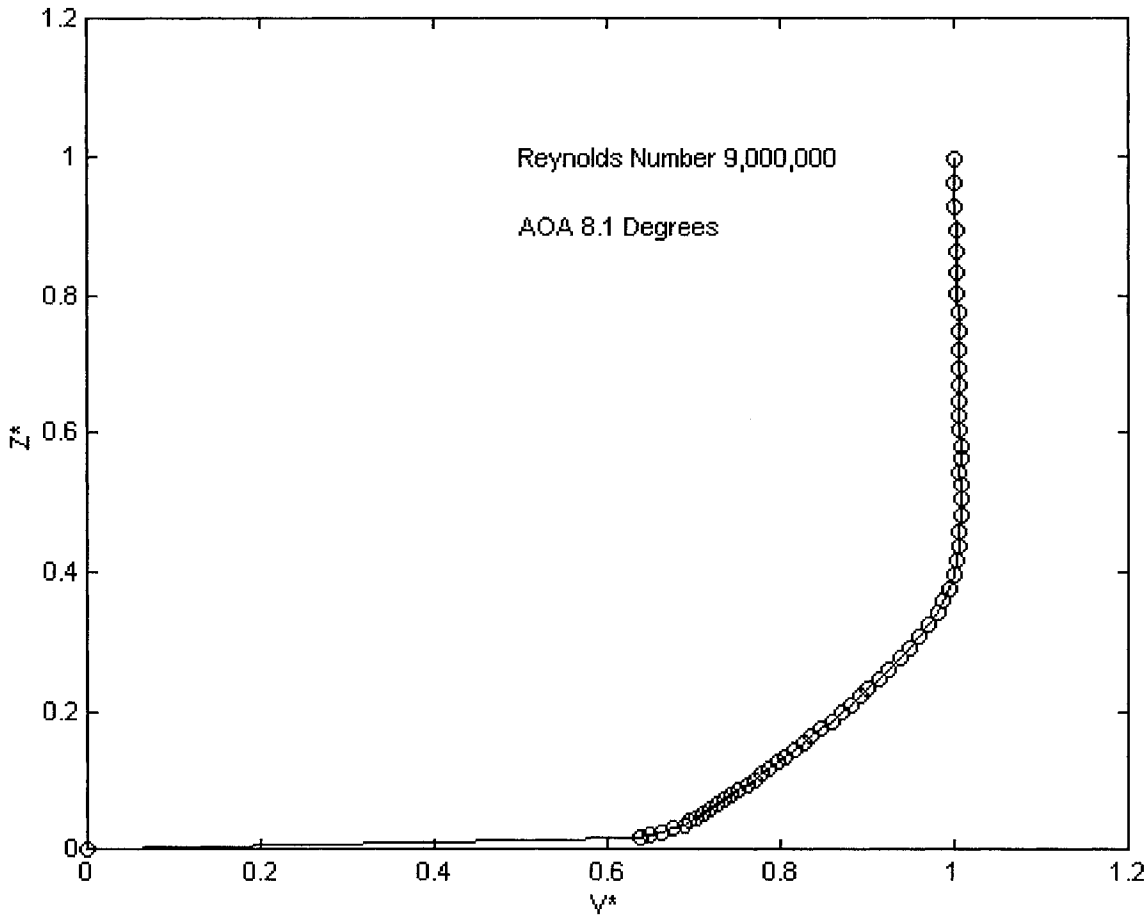

Figure 5.4 Velocity Profile Near Main Wing Surface at 8.1° AOA, R=9,000,000, x/c=0.45

Z/C	V/V_∞
0.0000000	0.0000
0.0003188	1.0587
0.0004132	1.0772
0.0005103	1.0990
0.0006129	1.1188
0.0007183	1.1428
0.0008293	1.1522
0.0009458	1.1656
0.0010651	1.1785
0.0011900	1.1930
0.0013204	1.2062
0.0014563	1.2174
0.0015978	1.2336
0.0017448	1.2475
0.0018974	1.2642
0.0020556	1.2784
0.0022192	1.2884
0.0023912	1.3053
0.0025688	1.3218
0.0027547	1.3359
0.0029489	1.3512
0.0031486	1.3707
0.0033567	1.3868
0.0035731	1.4035
0.0038006	1.4231
0.0040364	1.4416
0.0042806	1.4594
0.0045358	1.4787
0.0048021	1.4940
0.0050768	1.5143
0.0053625	1.5345
0.0056622	1.5547
0.0059729	1.5728
0.0062947	1.5929

Table 5.2(a) – Velocity Profile Behind Slat Wake at R_e = 9,000,000; 8.1 Degrees AOA

Z/C	V/V_∞
0.0066304	1.6083
0.0069800	1.6243
0.0073434	1.6373
0.0077207	1.6487
0.0081147	1.6572
0.0085253	1.6639
0.0089525	1.6676
0.0093964	1.6691
0.0098570	1.6695
0.0104120	1.6697
0.0107750	1.6701
0.0111530	1.6686
0.0115460	1.6697
0.0119570	1.6693
0.0123840	1.6688
0.0128280	1.6660
0.0132890	1.6656
0.0137690	1.6662
0.0142680	1.6677
0.0147870	1.6667
0.0153280	1.6655
0.0158910	1.6647
0.0164760	1.6621
0.0170840	1.6618
0.0177170	1.6620
0.0183740	1.6604
0.0190590	1.6597
0.0197720	1.6587
0.0205130	1.6579
0.0212840	1.6563
0.0220890	1.6558
0.0229240	1.6561
0.0237920	1.6544
0.0246970	1.6543
0.0256370	1.6544

Table 5.2(b) – Velocity Profile Behind Slat Wake at R_e = 9,000,000; 8.1 Degrees AOA

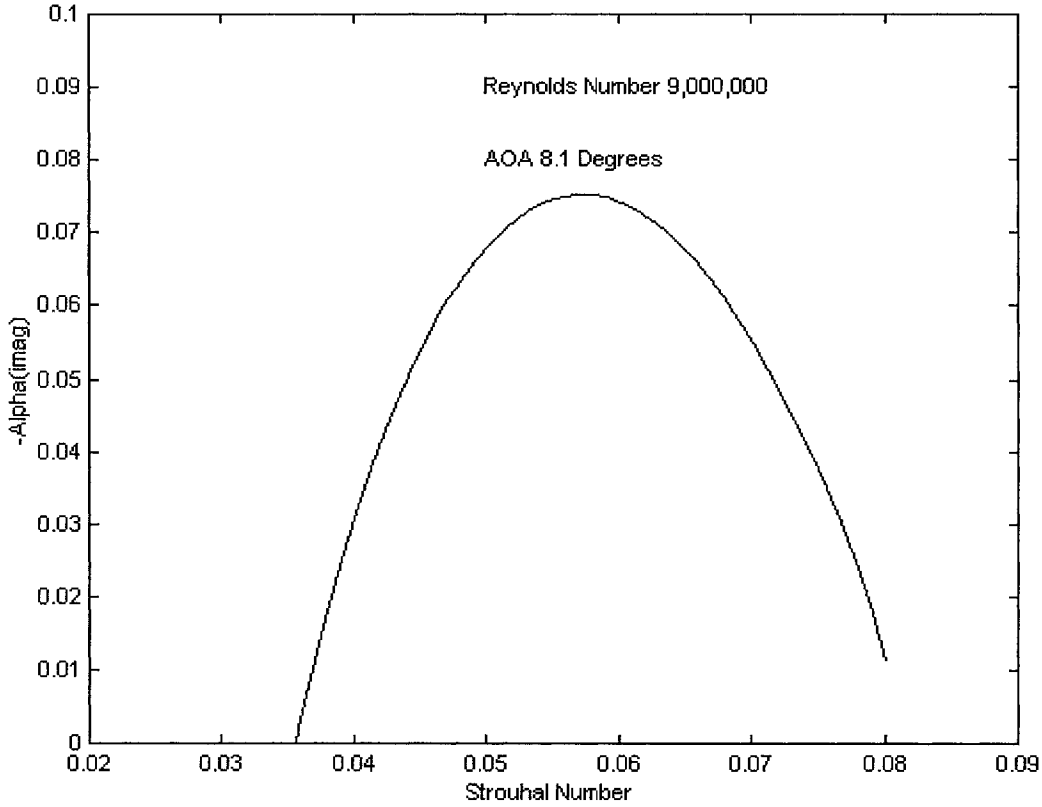

Figure 5.5 - Distribution of Eigenvalues at 8.1° AOA, R=9,000,000, x/c=0.45

exact same model that was the subject of this dissertation. Recall that for the model used in this dissertation, the Strouhal number corresponding to the peak amplification rate was 15. As was shown in Figure 1.22, the normalized frequency or Strouhal number generally decreases with increasing Reynolds number. Another interesting characteristic shown in Figure 5.5 is the fact that the range of Strouhal numbers is rather narrow. This fact is also in agreement with Linear Stability Theory, which postulates that the range of Strouhal number for an unstable boundary layer diminishes at the higher Reynolds numbers.

The results from an earlier classical experiment [Schubauer, G. and Skramstad, H., 1947] suggest that the evolution of transition to turbulence is facilitated by the presence of disturbances within a specified range of wavelengths. It is known that one advantage of turbulence is its tendency to maintain an attached boundary layer. To promote turbulence one must know the range of required wavelengths to induce into the flow. Information such as is provided by the above distribution of eigensolutions can provide the engineer with the range of wavelengths that have the largest potential of facilitating turbulence to maintain boundary-layer attachment and to avoid separation on a full-scale lifting surface.

5.3 Hot-Film Measurement of Vortex Periodicity

The vortex passage or natural frequency of these vortices has to be measured as they propagate in a chordwise direction. This was accomplished by using hot-film measurements to obtain both time-history information and to employ FFT analysis to produce power spectral plots of the data, showing the prominent frequency amplitudes, with the expectation that these plots will reveal the fundamental frequencies for the selected free-stream velocities. The measurements were made at a free-stream velocity of 10 m/s.

The dominant frequency was estimated by examining the power spectra obtained from hot-film measurements and by looking for the spectral component with the most prominent amplitude. Comparing the results from the theory with the hot-film data can validate the suitability of Linear Stability Theory for this model. This task posed a serious challenge, namely, of determining the optimum distance of the hot-film sensor from the surface of the model. The frequency detected by the sensor depends on the location of the sensor tip relative to the edge of the system of vortices. Ideally, the true vortex natural

frequency would be measured if the sensor could be placed right at the upper edge of the vortices. If the sensor were placed closer to the wall, the measured frequency would be higher than the true value. One idea was to examine the vertical profile of the Reynolds stress component that is coplanar with the plane formed by the free-stream and normal directions. Ideally, the magnitude of the stress would drop off immediately above the edge of the vortex. However, there are uncertainties associated with this approach because the decrease in Reynolds stress might not be precipitous enough to detect any sharp demarcation between the edge of the vortex and the flow field not embedded with swirling motion.

In an attempt to glean some understanding of the structure of the vortex system, the hot-film sensor was placed at three different heights from the wall of the model to obtain their respective power spectra. The data were examined to find a trend in the shifting of the most prominent spectral amplitude with variation in sensor height. The various sensor heights were 0.4, 0.5 and 0.6 in. The model had a 0° angle of attack and the free stream velocity was 10 m/s. The power spectra for this case are displayed in Figures 5.6 through 5.8. Although full interpretation of these spectra for the various probe heights was difficult, the nominal Strouhal number generally lies within a range between 25 and 30. The normalized frequency or Strouhal number is in Equation 5.2.

$$St = \frac{f * \ell}{U_\infty} \qquad (5.2)$$

The reference length was 18 in. and reference velocity was 10 m/s. Using this rather wide range of Strouhal number means that the fundamental frequency lies somewhere between 547 and 656 Hz. To make comparisons possible, the average of these two values will be

used to represent the fundamental frequency derived from hot-film measurements. Linear stability analysis predicted a fundamental frequency of 618.98 Hz, which was roughly midway between these two extremes.

These power spectra plots are similar to those published by Bhattacharjee [1986] in their study of disturbances within a shear layer downstream of an aft-facing step [Bhattacharjee, S., et al., 1986]. The plots clearly exhibit a rounded peak with a fairly broad bandwidth and Bhattacharjee [1986] decided to use the Strouhal number at the lower end of the rounded peak as the frequency corresponding to the passage frequency of the disturbance. The vortices can be idealized as consisting of a train of circular swirls that propagate downstream. Note that as the sensor is located nearer the center of the swirling mass of air that the measured values of the fluctuating velocities would be subject to more variability, and the period between changes in the output signal would be smaller. However, at the edge of the vortex system, the period between encounters of the sensor and consecutive vortices would be larger, which means that the frequency would be diminished. Roughly, the data show that the centroid of the peak appears to shift towards higher frequencies as the sensor height is increased. This trend indicates that, as the sensor height is increased, it is probably moving ever closer to the core of the system of vortices.

When this data were compared with the spectral results for the case of an empty tunnel, the peaks exhibited in the latter case are three orders of magnitude less. This

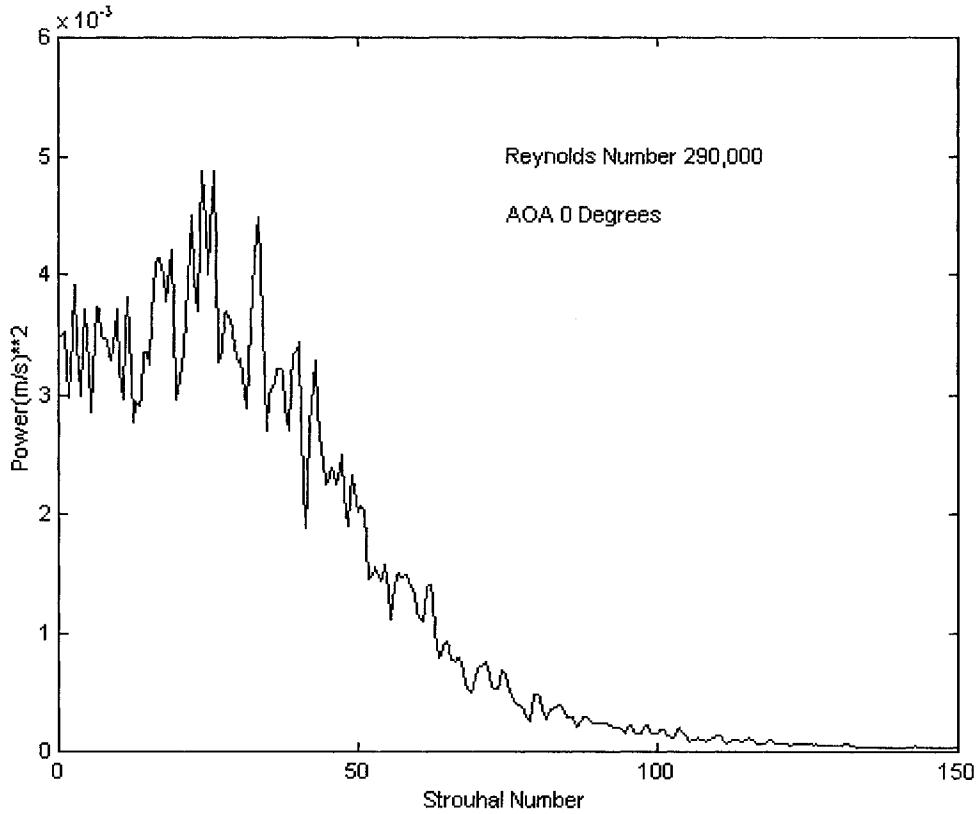

Figure 5.6 - Power Spectrum at V= 10 m/s, 0 Degrees AOA; Z = 0.022 c

suggests that the spectral data for the case when the model was installed is not significantly affected by the background disturbances.

To calculate the vortex-passing frequency based on the normalized number, a Strouhal number of 27.5 was used because this was the value that always appeared to be near the center of the rounded peak for all three cases. The frequency was calculated to be approximately 601.5 Hz. This frequency was compared with the results from flow visualization analysis and the predicted results from linear stability theory. Although these results were not used in this experiment as originally intended, they provided valuable insight into the validity of using stability theory to predict some of the viscous flow characteristics in the wake of the leading-edge slat. Perhaps theoretical results can be used

to unravel some of the intricacies associated with the interplay between slat configuration changes and amplification factions for certain disturbance frequencies. This would be valuable information that could be used to better understand and predict the phenomenon of turbulence in the wake. This ultimately can play a decisive role in controlling the flow field surrounding the trailing edge flap where boundary layer separation occurs. Because the aerodynamic lift is affected by the boundary-layer separation on the flap, this development has an impact on the overall lifting capability of the multi-element airfoil.

Another trend that was observed from the data was that the magnitude of the highest amplitude decreased as the height of the sensor from the model increases. The data showed that at a sensor height of 0.40 in the peak amplitude is close to 0.005 m^2/s^2, whereas the highest peaks for heights of 0.50 in and 0.60 in were a little over 0.0025m^2/s^2 and 0.0008 m^2/s^2, respectively. Again, the explanation for this observation was not decisively clear, but these results implied that as the sensor was positioned further from the wall, the parcels of air that it measured contained increasingly less energy. Referring again to the idealized model of the system of vortices, the local vorticity decreased as the sensor approached the center of core of the vortex because the tangential velocity of the swirling air diminished with decreasing radial distance from the core. Although the conclusions mentioned in the previous paragraph are not without speculation, the exhibited trend in the amplitude of the peak spectral component seemed to corroborate the idea that the sensor was approaching the center of the vortex system.

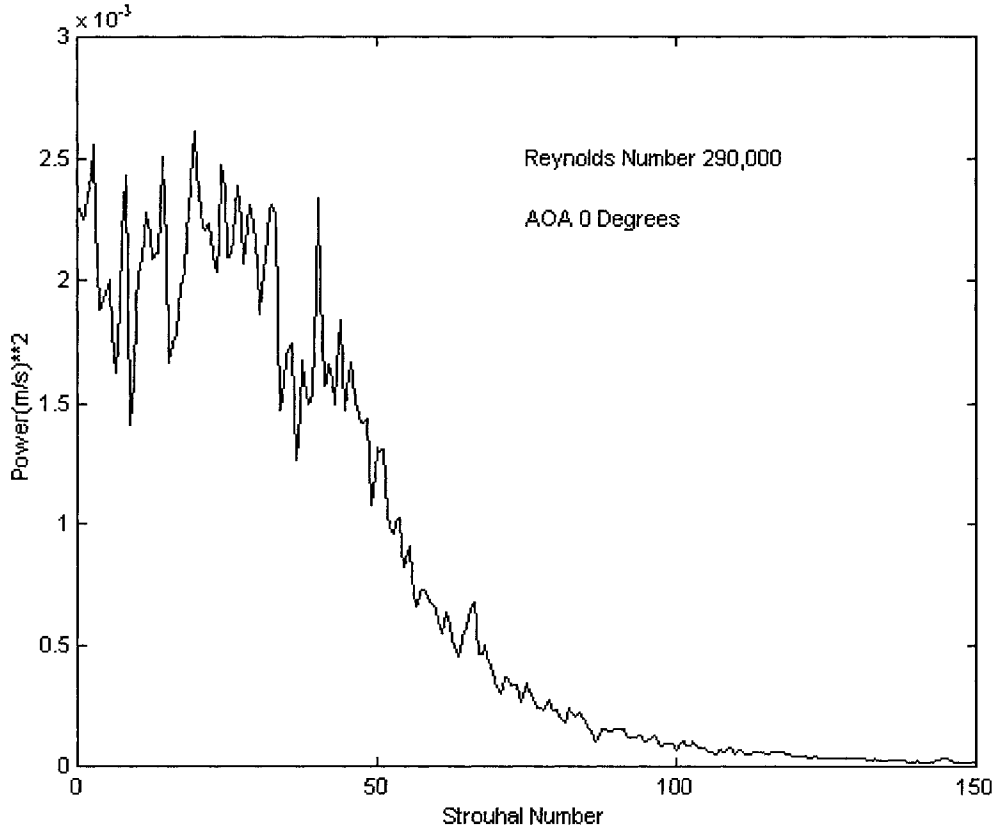

Figure 5.7 - Power Spectrum at V = 10 m/s, 0 Degrees AOA; Z = 0.028 c

If the above interpretation of the results is correct, then spectra for a larger range of sensor heights can be obtained and the corresponding amplitudes of the spectral peak can be recorded so that the size and structure of the vortices can be estimated. The highest spectral peaks should occur at the lower and upper edges of the system of vortices. The purpose of this study was to perform only a preliminary investigation into the feasibility of predicting flow parameters using stability theory.

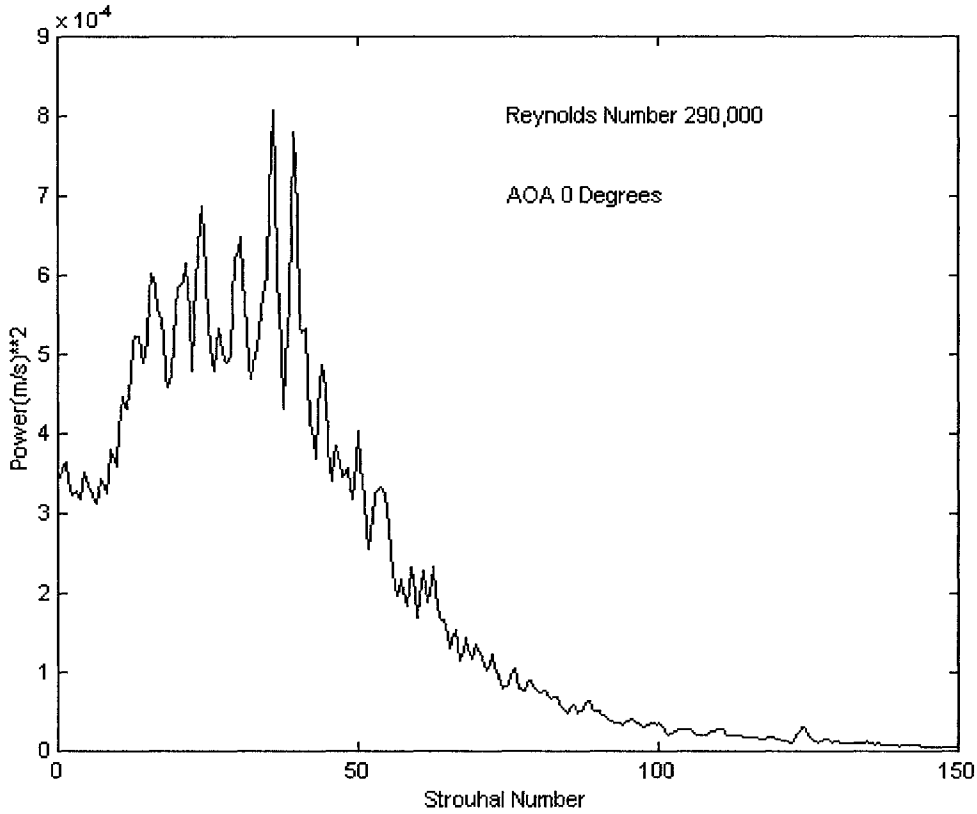

Figure 5.8 - Power Spectrum at V = 10 m/s, 0 Degrees AOA; Z = 0.033 c

Spectral data were also obtained with the hot-film sensor at free-stream velocities of 20 and 30 m/s at 0° angle of attack. These results are shown in Figures 5.9 and 5.10. The peaks of the power spectra occur at a Strouhal number of 15 for free-stream velocities of 20 and 30 m/s, which corresponds to natural frequencies of 656 Hz and 984 Hz, respectively. The first subharmonics for these natural frequencies are 328 Hz and 492 Hz, respectively. It is expected that for the free-stream velocity of 20 m/s, the system of shed vortices emanating from the slat would exhibit a high rate of merging near a forcing frequency of 328 Hz. The forcing mechanism enhances an instability that already exists within the flow [Oster, D. and Wygnanaski, I., 1982].

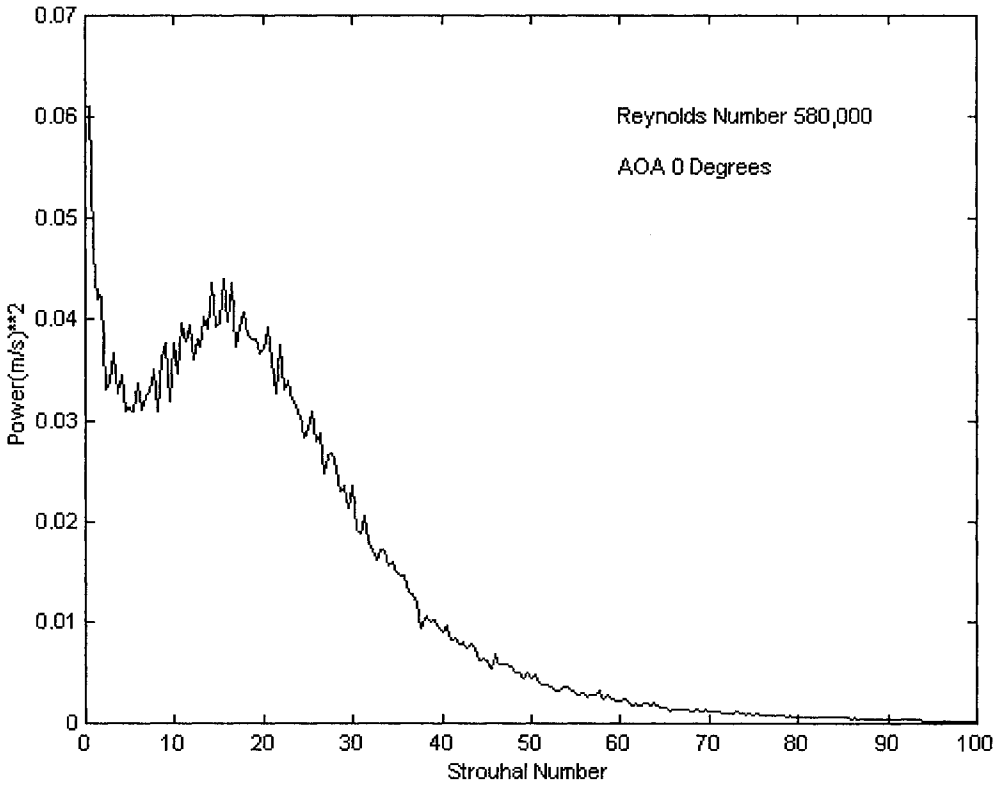

Figure 5.9 - Power Spectrum at V = 20 m/s, 0 Degrees AOA

The peaks of the power spectra shown in Figures 5.8 through 5.10 all occur at generally the same Strouhal number of 15. According to the Linear Stability Theory as shown in Figure 1.25 the Strouhal number decreases with increasing Reynolds number. The differences in Reynolds number for the three test conditions were not large enough to cause a significant change in Strouhal number at the peak spectral power. Recall from a previous section that a marked change in the non-dimensional frequency occurred when the Reynolds number was increased to a higher order of magnitude

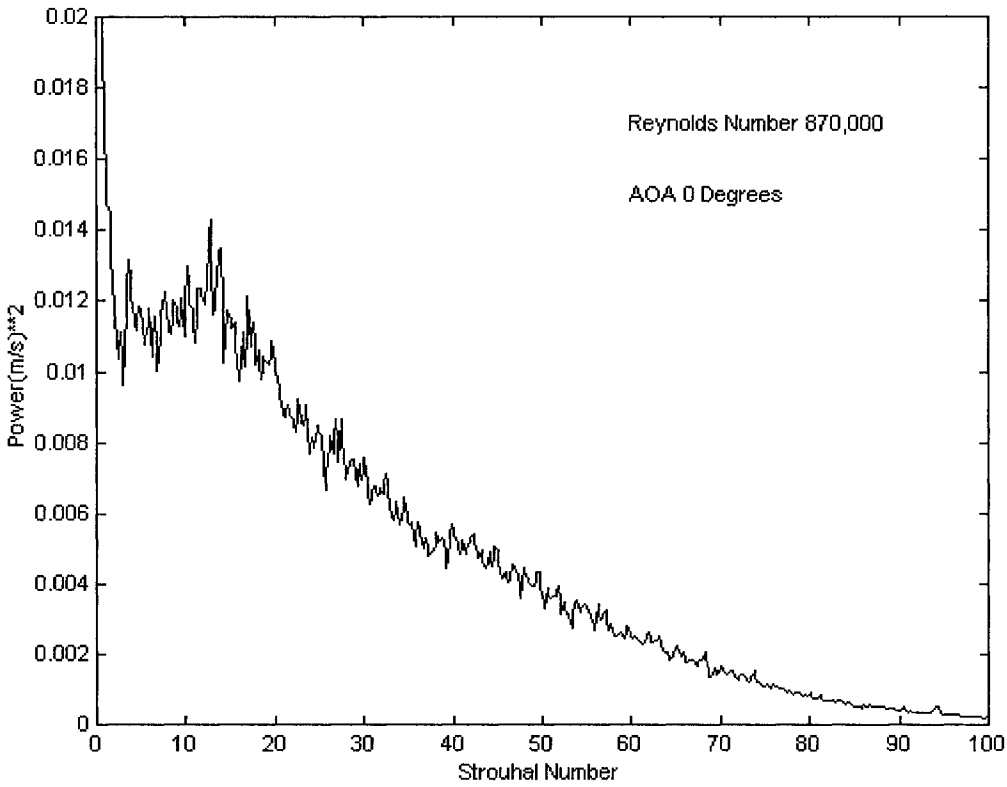

Figure 5.10 - Power Spectrum at V = 30 m/s, 0 Degrees AOA

5.4 Smoke Visualization of Vortex Flow

The flow visualization set-up as described in Chapter 4.6 was employed to corroborate data obtained from the hot-film sensor data. As Figure 5.11 shows, vortex structures appeared in the trail of smoke, albeit faint. The objective was to determine the wavelength of the vortex stream from the still photographs by identifying the wavelength from the leading edge of one vortex to the leading edge of an immediately subsequent vortex. A suitable length scale factor was required to obtain the actual wavelength between periodic structures appearing in the stream of smoke. The length scale factor was used to correct the wavelength, measured directly from the still photograph. The length scale factor

was obtained by computing the ratio of the apparent width of a single strip of masking tape, shown clearly on the model in the still photograph with the actual full-size width of the strip. The appropriate scale factor was determined to be 4.1333. This scale factor was then multiplied by the width between the regularly spaced structures as measured from the still photograph. Several photographs were obtained, but the photograph shown in Figure 5.11 shows most clearly the periodic structures in the trail of smoke. The photograph clearly shows an indication of periodicity within the smoke stream. This arises from the vortices, which seem to originate from the slot region immediately behind the leading edge-slat. The photograph reveals periodic circular structures embedded in the flow along with patches of dark areas. The vortex passing frequency can be approximated from the qualitative data demonstrated by these pictures. The quality of the image is less than ideal, but it still does reveal the presence of coherent structures.

The wavelength for a velocity of 10m/s as measured from the photograph was calculated according to Equation 5.3.

$$\lambda = (\text{scale factor}) \times (\text{vortex spacing in inches}) \times (\text{conversion to meters}) \quad (5.3)$$

scale factor – 4.1333

vortex spacing – 0.1875 in

Using the above equation and the required parameters at 10 m/s and at 0° angle of attack, the wavelength was measured from the flow visualization photograph was found to be 0.01968 m. To determine the vortex passage frequency from the wavelength the disturbance speed must be known. The wave speed, c, was thought to be practically equal to the local velocity near the edge of the vortices. The reference velocity used in this study was the velocity at the edge of the velocity profile, just below the start of the slat wake and

was found to be 13.3765 m/s. This is of course higher than the free-stream velocity due to the effect of the curved upper surface, which accelerates the air flowing around the upper surface. The natural or vortex passing frequency based on smoke visualization was then calculated from Equation 5.4.

$$f = \frac{U_{edge}}{\lambda} = \frac{13.3765 m/s}{0.01968 m} = 679 \, Hz$$

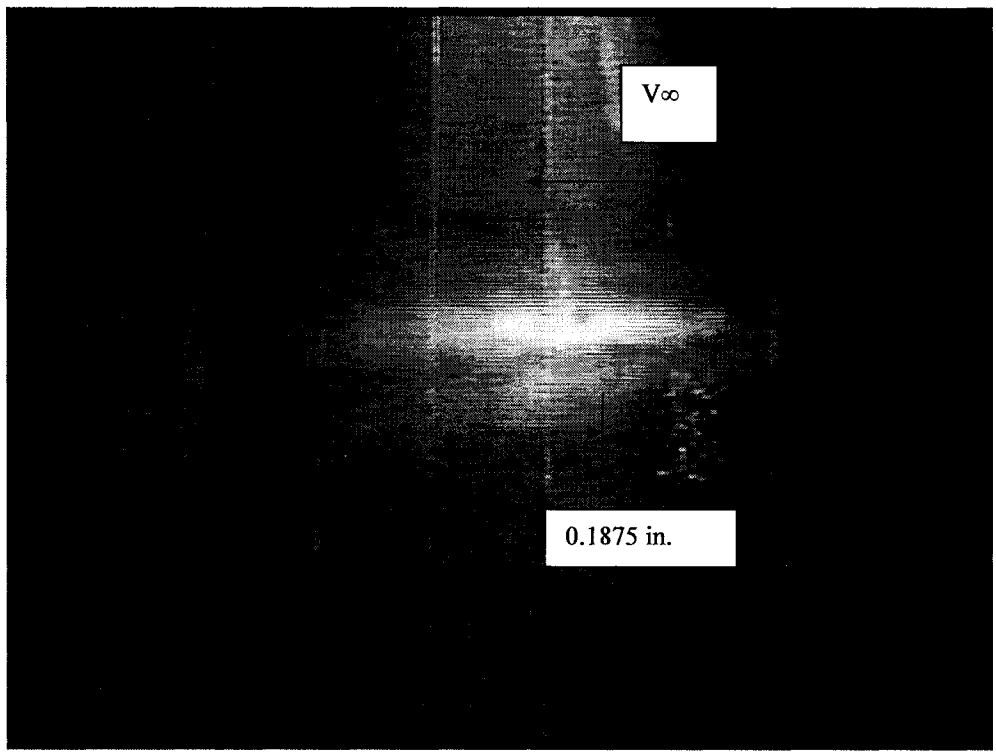

Figure 5.11 – Flow Visualization on Main Wing Upper Surface at V_∞ = 10 m/s, 0 ° AOA

5.5 Summary of Fundamental Frequency Study

In the previous analysis, three independent methods were utilized to determine the vortex passing frequency or natural frequency on a 2D multi-element airfoil for the free-stream velocity of 10 m/s at a 0° angle of attack. One method involved the use of a hot-film sensor to obtain measurements within the wake of the slat. The sensor was positioned so that it was as close as possible to the trailing edge of the slat. From this data, the power spectra were calculated for three different probe heights above the model surface. These data were subsequently plotted to display the range of frequencies that play a dominant role in the flow-field characteristics of the slat wake.

Another method to determine the natural frequency used smoke to visualize the periodic structure of the wake. Videotape was created during the test run and still digital images were produced to analyze the flow.

A third method involved the implementation of viscous Linear Stability Theory to predict the distribution of amplification rates for the various frequency components in the flow. The theory application should show that the most dominant frequency corresponded to that spectral component with the highest amplification rate.

The results from the three independent methods are shown in the Table 5.3.

	Hot-Film Sensor	Flow Visualization	Stability Theory
f_N	601.0 Hz	679 Hz	656 Hz

Table 5.3 – Summary of Vortex Passage Frequency Analysis.

These results indicate a marked agreement between the three methods. The results from the hot-film measurements were assumed to be the most accurate. If that datum is used as the reference then the flow visualization and stability theory were in error by 13% and 9%, respectively. These results are encouraging since they indicate that the natural frequency can be estimated with a fair degree of accuracy by any of the three methods used in this study. If a future experiment is conducted on this model or one similar to it, then these results can be used to adjust the operating frequency of some device, which can be used to transfer oscillatory energy to the naturally-occurring vortices originating from the slat.

5.6 Surface Pressure Measurements

The following data show the results of the surface pressure measurements without the Plexiglas ® sidewalls. These results were later compared with the data obtained with the sidewalls to ascertain their effect upon the flow field. These data were taken to help characterize the aerodynamic characteristics of the model used in this experiment. Data were obtained at angles of attack of 0°, 5°, 10° and 15° for free-stream velocities of 10, 20, and 30 m/s. The instrumentation that was used was the 9000 series scanning pressure system manufactured by PSI. Although the main test velocity used throughout this experiment was 20 m/s, it was thought best to also obtain measurements at other velocities in order to acquire a comprehensive understanding of the overall characteristics of the model. No capability existed to remotely alter the model attitude while the tunnel was running, so it was required that operations be temporarily suspended between each configuration modification. Data are shown separately for the leading edge slat, the main wing and the trailing edge flap.

5.6.1 Pressure Distribution at Zero Degrees Angle of Attack

Figure 5.12 shows the pressure distribution for a free-stream velocity of approximately 10 m/s at 0° angle of attack for the three lifting surfaces. The data show that a fairly large suction peak exists at the leading edge of the main wing. The data show that the pressure coefficient is approaching a value of - 4.0 at the main wing leading edge. According to Smith [1975], this suction pressure peak should even be higher in the case of an isolated wing (i.e., wing without a leading-edge surface). The circulation of the slat counteracts that of the wing to produce a lower velocity in the gap region, and modifies the leading-edge suction of the wing.

The pressure coefficient increases precipitously farther downstream and then exhibits a marked leveling off. This moderation of the pressure recovery is probably due to the displacement effect of the slat wake on the streamlines interposed between the wake and the main wing boundary layer. This region of surface pressure moderation is thought to occur upstream of the point of merger between the slat wake and main wing boundary layer. This phenomenon appeared at all three free-stream flow velocities at 0° angle of attack and was tempered for the higher angles of attack.

Farther downstream, the pressure coefficient on the upper surface increases to a value of roughly –1.0 and remains fairly uniform for a large portion of the remaining chord length. The relative uniformity of the pressure distribution is probably due to the fact that a large extent of the upper surface is considerably flat, and hence, is aligned with the oncoming flow at a 0° angle of attack. At the trailing edge of the wing, the upper surface pressure coefficient shows a marked increase towards recovery to free-stream static pressure.

The pressure coefficient on the lower surface reaches a maximum value at around 5% of the reference chord length and then gradually decreases and eventually levels off downstream. The data shown in Figures 5.13 and 5.14 are the results for free-stream velocities of 20 and 30 m/s, respectively. The overall trends for these data approximately duplicate the trends for the data at 10 m/s. However, a comparison of the results at the different speeds indicated that the suction peak at the leading edge increases markedly with increasing free-stream velocity, which was a Reynolds number effect. This of course is due to the lower surface pressure attendant with the higher velocities that accelerate around the leading edge from the lower to the upper surface.

The data for the leading-edge slat demonstrated the expected trends. On the upper surface of the slat the pressure coefficients are positive, because the slat rigging positioned the upper surface generally directly head-on with respect to the free-stream flow. This orientation results in a stagnation point being located on the upper surface of the slat.

For this geometry, boundary layer separation is most prone to occur on the upper surface of the trailing-edge flap. However, for this angle of attack there was no indication that boundary-layer separation had occurred.

5.6.2 Pressure Distribution at a 5° Angle of Attack

The data for this model attitude are shown in Figures 5.15 through 5.17. The pressure recovery on the upper surface did not show the moderation as demonstrated at a 0° angle of attack. This might suggest that, at the higher angle of attack, the effect of the slat wake displacement is not as pronounced and that the initial location of confluence has shifted farther downstream. The data show the expected trend of direct correlation of peak suction pressure with angle of attack. At a velocity of 10 m/s the peak suction pressure

coefficient was observed to approach a value of –5. Again, the peak suction pressure coefficient also increases with free-stream velocity.

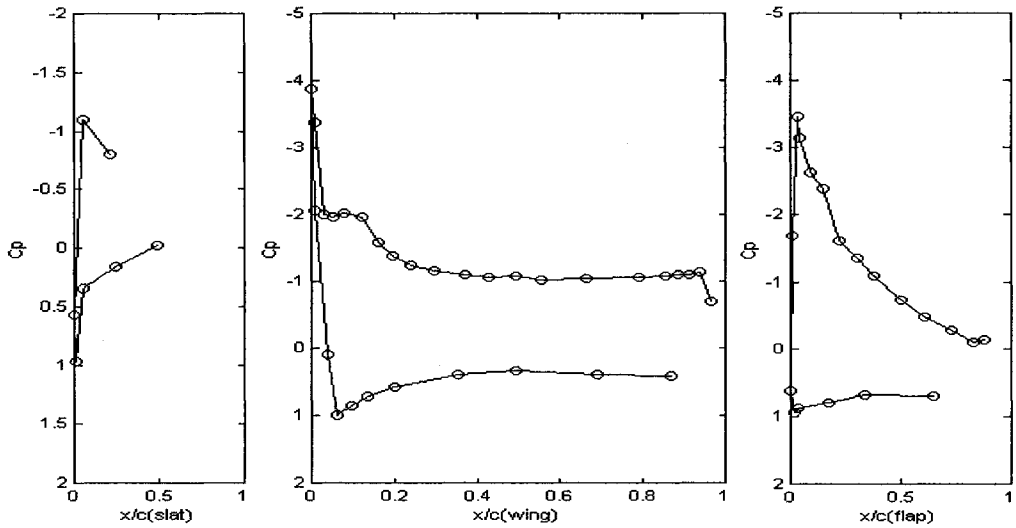

Figure 5.12 – Pressure Distribution at V_∞ = 10 m/s at 0° AOA

At the higher angle of attack, the envelope of the slat wake is displaced further away from the main wing so that it impinges on the boundary layer further downstream. Later it will be shown that the spreading rate of the slat wake can be controlled by acoustic excitation. Ordinarily, mixing between the wake slat and main wing boundary layer would cause a thickening of the boundary layer accompanied with a decrease in lift performance [Thomas, F. O., et al., 1998]. This might be responsible for the marked decrease in suction pressure near the trailing edge of the main wing. A byproduct of this fact is boundary-layer separation that occurs on the slat. However, the disadvantages or advantages of mixing between the slat wake and the wing boundary layer depend on whether vortex paring occurs due to external excitation at critical frequencies. This dissertation will show that vortex pairing induced by mixing is advantageous.

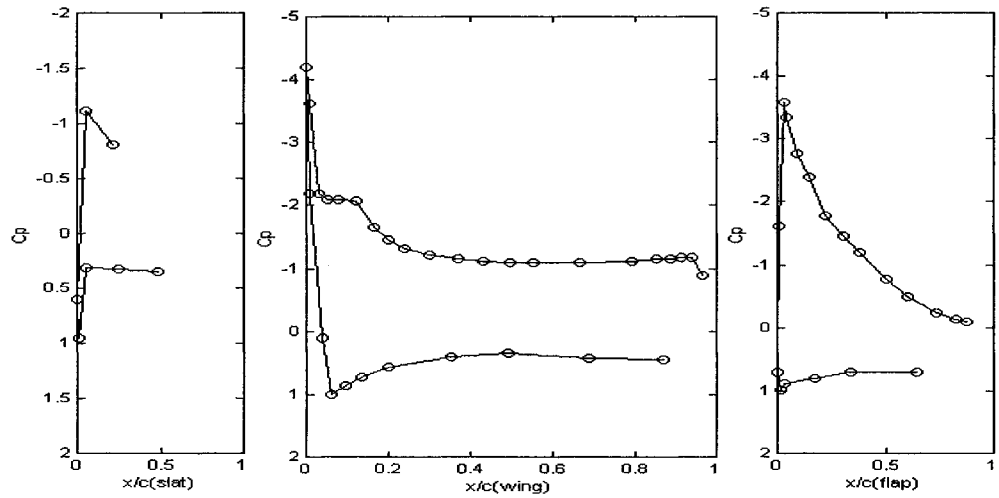

Figure 5.13 – Pressure distribution at V_∞ = 20.26 m/s at 0° AOA

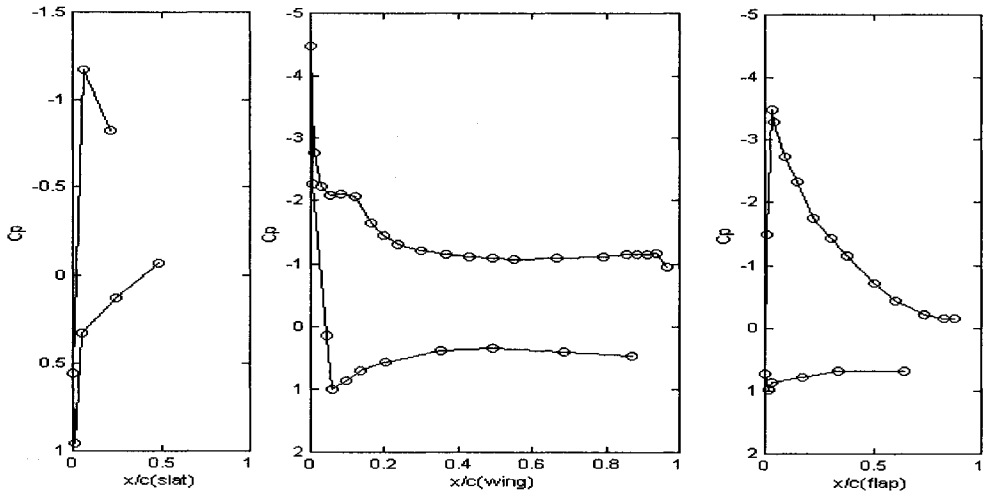

Figure 5.14– Pressure distribution at V_∞ = 29.92 m/s at 0° AOA

A correlation was noted between the rate of change of pressure recovery on the main wing and the occurrence of boundary layer separation on the flap. For the case of 10 m/s, separation on the flap occurs and the rate of change of the pressure recovery on the main wing for this case is greater than for either the 20 m/s or the 30 m/s cases. Separation on the flap does not occur for either of these latter two cases. The rate of change of the pressure recovery is expected to increase with angle of attack, however, the rate of recovery is much greater in the case of flap boundary layer-separation. At 10 m/s the data show that separation occurs for practically the entire chord length of the flap and the objective of this investigation was to moderate this by using boundary-layer control devices.

The upper surface of the leading-edge slat shows negative values of pressure coefficient, because at this angle of attack the upper surface is sufficiently turned away from the free-stream so that the near surface flow is being accelerated.

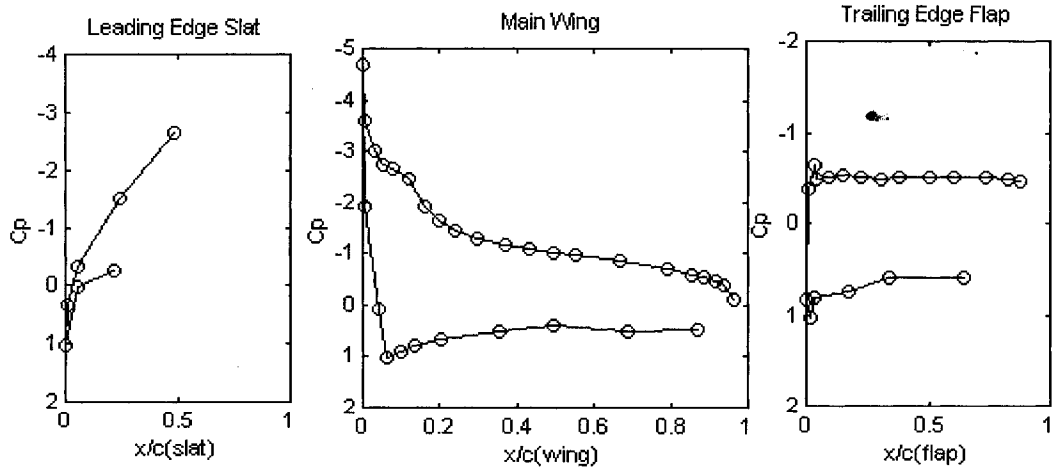

Figure 5.15 – Pressure distribution at V_∞ = 10.04 m/s at 5° AOA

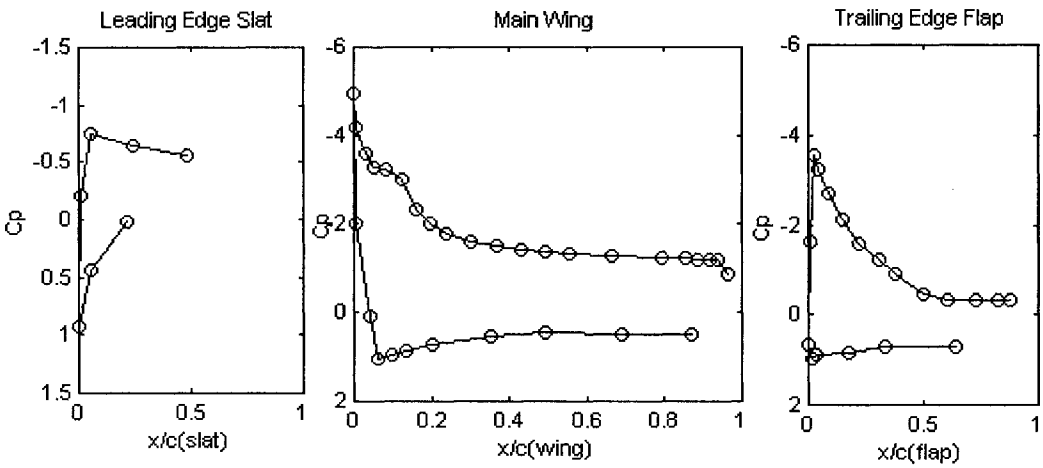

Figure 5.16 – Pressure distribution at V_∞ = 20.09 m/s at 5° AOA

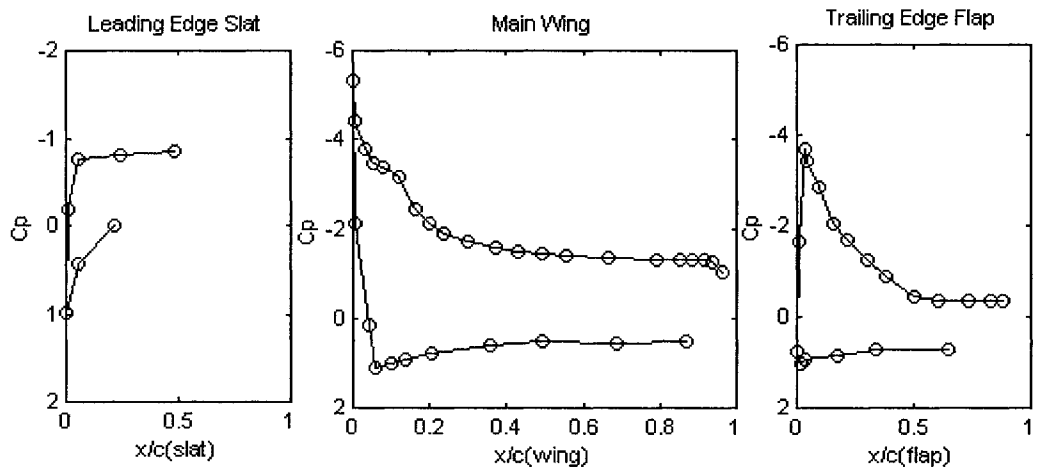

Figure 5.17 – Pressure distribution at V_∞ = 20.09 m/s at 5° AOA

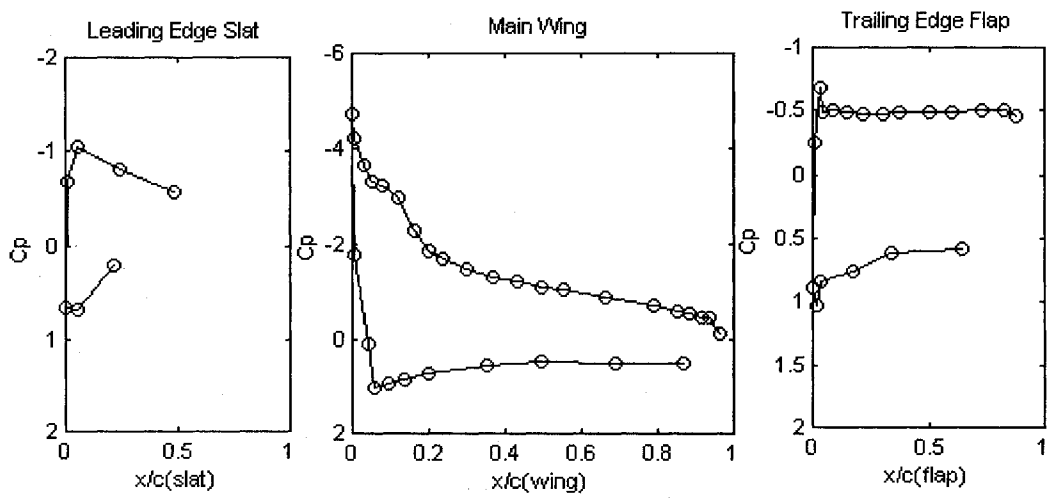

Figure 5.18 – Pressure distribution at V_∞ = 10.07 m/s at 10° AOA

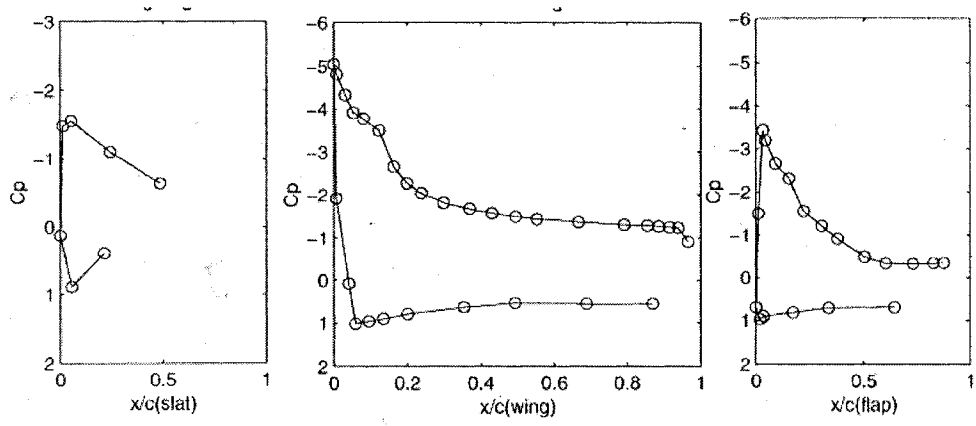

Figure 5.19 – Pressure distribution at V_∞ = 19.99 m/s at 10° AOA

5.6.3 Pressure Distribution at 10° Angle of Attack

The trends exhibit those similar to the test runs at a 5° angle of attack and are shown in Figures 5.18 through 5.20. Again, at a free-stream velocity of 10 m/s, the upper surface of

the main wing indicates a high rate of change of the pressure recovery and the associated flap separation. Note that the surface pressure recovers almost completely to the free stream static pressure.

5.6.4 Pressure Distribution at a 15° Angle of Attack

The data are depicted in Figures 5.21 through 5.23. At this high angle of attack, the adverse pressure gradient is so high that the boundary layer does not possess an adequate amount of kinetic energy to avoid separation. Therefore, boundary layer separation occurs on the trailing-edge flap for all three free-stream velocities.

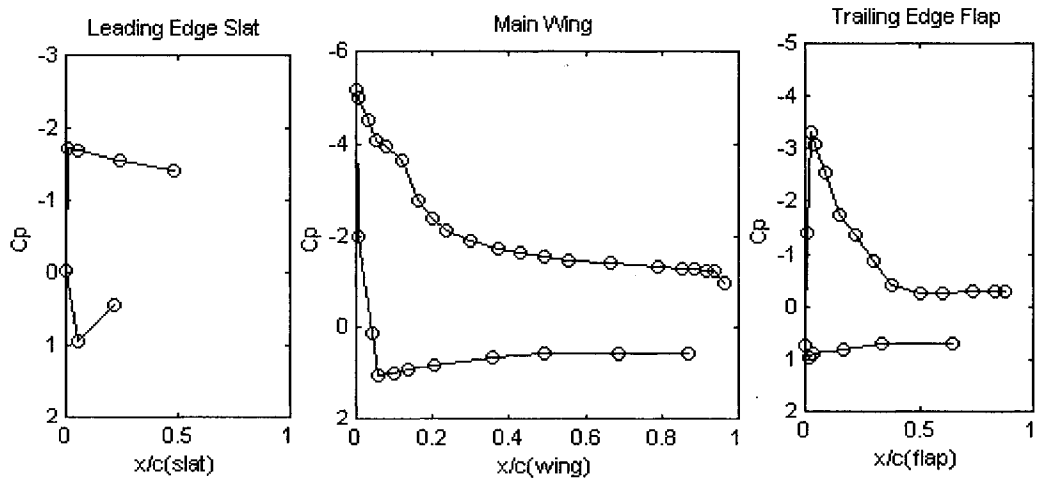

Figure 5.20 – Pressure distribution at V_∞ = 30.05 m/s at 10° AOA

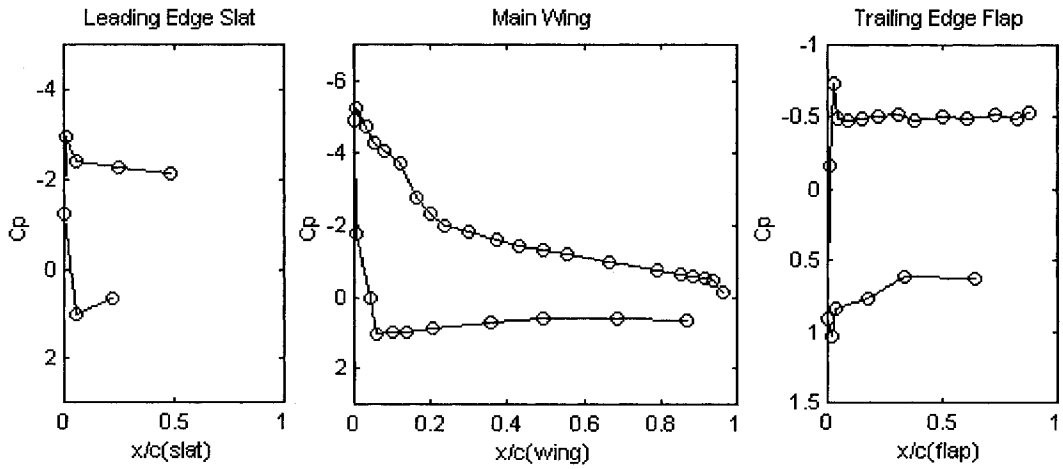

Figure 5.21 – Pressure distribution at V_∞ = 10.01 m/s at 15° AOA

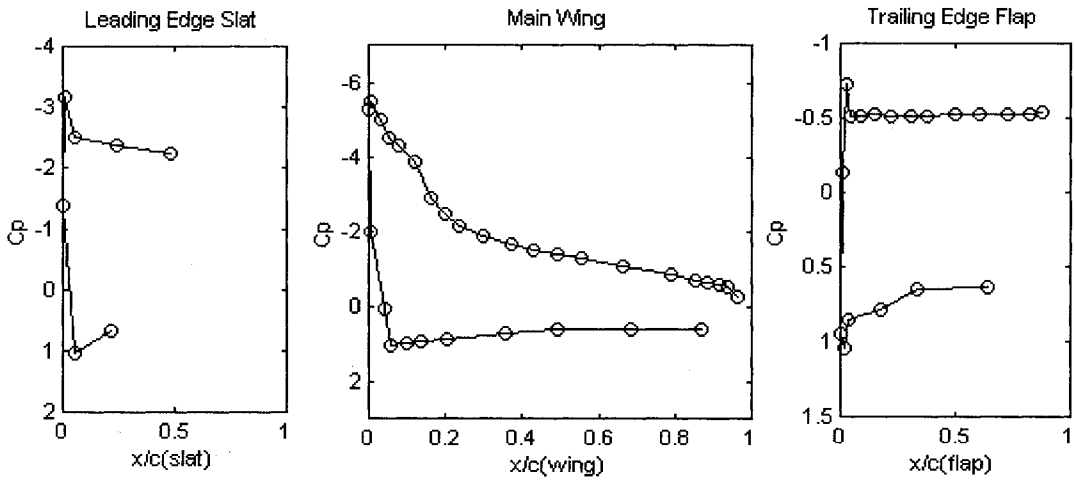

Figure 5.22 – Pressure distribution at V_∞ = 19.99 m/s at 15° AOA

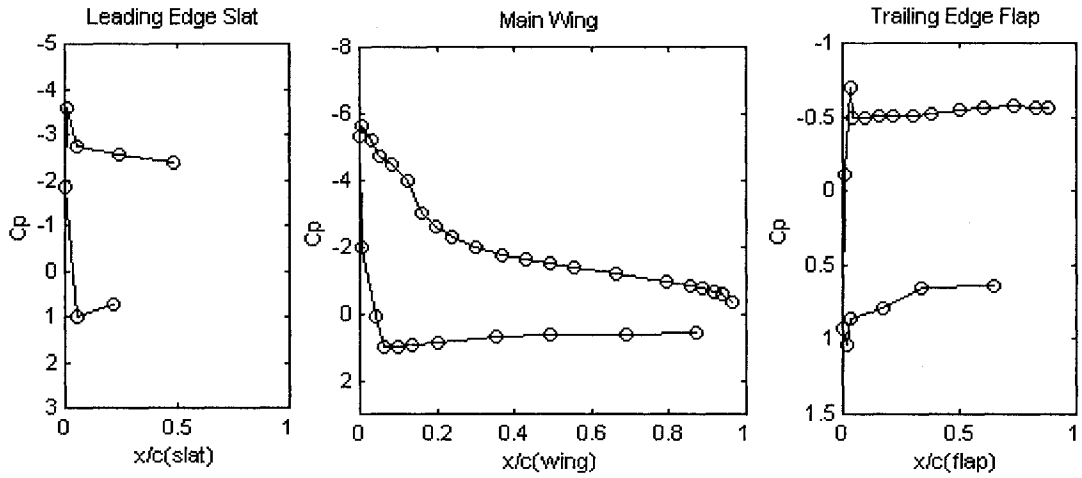

Figure 5.23 – Pressure distribution at V_∞ = 30.06 m/s at 15° AOA

5.7 Hot-Film Flow-field Surveys

This section presents the results of the hot-film flow field surveys when the model underwent external excitation by either the piezoelectric devices or the loudspeaker. A single axis hot-film sensor was used to measure the mean velocity profiles and turbulence intensity. Surface pressure measurements were obtained from the trailing edge flap, which was deliberately set at an angle of incidence to force the boundary layer on the flap to be just barely separated. To attain this state, the pressure measurements were taken on the flap starting at an angle of attack that was known to be past the incipient boundary layer separation state. The model angle of attack was then reduced until the boundary layer became attached and then slightly increased again until separation just occurred. The test condition used for this portion of the test was a free-stream velocity of 20 m/s and at an angle of attack of 19°. The initial approach was to excite the flow field at various operating frequencies and then observe the effect on the surface pressure distribution on the trailing

edge flap. The ideal objective would have been for the boundary layer to switch from a separated state to a reattachment state when either the piezoelectric devices or the loudspeaker energizes the flow field. As the experiment progressed, increasing emphasis was placed on studying the effect of the external forcing on the pressure distribution on the main wing.

5.7.1 Excitation Using Piezoelectric Devices

The two piezoelectric devices were placed side-by-side on the lower surface of the main wing between the two sidewalls, with their trailing edges being coincident with trailing edge of the main wing (see Figure 5.24). The electrical leads were soldered at the upstream edge of the devices. A thin strip of Kapton® tape was placed on the model surface beneath the devices to ensure that there would not be an electrical conduction path between the two devices through the metallic model.

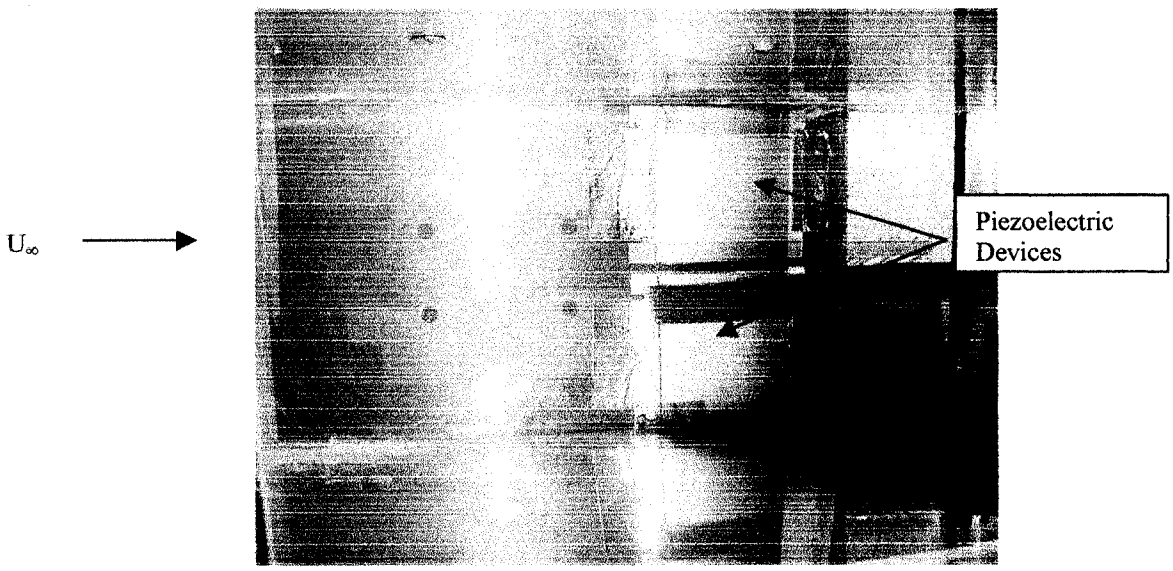

Figure 5.24 - Installation of Piezoelectric Devices on Model

Data were taken at various excitation frequencies to observe the effect on the surface pressure distribution, especially on the trailing-edge flap where separation occurred as well as on the upper surface of the main wing.

5.7.1.1 Mean Velocity Profiles

One of the more important requirements in this study was to establish a methodology to determine the degree of mixing that occurs within the boundary layer due to external excitation. The mixing of dissimilar and distinct flows, such as wakes and boundary layers, has been an ongoing objective in the fields of fluid mechanics and aerodynamics, and many research studies have been conducted to understand the nature of flow mixtures, particularly in the area of internal aerodynamics as applied to the study of aircraft engines.

Because the piezoelectric devices in this study were attached to the windward side of the main wing, their oscillations should energize the downstream flow of air that passes over them. Furthermore, the added energy in the parcels of air should, by convection, pass through the rear slot and travel above the upper surface of the trailing edge flap. Of course this air would be mixed with the wake of the main wing and would result in a more energized boundary layer on the upper surface of the flap. Assuming that enough energy has been transported to the flap from the devices, the boundary layer would have a tendency to remain attached with the attendant effect of increased lift.

5.7.1.1.1 General Observations

In this section, data are presented showing the trends of the velocity profile on the upper surface of the trailing-edge flap as a result of external excitation using the piezoelectric devices. The purpose of this part of the study is to determine if the

piezoelectric devices affect the velocity of the air, which passes through the rear slot and presumably mixes with the boundary layer on the flap. The velocity profile above the leeward side of the flap without external excitation was used as the reference data set. The highest velocity in the reference set normalized the velocity data derived from the hot-film measurements. The displacement in the lateral direction (i.e., in the direction of lift) was normalized by the largest displacement. The data of the velocity profiles for the frequencies of 0, 80, 90, 100, and 120 Hz are shown in Table 5.4. Computer-generated plots were produced displaying the normalized velocity profiles for the various excitation frequencies. Each plot shows the comparison between the case with external excitation and without any excitation. These plots are shown in Figures 5.25 through 5.28.

	Frequency (Hz)				
Z(in)	0	80	90	100	120
0.0000	0.00000	0.0000	0.00000	0.00000	0.00000
0.1969	11.05816	11.40156	11.00718	10.88758	11.16750
0.2069	10.79232	11.02176	10.94495	11.16527	10.93124
0.2169	11.10773	10.91680	11.02455	11.17175	10.91649
0.2269	11.03616	11.16851	11.06764	11.06920	11.07020
0.2369	11.15512	11.34064	11.66765	11.19136	11.20668
0.2469	11.59377	11.13865	10.80685	11.34198	11.06489
0.2569	10.80650	10.97040	11.38263	11.37843	11.09676
0.2669	11.09702	11.03614	10.96128	11.16228	10.92771
0.2769	10.78732	11.10188	11.06053	11.24938	11.41814
0.2869	11.14810	11.03596	10.95329	11.24490	11.12449
0.3869	11.41552	11.57488	11.87613	12.32567	11.36487
0.4869	13.09675	11.47737	11.64616	12.30503	12.53095
0.5869	12.26638	12.42107	13.02145	13.27690	13.72581
0.6869	12.97934	12.68506	13.04585	14.12219	13.76077
0.7869	14.23173	13.77649	14.20211	14.61935	14.22396
0.8869	14.08337	14.51156	14.19076	15.02811	14.94804
1.4669	18.78206	18.55580	18.09000	19.24026	19.00509
1.5669	19.50561	--	--	--	--
1.6669	19.41881	--	--	--	--

Table 5.4 Velocity Profiles on TE Flap using Piezoelectric Devices.

To attain a more direct grasp of the influence of the piezoelectric devices, the percentage deviations of the velocity were examined for both cases with and without excitation. The percentage deviations were calculated at each of the selected lateral sensor displacements. A positive percentage indicated that there was an increment in the mean velocity. These results are shown in Table 5.5.

One noteworthy observation was that at a displacement of 0.5869 in. above the flap surface the increment in mean velocity was nearly 12 percent at an excitation frequency of 120 Hz.

	Frequency (Hz)			
Z(in.)	80	90	100	120
0.1969	3.11	-0.46	-1.54	0.99
0.2069	2.13	1.41	3.46	1.29
0.2169	-1.72	-0.75	0.58	-1.72
0.2269	1.20	0.29	0.30	0.31
0.2369	1.66	4.59	0.32	0.46
0.2469	-3.93	-6.79	-2.17	-4.56
0.2569	1.52	5.33	5.29	2.69
0.2669	-0.55	-1.22	0.59	-1.53
0.2769	2.92	2.53	4.28	5.85
0.2869	-1.01	-1.75	0.87	-0.21
0.3869	1.40	4.03	7.97	-0.44
0.4869	-12.36	-11.08	-6.05	-4.32
0.5869	1.26	6.16	8.24	11.90
0.6869	-2.27	0.51	8.81	6.02
0.7869	-3.20	-0.21	2.72	-0.05
0.8869	3.04	0.76	6.71	6.14
1.4669	-1.20	-3.68	2.44	1.19

Table 5.5 Deviations of the Mean Velocity Using Piezoelectric Devices.

The data contained in Table 5.4 was averaged for each frequency. The average percentages were –0.45%, -0.02%, 2.38% and 1.33% for frequencies 80, 90, 100, and 120 Hz, respectively. The results indicated that there is an overall increment in the mean velocity when the piezoelectric devices were operating at the higher frequencies, especially at 100 Hz.

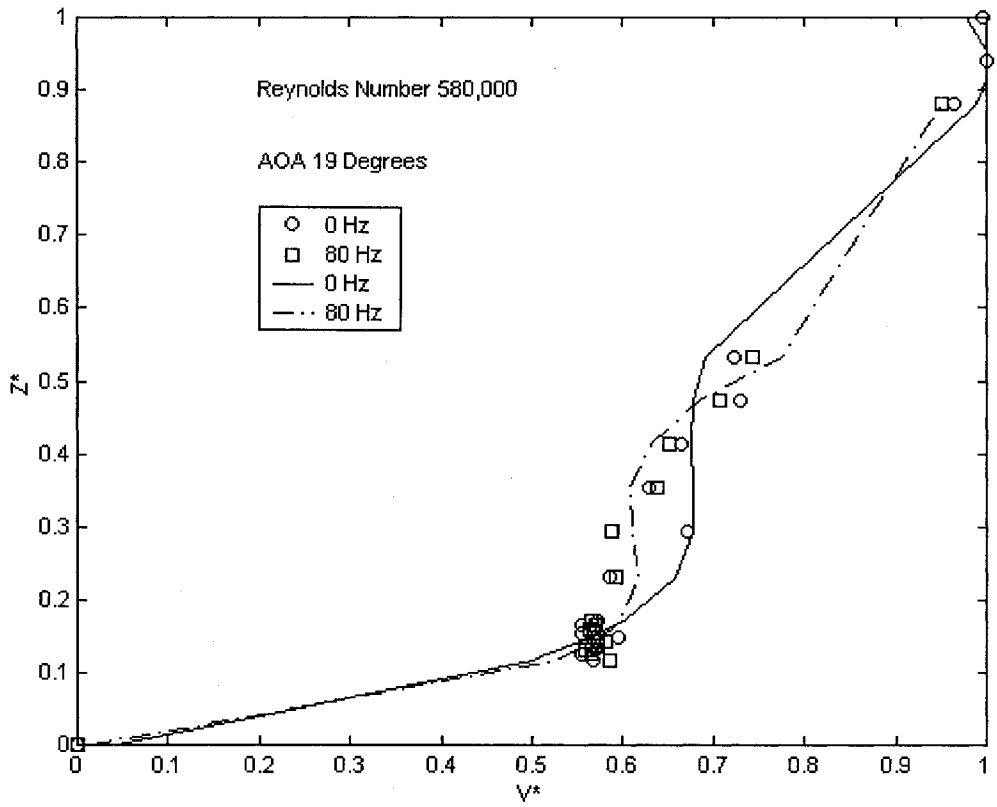

Figure 5.25 - Velocity Profile with Piezoelectric Devices on Flap at 0 and 80 Hz

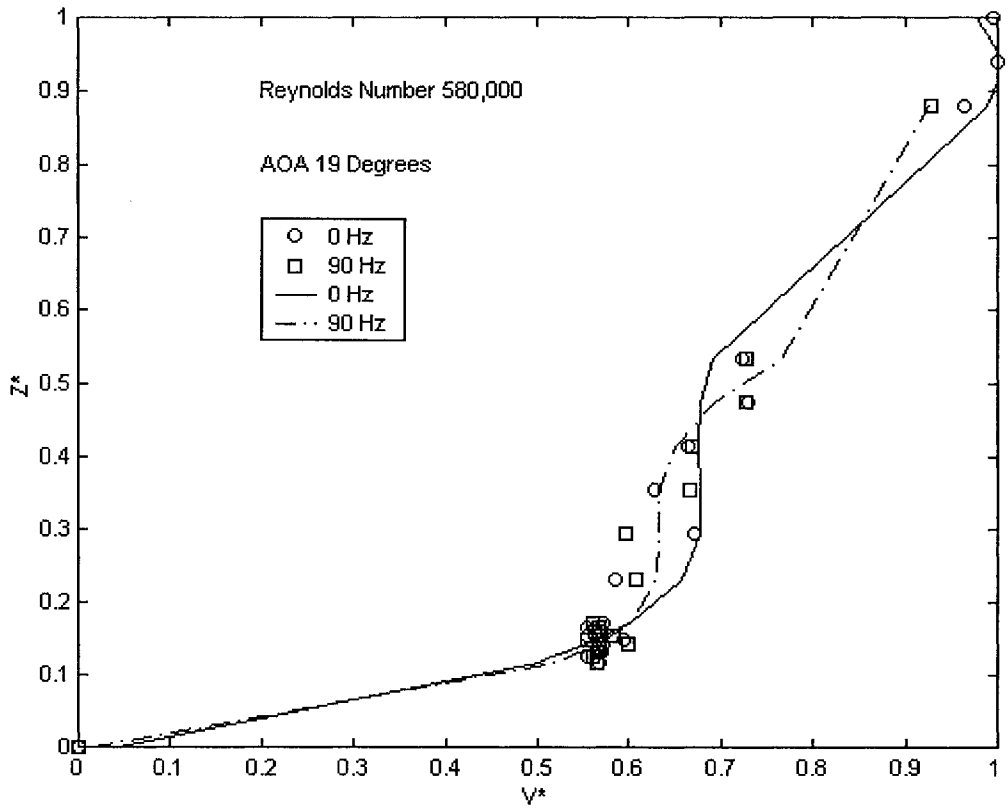

Figure 5.26 - Velocity Profile with Piezoelectric Devices at 0 and 90 Hz

As shown in Figure 5.26, when the piezoelectric devices were tuned at 90 Hz the data indicated that the velocity profile did not differ markedly from the baseline case. The two profiles crossed each other at various locations normal to the model surface, yet the overall differences in velocity were negligible.

Figure 5.27 shows the comparison of the baseline profile with the profile at 100 Hz. In this instance it is evident that the overall trend of the velocity profile at 100 Hz indicated a fuller distribution, which tends to delay boundary layer separation.

Figure 5.28 shows the data comparing the baseline results with the case when the piezoelectric devices were tuned at 120 Hz. The velocity distribution at the higher

frequency was slightly more full than that of the baseline profile, although the difference in profiles was not as marked as that shown in Figure 5.27. Even though the distribution induced by the excitation at 100 Hz did not result in any significant aerodynamic characteristics, at least the results showed that the velocity distribution was controllable. This is the first step in developing an effective flow control technique. The next step is to refine the method of flow control to optimize its effectiveness for a significant improvement in aerodynamic performance. Experimental results reported later in this dissertation showed that significant aerodynamic effects were achieved when the excitation occurred at a frequency directly related to the vortex passage frequency.

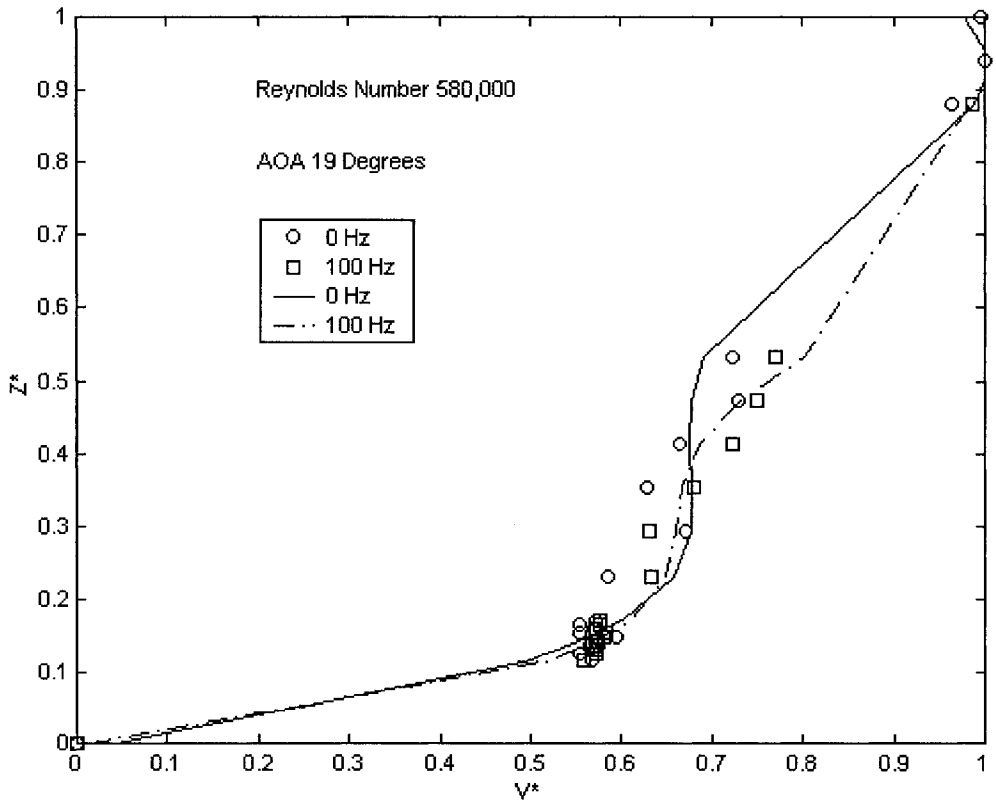

Figure 5.27 - Velocity Profile with Piezoelectric Devices at 0 and 100 Hz

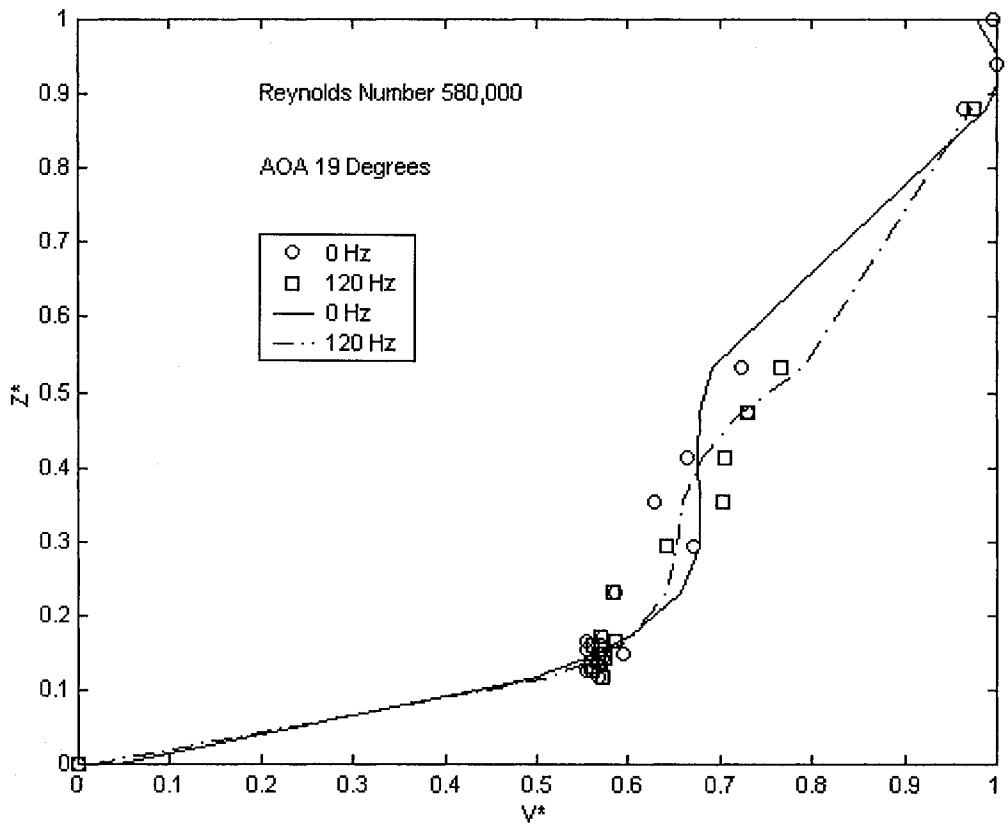

Figure 5.28 - Velocity Profile with Piezoelectric Devices at 0 and 120 Hz

5.7.1.1.2 Momentum Thickness

In another study [Oster, D. and Wygnanski, I, 1982] a different method was employed whereby the shear layer momentum thickness was used as an experimental indicator of the degree of mixing in the wake of a splitter plate. Ideally, as the momentum thickness is measured in an increasing downstream direction, the thickness is expected to increase because of the ever-increasing deficit of momentum across the mixing region. According to the reference [Currie, I., 1974], the momentum thickness is defined as the height of an idealized quiescent layer of air above a solid surface that has the same momentum deficit as the actual boundary layer. In this experiment, the momentum

thickness was expected to decrease due to the expected increase in velocity over the flap caused by the energy convected into the flow by the piezoelectric devices.

The momentum thickness was computed using the piezoelectric devices for the operating frequencies of 0, 80, 90, 100, and 120 Hz. Computations were also performed using the 75-watt loudspeaker at operating frequencies 80 and 120 Hz. The data was for a free-stream velocity of 20 m/s. The results of the computation of momentum thickness are shown in Table 5.6. The momentum thickness was computed by the FORTRAN computer code THETA, which uses the normalized velocity profile and performs a summation process that results in the numerical integration across the flow-field in the vertical direction from the model surface. The code is displayed in appendix F.2 and is provided with adequate internal documentation.

Forcing Frequency (Hz)	θ , Piezoelectric	θ , Loudspeaker
0.0	0.1512	0.1512
80.0	0.1558	0.1672
90.0	0.1625	--
100.0	0.1392	--
120.0	0.1441	0.1674

Table 5.6. Momentum Thickness of Velocity Profiles Using External Excitation.

Data presented in Table 5.6 show that in the case of the piezoelectric devices, the momentum thickness is significantly reduced at a frequency of 100 Hz when compared with the case for which there was no external excitation. Actually, the data show a reduction in momentum thickness of roughly 8% from a frequency of 0 Hz to 100 Hz. There was also a decrement in momentum thickness, albeit a smaller one, at a forcing

frequency of 120 Hz. This represented a reduction of about 5%. These results are somewhat related to results reported from a previous wind tunnel experiment [Kourounis,A., et al., 1996]. The purpose of their study was to investigate the interaction of an upstream wake on a turbulent boundary layer. The test consisted of an airfoil (NACA 0015) with a deflectable trailing-edge flap. By varying both the height of the model and the deflection angle of the flap, they were able to control the strength of interaction between the wake of the flap and the turbulent boundary layer that had been developed on the test section floor. Data were also obtained for the undisturbed case a well. In their study, they used momentum thickness as an indicator of the extent of mixing that had occurred between the wake and the boundary layer. They calculated momentum thickness at various axial stations and they found significant reductions in thickness from the undisturbed case.

In the case of acoustical forcing, the data show an increase in the momentum thickness for both frequencies when compared with the calculation in the absence of forced excitation. The increment was roughly 11% for both 80 and 120 Hz. This data would suggest that at these frequencies acoustical excitation causes the production of shear stress in the flow field above the trailing-edge flap. If additional time had been available, data would have been obtained for a more extensive selection of audio frequencies to identify any possible frequency for which a reduction in momentum thickness would have occurred.

The physical mechanisms responsible for the results described pertaining to forced excitation are not completely understood. The understanding of such phenomenon would be desirable because this would provide greater insight into energy transport processes. Such insight could be used to correct existing turbulence models and would result in improved reliability of CFD results.

Based on the findings of previous researchers [Bhattacharjee, S., 1986] and [Ahuja, K. K., 1983], a plausible explanation might be that the frequencies produced by either device could be acting either favorably or unfavorably with disturbances existing in the flow field. In the case of the piezoelectric devices, organized disturbances being shed directly from the devices themselves may not have preserved the same frequency once they have propagated to the vicinity of the flap. However, at the point in the flow field where disturbances originating from the piezoelectric devices interact with naturally occurring disturbances on the flap, some relationship could exist between the two local disturbances, which would increase the velocity in the shear layer. Previous findings [Bhattarcharjee, S., 1986] suggest that, when the excitation frequency is a subharmonic of the natural frequency in the shear layer above the flap vortex pairing would occur. This would result in more turbulent kinetic energy being transported into the shear layer and might explain the observed increments in mean velocity.

5.7.1.1.3 Profile Curvature Trends

The trends presented so far suggest that the piezoelectric devices provide a favorable effect on the separated boundary layer. Specifically, the data support the conclusion that when the devices were operated at 100 Hz the separated boundary layer exhibited characteristics that were conducive to reattachment. Due to the inherent strong interactions between the approaching wake and boundary layer on the flap, it is highly plausible that active control of the wake might have a significant and direct impact on the flap boundary layer and its propensity to separate. The following discussion focuses on the observed behavior of the near wake above the surface of the flap and how the presence of the piezoelectric devices affected that flow field. Without more detailed studies, it is

difficult to make conclusive assertions about the flow field surrounding the flap, particularly on the upper surface. This is due to the significant complexity of the flow field there, which encompasses the effects of the slat and main wing wakes, the jet of potential flow exiting from the rear slot and the boundary layer of the flap itself. It was hypothesized that the velocity profiles with the devices on showed a favorable trend with regards to boundary layer separation. To provide further evidence of this hypothesis, the curvature of the velocity profiles near the surface were compared for the selected operating frequencies. The basis for this approach is the well-established fact that near the model surface the degree of curvature exhibited by a velocity profile serves as an indicator of the extent of boundary-layer separation. However, it is not completely clear as to whether the curvature observed in the velocity profile is an indication of boundary-layer separation or if it is the result of the near wake due to upstream airfoil elements. This uncertainty is worsened by the fact that the effects of the wake tend to diverge for lower Reynolds numbers. Therefore, it is possible that the negative velocity gradient observed above the flap is due to a merging of the upstream wake and flap boundary layer. It is argued, however, that whether the off-body curvature of the mean velocity is to due the flap boundary layer, the main-element wake of a combination of the two, it is certainly preferable in any case to lessen the negative gradient of velocity in the direction of traverse. By mitigating the negative velocity gradient above the surface of the flap, higher velocities will be transported to the surface, resulting in a thinner boundary layer, which is less susceptible to separation. It is surmised that for higher and more realistic Reynolds numbers, the piezoelectric devices should be capable of greater amplitude of deflection so that it can energize a larger volume of air. Assuming that the observed effects are due purely to the wake region, other

researchers have found that the behavior of the wake has a direct influence on the aerodynamic lift of the flap. One particular discussion is involved with what is called wake flow reversal or off-body separation. This is the phenomenon, whereby the flow above the surface exhibits recirculation and flow reversal in the wake due to pressure gradients in the flow field. Petrov [1978] suggested that off-body separation in a wake was responsible for the reduction in the rate of lift gain on a flap. Also data by Braden et, al. [1986] indicated that the loads on a flap can be suppressed by separation occurring in the wake above the surface. However, more recent data [Nakayama, et al. 1990] suggested that there might be some flaws in this assumption.

To perform this analysis it is necessary to generate smooth velocity profiles so that their curvatures near the model surface can be more easily compared. The raw profile data demonstrated some irregularities near the model surface, which were smoothed by fitting fourth order polynomials through each profile. In a sense, this is a repeat of data shown earlier, but the smoothing process helps to clarify the effect of the device operating frequency on the measured velocity profiles. To fit the raw data, four polynomial coefficients were computed for each operating frequency. The form of the equation for each polynomial fit is shown in Equation 5.6.1.1.3-1.

$$V^*(Z^*) = C1 \times Z^{*4} + C2 \times Z^{*3} + C3 \times Z^{*2} + C4 \times Z \qquad (5.6.1.1.3\text{-}1)$$

The coefficients for each case are shown in Table 5.7.

Coefficients

Freq. (Hz)	C1	C2	C3	C4
0.0	-10.8903	24.6292	-18.5735	5.7697
80.0	-30.3673	54.3102	-31.4024	7.3326
90.0	-26.0873	47.5970	-28.4854	7.0196
100.0	-24.3643	44.8273	-27.2080	6.9350
120.0	-23.5034	43.3790	-26.4518	6.7876

Table 5.7 Polynomial Coefficients for Velocity Profiles.

The standard error of estimation of the approximate velocity profiles was computed to ascertain their accuracy with respect to the measured data. The standard error of estimation was computed as shown in Equation 5.6.1.1.3-2. The quantity in the parentheses is the deviation of the raw data and the polynomial fit.

$$E_{st} = \sum \frac{(V^* - V^*_{app})^2}{N} \qquad (5.6.1.1.3-2)$$

The computed values of standard error for each operating frequency are shown in Table 5.8.

Freq. (Hz)	E_{st}
0	0.00310
80	0.00086
90	0.00100
100	0.00077
120	0.00110

Table 5.8 – Standard Error of Estimation of Velocity Profiles.

The standard error of estimation as reported in Table 5.7 indicate that the polynomials, which were fitted through the data were generally accurate since the summation of the squares of the deviations is small.

The polynomials that were fitted through the measurements for the different operating frequencies were simultaneously plotted to determine trends in the degree of curvature in the velocity profiles. The results are shown in Figure 5.29. These results clearly show that for the baseline case of 0 Hz, the velocity profile exhibits the classic shape of positive curvature, indicative of either boundary-layer separation or near-wake effects. As the operating frequency increases, the curvature of the velocity profile becomes increasingly less positive. Furthermore, at the operating frequency of 100 Hz, the curvature of the profile is the least positive. These trends corroborate the trends reported previously, that is, when the piezoelectric devices were operated at 100 Hz the boundary-layer characteristics were the most favorable. The data suggest that although the boundary layer is still separated at 100 Hz, evidently, the adverse pressure gradient on the surface of the model has become less severe. In the experiment performed by Ying [1999] on the identical model it was found that the wake deficit from an upstream element resulted in an overall loss of lift on the downstream element. If the profile currently detailed is due to a wake deficit and not to boundary-layer separation, the narrowing of the wake can have an advantageous effect. Additionally, wake deficits can cause the unloading of an airfoil by forcing the streamlines to be deflected from the surface, which effectively is a decambering effect. This would be a contributing factor to any loss of lift. In the opinion of the author, this result was compelling evidence that the piezoelectric devices offered promise as an

effective technique to reduce or delay boundary-layer separation. This supports the hypothesis that these devices have the potential of enhancing aerodynamic lift.

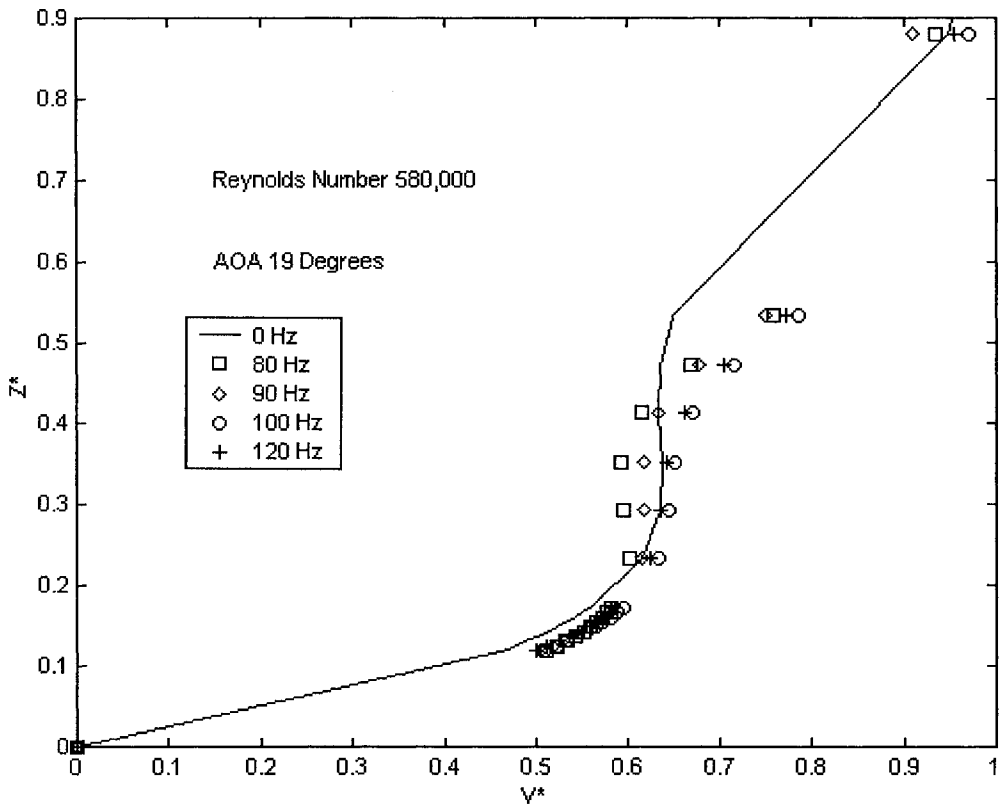

Figure 5.29 - Interpolated Velocity Profiles Near Flap Surface at $V_\infty = 20$ m/s, 19 Degrees AOA

5.7.1.4 Skin Friction Calculation Results

A FORTRAN program call SKINFRIC was written to compute the skin friction coefficient according to the above equation. Computations were performed for the various normalized velocity profiles for the selected operating frequencies of the piezoelectric devices. Since these equations are based on the behavior of a boundary layer not intruded by an impinging wake, it was necessary to calculate the momentum thickness and shape

factor using portions of the velocity profile that were fairly close to the surface and not significantly affected by the wake. The results of this analysis are shown in Table 5.9 for the various operating frequencies.

Frequency (Hz)	C_f (Skin Friction Coefficient)
0.0	0.000191
80.0	0.000203
90.0	0.000189
100.0	0.000186
120.0	0.000194

Table 5.9 – Calculated Skin Friction Coefficients on Main Wing for selected Frequencies at $V_\infty = 20$ m/s.

The results show that the largest reduction in skin friction coefficient from the baseline case of 0 Hz was at an operating frequency of 100 Hz. The data indicates a reduction of roughly 3 percent. Although the actual magnitude of the reduction is not large, it does however show a trend towards a boundary layer that is less severely separated. More, importantly this corroborates the earlier results, which intimated that the operating frequency of 100 Hz demonstrates the most favorable effect upon the separated boundary layer.

5.7.1.2 Turbulence Intensity Profiles

The flow field surrounding the trailing-edge flap of the model used in this study is dominated by a high degree of viscous effects because of the interaction of the main wing wake and the boundary layer that develops on the flap. This gives rise to significant turbulence and its attendant turbulent kinetic energy even without the presence of any external excitation. One of the aims of this study was to examine the role played by

turbulence intensity with regards to the development of a favorable mean velocity profile. A favorable velocity profile is one that helps to inhibit boundary-layer separation. Moreover, the extent that external excitation affects turbulence intensity should be explored as the intensity ultimately influences the mean velocity profile.

In this investigation, the hot-film sensor data were used to acquire the turbulence intensity profiles for the selected excitation frequencies. The turbulence intensities were calculated automatically by the TSI® IFA Thermal Anemometry Software Package. The transverse locations above the surface were identical to those locations when the velocity profile was obtained.

The data show that the percentages for turbulence intensity attained fairly high values, especially at locations far enough from the surface where the hot-film sensor was probably immersed in the wake region from the main wing. Another experimental investigation [Seifert, A. et al., 1998] was performed on a two-dimensional model in which piezoelectric devices were installed within a cavity that was machined into the upper surface of the wing. In that study, the researchers observed turbulence intensities in the streamwise direction as high as 20% when the model was positioned at 8° angle of attack for an excitation frequency of 170 Hz. Their measurements were obtained at a transverse displacement of 1 mm from the model surface. A transition strip (grit no. 100) was placed along the leading edge of the model.

In an experiment involving the study of boundary layer-wake interactions [Kourounis, A. et al, 1998] longitudinal turbulence intensities were as high as 7% in the wake of a two-dimensional airfoil that interacts with the boundary layer of the test section floor.

In a similar wind tunnel experiment, a multi-element airfoil was tested in the NASA Langley Low Turbulence Pressure Tunnel (LTPT) and fluctuating components were measured using a hot-wire anemometer. The chord length of the model in the stowed configuration was 22 in. The fluctuating flow properties for a 10 °angle of attack and a Reynolds Number based on chord length of 3 million were shown in Figures 2.6 and 2.7. The turbulence intensity profiles in the direction of the free stream were shown in Figure 5.31. Based on the plotted data from both Figures 2.6 and 2.7, the maximum free stream turbulence intensity under the stated model configuration and flow conditions was roughly 13%. The reported turbulence for the LTPT is 0.1% where the turbulence in the empty ODU LSWT at the Reynolds number of 290,000 (20 m/s) was 0.12%.

One fact that could contribute to the high turbulence intensities on the trailing edge flap model in this experiment was the presence of a composite wake at a 19° angle of attack that originates from both a leading-edge slat and a main wing. At sensor locations farther away from the surface than that shown in Table 5.6 the anemometer LED display panel indicated that the sensor was being subjected to intolerable oscillations.

In one research study [McGinley, C. et al., 1998], hot-wire measurements were obtained from the flow field surrounding a multi-element airfoil. Profiles were obtained of the Reynolds stress, mean velocity, and turbulence intensity for different model configurations, angle of attack, and Reynolds number. For one test case, the hot-wire sensor was placed in the wake of the slat. The model was placed at a 19° angle of attack and the Reynolds number was 9 million based on stowed chord length. They found that the turbulence intensity in the stream-wise direction was as high as 4 %. Again, this is much lower than the results shown in this study, but remember that the turbulence intensity data reported in

this study were obtained on the trailing-edge flap and not immediately behind the slat. In the confluence region on the flap, significant velocity gradients exist because of the interactions of the wakes from both the upstream slat and main wing. These gradients have the effect of increasing the amount of turbulence and of decreasing dissipation. This would at least partially contribute to the elevated turbulence that was observed.

Experimental results [McGinley,C. et al., 1998] demonstrate that at high angles of attack the turbulence increases and the wake region from an upstream element is more spread out as it decelerates. One other reason that could account for the rather high levels of turbulence intensity was the fact that the thin Plexiglas® sidewalls oscillated during the test run. Although this was unavoidable unless thicker sidewalls were used, this situation undoubtedly introduced some unwanted disturbances in the flow field. Nevertheless, the trends shown by the data afford some valuable information concerning the potential usefulness of employing external excitation to control the flow field surrounding an airfoil.

In another study [Zhou and Squire, 1985], turbulence intensities were measured in a wake of a symmetric airfoil that interacts with the boundary layer of a wind tunnel wall. They found intensities as high as 12 %. This is lower than what was measured in this study on the trailing-edge flap, but again the study herein involved the combining of two upstream wakes, which enhanced velocity gradients and viscous interactions.

The profiles of turbulence intensity are shown in Figures 5.30 through 5.32. Each figure shows a comparison between the profiles for the case of no external excitation and the case where the devices were driven at a selected frequency. In examining these profiles of turbulence intensity, keep in mind those trends already observed for the mean velocity profiles. Hopefully, this cross study will provide insight into at least the rudimentary

aspects of the kinetic energy and momentum transport phenomena involved with this model. An interesting study would try to determine if the observed trends are in agreement with well-established phenomenological models that describe and predict complex viscous interactions. Zhou and Squire [1985] obtained flow field measurements of a multi-element airfoil with varying degrees of wake/boundary-layer interaction. They found that for the case when the wake of a forward element merged with the a downstream boundary layer that the boundary layer thickened and that the turbulence intensity and turbulent kinetic energy shifted away from the wall. However, this dissertation differs in that a specifically tuned source of external forcing was used to diffuse the turbulent kinetic energy back to the wall to make the boundary layer less susceptible to separation.

A comparison of the turbulence intensity profiles of the trailing-edge flap between the excitation frequencies of 0 and 80 Hz is shown in Figure 5.30. A fair amount of irregularity exists in the profiles near the normalized distance of 0.1. The reason for this phenomenon is not known. However, the data show that, generally, the turbulence intensity at 80 Hz is not decisively greater than that measured at 0 Hz. The only exception to this statement exists at the region far away from the model surface where the turbulence intensity for the case of 80 Hz surpasses the results taken at 0 Hz. This result is consistent with the velocity profile data in that there was no marked difference in the magnitudes of the mean velocity between these two excitation frequencies.

Again, the data shown in Figure 5.31 directly above indicates that at a drive frequency of 90 Hz there is no significant increase in turbulence intensity except in the far-field wake region. This also is compatible with the mean velocity data as there was no

marked difference between the velocity distributions at the two frequencies, of 80 and 90 Hz.

The turbulence in the flow field is apparently sensitive to the frequency of external excitation. If the relationship can be established between the turbulence intensity for a particular Reynolds number and the excitation frequency then some control can be exercised to minimize boundary-layer separation.

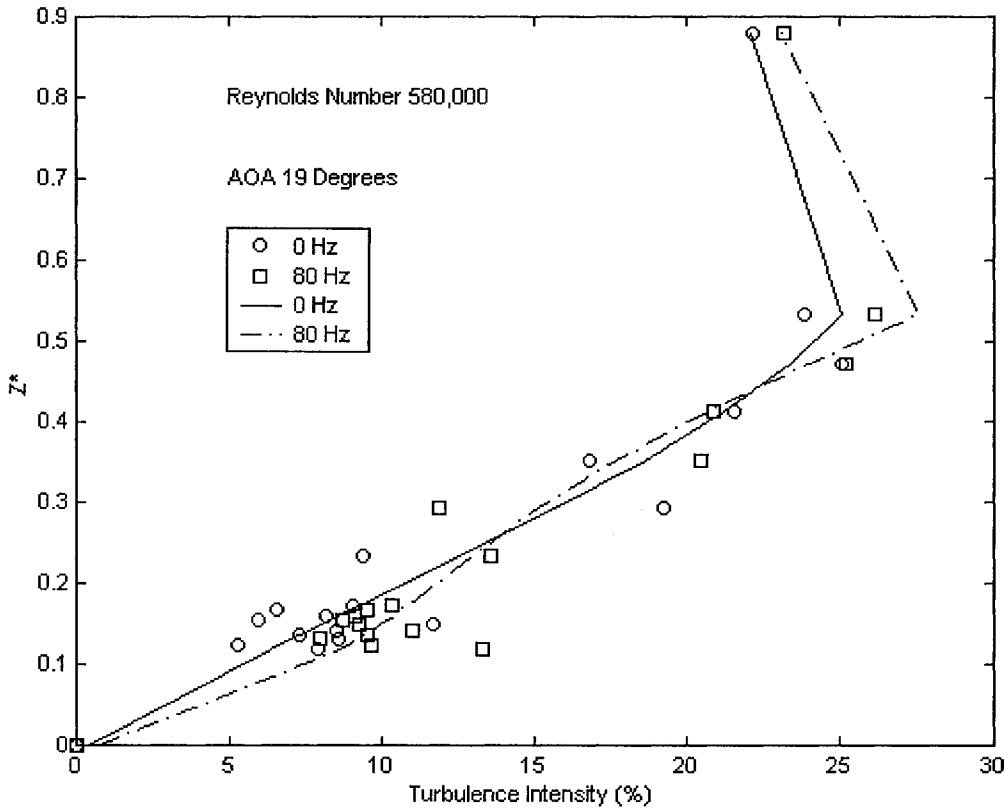

Figure 5.30 - Turbulence Intensity Profile for Piezoelectric Device at 0 and 80 Hz.

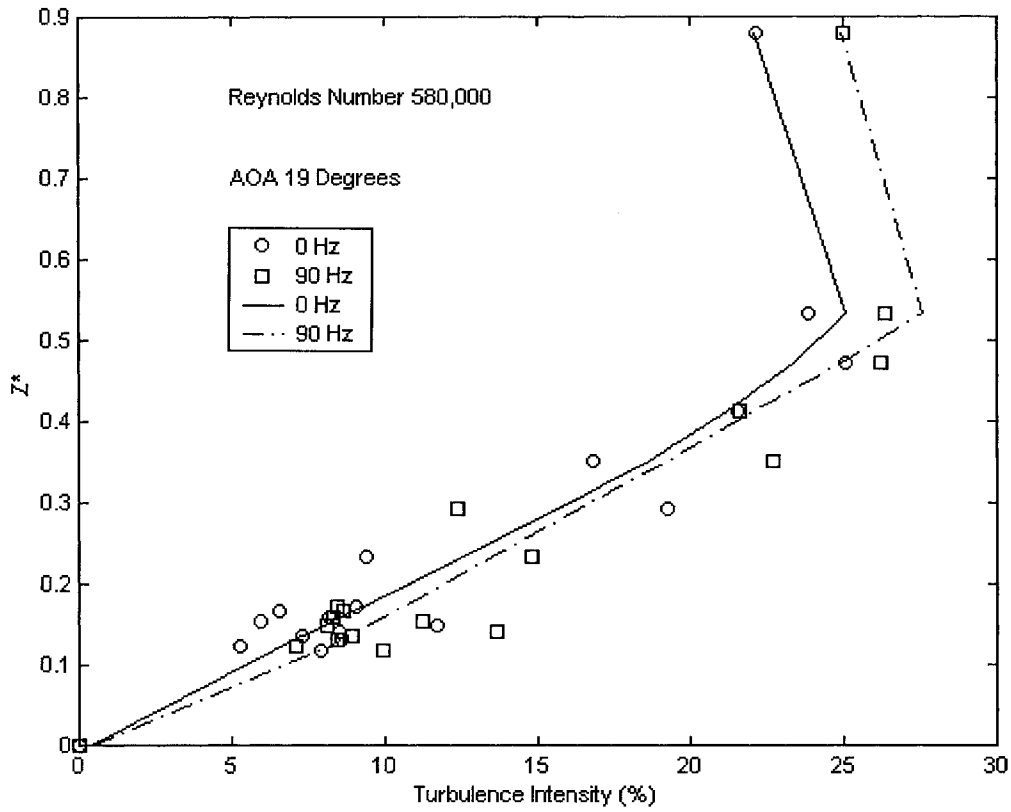

Figure 5.31 - Turbulence Intensity Profile for Piezoelectric Devices at 0 and 90 Hz.

An interesting study would be to determine not only if the dynamics of the flow field surrounding the trailing-edge flap responds to changes in mode and frequency of external excitation, but just as importantly to determine if these changes occur at narrow bandwidths. In other words, how finely tuned should the devices be to incur change? The data shown in Figure 5.32 indicates that at an actuation frequency of 100 Hz, a significant increase in the turbulence intensity occurs. Generally, the profile at the higher frequency is wholly displaced from the reference or baseline profile at 0 Hz.

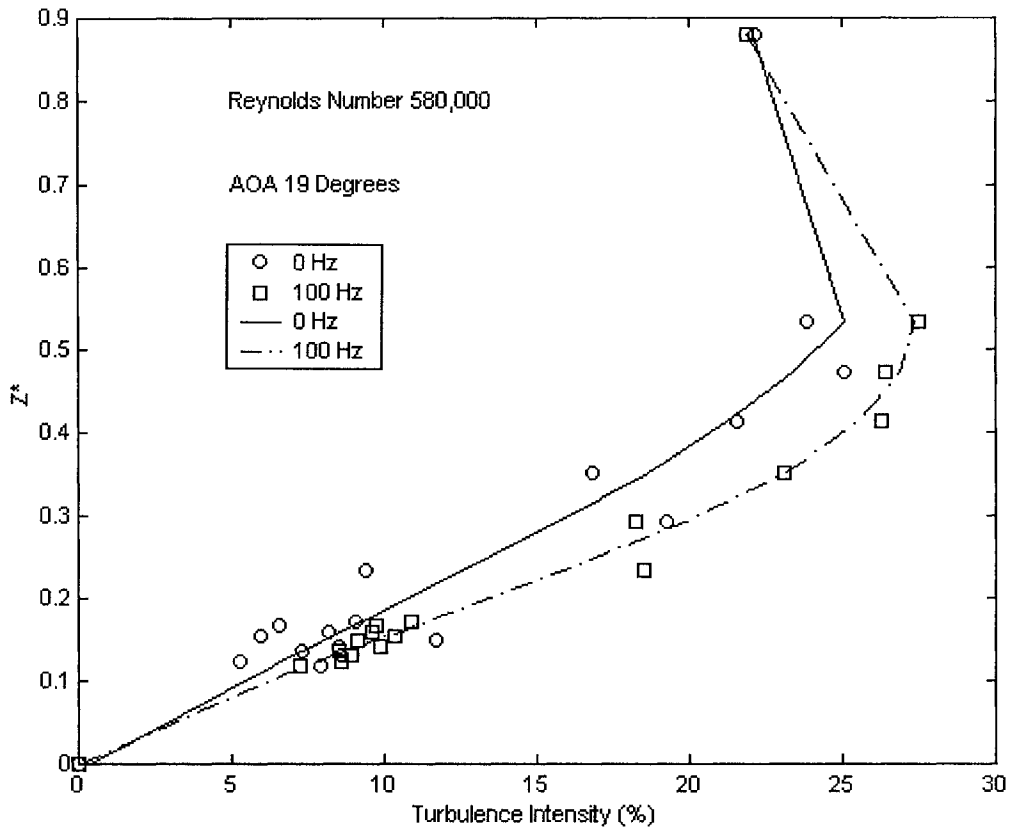

Figure 5.32 - Turbulence Intensity for Piezoelectric Devices at 0 and 100 Hz.

This trend has relevance to what was demonstrated by the mean velocity profile at the same drive frequency, which showed that the mean velocity likewise increased. This would suggest that the piezoelectric devices at this frequency are actively promoting some underlying physical transport phenomenon. Based on the theory of turbulence promulgated by both Boussinesq and Prandtl, the correlation of the fluctuating velocities can be modeled as being directly proportional to the gradient of the mean velocity profile in the transverse direction. Extensive experimental results have mostly confirmed this model. This proportionality has extremely useful repercussions with regards to the transport of important physical quantities in a turbulent flow field.

One of the more problematic realities of turbulence modeling is the fact that the Reynolds stresses from interactions between eddies cannot be derived a priori. As a result, theorists have resorted to many types of empirical model to achieve resolution of the closure problem. One of the more celebrated proposals is the one introduced by Joseph Boussinesq in 1877 [White, F., 1991]. It is stated in Equation 5.6.1.2.

$$\tau_t = -\rho\,\overline{u'v'} = \mu_t \frac{\partial \overline{u}}{\partial y} \qquad (5.6.1.2)$$

This is the model for the Reynolds stress tensor, which is the negative of the density multiplied by the correlation between the fluctuating velocities in the streamwise and normal directions. The term μ_t is the eddy viscosity, which is analogous to the dynamic viscosity associated with molecular interactions between layers of fluids. Ideally, measurements of the Reynolds stresses in the flow above the flap would have been advantageous. This would have required the use of a crossed hot-film sensor to measure fluctuating velocities in two directions. No data of this type were taken so that inferences had to be made about the normal fluctuating velocities. The data shown in Figure 5.33 show the plots of turbulence intensities in all three directions over a flat plate [Schlicting, H., 1951].

The plots show that for distances near the wall, the turbulence intensities are highly anisotropic, but for normalized distances closer to the edge of the boundary layer the turbulence is progressively becoming isotropic. Another observation is that the turbulence intensities in all three directions and the Reynolds stress approaches zero

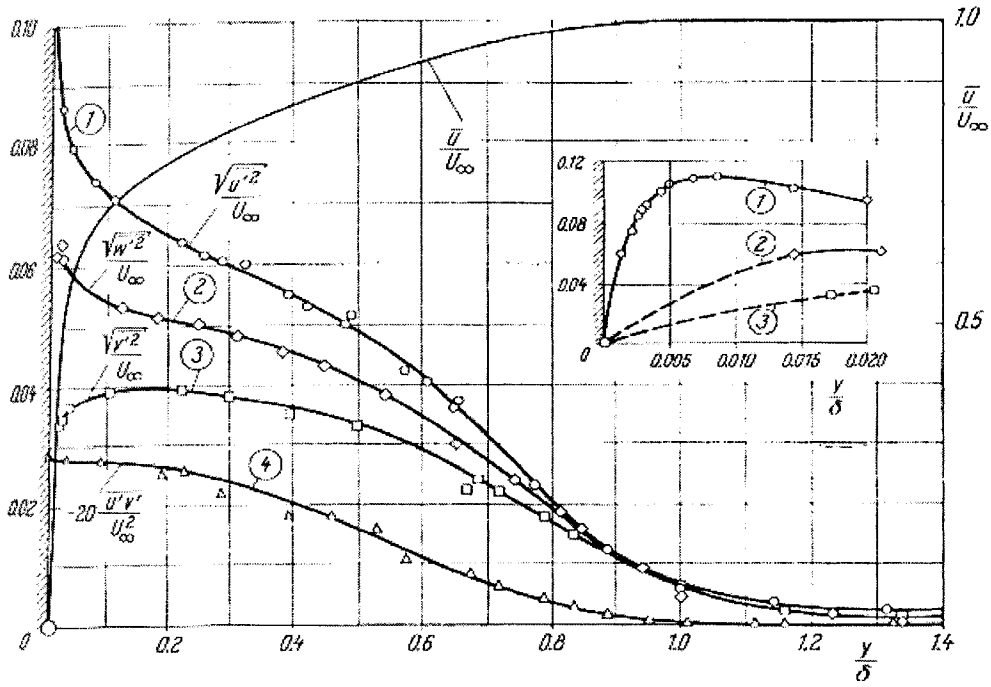

Figure 5.33 - Comparison of Turbulence Intensities for all three Components and the Reynolds Stress.

as measurements are taken closer to the edge of the boundary layer. The important fact derived from this data is that, with the exception of the flow very near the wall, the magnitudes of the turbulence intensities follow roughly the same monotonic trend. That is to say that, as the magnitude of one component decreases, so do the two remaining components.

Moreover, the data show that the Reynolds stress follows the same monotonic trend as the stream-wise turbulence intensity. Even though the above data is for a flat plate, the assumption was made that the nature of the relationship between the turbulence intensity and the Reynolds stress would be preserved for the case of the model under investigation.

This suggests that an increase in stream-wise turbulence intensity can be translated into a comparable increase in Reynolds stress and mean velocity gradient. Because the velocity gradient is usually indicative of a diffusion process, the assumption can be made that momentum is being diffused from the higher velocity regions of the far-field wake to regions closer to the wall. This theory would offer the rationale for the observed increment in mean velocity when an increment in turbulence intensity had occurred.

Gradients are usually associated with diffusive phenomena such as with mass, momentum, and heat. The results presented herein demonstrate that the larger turbulence intensity at 100 Hz is associated with a stronger gradient of momentum, which in turn strengthens the diffusion of momentum into the direction of the model surface. This is a desirable effect because, at least in principle, the boundary layer could be enriched with enough momentum to withstand an adverse pressure gradient and either postpone or avoid separation. Thus, installation of such devices on strategically selected locations can control the aerodynamic lift of an aircraft. Integration of these devices into the overall design of the aircraft would be necessary to minimize undesirable effects such aerodynamic interference or drag.

The turbulence intensity profiles for the cases when the piezoelectric devices were set at 0 and 120 Hz are shown in Figure 5.34. Again, the profile at the higher frequency generally demonstrated increased values of turbulence intensity for the increased displacement heights above the model surface. The trend of turbulence intensity follows the trend that was found for the mean velocity profiles for the case when the piezoelectric devices were in operation. Increased turbulence intensity is manifested as an increase in mean velocity. The overall increase in turbulence intensity, when compared with the

baseline data, was determined for the selected operating frequencies. The increments in turbulence intensity were 19.02%, 17.29%, 22.26%, and 19.37% for the frequencies of 80, 90, 100 and 120 Hz, respectively. As expected, the actuation of the piezoelectric devices increased the turbulence intensity for all four frequencies. Note, however, the largest increment occurred at a drive frequency of 100 Hz. This further suggests that for this configuration and free-stream velocity the aerodynamic characteristics are especially responsive to this operating frequency. Moreover, the data indicated that conducting studies to determine the operating frequency corresponding to the most favorable velocity profile can possibly optimize the aerodynamic performance of this model.

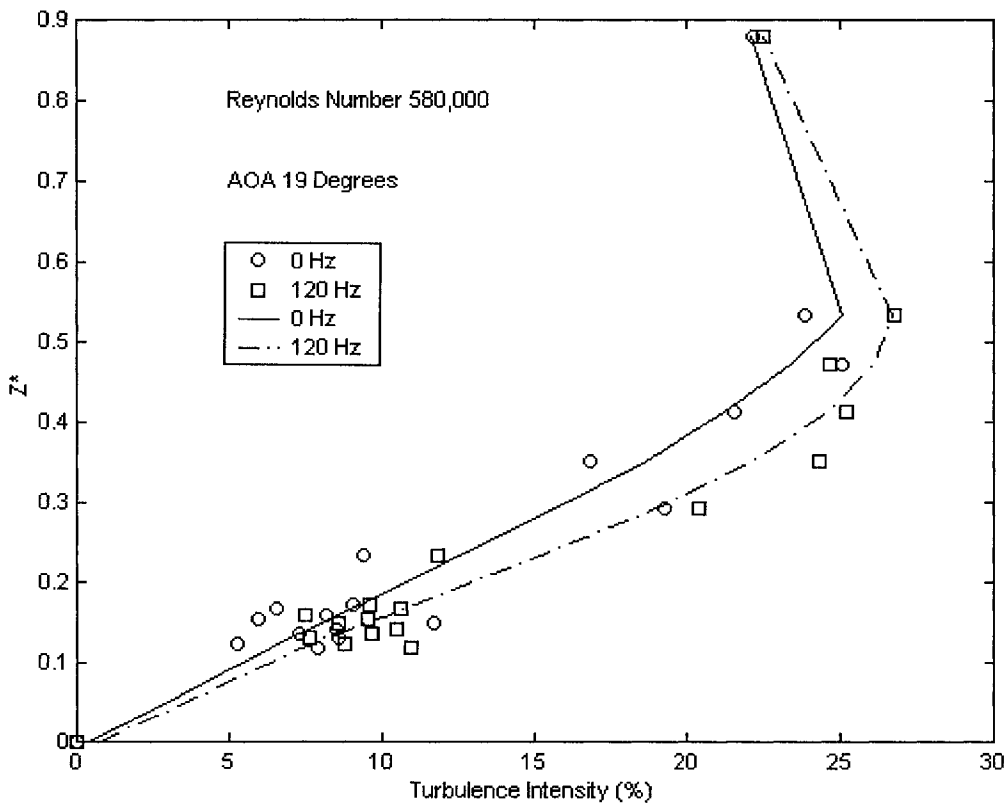

Figure 5.34 - Turbulence Intensity for Piezoelectric Devices at 0 and 120 Hz

5.7.2 Excitation by Loudspeaker

As with the measurements using the piezoelectric devices, profiles of both mean velocity and turbulence intensity were obtained from the trailing-edge flap using the hot-film sensor. Figure 5.35 shows the loudspeaker mounted into the wall of the test section. The sensor was placed at the same model longitudinal station where the data was obtained for the case of piezoelectric excitation. Because of time constraints, the amount of data for the case of acoustical excitation was relatively limited. For this part of the experiment, only frequencies of 80 and 120 Hz were tested when profiles of mean velocity and turbulence intensity profiles were acquired. Although the piezoelectric devices were not in operation, they were left on the model to avoid making any geometry changes to the model.

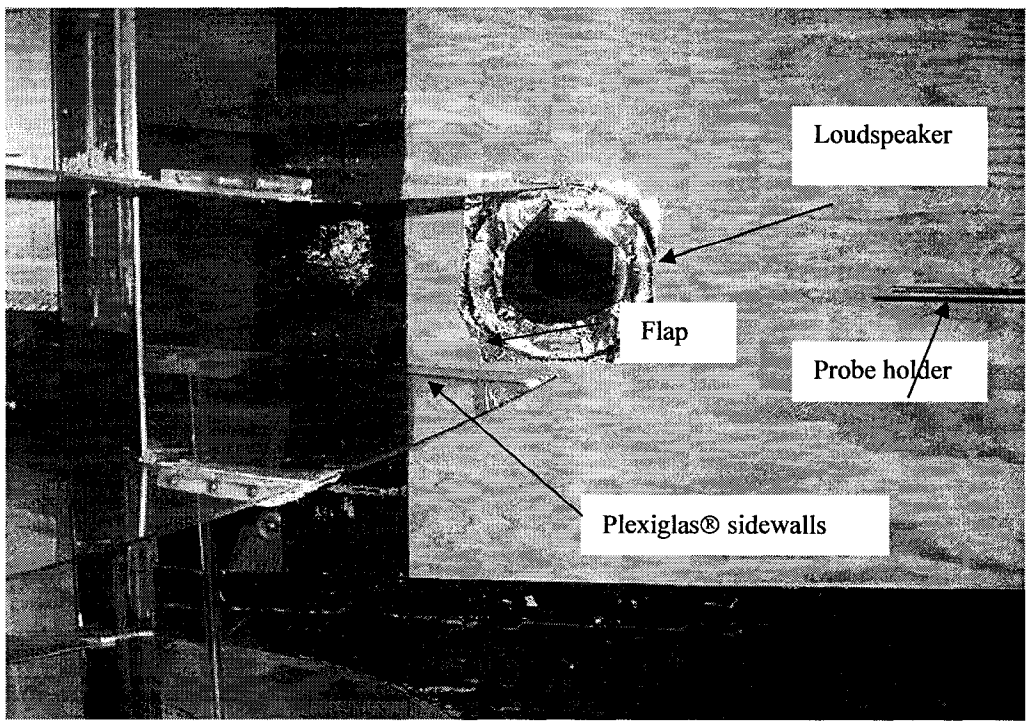

Figure 5.35 – Installation of Loudspeaker in Test Section Wall of ODU LSWT.

The loudspeaker was placed near the trailing-edge of the main wing and of the flap to optimize its directivity onto the region of interest on the model. This was done since the boundary-layer separation was known to have developed on the trailing-edge flap.

The displacement steps of the hot-film sensor that were used in the acquisition of the profiles were identical to those that were used for the test case when the effects of the piezoelectric devices were being studied. The data were copied from the output of the IFA Thermal Anemometry Software Package and transferred to a Microsoft® Excel® spreadsheet program. The data were afterwards plotted using a MATLAB® utility.

5.7.2.1 Mean Velocity Profiles

An experimental study was performed [Dovgal, A., 1986] whereby a loudspeaker was used to control the boundary layer on a two-dimensional wing. The free-stream velocity used in their study was 5.7 m/s. Their data indicated that, at an acoustical frequency of 85 Hz, they were able to produce significant increments in the mean velocity profile. They concluded that the acoustic oscillations generated by the loudspeaker were transformed into vortical waves and that these waves favorably interacted with the naturally occurring waves in the flow field above the wing, resulting in reattachment on an initially separated boundary layer.

The mean velocity data were obtained to determine if a more favorable velocity profile could be achieved by acoustical excitation. The velocities in the profile were normalized by using the velocity measured at the edge of the inviscid potential core that was obtained for the velocity profile at 0 Hz. The displacement heights were accordingly normalized by using the height from the surface at that model station to the edge of the

potential core. Figure 5.36 shows the profiles of mean velocity for the case of no excitation and for the case of excitation at 80 Hz.

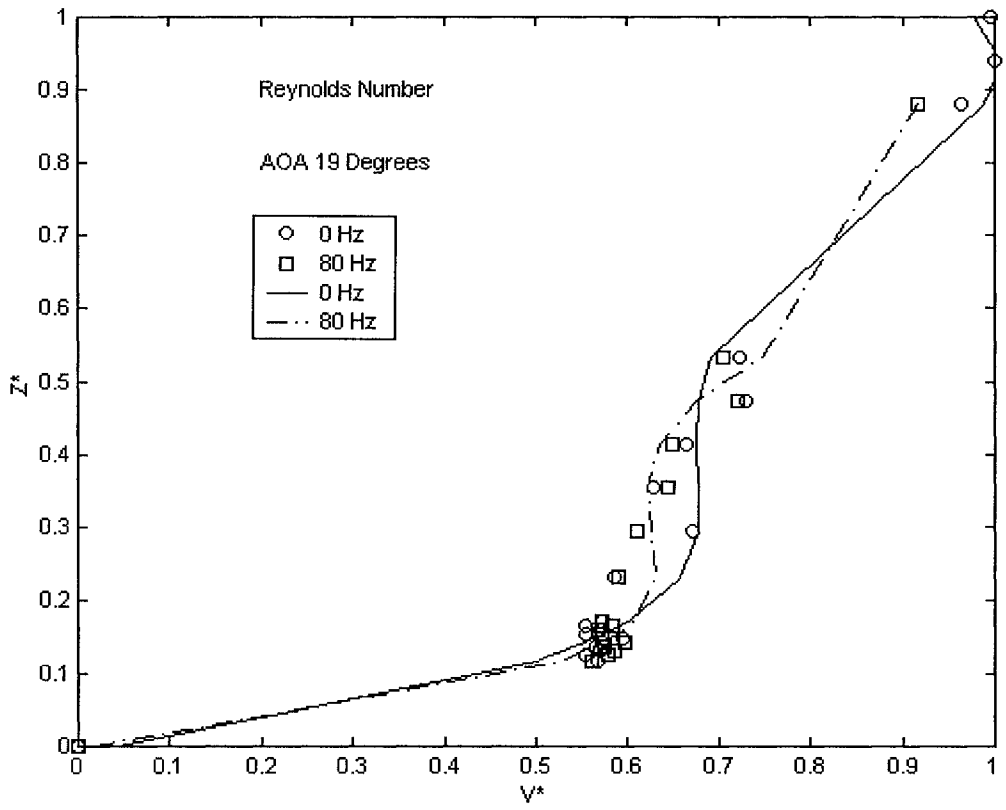

Figure 5.36 - Velocity Profile on Flap without Forcing and Loudspeaker at 80 Hz

The data in Figure 5.36 show that the velocity profile at 80 Hz does not suggest that the mean velocity profile is increased by acoustical excitation at this frequency. In fact, there appears to be an overall diminution of mean velocity. At best, the mean velocity profile is unaffected, and at worst the mean velocity is actually decreased to this audio excitation frequency. Further tests would need to be conducted to fully understand the

mechanism responsible for this phenomenon. Possibly at 80 Hz the sound source increases the amount of shear in the flow field, which has the effect of retarding the mean velocity.

This experiment has already shown that, when the piezoelectric devices were operated at the same frequency, no significant increments in mean velocity were observed.

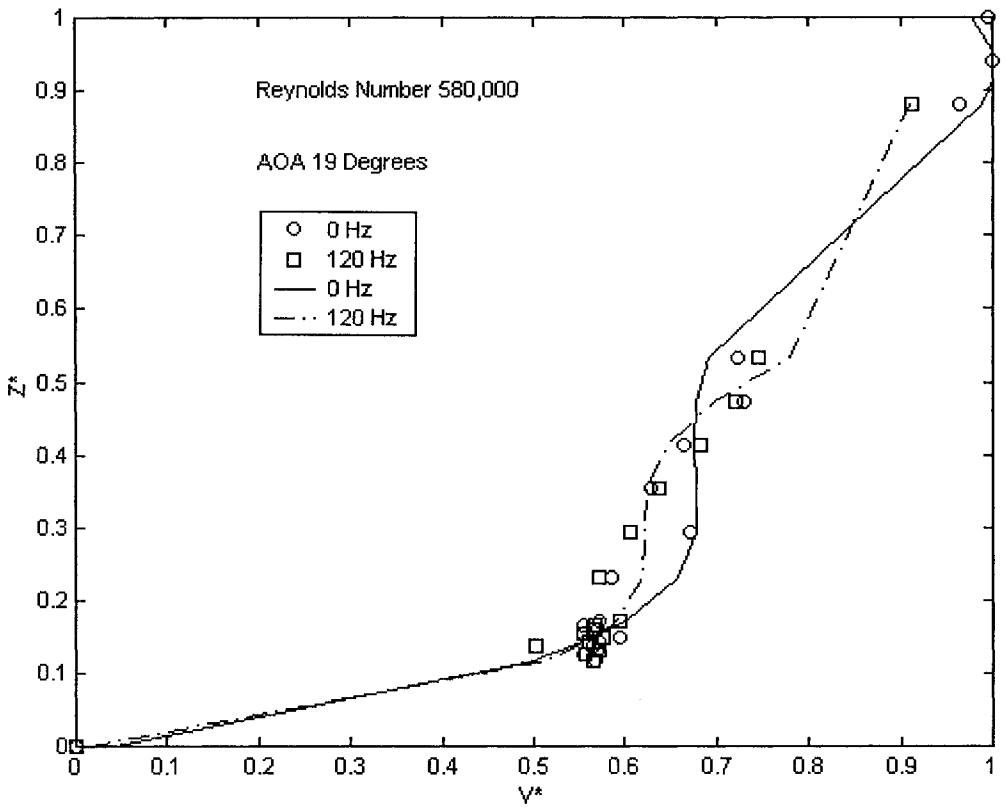

Figure 5.37 - Velocity Profile on Flap without Forcing and Loudspeaker at 0 and 120 Hz

Figure 5.37 shows the data comparing the mean velocity profiles at no excitation and at 120 Hz. Unfortunately, no data were obtained at 100 Hz which was the operating frequency corresponding to the maximum increment of mean velocity when the

piezoelectric devices were used. Nevertheless, the data shown in Figure 5.37 suggest that no marked increases in mean velocity occurred at an operating frequency of 120 Hz. Recall that in the case of the piezoelectric devices, there was a marked increment in mean velocity at this frequency. More data for a wider range of audio frequencies would be required to make a better assessment of the effect of acoustical energy on the aerodynamic characteristics of a multi-element airfoil.

5.7.2.2 Turbulent Intensity Profiles

The turbulence profiles on the flap were obtained for the excitation frequencies of 80 Hz and 120 Hz using the set up and instrumentation described previously. Figure 5.38 displays a comparison of the profiles of turbulence intensity for no external excitation and an operating frequency of 80 Hz. The data show that for normalized distances roughly less that 0.5 there is no decisive indication if the turbulence intensity is affected. However, for higher normalized distances the turbulence intensity is rather decisively increased when the loudspeaker is tuned to 80 Hz. It appears that in principle, the loudspeaker could be used to control the turbulence intensity, although as has been shown earlier, the velocity profile does not appear to be significantly affected. Intuitively, changes in turbulence intensity should occur to the extent as demonstrated by the data that this fact would manifest itself in significant changes in the velocity profile. However, because the purpose of this study was to focus on techniques to control and modify the flow field about a multi-element airfoil, the implementation of acoustic external excitation has been shown to be worthy of further study as a viable means to achieve control aerodynamic lift.

Although it is not the purpose here to propose any design incorporating the use of acoustic excitation, it would be possible that for a full-scale wing an array of sound

generations could be flush mounted in the surface of a wing. In this way, the sound source would be directly embedded within the boundary layer. Another application would be to embed an array of sound generators in the vertical tail to improve directional stability.

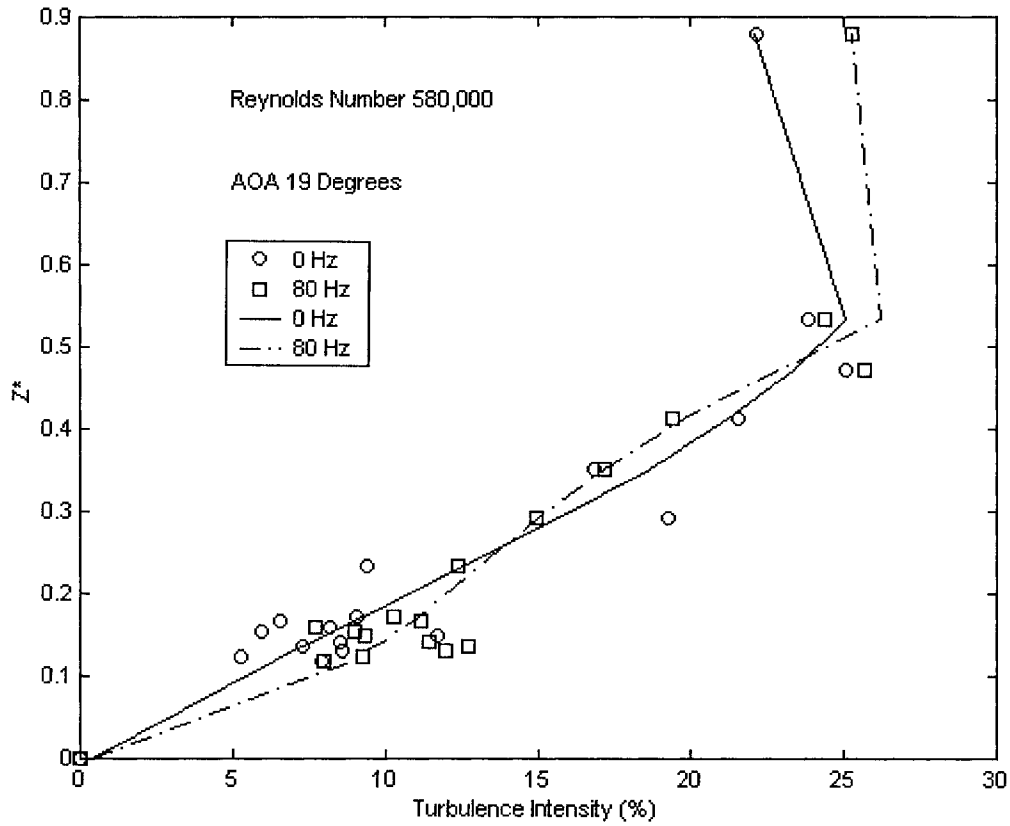

Figure 5.38 - Turbulence Intensity on Flap with Loudspeaker at 0 and 80 Hz

Figure 5.38 shows a comparison of the turbulence intensity profiles for no excitation and for an acoustical excitation of 120 Hz. The data show a trend similar to the profile for the case of 80 Hz. Most notably, the turbulence intensity at the higher normalized distances is clearly increased when the loudspeaker is tuned at 120 Hz. The critical normalized distance where the turbulence intensity increases is near $Z^* = 0.5$ for

both 80 and 120 Hz. Further tests need to be performed to determine the frequency dependence of this phenomenon.

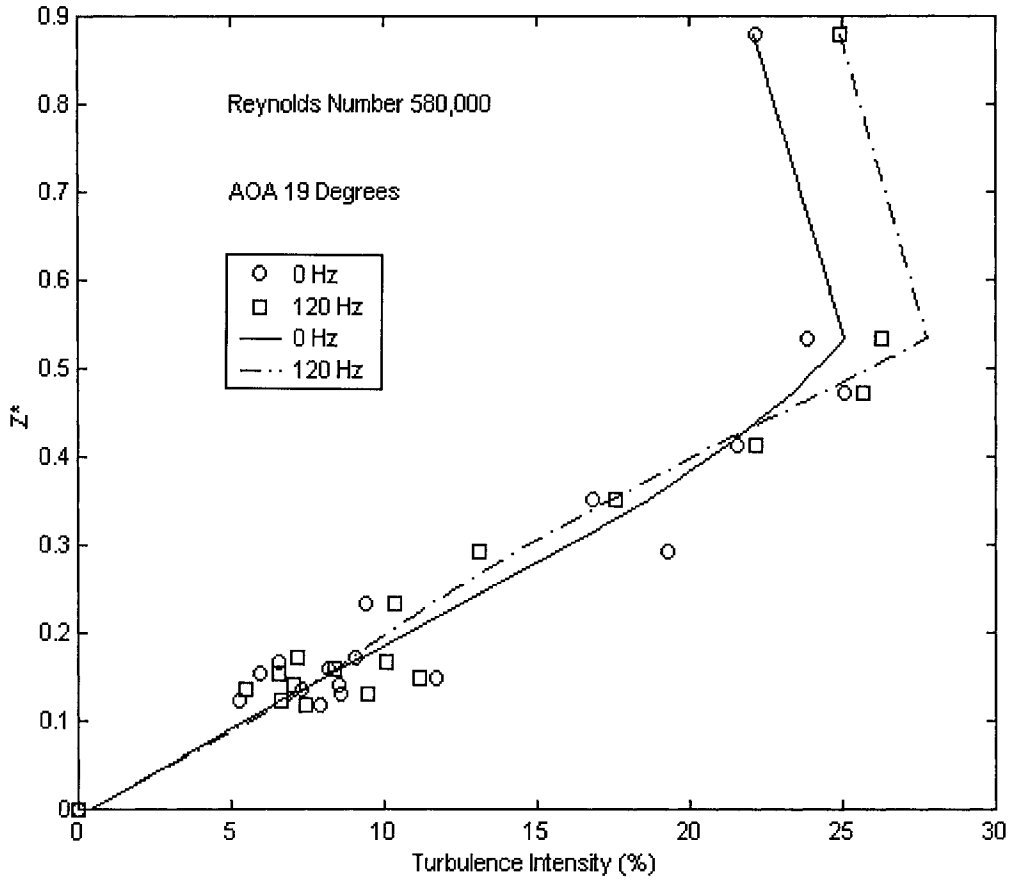

Figure 5.39 - Turbulence Intensity on Flap with Loudspeaker at 0 and 120 Hz

The turbulence intensity on the flap with acoustic excitation did not show conclusively that the boundary layer had been improved. Subsequent data will show that the pressure distributions on the flap as well as on the main wing provide more information with regards to the benefits of external excitation. Although the main element of interest was the flap, it is equally as important to examine the pressure distributions on the entire

model to assess the interactions between the separate flow fields surrounding each individual airfoil element.

5.8 Global Effects of Piezoelectric Excitation

An earlier discussion focused on the effect of the piezoelectric devices on the aerodynamic characteristics specifically of the trailing edge flap. Presently will be shown the results of an examination of the global characteristics that arise from the integrated effects of the three wing elements. This was investigated because of the interactions among the three elements, which completely underscores the fact that high-lift airfoils are inherently complex. The interplay between the various shear layers such as in the region of confluence is the source of one type of uncertainty and another are the mechanisms that may be responsible for local flow characteristics that are the result of feedback from downstream elements.

The pressure distributions over the entire model at 19° angle of attack for the various operating frequencies were plotted and are depicted in Figure 5.40 and tabulated in Table 5.9. The data clearly show that for frequencies of 0, 80 and 90 Hz, there are no significant variations in surface pressures. However, at both 100 and 120 Hz, there is definitely an increased amount of suction on the upper surface of the wing and leading edge slat. The increase of suction on the trailing edge could be due to the increased circulation at the leading edge of the main wing. This is predicated on the Circulation effect described earlier. As previously stated, the active devices were located on the lower surface of the main wing near the rear cove region. The results presented suggest that some type of influence is being propagated upstream from the lower surface to a model station that is not only upstream but also on the opposite surface. It is speculated that the devices affected the

jet of air that emerged from the rear slot and that the flow field at the trailing edge of the main wing produced effects, which were transferred upstream to the wing. Another explanation is that the effects originating at the devices propagated upstream along the lower surface and then were entrained into the flow through the slot separating the leading edge slat and the main wing. The data suggest that the effect of the devices on the lift was most significant on the main wing than on either of the other two wing elements.

A FORTRAN computer program was written to calculate the lift coefficient by integrating the pressure coefficient around the entire wing. The most marked change was found on the wing and on the slat. This program was used to determine the lift increments on the three wing components due to the devices operating at the various frequencies. The results are shown in Table 5.10. The data in Table 5.10 indicates that the largest effect occurred at an operating frequency of 100 Hz. In fact, the lift increment on the main wing alone accounted for a 5.5% increase in lift force. The original objective was to use the devices to bring about boundary layer reattachment on the separated trailing edge. Although the devices did appear to mitigate the boundary layer separation on the flap, reattachment did not occur. However, the data presently shown indicated that the devices could enhance the lift on the main wing even though it did not involve the removal of any separated boundary layers. In principle, these devices have been shown to be a credible technique for improving the high-lift performance of airfoils. The technology involved in the manufacture of these devices must be developed such that they could be practically be used for full-scale aircraft. This would include improvements in their ruggedness, power consumption and amplitude of deflection. The results are overwhelming that for the sake

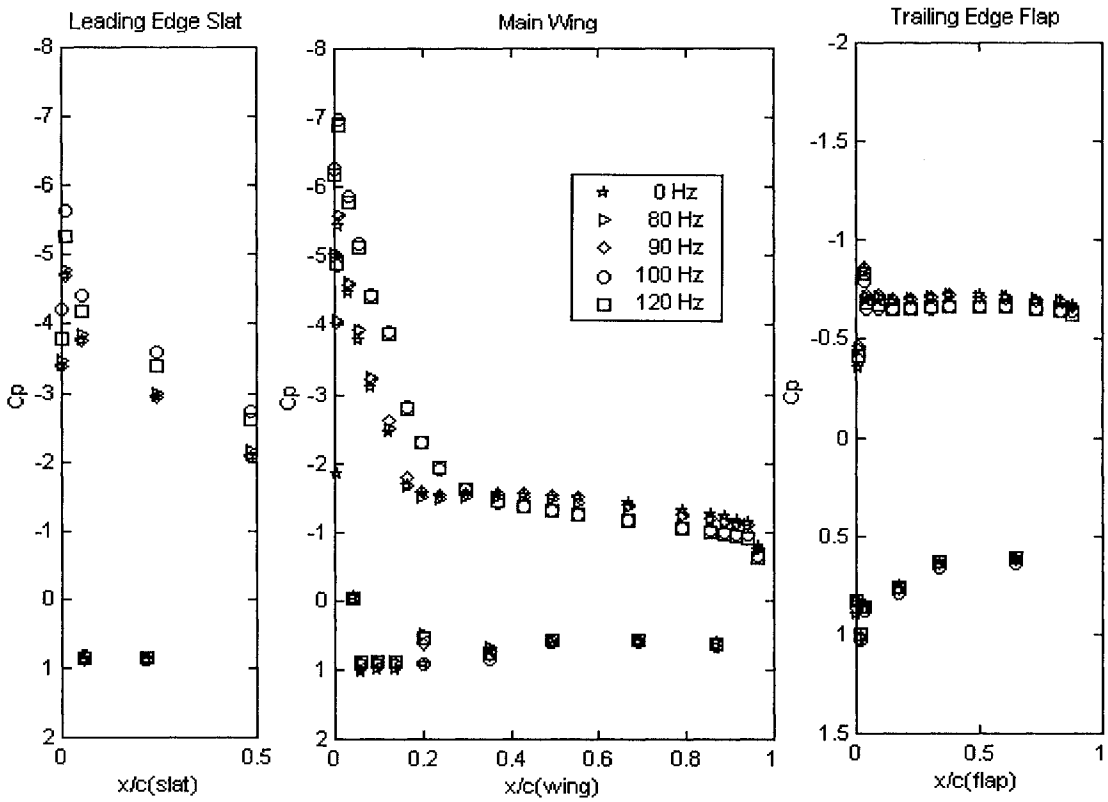

Figure 5.40 - Pressure Distribution at V_∞ = 20 m/s at 19° AOA with Piezoelectric Excitation

Freq. (Hz)	C_L(Wing)	C_L(Flap)	C_L(Slat)	C_L(Total)
0.0	2.13	0.68	1.57	4.38
80.0	1.99	0.69	1.61	4.29
90.0	2.07	0.69	1.57	4.33
100.0	2.24	0.67	1.89	4.80
120.0	2.16	0.66	1.80	4.62

Table 5.10 Lift Coefficient on Wing with Piezoelectric Excitation at V_∞ = 20 m/s at 19° AOA

of advancements in high-lift aerodynamics this is one technology that merits further inquiry.

The piezoelectric devices were also operated at frequencies of 0 and 320 Hz at 15° angle of attack. This was done to further substantiate the effectiveness of the piezoelectric devices. Data were obtained for four different test runs for each frequency and for the same flow conditions and model attitude. The data trend indicated consistently that when the devices were operated at 320 Hz the lift coefficient was higher than when the devices were turned off. The pressure distributions were obtained in a continuous mode, which means that the tunnel was not turned off and on between frequency settings. This was done to minimize the possibility of introducing unwanted changes in the test set up that could cause modifications in the flow field conditions and lead to erroneous interpretations of the test results.

Figures 5.41 and 5.42 show the pressure distributions on the model for four individual test runs for the above-stated test conditions. The data are tabulated and shown in Appendix C. Generally, the data show that there was not a significant amount of variation in the pressure distributions for each of the two selected operating frequencies. The distributions on the slat were questionable and could have been attributed to flow-induced divergence of the Plexiglas® sidewalls. The most striking result from these plots is the fact that the boundary layer on the trailing edge flap was attached when the devices were operating at 320 Hz and was separated at 0 Hz. This trend was repeated for the four test runs and definitely indicated the potential of using these devices to facilitate boundary-layer reattachment. Another observation was that the leading-edge suction peak on the main wing was diminished at the higher frequency. On the flap the leading-edge suction increased, which was compatible with the conjecture of increased air-flow velocity at 320 Hz, causing the boundary layer to reattach. A FORTRAN computer program was written

to combine and average the distributions for each individual frequency to establish composite distributions at 0 and 320 Hz. The composite data are plotted in Figure 5.43. When the composite distributions were plotted, the data show that the distribution of surface pressure coefficient at 320 Hz displays a greater overall upper-surface suction on the main wing, when compared with the baseline case. This was especially true near the trailing edge of the main wing, which was the region of the main wing that was in closest proximity to the piezoelectric devices located on the lower surface. This validates the results shown previously for the model at 19° angle of attack.

The same FORTRAN program that was used previously to compute the lift coefficient was run for this these data. The resulting lift coefficients are displayed in Table 5.11 for the different test runs. No lift coefficients for the slat were shown, because the data were questionable. As was shown for the previous set of test conditions, the piezoelectric devices caused a notable increment in lift coefficient on the main wing.

C_L (Lift Coefficient)

	0 Hz		320 Hz	
Test Run	C_L(Wing)	C_L(Flap)	C_L(Wing)	C_L(Flap)
1	1.47	0.66	1.71	0.90
2	1.58	0.66	1.72	0.91
3	1.57	0.66	1.68	0.89
4	1.50	0.65	1.64	0.87

Table 5.11 Lift Coefficient on Wing with Piezoelectric Devices at V_∞ = 20 m/s at 15° AOA

When the above lift coefficients for the main wing were averaged for each operating frequency, the mean lift coefficients at 320 Hz was calculated to be 1.6880 and the average lift at 0 Hz was 1.5334. The standard deviations of the lift coefficient were

0.0302 and 0.0461 for 360 and 0 Hz, respectively. The relatively low standard deviations are indicative of the significant consistency of the data and gave credence to the effectiveness of these devices. Using the mean lift coefficient for each operating frequency the piezoelectric devices were responsible for an increase of 10%. As has already been remarked, the notable increases in suction on the upper surface of the wing occurred near the trailing edge of the main wing. Since data previously reported in this study indicated that the flow velocity over the flap increased when the devices are activated, the higher suction at the main wing trailing edge could be due to the entrainment on the rear region of the main wing. This phenomenon confirms the theory [Smith, A. O., 1975] that circulation around the flap induces an increment in velocity on the main wing. Although the original intent was to directly influence the flow field over the flap, these results suggest that these devices can be used to establish a more favorable pressure gradient on the main wing as well. The data show that in spite of the reduced leading-edge suction on the main wing at 320 Hz compared with the baseline case, the overall lift coefficient was improved when integrated all over the entire main wing.

Although some of the results reported for 19° AOA were promising, the data presently presented at 15° AOA were far more encouraging. These test results offer the hope that with further research these devices can be optimized to augment existing elements of aircraft design to achieve higher aerodynamic lift.

The data also show the effect of the piezoelectric devices on the flap for the same test conditions. For the baseline conditions at 0 Hz the boundary layer is separated. When the devices were tuned at 320 Hz the boundary layer on the flap is clearly attached. The

devices increased the circulation around the flap causing the pressure gradient there to become more favorable and the boundary layer to reattach.

The surface pressure coefficient on the upper surface of the main wing was most favorable at 320 Hz because at a free-stream velocity of 20 m/s this frequency is a subharmonic of the natural or vortex passage frequency. It was shown earlier that the highest rate of amplification occurs at a disturbance frequency that is a subharmonic of the natural frequency.

Pressure distributions were also obtained for the operating frequencies 240 and 260 Hz. These distributions represent averages of two runs for each frequency and are shown in Figures 5.44 and 5.45. The distributions on the main wing for the two frequencies were practically unchanged from the baseline case. The boundary layer on the flap was separated for both frequencies. However, on the slat the data show significant variation between test runs as shown in Figure 5.22. The surface pressures on the leading-edge slat as shown in Figure 5.44 are much lower and could possibly be the result of separation occurring due to flow-induced misalignment of the sidewalls. It is theorized that with divergence of the leading edge region of the sidewalls, separation occurred and the cross flow of the resulting swirling air would produce lower surface pressures. When the data are compared with the results obtained and shown in Figure 5.22 without the sidewalls the distributions on the main wing and flap for both configurations are comparable. The apparent anomalies in the flow field had dissipated further downstream of the model.

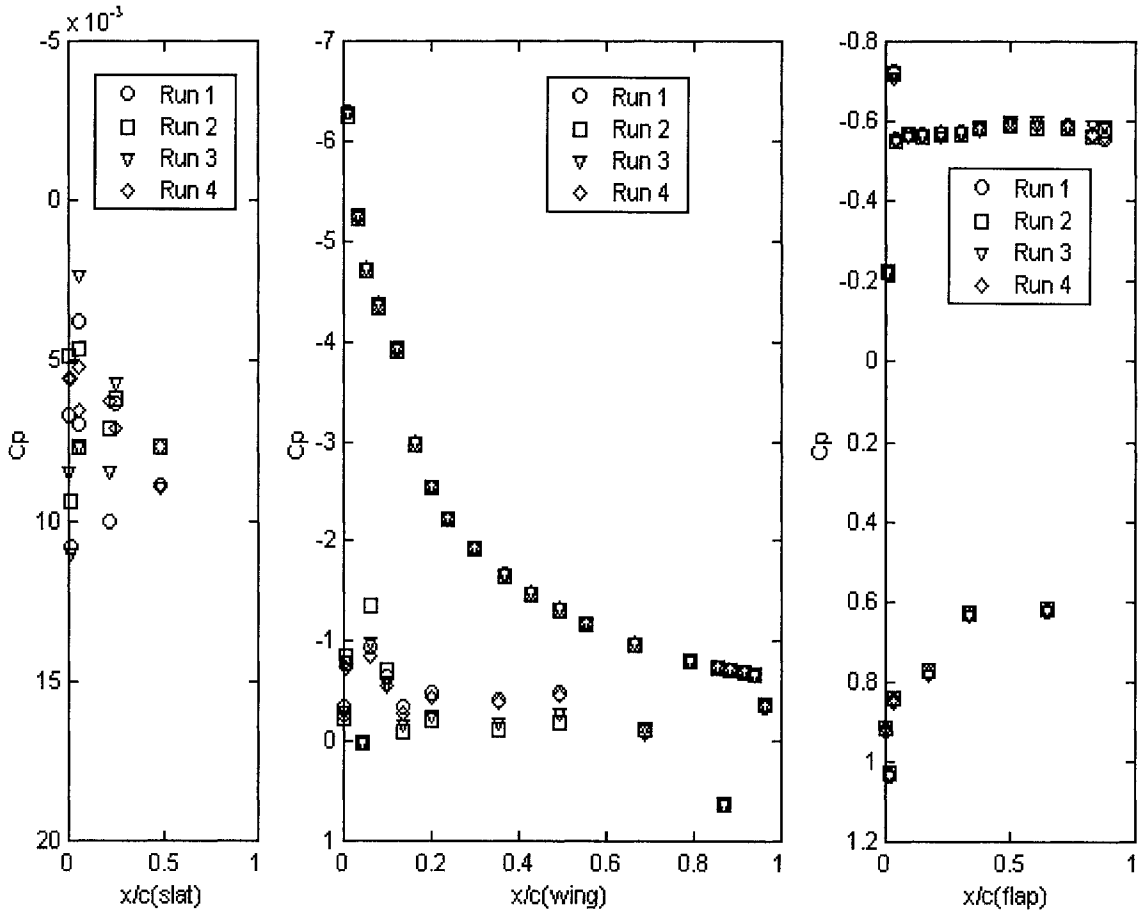

Figure 5.41 - Pressure Distributions with Piezoelectric Devices at 15° AOA, V = 20 m/s at 0 Hz

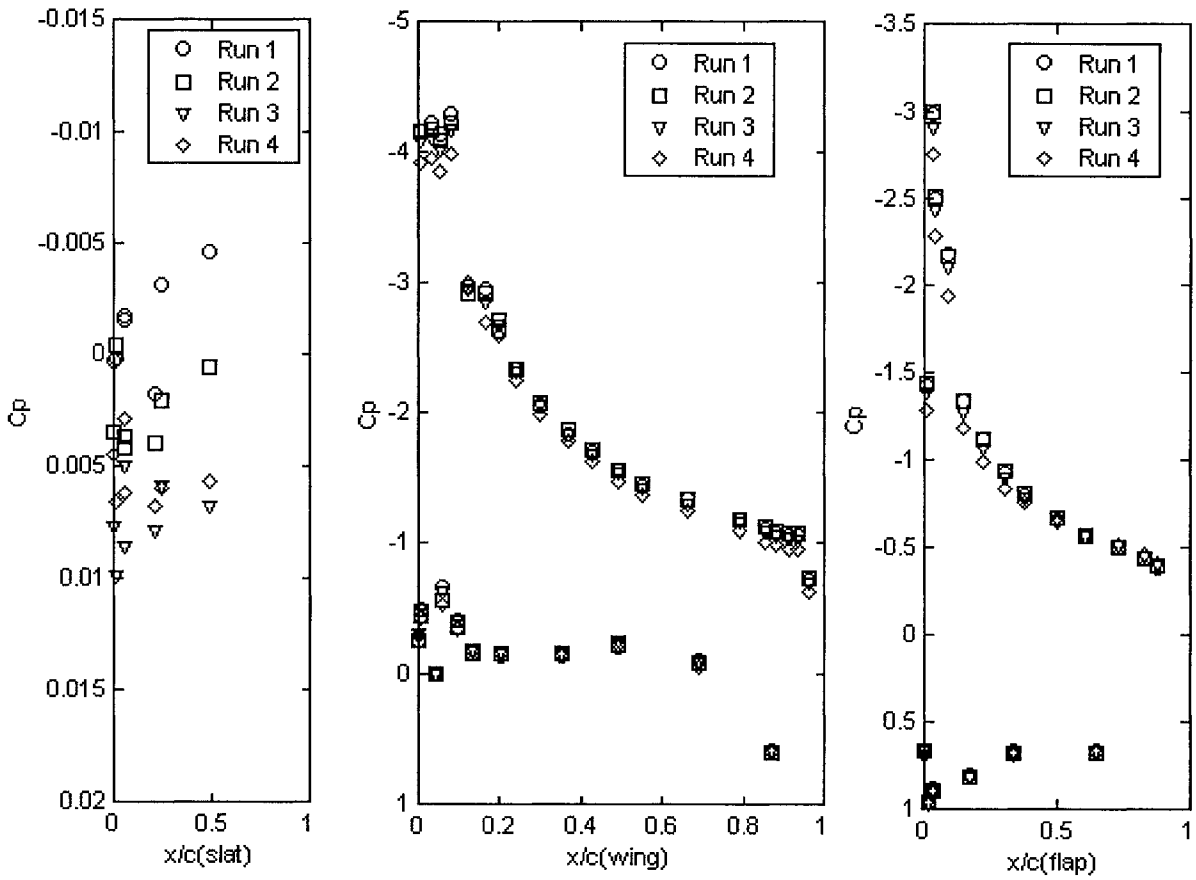

Figure 5.42 - Pressure Distributions with Piezoelectric Devices at 15° AOA, V = 20 m/s at 320 Hz

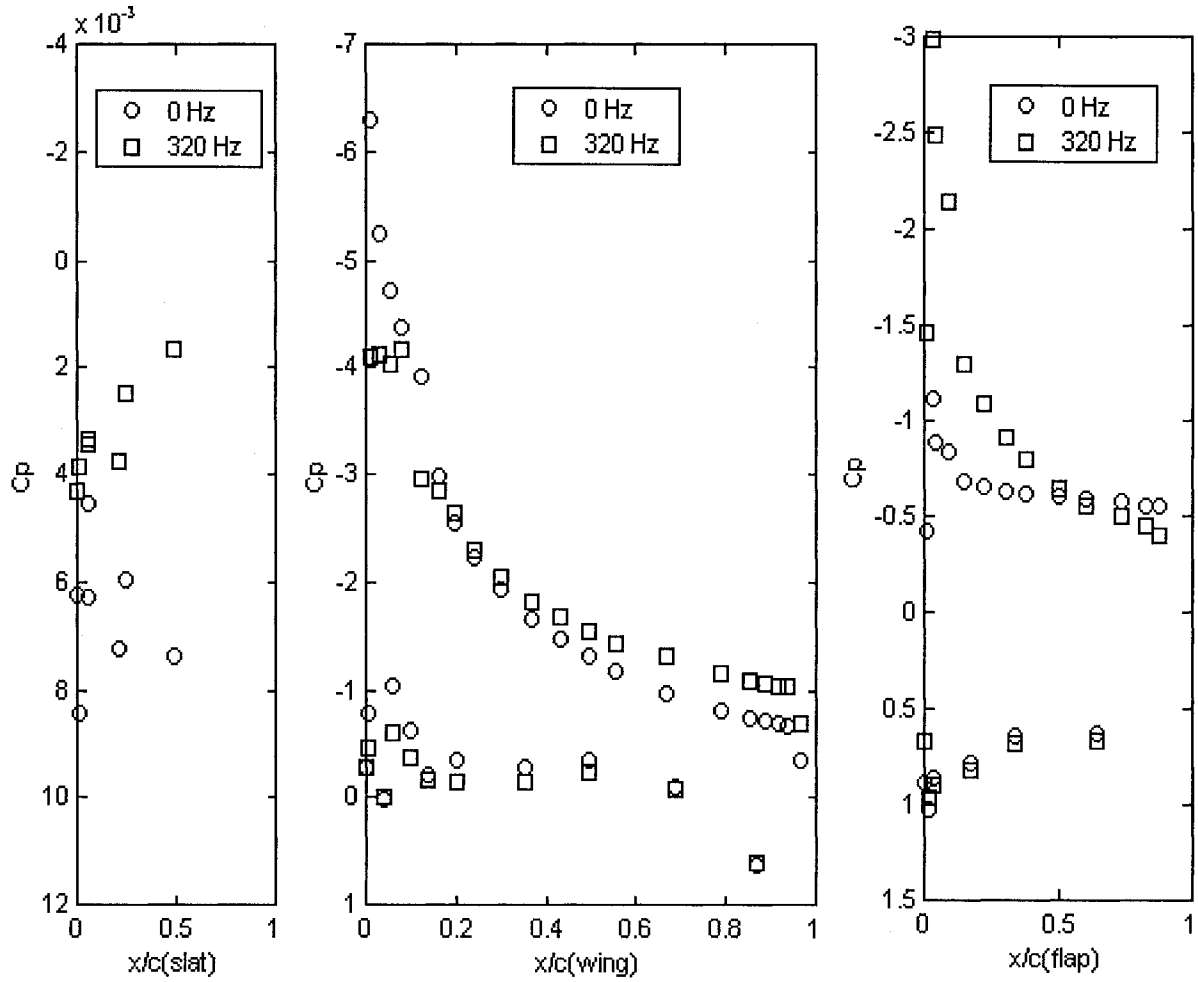

Figure 5.43 – Average Pressure Distribution with Piezoelectric Devices at 15° AOA, V_∞ = 20 m/s at 0 and 320 Hz

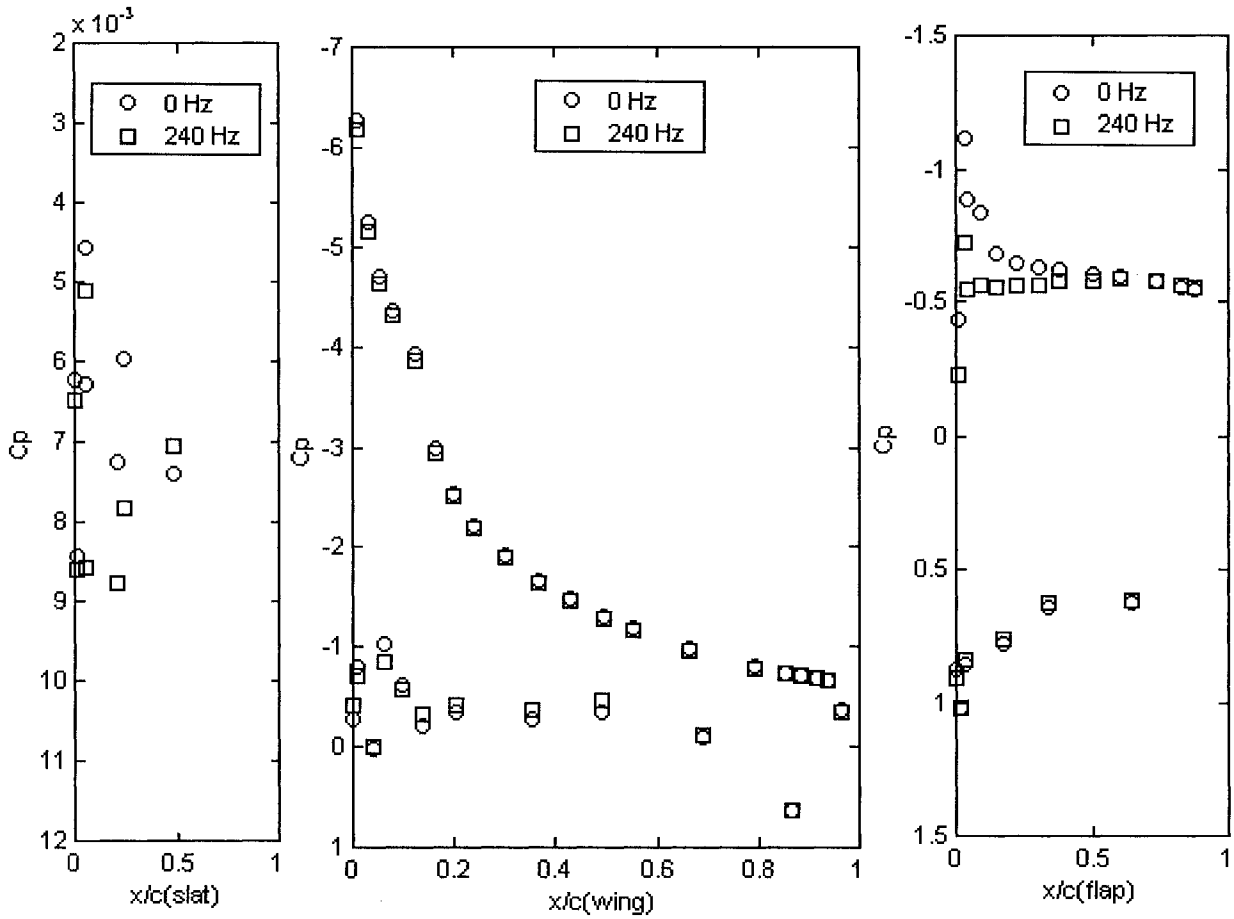

Figure 5.44 – Average Pressure Distribution with piezoelectric Devices at 15° AOA, V_∞ = 20 m/s at 0 and 240 Hz

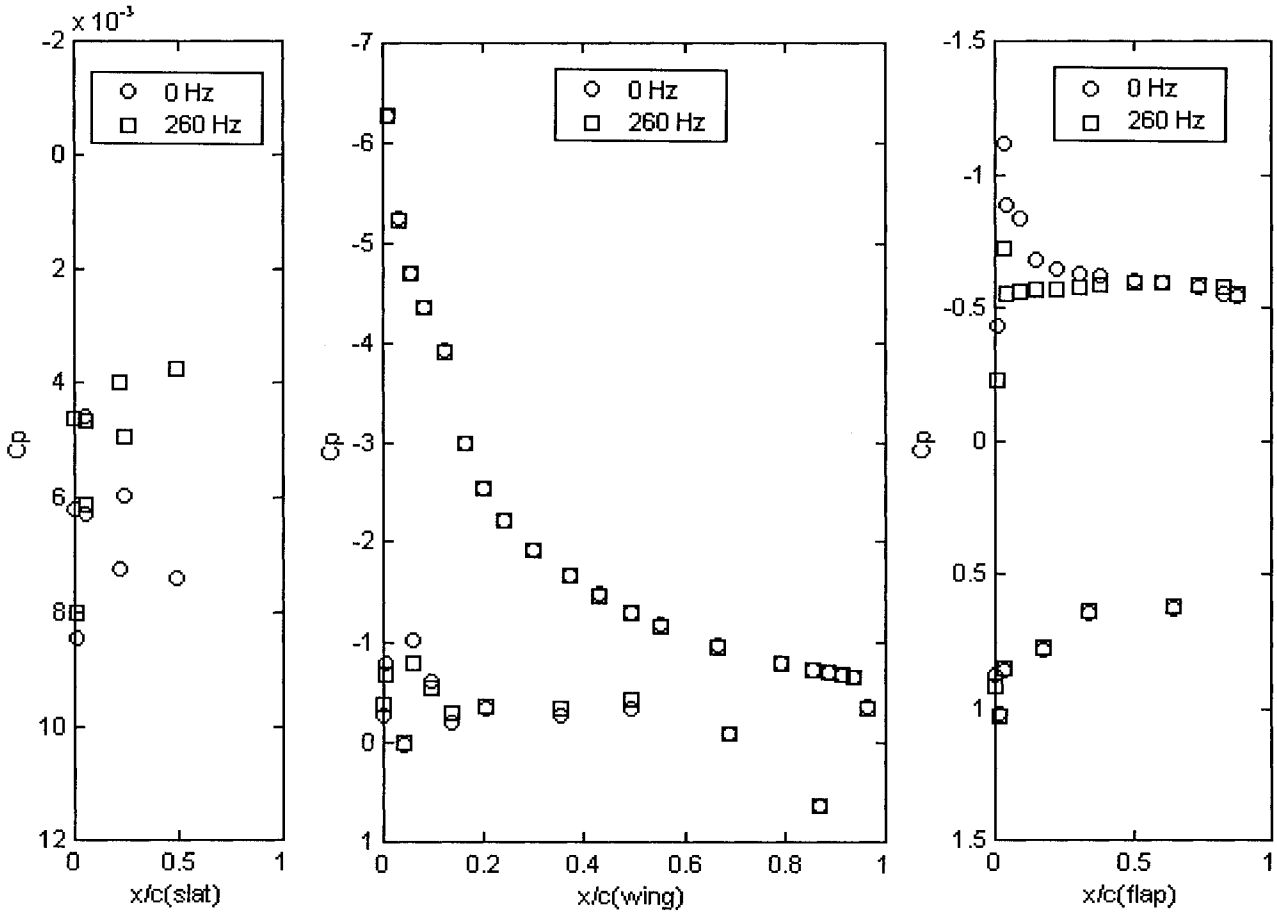

Figure 5.45 – Average Pressure Distribution with Piezoelectric Devices at 15° AOA, V_∞ = 20 m/s at 0 and 260 Hz

The magnitude and sign of the pressure gradient on any lifting surface is an indication of the degree of susceptibility of the boundary layer to separation. It is universally understood that the lower the pressure gradient, the more resistant the boundary layer is to separation. Distributions of the pressure gradient were plotted and compared for the various selected excitation frequencies of the piezoelectric devices. The pressure gradient was calculated by approximating the derivative of the pressure coefficient at selected values of chord-wise location using the three-point forward difference formula as shown in Equation 5.6.2.4-1 [Fausett, L. V, 1999].

$$\frac{d C_p}{dx} \approx \frac{-C_p^{i+2} + 4C_p^{i+1} - 3C_p^{i}}{x^{i+2} - x^{i}} \qquad (5.6.2.4\text{ -}1)$$

These results are shown in Figure 5.53 and indicate striking differences between the various frequencies. It is noted that the overall level of the pressure gradient decreases directly with increasing excitation frequencies. The distribution that had the lowest overall magnitude was for the excitation frequency of 320 Hz, which is in agreement with the observed increments of lift coefficient near the rear portion of the main wing. Additionally, the distribution for 320 Hz exhibited a wave-like characteristic with an amplitude that was clearly larger than for the other three cases. It is noteworthy that these pressure gradient distributions bear a marked resemblance to the distribution of normalized velocity that was obtained in a previous experiment (Chih-Ming, H. and Huang, L., 1982) involving an axisymmetric jet as shown in Figures 1.13 and 1.14 of this dissertation. The waviness in the distribution is apparently a result of the forcing frequency that induces variations in the

boundary layer. These results are interesting because they show that even though the distributions at 240 and 260 Hz were not favorably enough to increase the lifting capability of the main wing, the piezoelectric devices still manifested a noticeable effect on the distribution of pressure gradient. An attempt was made to correlate the apparent periodicity of the pressure coefficient gradient with the vortical dynamics associated with the flow field surrounding the main wing. It was surmised that the wave-like nature of the pressure gradient distribution, was attributed to the system of vortices being generated at the trailing edge of the slat. The periodicity was most strikingly demonstrated for the excitation frequency of 320 Hz and so the frequency of the passing vortices was estimated using this particular data set. The wavelength of the vortex system was estimated by calculating the distance between the first two relative peaks shown in the distribution. This displacement was found to be roughly 0.057 m and the velocity near the model surface was roughly 30 m/s based on hot-film measurements. The vortex passing frequency was calculated using Equation 5.6.2.4-2.

$$f = \frac{v}{\lambda} \qquad (5.6.2.4-2)$$

When the appropriate numerical values are substituted in Equation (5.6.2.4-2) the frequency is estimated at 529 Hz. This estimate is not too dissimilar to the vortex passing frequency of 656 Hz that was found earlier from the hot-film power spectra. This result suggests that the periodicity of the pressure gradient distribution was caused by the interaction of the shed vortices with the boundary layer on the upper surface of the main wing. Furthermore, the fact that this phenomenon is most apparent at the excitation

frequency of 320 Hz suggests that the vortices have coalesced due to the process of vortex pairing, which ultimately gave rise to the observed significant increment in lift coefficient. The spacing of the peaks in the distribution dilated in the downstream direction, which indicates that the vortices were also spreading out with increasing distance from the slat. When these results are compared with the pressure coefficients it is seen that the most marked effect on the main wing occurred near the trailing edge and it was apparently due to the fact the system of vortices had coalesced into a more fully energetic swirl of air at this location. The marked increase in amplitude of the distribution with downstream position was indicative of a progressively growing system of vortices due to vortex amalgamation.

In a previous study [Cho, S. K., 1998] it was shown that when the natural frequency of an axisymmetric jet was modulated with the first subarmonic with a phase difference of 272° that there occurred an increased amount of vortex pairing along with increased turbulence intensity. As already mentioned, Cho et al. [1998] demonstrated that when vortex pairing occurs there is a transfer of energy from the mean velocity to the fluctuating velocity. Essentially, this means that the turbulent kinetic energy was increased in the boundary layer particularly at downstream locations. It can be inferred from the results reported in this dissertation that vortex pairing has occurred at 320 Hz and that the increased turbulent kinetic energy helped to enhance aerodynamic lift at the rear of the main wing and to mitigate the separation on the flap. From a mathematical perspective, this explanation has merit when both Equations 1.4 and 1.5 are examined. They show that when the turbulent stress component is increased in Equation 1.5 that the second derivative term on right-hand side of Equation 1.4 becomes more negative. This is the required condition for a curvature of the velocity profile that favors an attached boundary layer.

Power spectra were obtained of the pressure gradient data to gain additional insight into the interaction between the device oscillations and the ensuing boundary-layer characteristics. The MATLAB utility SPECTRUM was used to convert the data from the spatial domain to the frequency domain to obtain power spectra for the various excitation frequencies. Another MATLAB utility, SPECPLOT was used to plot the spectral data. The data were plotted with the frequency axis being normalized such that the maximum value of the frequency was equal to one. The sampling or Nyquist frequency was equal to 2. The plot of the power spectra is displayed in Figures 5.47. This analysis was performed merely to calculate the relative levels of energy in the flow field for the various excitation frequencies. The spectra indicate that the power spectrum at 320 Hz displayed a prominent peak at around a normalized frequency of .40. The spectra for the lower excitation frequencies were relatively broad band and did not show any characteristic peak. A comparison of these spectra demonstrated that the boundary layer at 320 Hz was more energized and that this fact gives further validation to this technique of lift augmentation. The fact that the power spectrum at 320 Hz contained more energy was reflected in the fact that the velocity of the flow over the upper surface of the main wing exceeded the surface velocities for the other frequencies. This resulted in the observed greater suction and lower surface static pressures.

It is noteworthy that the power spectra for the lower frequencies overlapped and were generally indistinguishable from each other, including the baseline case for 0 Hz. The system of vortices in the slat wake for the frequencies, 0, 80 and 90 Hz were undoubtedly incoherent and three dimensional and therefore were incapable of efficiently transporting turbulent kinetic energy down into the boundary layer.

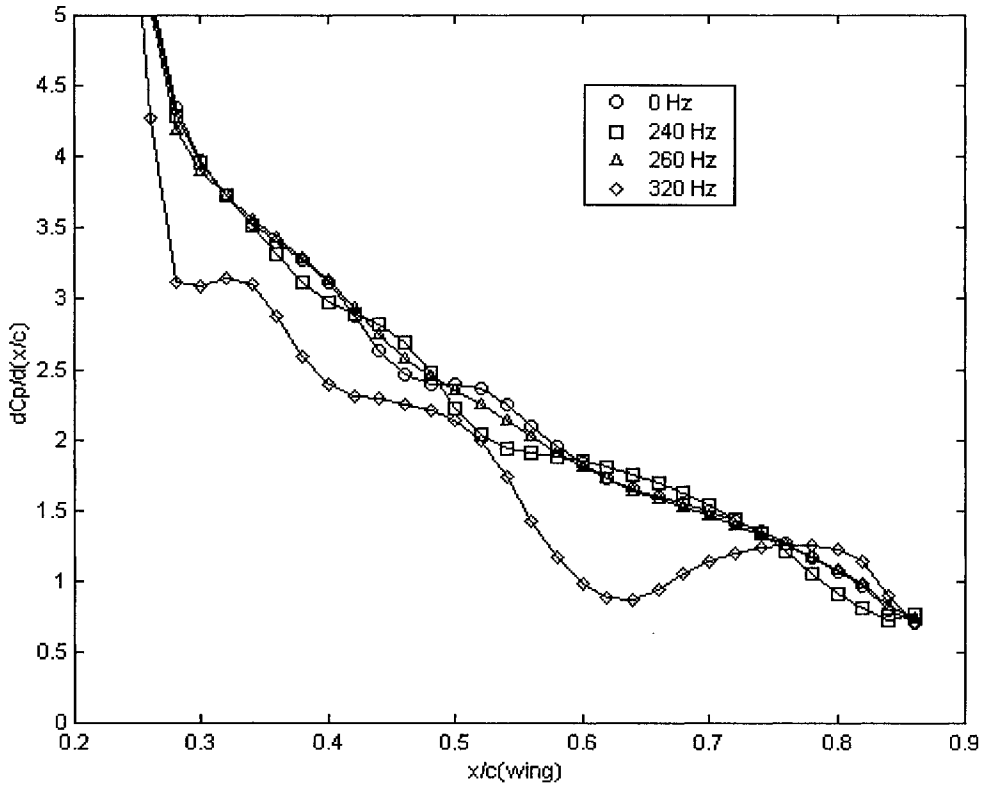

Figure 5.46 – Pressure Coefficient Gradient on Main Wing at V = 20 m/s, 15° AOA

This method of examining the distribution of the pressure gradient coefficient and its power spectrum is original and offers a potentially good technique for assessing the relative effectiveness of a variety of external excitation frequencies. The results of this method suggest that one can make a correlation between the amplitude of the spectrum and the ability of the corresponding excitation frequency to engender boundary-layer reattachment.

It is conceivable that a study could be conducted to vary the geometric parameters of the model to determine how these changes affect the pressure coefficient gradient and its

attendant power spectrum. This could offer a first order approximation of the correct frequency to initiate vortex pairing.

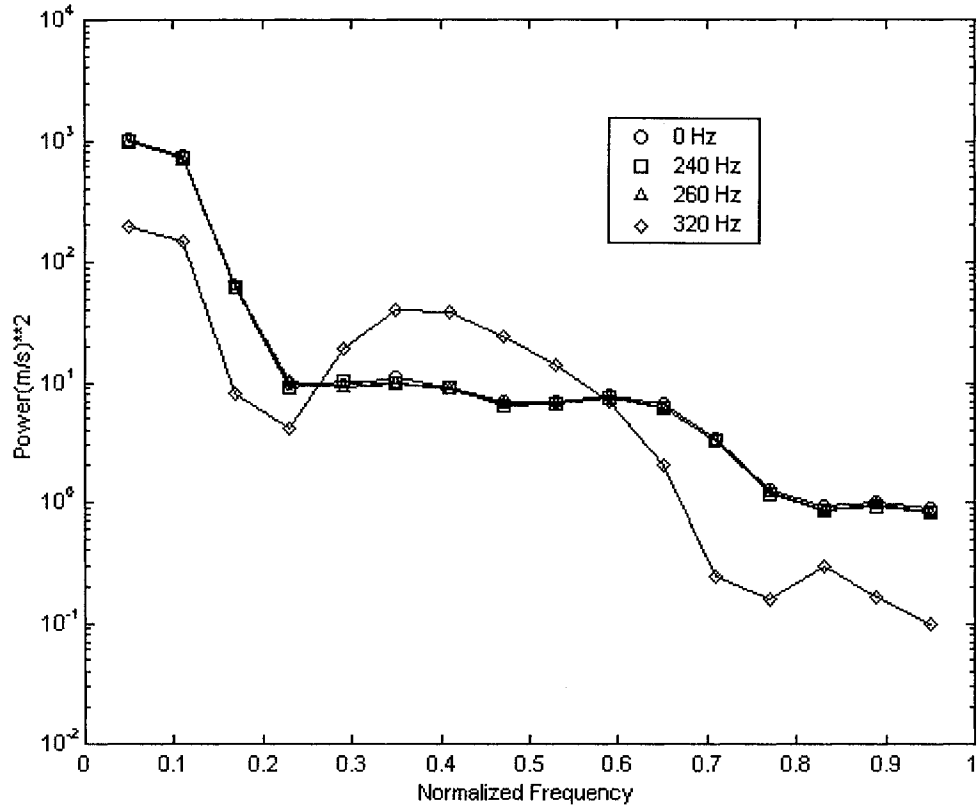

Figure 5.47 – Power Spectrum of Pressure Coefficient Gradients on Main Wing at V = 20 m/s, 15° AOA

5.9 Global Effects of Acoustic Excitation

Earlier results on only the trailing edge flap, indicated that the acoustic excitation provided by the loudspeaker did not show any signs of favorably affecting the region of boundary layer separation. The data presently being considered was for a free stream velocity of 20 m/s at 19° AOA. The data shown in Figure 5.48 shows the differences in the surface pressure distributions for the three elements of the wing. Tabulated data are shown in appendix D. The data indicate that on the main wing there occurred a significant increase

in suction on the upper surface at an operating frequency of 80 Hz. There was practically no change between the baseline case of 0 Hz and the case at 120 Hz.

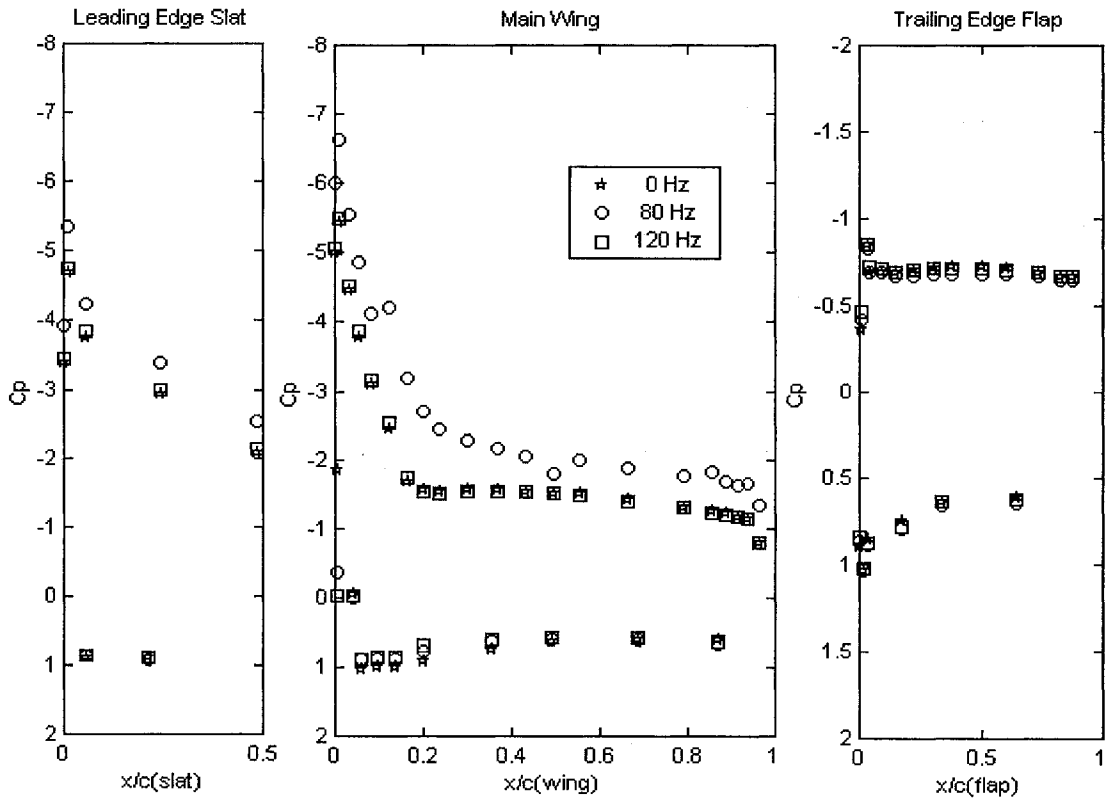

Figure 5.48 - Pressure Distribution at V_∞ = 20 m/s at 19° AOA with Acoustic Excitation

To calculate the overall lift, the same FORTRAN computer program was used to integrate the pressure coefficients over the all three wing elements. The results are indicated in Table 5.12. As the previous data showed, the most marked changes occurred on the main wing and the leading edge slat.

Freq. (Hz)	C_L(Wing)	C_L(Flap)	C_L(Slat)	C_L(Total)
0	2.13	0.68	1.57	4.38
80	2.75	0.68	1.80	5.23
120	2.10	0.69	1.60	4.39

Table 5.12 - Lift Force on Main Wing Using Acoustic Excitation at $V_\infty = 20$ m/s at 19° AOA

The results in Table 5.12 show the extent of the lift increment that was gained through acoustic excitation at 80 Hz. The lift had increased by roughly 30% because of the acoustical excitation. This represents an extraordinary increment in aerodynamic lift. These results are similar to the results from an earlier experiment [Seifert, A., et. al, 1998]. The results of this previous study were shown in Figure 1.12 and demonstrated an increment of 35% when the model was oriented at 15° AOA. These results suggest that in principle, a noise source could be used to positively affect lift. In both the previously cited experiment and in the one currently being discussed, the flow field on the upper surface was directly targeted by some energy source. This arrangement had a marked impact on the pressure distribution on the upper surface of the main wing. The results here also confirm the conclusions reported in an earlier wind tunnel experiment [Dogval, A. V., et al., 1986]. It is hypothesized that vortex pairing occurred, in which case the energy and momentum in the system of vortices were more readily transported to the surface of the model. Additional research is needed to identify the proper placement of such a device on a full-scale aircraft as well as the consideration of destructive acoustic interference and how it could be managed to avoid its unfavorable effects.

The following will attempt to offer a plausible explanation for the marked increase in lift coefficient that was observed for the case when the flow field around the model was externally excited by the loudspeaker at a frequency of 80 Hz. No such increments in lift were observed at excitation frequencies of 0 and 120 Hz. The pressure distribution on the upper surface of the main wing exhibited a leveling off at the model longitudinal location where the pressure recovery began. Other wind tunnel experiments using either the identical or similar model have presented pressure distributions, which demonstrate this same characteristic feature. In one study [Landman, D., 1989], pressure distributions were obtained showing the effect of changing the vertical position of the trailing edge flap. In this study [Landman, D., 1998] surface pressure distributions were obtained for various gap distances. The purpose of the test was to determine the effect of gap size on stall progression on the flap. The leveling off in the upper surface distribution occurs around x/c = 14% at the end of a region that demonstrated some degree of leveling off. It is attributed to the interaction between the slat wake and the main wing boundary layer.

The distributions all exhibit the characteristic leveling off on the main wing upper surface. This abrupt change of slope in the pressure distribution is due to the merging of the slat wake with the boundary layer on the main wing. The main wing boundary-layer flow is abruptly decelerated at the axial location where the slat wake interacts with the main wing boundary layer. It is conjectured that at this location the suddenly retarded flow is mainly responsible for the precipitous increase in the surface static pressure. The closer the location of the wake/boundary-layer interaction is to the leading edge of the main wing the smaller the available wing surface area to achieve adequate lift. Consequently, more wing

loading can be achieved by delaying the merging of the slat wake and the main wing boundary layer.

In a previous study [Nakayama, A., et al., 1990], measurements were obtained in the wake region of the slat at a free-stream Mach number of 0.2 and at two angles of attack. This study was conducted for two test cases, namely, test cases A and B, which were for 10° and 18° angles of attack, respectively. Figure 5.49 shows the surface pressure distributions for the two test cases. The distribution on the upper surface of the main wing for case A shows more of a plateau near the wake of the slat. At this lower angle of attack the slat wake is in closer proximity to the main wing than for case B and therefore interacts with the boundary layer at a location further upstream.

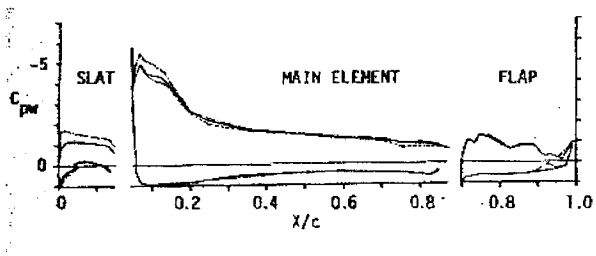

Figure 5.49(a) – Surface Pressures on Multi-Element Airfoil in NASA, Langley LTPT, Test Case A

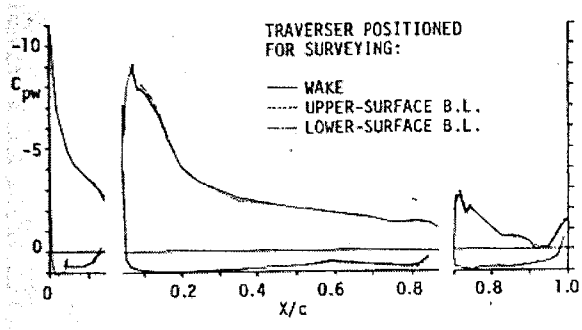

Figure 5.49(b) – Surface Pressures on Multi-Element Airfoil in NASA, Langley LTPT, Test Case B

In general, the above description of the interplay between the wake/boundary-layer interaction and lift is true. However, external periodic excitation of the wake at specific frequencies can lead to a totally different result. It is believed that this is the mechanism responsible for the observed increments of lift coefficient at 80 Hz.

The wake from the leading edge slat is susceptible to divergence or spreading due to periodic excitation at a class of suitable frequencies. Bhatacharjee [1986] showed that when the free shear layer behind an aft-facing step is perturbed by an acoustic signal tuned at a subharmonic of the vortex passing frequency that the wake became more divergent. Moreover, measurements indicated that turbulent kinetic energy was transferred from the shear layer to the boundary layer on the floor of the tunnel test section. The transfer of turbulent kinetic energy arises from the vortex pairing, which results when the flow is excited at selected frequencies. The effect of the added turbulent kinetic energy to the boundary layer is to increase the velocity near the surface, which leads to higher aerodynamic lift. Tordella and Christiansen [1989] also showed that the spreading of a wake from a splitter plate and vortex pairing could be achieved by mechanical periodic excitation. Furthermore, work done by Strange and Crighton [1983] and by Crow and Champagne [1971] indicated that an axisymmetric jet could be artificially made to spread when excited by a loudspeaker tuned to specific frequencies.

The data in this study demonstrate that the pressure distributions at 0 and 120 Hz do not exhibit a leveling off and therefore do not indicate any significant merger of the slat wake and main wing boundary layer. The data suggest that vortex pairing occurs at a frequency of 80 Hz, which has the effect of spreading the slat wake, causing the merger of the wake and main wing boundary layer. Assuming that vortex pairing occurred within the

slat wake, turbulent kinetic energy was diffused to the model surface, which accounts for the lift increment.

In a previous study [Christopher and Pastouchenko, 2001], the researchers correlated the extent of wake spreading behind a slat and the Strouhal number of an acoustic wave emanating from the slat. A comparison was made between their results and a comparable definition of Strouhal number in the current study. The power spectrum for the slat wake was obtained using the hot-film sensor at a free-stream velocity of 20 m/s at 0° angle of attack with no external excitation. The power spectrum is shown in Figure 5.50 where the Strouhal number was calculated using a reference length of 0.5 in, which was the gap between the slat and the main wing. The jet velocity was 30 m/s, which was greater than the free stream velocity due to the flow acceleration caused by the upper surface curvature of the main wing. The data in Figure 5.50 showed that a peak occurs around a Strouhal number of 0.3, which agreed well with the result from the previous study [Crow, S. C., and Champange, F. H., 1971]. This Strouhal number corresponded to a frequency of 685 Hz, which is also equal to the fundamental frequency of the model at this free stream velocity. As has already been stated, the model in this study performed favorably when the loudspeaker was tuned to 80 Hz, which is a third subharmonic of 640 Hz, the latter being significantly close to the fundamental frequency. These results suggested that external excitation induced vortex pairing in the slat wake was responsible for the more divergent slat wake that resulted in turbulent kinetic energy being transported to the main wing boundary layer. The kinetic energy added to the boundary layer decreased the surface static pressure, which translates into more aerodynamic lift. It is recalled from a previous section that when the piezoelectric devices were tuned at 320 Hz the lift coefficient on the main

wing was also elevated. This frequency also lies close to the first subharmonic of the fundamental frequency at an air speed of 20 m/s. Previous results using the piezoelectric devices corroborated the findings observed during the acoustical portion of the study.

The fact that needs to be emphasized is that a more divergent slat wake is not a sufficient condition for an increment in aerodynamic lift to occur. The process of vortex pairing is the key mechanism that is responsible for the added lift because it ensures that the embedded vortices are more coherent and two-dimensional. This, in turn, enhances the transportability of the turbulent kinetic energy.

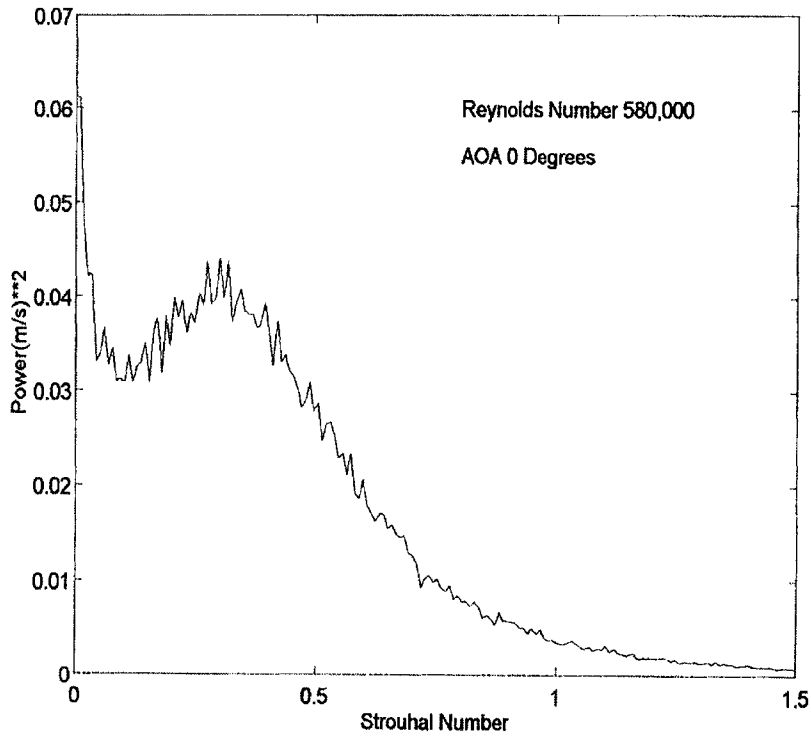

Figure 5.50 – Power Spectrum on Main Wing at 20 m/s at 0° AOA

In the case with the piezoelectric devices, the distribution of pressure coefficient gradient in the case of acoustic excitation was examined to determine the interplay between

the acoustic energy source and the dynamics of the shed vortices from the leading edge slat. The receptivity of the boundary layer to the acoustic source was greater in the case of the loudspeaker compared with the piezoelectric devices since the loudspeaker directly faced the upper surface of the main wing. This could account for the larger increment in lift coefficient.

The pressure gradient coefficient distributions for 0, 80 and 120 Hz are shown in Figure 5.51 The data clearly show that the wave-like distribution for the case of 80 Hz demonstrated a much larger amplitude than what was shown in either the baseline or 120 Hz cases. This suggests that the energy transferred to the boundary layer in the case of 80 Hz was markedly greater than in any other case. The vortex passing frequency was calculated as in the case of the piezoelectric devices. The peaks in the distribution for the case of 80 Hz occurred at normalized distances close to the distance measured in the case of the excitation by piezoelectric devices. The periodicity of the distribution shows significant amplitude, particularly at 80 Hz and is indicative of the effect of the vortex system on the upper surface of the main wing.

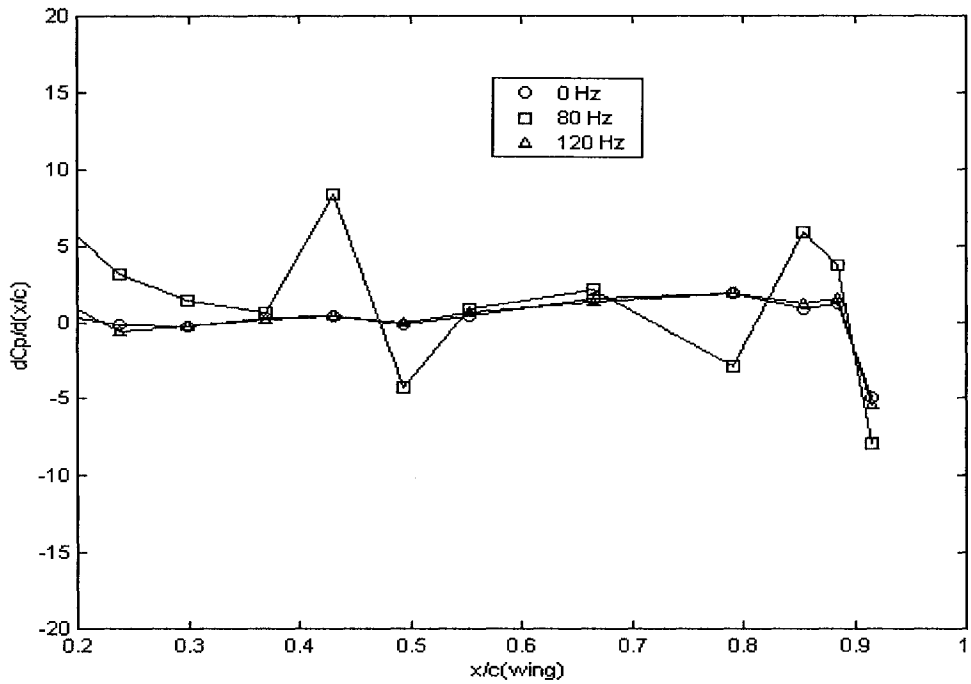

Figure 5.51 – Pressure Coefficient Gradient on Main Wing for Acoustic Excitation, V = 20 m/s, 15° AOA

The power spectrum was determined as previously explained for the piezoelectric devices and is shown in Figure 5.52. The data show that the flow field with the highest level of energy was for an acoustic excitation of 80 Hz, which corroborates the pressure coefficient distribution at this frequency showing a sizable increment in lift on the main wing. These results substantiate the premise that vortex pairing has occurred for this frequency. It is noted that no such increase in lift was observed for the piezoelectric excitation at this frequency. This was probably due to the fact that the loudspeaker was better able to affect the flow field since its output was more directly targeted at the upper surface of the main wing.

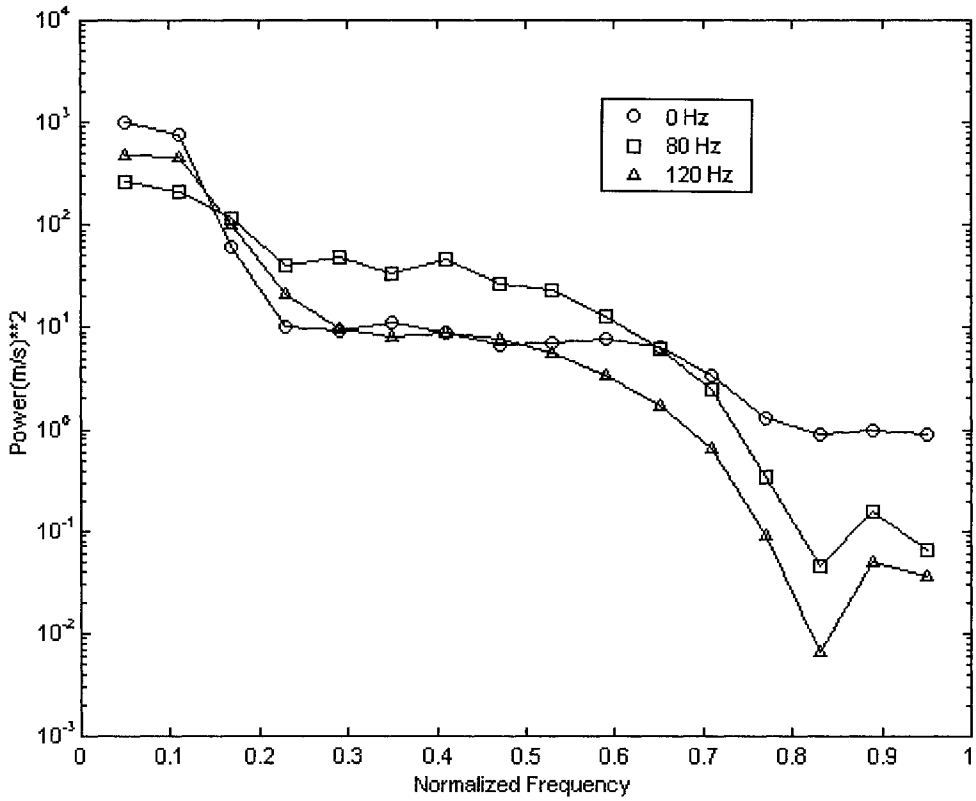

Figure 5.52 – Power Spectrum of Pressure Coefficient Gradient for Acoustic Excitation on Main Wing at V = 20 m/s, 15° AOA

5.10 Cross-Correlation Study

In this part of the study, data from two hot-film probes were analyzed to examine the cross-correlation of their simultaneous outputs for various probe separation distances. This was done to provide an indication of the dimensionality of the system of spanwise vortices. As the works of Oster and Wygnanski [1982], and Ho and Huang [1982] both suggest, a direct relationship exists between the degree to which the system of vortices is two-dimensional and the cross correlation between the two hot film measurements. Bhattacharjee et al.[1986], examined the zero-time delay cross correlation between pairs of sensors at varying spanwise separation distances. Their results showed that when external

forcing of the flow field occurred at a subharmonic of the fundamental frequency, the cross correlation showed a marked increase as compared with the natural case. This is considered a favorable result because a high correlation would imply the occurrence of substantial vortex pairing. This, in turn, promotes mixing of the viscous layer and the convection of higher energy air into the boundary layer with the attendant delay of boundary-layer separation. This phenomenon was expected to have the favorable consequence of increased lift.

Data were collected at test velocities, 10, 20 and 30 m/s and at 0°, 5° and 10° angles of attack. Two hot-wire sensors were used for this part of the study. Sensor number 1 was mounted to a special-made translatable sliding table that was capable of movement in one direction with a lead screw. This assembly was affixed to the traversing strut in the test section. The first probe was positioned on the centerline of the model. Sensor number 2 was mounted to the slide mechanism that was permanently attached to the strut that is normally used for making surveys. Sensor number 2 was locate off the centerline of the model and was remotely positioned at varying spanwise locations of 10, 15 and 20 cm from sensor number 1. Effort was made to ensure that both sensors were at the same longitudinal and lateral position in the test section coordinate system. The data showed that for no external excitation the cross-correlation was very small, which indicated that the system of vortices was not significantly correlated in the lateral direction. This result suggests that the system of vortices was not coherent and hence was three dimensional. The cross-correlation results are shown in figures 5.53 through 5.55. Appendix F.3 details the algorithm for computing the cross correlation coefficient.

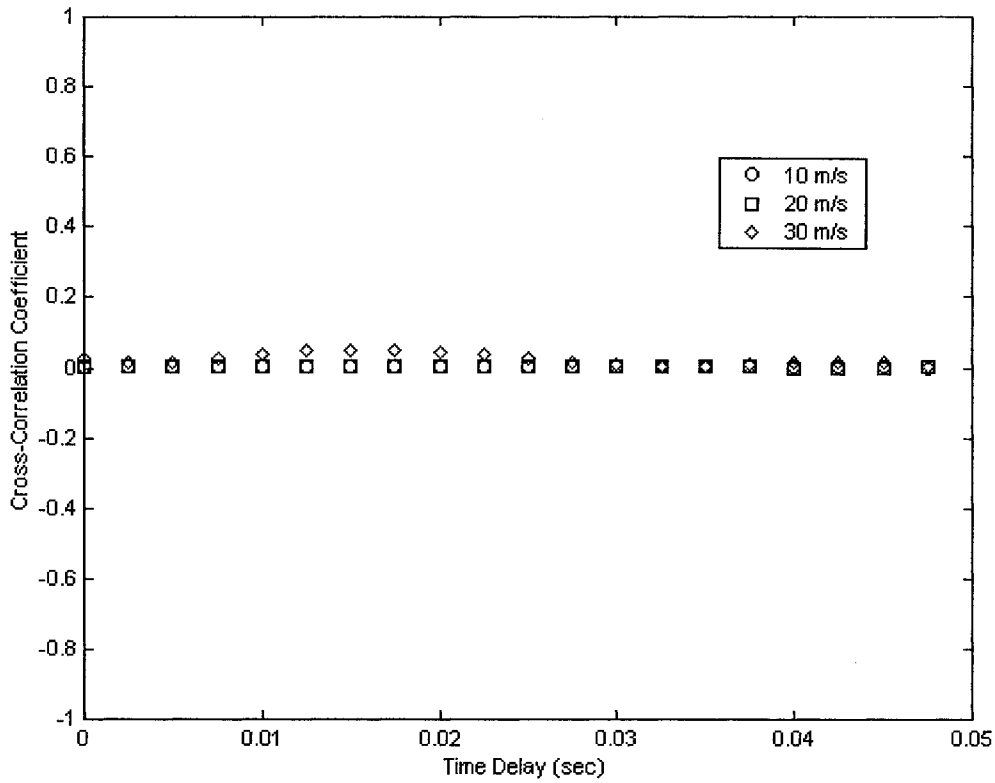

Figure 5.53 – Cross-correlation coefficient versus time delay for $\Delta Z = 10$ cm, 0° AOA

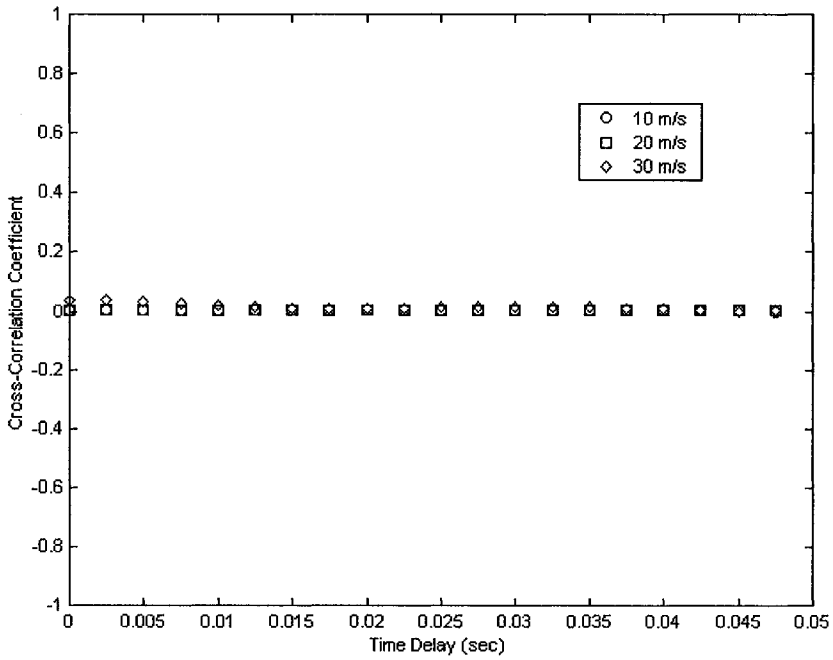

Figure 5.54 – Cross-correlation coefficient versus time delay for $\Delta Z = 15$ cm, 0° AOA

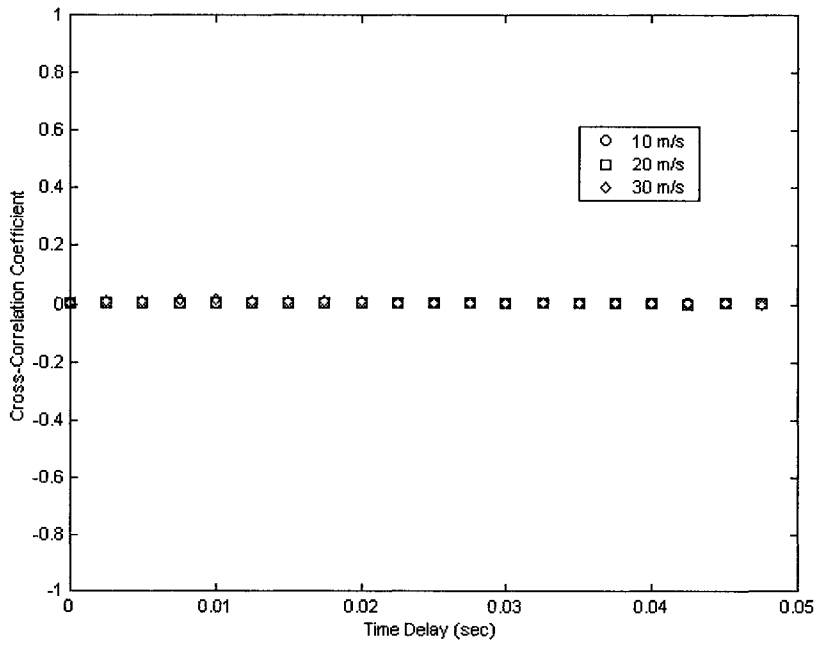

Figure 5.55 – Cross-correlation coefficient versus time delay for $\Delta Z = 20$ cm, 0° AOA

CHAPTER 6

DISCUSSION OF RESULTS

This dissertation has explored various facets of the flow characteristics about a multi-element airfoil and, most importantly, the implementation of two specific modes of excitation in an attempt to control aerodynamic performance of the airfoil. The study examined the application of viscid Linear Stability Analysis to the task of predicting the most dominant frequency in the region just aft of the leading-edge slat. Then, piezoelectric devices and a loudspeaker were used to modify the mean velocity profile and surface pressure distribution on a separated boundary layer existing on the trailing- edge flap.

When this experiment was first proposed, viscid Linear Stability Analysis was to be used to provide at least an estimate of the required operating frequency for the piezoelectric devices. Based on previous wind tunnel experiments, the system of vortices emanating from the slat could be affected by applying some type of external excitation to the vortices with the expectation that they would amalgamate, travel downstream, and transfer momentum to the flow field surrounding the trailing-edge flap. This added momentum would promote boundary-layer reattachment. An earlier wind tunnel study [Bhattacharjee, S. et al., 1986] showed that vortex amalgamation or vortex pairing, as it is sometimes called, could be induced by energizing the vortices using an external source whose frequency is a subharmonic of the vortex passage frequency. The motivation behind using linear stability analysis and smoke visualization was to determine the vortex passage frequency. The results showed that viscous Linear Stability Analysis could be used to provide reasonably good predictions of the most dominant frequency in the flow field.

The foremost objective of this experiment, however, was to find a suitable technique that could be used practically to excite the surrounding flow field in an attempt to modify the aerodynamic characteristics of an airfoil. The two modes of excitation were piezoelectric devices and a loudspeaker. The piezoelectric devices were installed on the model at various locations on the model. Initially, they were placed in the cove region of the slat to excite the vortices originating there. At the beginning stages of the study, the surface pressure distribution on the flap was used exclusively to evaluate the effectiveness of a particular device location. Because reattachment of a separated boundary layer could not be achieved using the original configuration, the devices were relocated. The devices were ultimately placed on the lower surface of the main wing near the aft-facing step just upstream of the rear cove region. The energized air surrounding the devices would then be entrained into the exiting flow, thereby transporting turbulent kinetic energy to the flap. Hopefully, modifications in the flow field could be induced so that a favorable pressure distribution could be developed on the flap, which would inhibit boundary-layer separation. Examination of such quantities as mean velocity, turbulence intensity profiles, and the momentum thickness determined the effect of forcing on the flow field. The following sections summarize the significant results of the various measurements obtained in this experiment, the relevance of the results to high-lift research, and recommendations for future work.

The following section presents a description of what the author feels are some of the more prominent results, which have relevancy to high-lift aerodynamics. Lastly, the author lists some of the experiments that are recommendable for future work in this area of research.

6.1 Summary of Significant Results

The mean velocity profiles at the trailing-edge flap were obtained to determine the effectiveness of the piezoelectric devices and the loudspeaker with regard to altering the aerodynamic characteristics of the flap. The initial attitude of the model was at 19° angle of attack at a free stream velocity of 20 m/s. The data showed that the mean velocity profile on the flap was significantly increased when the piezoelectric devices were operated at 100 Hz. For frequencies of 80 and 90 Hz, the mean velocity did not seem to be affected by the oscillating piezoelectric devices. At an operating frequency of 120 Hz, a smaller increase in the mean velocity profile resulted. The ultimate objective was to moderate the surface pressure distribution on a separated flap. However, notwithstanding the changes caused by the oscillating devices at 100 Hz, no great changes in the surface pressure distribution were noted. However, on the trailing-edge flap there was observed a small, although noticeable change in the surface static pressure distribution. This result lends credence to the speculation that piezoelectric devices offer some potential to favorably affecting the region of pressure recovery on the flap. In spite of this result, the boundary layer on the flap was never switched from a separated state to an attached state. The reason for this can be deduced from observation of the mean velocity profile at 100 Hz. Although a significant increment in mean velocity was achieved, note that this increment occurs generally off the body surface. If the increment in velocity could have occurred closer to the wall then the surface pressure distribution might have been altered to be more favorable to reattachment. Perhaps design changes or configuration changes could have caused the air discharged through the slot of the flap to flow deeper within the boundary layer.

The momentum thickness was also used to evaluate the effectiveness of the piezoelectric devices with regard to altering the mean velocity profile on the flap. Greater values of momentum thickness are associated with velocity deficits. Accordingly, the momentum thickness should decrease as the velocity deficit is diminished. This is exactly what the data show for the case of the piezoelectric devices operating at 100 and 120 Hz. The momentum thickness for these two frequencies was less than for the case of no external excitation. This really does not provide any more information than what the velocity profiles already provide, but it merely permits another interpretation of the observed trend using a well-known boundary-layer parameter.

The velocity profile on the trailing edge flap was made smoother by calculating a fourth order polynomial fit. This allowed the observer to see the trends more clearly without the obfuscation of data containing significant profile irregularity. The interpolated profiles exhibited the classical S shape associated with either reverse flow or wake interference. Regardless of the cause, it is desirable to have a velocity profile that is fuller. The results show that the profiles demonstrated either less reverse flow or wake interaction when the piezoelectric devices were operated at 100 Hz.

As another test of the effectiveness of the piezoelectric devices, the skin friction was computed for the selected operating frequencies. The results corroborated what was found earlier. The calculated skin friction was the lowest when the piezoelectric devices were operated at 100Hz. The results suggest that at this particular frequency, the flow in the boundary layer is being led to the state that most closely approaches that of incipient separation.

For the case of the loudspeaker, the operating frequencies were restricted to 80 and 120 Hz. The velocity profiles were obtained and the results reveal that there were no significant increments in mean velocity at either frequency. This is rather inconclusive and if more time had been available, profiles could have been obtained at a greater number of audio frequencies.

Another quantity that reveals insight into the physics flow is the turbulence intensity. One important task was to ascertain if any observed increase in turbulence intensity in the flow field could be sensitive to the actuation frequency. In one wind tunnel experiment [Oster, D. and Wygnanski, I., 1982] turbulence intensities were measured in the wake of a splitter plate that was located in the contraction region. The splitter plate separated two flows of dissimilar velocities. Attached to the trailing edge of the plate was a pivoted flap that was capable of being oscillated when driven by a current set at different operating frequencies. Their experimental results showed that the turbulence intensity did not increase except for the case when the operating frequency was set at 60 Hz. In this experiment, the turbulence intensity showed the largest increment when the operating frequency of the piezoelectric devices was 100 Hz. This result supports the conclusion from the earlier test, which was that the largest increment in mean velocity occurred at 100 Hz. The fluctuating velocities that comprise both the turbulence intensity as well as the Reynolds stresses are oftentimes modeled as being directly proportional to the gradient of the mean stream-wise velocity. Therefore, high values of the fluctuating stream-wise velocity are associated with steep gradients, which is tantamount to large diffusion effects, and the latter fact is mainly responsible for the increments in mean velocity. As mentioned previously, in principle, these piezoelectric devices can be used to diffuse momentum to the

model surface, which can serve to mollify the adverse pressure gradient in the case of boundary-layer separation.

The rate of change of turbulent kinetic energy in a viscous region can be aptly described by Equation 6.1.

$$\frac{\partial KE}{\partial t} = \int_0^{\delta} -\rho \overline{u'v'} \frac{\partial u}{\partial y} dy - \mu \int_0^{\delta} \left(\frac{\partial u'}{\partial y} - \frac{\partial v'}{\partial x}\right)^2 dy \qquad (6.1)$$

The first term on the right-hand side is the production term, and because it generally has a positive value, both factors of the first integral are usually positive. That is, as shown in Equation 6.2:

$$-\rho \overline{u'v'} > 0 \qquad \frac{\partial u}{\partial y} > 0 \qquad (6.2)$$

The left-most term is the Reynolds stress and the right-most term is the mean velocity distribution. Although the above inequalities are most often found to be true, numerous experimental studies[Hinze, J. O., 1970], [Margolis, S., 1963], indicate that there are isolated instances in which these two terms have opposite signs. This would suggest that the eddy viscosity is negative which would be a violation of Boussinesq's model for turbulent shear stress. The second term on the right-hand side of that same Equation 6.1 is the contribution from the dissipation of energy and, as is expected, is always negative and essentially measures the local vorticity in the flow. The net rate of turbulent kinetic energy depends on whichever of these two terms dominates. The data in the case of the piezoelectric devices at operating frequencies of 100 Hz and 120 Hz showed that both the streamwise turbulence intensity, and accordingly the Reynolds stress and the mean velocity

profile increased when compared with the baseline measurements at 0 Hz. This would suggest that the production component of the rate of turbulent kinetic energy increased for both of these reasons. As the rate of kinetic energy increases, some means will have to be taken to ensure the transport of this added kinetic energy down to the boundary layer to hinder its separation.

As in the case when the loudspeaker was used, the turbulence intensity showed an increment mainly in the far field away from the model surface for both operating frequencies of 80 and 120 Hz. The turbulence intensity profiles for the case of the loudspeaker was not as uniformly displaced from the profile at 0 Hz as was demonstrated with the piezoelectric devices. For a certain range of normalized distances from the model, the turbulence intensity was lower at either 80 or 120 Hz when compared with the case for no forcing. At higher distances the trend was reversed. This was not what was observed for the piezoelectric devices at 100 and 120 Hz. In those cases the turbulence intensity was larger throughout the region of confluence.

The ultimate test for the effectiveness of either of these techniques is the static pressure distribution, which occurs on the trailing edge flap as a result of the external excitation. The data showed that small favorable changes in the pressure distribution were brought about when the piezoelectric devices were operating at frequencies of 100 and 120 Hz. At these two frequencies the pressure plateau indicated a slight but noticeable shift in the positive direction, almost as a prelude to a pressure recovery. The latter would have been indicative of boundary-layer reattachment. This result corroborates the demonstrated trend of a fuller mean velocity profile and larger turbulence intensity values that occurred at these two frequencies. When boundary-layer separation occurred at the specific flow

conditions and model attitude, the pressure distribution exhibited the characteristic flat contour at a high negative pressure coefficient. Although the static pressure on the upper surface is negative, which might appear to be a favorable effect, the fact that the boundary layer has separated means that the streamline flow is being deflected from the surface thereby causing a downward reaction force on the flap. This decambering of the flap results in an overall reduction in aerodynamic lift. Although boundary-layer reattachment did not take place, at least the data showed that the piezoelectric devices precipitated changes in the flow field that demonstrated a favorable trend.

Although the major focus was on removing the boundary-layer separation that formed on the trailing-edge flap, a more global inspection of the pressure distributions on the component surfaces revealed that more leading edge suction occurred on the main wing when the devices operated at 100 Hz. The lift increment compared with the baseline configuration was nearly 5.5%

Global examination was also done for the case of the loudspeaker. The data showed the remarkable result that on the main wing there was induced a large increase in suction that resulted in a nearly 30% increase in total lift. Although there were certainly no marked changes on the flap to reverse the effects of boundary-layer separation, there were very positive changes that were induced on the main wing.

The most significant result in this study using the piezoelectric devices was for an excitation frequency of 320 Hz. The free-stream velocity was 20 m/s at 15° angle of attack. The pressure distribution on the rear portion of the main wing exhibited a greater suction than what was shown for the baseline frequency of 0 Hz. This contributed to a 10% increment in lift coefficient on the main wing. The distribution of pressure coefficient

gradient was plotted and revealed a periodicity that correlated with the system of shed vortices originating from the trailing edge of the slat. The devices were tuned at a frequency, which precipitated vortex pairing and the transport of turbulent kinetic energy from the shear layer into the boundary layer. The added energy was enough to increase the velocity near the surface of the model to lower the static pressure. This phenomenon also had a favorable effect on the trailing edge flap as demonstrated by the fact that the boundary layer switched from being separated to being attached.

A greater aerodynamic lift was achieved by exciting the flow field of the model with an acoustic energy source at 80 Hz. The pressure distribution on the main wing showed a characteristic plateau, which was indicative of the interaction between the slat wake and the main wing boundary layer. Distributions of pressure coefficient gradient were also plotted and as was shown with the piezoelectric devices exhibited a periodic or wave-like profile. The amplitude of the wave in the distribution was significantly increased at 80 Hz. This was indicative of the interplay between the shed vortices and the main wing boundary layer.

6.2 Relevance to High-Lift Research

The results documented in this dissertation, along with other experiments involving piezoelectric devices [Seifert, A., 1998] demonstrate conclusively that such devices in principle can be used to provide favorable aerodynamic characteristics to lifting bodies. If this technology were implemented into the design of future aircraft, it would probably serve more as an auxiliary system to fine tune the lift primarily provided by more traditional devices such as elevons and flaps. Furthermore, such devices could also be used to augment the stability and control of aircraft. For example, it might be possible to use

piezoelectric devices to make minor yet crucial adjustments to the various stability derivatives associated with aircraft.

This experiment focused on the lift of an airfoil, but if boundary-layer separation can be reduced, then there could be the added advantage of also decreasing the pressure drag. Besides lifting surfaces, avoidance of boundary-layer separation is desirable on any protuberance such as a cockpit canopy or a stores cavity, both of which are examples that provide sources of drag. Aircraft would not be the only system that could benefit from this technology. Land-based vehicles such as cars, trucks, and trains could possibly derive a benefit in the form of reduced pressure drag. However, unlike this study, designs incorporating the use of such devices necessitate that practical modifications be performed to minimize skin friction and form drag, wherever possible. Emphasis must be placed on making these devices conformable to whatever hardware they are to be attached.
One very important contribution that piezoelectric devices would provide is the augmentation of lift without intolerable mechanical complexity. The current trend is to reduce the number of wing elements and therefore, lift-augmentation devices could be especially beneficial because they would offer even greater simplicity.

With few mechanical parts, they can be made reliable and relatively inexpensive to service. Another factor is that they are lightweight. Even if such devices were manufactured to be large enough for full-scale aircraft, their weight would still be miniscule in comparison with the total weight including fuel. Thus, what they add to the weight of the aircraft would certainly be nullified by the advantages they provide in terms of lift increment and possibly diminished drag.

After having extolled the potential benefits of using such devices, their advantages must be tempered by some possible or inevitable drawbacks.Two of these that have already been mentioned, include increments in drag and weight. Another possible drawback could be their expense. To be fitted for a full-scale aircraft, either an array of many rather small devices or a relatively few number of fairly large devices must be employed. The cost associated with the manufacturing of such large devices as well as the effect that their inertia would have on their ultimate performance have yet to be determined. Another concern is the expense in terms of the electrical power that would be consumed and any possible complexities associated with incorporating them into the existing electrical system. Moreover, what are the safeguards that must be implemented to ensure their ruggedness and resistance to mechanical fatigue due to constant cycling? These are just some of the questions that must be addressed in order to render this technology both efficient and practical.

6.3 Recommendations for Future Work

The wind tunnel experiment as reported in this dissertation, along with the attendant results, hopefully add to the database concerning the characteristics of this particular model as well as provide some insight, albeit minimal to the general research topic of high-lift aerodynamics. However, because of the inevitable time restraints and some technical challenges too, more questions persist and which if answered could have provided a wealth of information concerning high-lift issues, both quantitative and qualitative. The following discussion will attempt to outline those action items that await future inquiry.

The data clearly show that piezoelectric devices show promise as a technique for augmenting aerodynamic lift. Although the placement of the devices on the model used in

this experiment was decidedly advantageous, a parametric study needs to be done to determine the optimal location for installation of these devices. One candidate location could be nearer the leading edge of the main wing. Originally, this was planned, but was abandoned because, at the time, no aerodynamic benefit was immediately realized. Yet, this particular placement is credible since the source of the excitation would be closer to the energy-rich vortices being shed from the slat. Another possible location could be on the lower surface of the trailing-edge flap. Many combinations of operating frequencies and placements of these devices could be tested to find the best configuration to achieve the highest possible lift. Moreover, different types of piezoelectric devices could be tried, for example, ones capable of attaining a larger amplitude.

The research tool that would have been very beneficial in providing a great deal of qualitative information is the Particle Image Velocimeter (PIV) System that was purchased from TSI® by Old Dominion University towards the end of the data acquisition phase of this research investigation. Specifically, imaging needs to be captured of the flow on the lower surface of the model in the rear cove region just upstream of the slot between the main wing and the trailing-edge flap. This would have provided needed qualitative data to investigate the changes in the flow field of this region that were precipitated by the oscillating devices. The PIV system could have possibly revealed the presence of distinct device-generated structures in the flow that interacted with the model geometry and naturally occurring streamlines to bring about the results as reported. Certainly, imaging needs to be performed as well on the model upper surface in the rear slotted region to visualize changes in the flow pattern as a function of excitation frequency. This information would have provided more readily available insight into ways to optimize the

favorable effects of the piezoelectric devices. For example, once a more visual understanding is obtained of the actual dynamic mechanisms responsible for the observed increments in the mean velocity profile, appropriate adjustments can be made such as proper placement of the devices and the determination of their optimal operating frequency.

Another unanswered question was the extent to which the leading-edge slat had an influence on the dynamics of the flow field in the vicinity of the trailing-edge flap. Smoke visualization data did reveal the presence of a system of vortices that was generated by the slat, but just what is its effect on the global aerodynamic characteristics? One of the original attempts at finding a useful placement of the devices was to install them on the windward side near the leading-edge slot. This was abandoned in favor of the final placement that was adopted. The reason for this was because, at the time this configuration was tried, the pressure distribution on the flap did not change from a separated state to an attached state. So this configuration lacked prospects for future consideration. In hindsight, acquisition of velocity profiles on the flap would have been beneficial as was done for the final configuration. Furthermore, it would be instructive to retry this arrangement with a PIV system to confirm the theory that the oscillating devices favorably affected the behavior of the leading-edge system of vortices. Could these devices be used to control the extent of the vortex interaction on the trailing-edge flap? Could this interaction have been used to cause beneficial effects on the separated trailing- edge flap?

Data needs to be obtained for a more extensive range of free-stream velocities and model angles of attack. Although the reported results provide some clues into how these devices can benefit high-lift research, this really only skims the surface of their potential usefulness for a range of flow conditions and model geometry. The rigging of the slat and

flap need to be changed to determine the effect that model geometry has on the effectiveness of these devices.

Although it would have meant altering the geometry of the model, a machined cavity in the surface of the model to flush mount the piezoelectric devices would have been beneficial. This would have minimized any undesirable interference effects from the presence of the devices themselves. Such a cavity could be made on either the lower or upper surface of the model. A plausible location at which to place the cavity would be either at the trailing edge of the main wing or on the leading edge of the flap itself. Either option would ensure that the influence of the devices would have their greatest impact on the boundary layer of the flap because of their close proximity to the flap.

The data show that the excitation due to the loudspeaker had an apparently adverse effect on the mean velocity profile of the trailing-edge flap, at least for the two frequencies selected. More audio frequencies need to be tested and the loudspeaker should to be placed at different locations relative to the flap. The reported results could have been influenced by the fact that the loudspeaker may not have been at the location in the wind tunnel to ensure maximum receptivity of acoustical energy at the flap. Further testing could possibly reveal if the dynamics of the acoustical effect are inherently different from the mechanical effects of the piezoelectric devices. Again, the PIV system would have been instrumental in making that determination.

More candidate devices need to be tested to add to the understanding of how flow fields can be controlled to reduce boundary-layer separation. One other candidate device is the vortex generator. It would be instructive to use flow visualization or imaging of the flow field when these devices are placed at various locations on the model.

CHAPTER 7

CONCLUSIONS

A 2D multi-element airfoil was tested in the Low-Speed Wind Tunnel at Old Dominion University. The objective of the experiment was to determine if piezoelectric devices or a loudspeaker could be used to favorably alter the flow field surrounding the airfoil. The intent was to produce a favorable pressure distribution on the main wing and trailing-edge flap to mitigate boundary-layer separation. The achievement of this objective would ultimately lead to the attainment of increased aerodynamic lift.

The approach adopted in this experiment was to use the naturally occurring vortices on the airfoil itself to transfer momentum and kinetic energy to the boundary layer. In this way the air flowing in the boundary layer would be energized enough to overcome separation, resulting in improved lift. It was surmised that the phenomenon of vortex pairing was the primary mechanism responsible for the transport of energy into the boundary layer and is characterized by the generation of a system of coherent vortices. Vortex pairing was facilitated by externally exciting the flow field at a specific frequency, which was correlated with the frequency of vortices being shed from the trailing edge of the leading edge slat. The vortex-passing frequency was determined using a hot-film sensor placed in the wake of the slat to obtain the power density spectrum of the flow. The vortex-passing frequency corresponded to the rounded peak in the spectrum. However, vortex pairing occurred when the excitation frequency was tuned at a subharmonic of the vortex-passing frequency.

The best results were for a model angle of attack was 15° at a free-stream velocity of 20 m/s. Based on the hot-film sensor data as shown in Figure 5.9 the rounded peak

occurred near a Strouhal number of 15, which corresponded to a vortex-passing frequency of 656 Hz. One of the more remarkable results from this study was the fact that the lift coefficient on the main wing increased by 10% when the model was instrumented with the piezoelectric devices tuned at 320 Hz, which was approximately the first subharmonic.

Plots were produced of the pressure coefficient distribution, which showed a marked amount of suction near the trailing edge of the main wing. Plots were also made of the pressure gradient coefficient distribution on the main wing for the selected operating frequencies of the devices. The results showed that the pressure gradient distribution demonstrated a wavelike characteristic, which was caused by the periodic interaction of the coherent system of vortices with the boundary layer on the main wing. Since this phenomenon did not occur for the other frequencies, it is reasonable to assume that the amplitude of the vortices with their attendant increment in lift is sensitive to specific operating frequencies. It is hypothesized that at a frequency of 320 Hz, the spreading rate of the vortices grows to such extent that their outer regions of circulation come in contact with the upper surface of the wing and transport energy to the boundary layer. Earlier studies [Oster, D. and Wygnanski, I, 1982] have demonstrated how vortices grow when subjected to external forcing at subharmonics of the fundamental frequency.

The most significant impact of the acoustic excitation was the fact that on the main wing, the surface distribution manifested a tremendous increase in suction. When the total lift was computed on the main wing alone, an increase of roughly 30 % was realized.

The pressure coefficient gradient distribution at 80 Hz was plotted and showed a wavelike characteristic that was similar to the same type of distribution when the model was instrumented with the piezoelectric devices operating at 320 Hz. The pressure

coefficient distribution for the case when the loudspeaker was tuned at 80 Hz demonstrated a leveling off near the near wake of the slat, which is indicative of a forward shift in the impingement of the slat wake onto the main wing boundary layer. It is theorized that the acoustic source at 80 Hz is responsible for the spreading of the slat wake and the forward shift of the impingement point. It should be noted that 80 Hz approximates the third subharmonic of the fundamental frequency that was found experimentally to be 656 Hz. Earlier studies [Chih-Ming, H. and Huang, L., 1982] demonstrated that vortex pairing can occur several harmonics away from the natural frequency. The vortices embedded in the slat wake can then move closer to the upper surface of the wing to more effectively interact with the boundary layer. Again, the principle is the same as with the piezoelectric devices. The excitation causes the system of vortices to interact more closely to the main wing boundary layer, resulting in an increase of kinetic energy being fed into the boundary layer. This phenomenon manifests itself in an observed increase in suction on the main wing upper surface.

REFERENCES

Ahuja, K. K., "Acoustic Control of Separation," Bulletin of the American Physical Society, Vol. 28, 1983, p 1388

Bario, F., Charnay, G. and Papailiou, K. D.; "An Experiment Concerning the Confluence of a Wake and a Boundary Layer" Transactions of the ASME, Vol. 104, March 1982

Bhattacharjee, S., Scheelke, B., Troutt, T. R.; "Modification of Vortex Interactions in a Reattaching Separated Flow," AIAA Journal, Vol. 24, No. 4, April 1986

Bourassa, Corey, Thomas, Flint and Nelson, Robert C.; "Experimental Investigation of Turbulent Boundary Layer Relaminarization with Application to High-Lift Systems: Preliminary Results," AIAA Paper 2000-4017, 2000

Braden, J. A., Whipley, R. R., Jones, G. S., and Lilley, D. E., "Experimental Study of the Separating Confluent Boundary Layer," AIAA Paper 86-0505, Jan. 1986

Browand, F. K. and Troutt, T. R., "A Note on Spanwise Structure in the Two-Dimensional Mixing Layer," Journal of Fluid Mechanics, Vol. 97, April 1980, pp. 771-816

Brown, G. L., and Roshko, A., "On Density Effects and Large Structure in Turbulent Mixing Layers," Journal of Fluid Mechanics, Vol. 64, No. 4, July 1974, pp. 775-816

Champagne, F. H, Pao, Y.H., Wygnanski, I. J., "On the Two-Dimensional Mixing Region", Journal of Fluid Mechanics, Vol. 74, 1976, pp. 209-250

Chin, V. D., Peters, D. W., Spaid, F. W., and McGhee, R. J., "Flowfield Measurements about a Multi-Element Airfoil at High Reynolds Number", AIAA Paper, AIAA-93-3137, AIAA 24th Fluid Dynamics Conference, July 6-9, 1993, Orlando, FL

Cho, S. K., You, J. Y. and Choi, H., "Vortex Pairing in an Axisymmetric Jet Using Two-Dimensional Acoustic Forcing at Low to Moderate Strouhal Numbers," Experiments in Fluids, Vol. 25, 1998

Coles, D. E., and Hirst, E. A., "Computation of Turbulent Boundary Layers – 1968 AFOSR-IFP Stanford Conference," Proc. 1968 Conf., Vol. 2, Stanford University, Stanford California

Crow, S. C. and Champagne, F. H., "Orderly Structures in Jet Turbulence," Journal of Fluid Mechanics, 1971, Vol. 48

Currie, I. G.; Fundamental Mechanics of Fluids, McGraw-Hill Book Company, 1974
Drela, M., "Design and Optimization Method for Multi-Element Airfoils," AIAA Paper 93-0969, Feb. 1993

Dovgal, A. V., Kozlov, V. V., and Simonov, O. A., "Experiments on Hydrodynamic Instability of Boundary Layers with Separation", IUTAM Synposium, London, England 1986

Fausett, Laurene V., "Applied Numerical Analysis Using MATLAB®," Printice Hall, Upper Saddle River, NJ, 1999

Fowler, H. D., "Variable Lift," Western Flying, Nov. 1931, p. 31

Gad-el-Hak, M., and Bushnell, D. M., "Separation Control: Review," Journal of Fluids Engineering, Vol. 113, March 1991

Gailitis, A. and Lielausis, O., "On a Possibility to Reduce Hydrodynmical Resistance of a Plate in an Electrolyte in Applied Magnetohydrodynamics" Reports of the Physics Institute, Vol. 12, 1961

Goldstein, R. J, "Fluid Mechanics Measurements", Hemisphere Publishing Corporation, 1983

Harris, R.G. and Bradfield, F. B., "Model Experiments with Variable Camber Wings," R&M No. 677, June 1920, Aeronautical Research Council, London

Hilderbrand, F. B.; Introduction to Numerical Analysis, McGraw-Hill, Inc. 1974

Hinze, J. O.; Turbulence, An Introduction to Its Mechanism and Theory, McGraw-Hill Book Company, 1959

Ho, Chih-Ming and Huerre, Patrick; "Perturbed Free Shear Layers", Annual Review of Fluid Mechanics, Vol. 16, 1984

Ho, C-M and Huang, L. S.; "Subharmonic and Vortex Merging in Mixing Layers," Journal of Fluid Mechanics, Vol. 119, 1982, pp. 443-473

Hoerner, S. F., "Fluid Dynamic Lift," 2nd Ed., Hoerner Fluid Dynamics, Vancouver, WA, 1985

Hwang, K. S., Sung, H. J. and Hyun, J. M., "AnExperimental Study of Large Scale Vortices over a Blunt-Faced Flat Plate in Pulsating Flow," Experiments in Fluids, Vol. 30, 2001

Jasper, D., Agrawal, S., and Robinson, B. A., Navier-Stokes Calculations on Multi-Element Airfoils Using a Chimera Based Solver,"High-Lift Systems Aerodynamics, AGARD CP-515, Sept. 1993, Paper No. 8

Johnson, L. J. and Stolcis, L., "Prediction of the High-Lift Performance of Multi-Element Aerofoils Using an Unstructured Navier-Stokes Solver," High-Lift System Aerodynamics, AGARD CP-515, Sept. 1993, Paper No. 13

Johnston, J. P., "Pitched and Skewed Vortex Generator Jets for Control of Turbulent Boundary Layer Separation: a Review," 3rd ASME/JSME Joint Fluids Engineering Conference and FED Summer Meeting/Exhibition, San Francisco, July 18-22, 1999

Jones, K. M., Biedron, R. T., and Whitlock, M., "Application of a Navier-Stokes Solver to the Analysis of Multielement Airfoils and Wings Using Multizonal Grid Techniques," AIAA Paper, 95-1855, June 1995.

Kays, W.M. and Crawford, M. E.; "Convective Heat and Mass Transfer", McGraw-Hill Publishing Company, 1980

Kermode, A. C.; Mechanics of Flight, Longman Group Limited, 1996

Klausmeyer, Steven M., Papadakis, Michael and Lin, John; "A Flow Physics Study of Vortex Generators on a Multi-Element Airfoil", AIAA Paper 96-0548, 34th Aerospace Sciences Meeting and Exhibit, January 15-18, 1996

Klausmeyer, S. M. and Lin, J. C., "Comparative Results from a CFD Challenge over a 2D Three-Element High-Lift Airfoil, NASA TM 112858, May 1997

Kline, S. J. and McClintock, F. A.; "Describing Uncertainties in Single Sample Experiments", Mechanical Engineering, Vol. 75, 1953

Kourounis, Antonis E., Papailiou, Demosthenes D., and Koutmos, Panagiotis; "Turbulent Boundary Layer-Wake Interaction Study", Progress in Astronautics and Aeronautics, Vol. 182, American Institute of Aeronautics and Astronautics, Inc. 1998

Lachmann, G. V., "Boundary layer and Flow Control; Its Principles and Application," Vol. I, Pergamon Press, 1961

Landman, D., "Experimental Geometry Optimization Techniques for Multi-element Airfoils," Ph.D Dissertation Old Dominion University,1998

Long, P. Yip, Paul, M. H., Van Dams, C. P., "In-Flight Measurements on a Subsonic Transport High-Lift Wing Section", Journal of Aircraft, Vol. 32, No. 3, May-June 1995

Mack, M. D., and McMasters, J. H.;"High Reynolds Number Testing in Support of Transport Airplane Development", AIAA Paper 92-3982, 1992

Malik, M. R.,Chuang, S. and Hussaini, M. Y.; "Accurate Numerical Solution of Compressible, Linear Stability Equations", Journal of Applied Mathematics and Physics, Vol. 33, No. 2, March 1982
Margolis, S., "An Investigation of a Curved Mixing Layer, report 3227-E, Dept. of Mechanical Engineering, Pennsylvania State University, University Park, 1993

Maskew, B., "Program VSAERO. A Computer Program for Calculating the Non-Linear Characteristics of Arbitrary Bodies," NASA CR-166476, 1982

McGinley, C. B., Anders, J. B., and Spaid, F. W.; "Measurements of Reynolds Stress Profiles on a High-Lift Airfoil", AIAA Paper 98-2620, 1998

McLean,J.D.,Crouch, J. D., Stoner, R. C., Sakurai, S., Seidel, G. E., Feifel, W. M., and Rush, H. M.; Study of the Application of Separation Control by Unsteady Excitation to Civil Transport Aircraft, NASA/CR – 1999-209338, June 1999

Mossi, K. M. and Bishop, R. P., "Characterization of Different Types of High Performance THUNDER™ Actuators," FACE International Corporation, Norfolk, VA

Nakayama, A., Kreplin, H. P., and Morgan, H. L.; "Experimental Investigation of Flowfield About a Multielement Airfoil", AIAA Journal, Vol. 28, No. 1, 1990

Nosenchuck, D. M., Brown, G. L., Culver, H. C., Eng, T. I. and Huang, I. S., "Spatial and Temporal Characteristics of Boundary Layers Controlled with the Lorentz Force," Proceedings of the Twelfth Australasian Fluid Mechanics Conference, Vol. 1, Dec. 1995

Oster, D. and Wygnanski, I., "The Forced Mixing Layer Between Parallel Streams," Journal of Fluid Mechanics, Vol. 123, 1982, pp. 91-130

Page, F. H., "The Handly Page Wing," The Aeronautical Journal, June 1921, p. 263

Paschal, K. Jenkins, L. and Yao, C.; "Unsteady Slat-Wake Characteristics of a High-Lift Configuration," AIAA Paper No. 2000-0139, 38th Aerospace Sciences Meeting & Exhibit, January 10-13, 2000/ Reno, NV

Paschereit, C. O., Wygnanski, I. and Fiedler, H., "Experimental Investigation of Subharmonic Resonance in an Axisymmetric Jet," Journal of Fluid Mechanics, Vol. 283, 1995

Petrov, A. V., "Certain Types of Separated Flow over Slotted Wings," Fluid Mechanics-Soviet Research, Vol. 7. No. 5, 1978, pp 80-89

Prandtl, L., "Über Flüssigkeitsbeweung bei sehr kleiner Reibung," III International Mathematiker-Kongress, Heidelberg, 1904

Roth, J. R., Sherman, D. M. and Wilkerson, S. P., "Boundary Layer Flow Control With A One Atmosphere Uniform Glow Discharge Surface Plasma," 36th Aerospace Sciences Meeting and Exhibit, Jan. 12-15, 1998, Reno NV

Schlichting, Hermann, Boundary-Layer Theory, McGraw-Hill, New York, 1955

Schubauer, G. B. and Skramstad, H. K., "Laminar Boundary-Layer Oscillations and Transition on a Flat Plate", Journal of the Research of The National Bureau of Standards, Research Paper RP1722, Vol. 38, February 1947

Seifert, A., Darabi, A., and Wygnanski, I., "Delay of Airfoil Stall by Periodic
Excitation," Journal of Aircraft, Vol. 33, No. 4, 1996, pp. 691-699

Seifert, A., Eliahu, S., Greenblatt, D. and Wygnanski, "Use of Piezoelectric Actuators for Airfoil Separation Control," AIAA Journal, Vol. 36, August 1998

Shevell, R. S.; Fundamentals of Flight", Prentice-Hall, Englewood Cliffs, California, 1983

Shuster, D. M. and Birckelbaw, L. D., "Numerical Computations of Viscous Flow Fields About Multi- Component Airfoils," AIAA Paper 85-0167, Jan. 1985

Smith, A.M.O., "High-Lift Aerodynamics," Journal of Aircraft, Vol. 12. No. 6, June 1975, p. 501

Smith, F. T. and Brown, S. N.; Boundary-Layer Separation,Proceedings of the IUTAM Symposium London, August 26-28, 1986, Springer-Verlag, Heidelberg, 1987

Spaid, F. W., and Lynch, F. T., "High Reynolds Number, Multi-Element Airfoil Flowfield Measurements", AIAA Paper, AIAA 96-0682, 34th Aerospace Sciences Meeting and Exhibit, January 15-18, 1996, Reno NV

Strange, P. J. and Crighton, D. G., "Spinning Modes and Axisymmetric Jets. Part 1." Journal of Fluid Mechanics, 1983, Vol. 134

Talay, Theodore; Introduction to the Aerodynamics of Flight, NASA SP-367, 1975

Tam, C. K. W. and Pastouchenko, N., "Gap Tones," AIAA Journal, Vol. 39, No. 8, August 2001

Taneda, S., "Oscillation of the Wake behind a Flat Plate parallel to the Flow," Journal of the Physical Society of Japan, Vol.13, No. 4, April, 1958

Thomas, F. O., Nelson, R. C., and Liu, X.; "An Experimental Investigation of the Unsteady Effects in a High-Lift System," AIAA paper AIAA 98-0704, 36th Aerospace Sciences Meeting and Exhibit, January 12-15, 1998, Reno NV

Tordella, D. and Christiansen, W. H.,"Spectral Observations in a Forced Mixing Layer," AIAA Journal, Vol. 27, No. 12, December 1989, pp. 1741-1743

Troutt, T. R., Scheelke, B., and Norman, T. R., "Organized Structures in a Reattaching Separated Flow Field," Journal of Fluid Mechanics, Vol. 143, 1984, pp. 413-427

Vatsa, V. N., Sanetrik, M. D., Parlette, E. B., Eisenman, P. and Cheng, Z., "Multi-Block Structured Grid Approach for Solving Flows over Complex Aerodynamic Configurations," AIAA Paper 94-0655, Jan. 1994

White, Frank M.; Viscous Fluid Flow, McGraw-Hill, Inc. 1991

Weier, T., Fey, U., Gerbeth, G., Mutschke, G., Lielausis, O., and Platacis, E., "Boundary Layer Control by Means of Wall Parallel Lorentz Forces," Magnetohydrodynamics, Vol. 37, 2001

Weyl, A. R., "High-Lift Devices and Tailess Airplanes," Aircraft Engineering, October 1945, p. 292

Winant, C. D. and Browand, F. K., Journal of Fluid Mechanics, Vol. 78, 1974
Ying, Susan X., Spaid, Frank W., McGinley, Catherine B. and Rumsey, Christopher L.; "Investigation of Confluent Boundary Layers in High-Lift Flows", Journal of Aircraft, Vol. 36, No. 3, May-June 1999

Yip, L. P, Whitehead, J. H., Miley, S. J., Bertelrud, A., Willard, P. E., van Dam, C. P., Hardin, Potter, R. C., and Edge, D. C., "The NASA B737-100 High-Lift Flight Research Program-Measurements and Computations." Proceedings from the Conference on High Lift and Separation Control, University of Bath, UK, March 29-31, 1995

Zhou, M. D., and Squire, L. C., "The Interaction of a Wake with a Turbulent Boundary Layer," Aeronautical Journal, Vol. 89, 1985, pp. 72-81

"9000 Series Intelligent Pressure Scanners Users Manual," Pressure Systems, Inc.

APPENDIX A: PRESSURE TAP LOCATIONS

Chordwise Pressure Tap Locations (inches)

Main Element

x	y
12.9509	0.8657
10.2531	-0.2846
7.3433	-0.6238
5.2701	-0.6719
3.50	-0.5842
2.258	-0.5028
1.4458	-0.4425
0.8973	-0.3653
0.6151	-0.3207
0.1002	-0.1933
0.0	-0.02
0.1128	0.3227
0.4618	0.6252
0.7915	0.8016
1.1973	0.9609
1.8217	1.1335
2.4319	1.2130
2.9578	1.2592
3.5486	1.3423
4.4506	1.3546
5.5030	1.3957
6.4057	1.1416
7.3678	1.4232
8.2370	1.4165
9.9148	1.3676
11.7881	1.2535
12.7296	1.1678
13.1866	1.1183
13.6304	1.0647
13.9826	1.0180
14.3795	0.9611

Flap

x	y
3.4779	-0.0283
1.8160	-0.1563
0.9242	-0.2957
0.1926	-0.2774
0.0999	-0.2357
0.0	0.02
0.0541	0.1606
0.165	0.2640
0.2266	0.3013
0.4907	0.4049
0.8160	0.4764
1.1862	0.5191
1.6348	0.5350
2.0364	0.5248
2.7149	0.4643
3.2550	0.3860
3.9512	0.2653
4.4727	0.1519
4.7348	0.0855

Slat

x	y
0.5563	-0.4431
0.1501	-0.2534
0.0	-0.03
0.0296	0.1165
0.1403	0.2457
0.6318	0.4797
1.264	0.6349
2.1667	0.7815

APPENDIX B: SURFACE PRESSURE MEASUREMENTS WITH PIEZOELECTRIC EXCITATION

	Frequency (Hz)				
Port No.	0	80	90	100	120
1	-5.01169586	-5.03417826	-5.03416538	-6.24995375	-6.18412685
2	-5.42416000	-5.59917879	-5.58142090	-6.98215723	-6.89433575
3	-4.45962858	-4.59559917	-4.58792448	-5.85361147	-5.78153753
4	-3.78590679	-3.93974161	-3.93556690	-5.18758059	-5.12889719
5	-3.09905934	-3.23906374	-3.22236490	-4.43294144	-4.41476393
6	-2.44886494	-2.50038266	-2.61697793	-3.90000510	-3.85560322
7	-1.68872333	-1.68467557	-1.78348017	-2.81348872	-2.79464269
8	-1.55090523	-1.51443887	-1.59873283	-2.30412889	-2.29266191
9	-1.54374242	-1.48433781	-1.54184091	-1.91032946	-1.92386293
10	-1.55206358	-1.50725508	-1.56277871	-1.60846734	-1.62122047
11	-1.55605268	-1.49221623	-1.56053233	-1.43274987	-1.44190037
12	-1.53800988	-1.49089444	-1.55005014	-1.35425615	-1.35607672
13	-1.51415181	-1.46706557	-1.53105760	-1.30500507	-1.29124081
14	-1.49578691	-1.41579700	-1.49300766	-1.25629842	-1.23855150
15	-1.42042422	-1.36016428	-1.38863742	-1.16093862	-1.15595019
16	-1.30096817	-1.22804487	1.24130821	-1.06199121	-1.04879367
17	-1.23375225	-1.17734790	-1.18817401	-1.00904262	-0.98947293
18	-1.20557702	-1.13389325	-1.16135013	-0.98576832	-0.95819139
19	-1.17453253	-1.09531283	-1.13413370	-0.96472079	-0.93466908
20	-1.14249516	-1.09388840	-1.11143947	-0.95073861	-0.91793072
21	-0.79604113	-0.74371648	-0.75683397	-0.63590318	-0.60841227

Table B.1 Surface Pressures on Upper Surface of the Main Wing for Selected Frequencies for Piezoelectric Devices

	Frequency (Hz)				
Port No.	0	80	90	100	120
1	-1.85465455	-4.06376600	-4.03188419	-4.86563015	-4.88387251
2	-0.04613832	-0.02331295	-0.01978362	-0.00932512	-0.01148496
3	1.03348470	0.89684212	0.90349013	0.93609393	0.88951755
4	1.01137447	0.90120047	0.91214806	0.93880045	0.88498050
5	0.98926413	0.90555882	0.92080599	0.94150698	0.88044351
6	0.90890771	0.48655593	0.64005989	0.93044716	0.54421788
7	0.73884541	0.68694645	0.80725831	0.85611016	0.76910096
8	0.62299138	0.59287691	0.58775818	0.60516769	0.58341402
9	0.59075010	0.58920735	0.59578735	0.60806805	0.58398658
10	0.61746269	0.63226336	0.64650387	0.65798438	0.64319509

Table B.2 Surface Pressures on Lower Surface of the Main Wing for Selected Frequencies for Piezoelectric Devices

	Frequency (Hz)				
Port No.	0	80	90	100	120
1	0.90300673	0.83624727	0.83329695	0.86291701	0.83679950
2	-0.35882041	-0.45332167	-0.46279845	-0.39064875	-0.41175532
3	-0.85557115	-0.84703612	-0.86639661	-0.79800409	-0.83490932
4	-0.68994129	-0.71737581	-0.72843671	-0.65797609	-0.68556172
5	-0.69862878	-0.71285331	-0.72306430	-0.65300292	-0.67666894
6	-0.68904597	-0.69703782	-0.70284379	-0.65663177	-0.65783036
7	-0.70372903	-0.70250410	-0.70112580	-0.65289843	-0.65657890
8	-0.71794814	-0.71725565	-0.71195334	-0.65492183	-0.66212857
9	-0.72390527	-0.71971768	-0.72650027	-0.66576445	-0.66270399
10	-0.72380775	-0.71763372	-0.71696860	-0.66483527	-0.66808975
11	-0.71718872	-0.71495485	-0.70507538	-0.66457134	-0.66290540
12	-0.69587183	-0.70044363	-0.68899345	-0.65577132	-0.65579057
13	-0.67017281	-0.69566613	-0.68934476	-0.64042830	-0.64291888
14	-0.67313069	-0.66752881	-0.66161466	-0.64076644	-0.62858284

Table B.3 Surface Pressures on Upper Surface of the Flap for Selected Frequencies for Piezoelectric Devices

	Frequency (Hz)				
Port No.	0	80	90	100	120
1	1.03780484	1.01293504	1.01220560	1.03563173	1.00488496
2	0.84928012	0.86825639	0.86337388	0.88476175	0.86121655
3	0.74856716	0.77621216	0.77155215	0.78962195	0.76543278
4	0.63463974	0.63763285	0.63954031	0.65785241	0.63564301
5	0.61003399	0.61224771	0.61813611	0.63995272	0.61706334

Table B.4 Surface Pressures on Lower Surface of the Flap for Selected Frequencies of Piezoelectric Devices

	Frequency (Hz)				
Port No.	0	80	90	100	120
1	-3.37990808	-3.46215463	-3.38636041	-4.19988251	-3.78418756
2	-4.68821621	-4.78416061	-4.69127321	-5.62292480	-5.26295662
3	-3.75466132	-3.82653284	-3.74899220	-4.40146923	-4.17179060
4	-2.91841841	-2.99769664	-2.91821456	-3.57138944	-3.39705348
5	-2.08217549	-2.16886044	-2.08743715	-2.74130964	-2.62231636

Table B.5 Surface Pressures on Upper Surface of the Slat for Selected Frequencies of Piezoelectric Devices

	Frequency (Hz)				
Port No.	0	80	90	100	120
1	0.84668100	0.86956066	0.87500727	0.82571828	0.85379106
2	0.90374237	0.88040817	0.88176119	0.90105325	0.86478692

Table B.6 Surface Pressures on Upper Surface of the Slat for Selected Frequencies of Piezoelectric Devices

APPENDIX C: PRESSURE MEASUREMENTS FOR PIEZOELECTRIC EXCITATION AT SELECTED TEST RUNS

Port No.	Run 1	Run 2	Run 3	Run 4
1	-.34904000	-.23194000	-.30276000	-.24811000
2	-6.28235000	-6.24876000	-6.30294000	-6.28928000
3	-5.24270000	-5.21969000	-5.26545000	-5.24690000
4	-4.70249000	-4.69087000	-4.72954000	-4.71146000
5	-4.35997000	-4.34311000	-4.37812000	-4.37563000
6	-3.91564000	-3.90330000	-3.93999000	-3.91870000
7	-2.97647000	-2.96717000	-2.99539000	-2.98490000
8	-2.53223000	-2.52979000	-2.54789000	-2.54022000
9	-2.21805000	-2.22209000	-2.23662000	-2.22241000
10	-1.91678000	-1.91013000	-1.93130000	-1.91504000
11	-1.65963000	-1.65468000	-1.67484000	-1.65989000
12	-1.46723000	-1.46745000	-1.49145000	-1.47412000
13	-1.30510000	-1.30500000	-1.32745000	-1.31375000
14	-1.17472000	-1.17624000	-1.18884000	-1.17324000
15	-.96589000	-.96834000	-.98883000	-.97232000
16	-.80415000	-.79078000	-.80749000	-.80059000
17	-.74134000	-.73805000	-.74746000	-.73678000
18	-.71471000	-.70979000	-.72398000	-.71250000
19	-.69154000	-.68670000	-.69950000	-.68627000
20	-.66691000	-.66611000	-.67432000	-.66637000
21	-.35365000	-.36152000	-.36709000	-.35593000

Table C.1 Surface Pressures Coefficients on Upper Surface of the Main Wing at 15° AOA for 0 Hz Piezoelectric Excitation Frequency

Port No.	Run 1	Run 2	Run 3	Run 4
1	-.78698000	-.84955000	-.79108000	-.73389000
2	.00865000	.01034000	.00857000	.00884000
3	-.94767000	-1.33674000	-.98461000	-.83772000
4	-.64108000	-.71643000	-.57090000	-.55682000
5	-.33449000	-.09612000	-.15720000	-.27592000
6	-.48285000	-.21039000	-.26180000	-.44499000
7	-.41995000	-.11843000	-.19274000	-.38232000
8	-.49079000	-.17523000	-.28240000	-.44816000
9	-.09899000	-.12589000	-.12996000	-.06664000
10	.63137000	.62620000	.63359000	.62941000

Table C.2 Surface Pressures Coefficients on Lower Surface of the Main Wing at 15° AOA for 0 Hz Piezoelectric Excitation Frequency

Port No.	Run 1	Run 2	Run 3	Run 4
1	.92338000	.91565000	.92318000	.92661000
2	-.22343000	-.22181000	-.22186000	-.22693000
3	-.72514000	-.71744000	-.71066000	-.72321000
4	-.55687000	-.54928000	-.54700000	-.55166000
5	-.56451000	-.56653000	-.55959000	-.56431000
6	-.56448000	-.56222000	-.56472000	-.56472000
7	-.56842000	-.56445000	-.56310000	-.56955000
8	-.57418000	-.56802000	-.57101000	-.57118000
9	-.58281000	-.58109000	-.58203000	-.57887000
10	-.58994000	-.58812000	-.59825000	-.58814000
11	-.59478000	-.58377000	-.59974000	-.58928000
12	-.58980000	-.58195000	-.59091000	-.58593000
13	-.56623000	-.56289000	-.58844000	-.56535000
14	-.55356000	-.57606000	-.58741000	-.55904000

Table C.3 Surface Pressures Coefficients on Upper Surface of the Flap at 15° AOA for 0 Hz Piezoelectric Excitation Frequency

Port No.	Run 1	Run 2	Run 3	Run 4
1	1.03647000	1.02933000	1.03588000	1.03453000
2	.84835000	.84054000	.84767000	.85263000
3	.77522000	.77141000	.78162000	.77838000
4	.63211000	.62760000	.63858000	.63561000
5	.62204000	.61920000	.62274000	.62340000

Table C.4 Surface Pressure Coefficients on Lower Surface of the Flap at 15° AOA for 0 Hz Piezoelectric Excitation Frequency

Port No.	Run 1	Run 2	Run 3	Run 4
1	.00666000	.00486000	.00844000	.00554000
2	.01084000	.00941000	.01101000	.00556000
3	.00373000	.00462000	.00233000	.00655000
4	.00632000	.00615000	.00565000	.00711000
5	.00890000	.00767000	.00897000	.00768000

Table C.5 Surface Pressure Coefficients on Upper Surface of the Slat at 15° AOA for 0 Hz Piezoelectric Excitation Frequency

Port No.	Run 1	Run 2	Run 3	Run 4
1	.00700000	.00765000	.00768000	.00515000
2	.01006000	.00712000	.00847000	.00623000

Table C.6 Surface Pressure Coefficients on Lower Surface of the Slat at 15° AOA for 0 Hz Piezoelectric Excitation Frequency

Port No.	Run 1	Run 2	Run 3	Run 4
1	-.50267000	-.25732000	-.25696000	-.29835000
2	-4.53913000	-4.16220000	-4.15937000	-4.09507000
3	-4.89602000	-4.22830000	-4.17709000	-4.10730000
4	-4.79410000	-4.14038000	-4.08673000	-4.02263000
5	-4.95884000	-4.29292000	-4.23162000	-4.17128000
6	-3.54251000	-2.95549000	-2.91686000	-2.93789000
7	-3.32596000	-2.95026000	-2.90350000	-2.84737000
8	-2.74259000	-2.62153000	-2.69965000	-2.67318000
9	-2.46752000	-2.32225000	-2.32153000	-2.30262000
10	-2.20789000	-2.04778000	-2.07051000	-2.04427000
11	-1.96043000	-1.82927000	-1.85516000	-1.82888000
12	-1.80829000	-1.68860000	-1.70249000	-1.67988000
13	-1.67488000	-1.55035000	-1.55992000	-1.53329000
14	-1.54328000	-1.43146000	-1.45354000	-1.41829000
15	-1.43232000	-1.32385000	-1.33204000	-1.30150000
16	-1.31147000	-1.17939000	-1.18491000	-1.15739000
17	-1.24740000	-1.10809000	-1.12232000	-1.08802000
18	-1.19282000	-1.07853000	-1.09327000	-1.06086000
19	-1.19009000	-1.05681000	-1.07417000	-1.04432000
20	-1.18812000	-1.05197000	-1.06907000	-1.02758000
21	-.82849000	-.71596000	-.73289000	-.69805000

Table C.7 Surface Pressure Coefficients on Upper Surface of the Main Wing at 15° AOA for 320 Hz Piezoelectric Excitation Frequency

Port No.	Run 1	Run 2	Run 3	Run 4
1	-.78800000	-.49978000	-.44387000	-.48862000
2	.00078000	.00780000	.00324000	.00110000
3	-.94217000	-.66070000	-.55610000	-.62827000
4	-.66829000	-.40481000	-.35633000	-.40372000
5	-.39441000	-.14893000	-.15657000	-.17918000
6	-.50942000	-.13011000	-.14651000	-.16326000
7	-.43550000	-.13595000	-.14173000	-.15688000
8	-.51418000	-.20225000	-.22501000	-.25370000
9	-.19918000	-.10374000	-.07547000	-.08173000
10	.53929000	.59628000	.59834000	.59680000

Table C.8 Surface Pressure Coefficients on Lower Surface of the Main Wing at 15° AOA for 320 Hz Piezoelectric Excitation Frequency

Port No.	Run 1	Run 2	Run 3	Run 4
1	.62914000	.66361000	.66796000	.67131000
2	-1.76585000	-1.42326000	-1.43384000	-1.38610000
3	-3.30715000	-2.98516000	-3.00210000	-2.91492000
4	-2.72226000	-2.49558000	-2.51312000	-2.44007000
5	-2.29686000	-2.17844000	-2.17117000	-2.09798000
6	-1.38035000	-1.32721000	-1.33226000	-1.26911000
7	-1.14013000	-1.11229000	-1.11390000	-1.06743000
8	-.95048000	-.92768000	-.92948000	-.89188000
9	-.81153000	-.79965000	-.80880000	-.78231000
10	-.62501000	-.65261000	-.66384000	-.65110000
11	-.51969000	-.56209000	-.56562000	-.56603000
12	-.45132000	-.49513000	-.49790000	-.50805000
13	-.44780000	-.43318000	-.43707000	-.44399000
14	-.40354000	-.38806000	-.39262000	-.40199000

Table C.9 Surface Pressure Coefficients on Upper Surface of the Flap at 15° AOA for 320 Hz Piezoelectric Excitation Frequency

Port No.	Run 1	Run 2	Run 3	Run 4
1	.94563000	.95766000	.96781000	.96060000
2	.90679000	.89096000	.90175000	.89456000
3	.81826000	.80753000	.81766000	.81445000
4	.68102000	.66750000	.68182000	.67705000
5	.67419000	.66433000	.67430000	.67057000

Table C.10 Surface Pressure Coefficients on Lower Surface of the Flap at 15° AOA for 320 Hz Piezoelectric Excitation Frequency

Port No.	Run 1	Run 2	Run 3	Run 4
1	.00551000	.00029000	.00350000	.00768000
2	.00315000	.00018000	-.00044000	.00990000
3	.00356000	-.00170000	.00369000	.00496000
4	.00163000	-.00314000	.00213000	.00589000
5	-.00030000	-.00459000	.00057000	.00682000

Table C.11 Surface Pressure Coefficients on Upper Surface of the Slat at 15° AOA for 320 Hz Piezoelectric Excitation Frequency

Port No.	Run 1	Run 2	Run 3	Run 4
1	.00317000	-.00146000	.00416000	.00858000
2	-.00146000	.00175000	.00396000	.00789000

Table C.12 Surface Pressure Coefficients on Lower Surface of the Slat at 15° AOA for 320 Hz Piezoelectric Excitation Frequency

APPENDIX D: SURFACE PRESSURE MEASUREMENTS WITH ACOUSTIC EXCITATION

Frequency (Hz)			
Port No.	0	80	120
1	-5.01169586	-6.00356245	-5.05685806
2	-5.42416000	-6.62718391	-5.50296593
3	-4.45962858	-5.53747082	-4.52698517
4	-3.78590679	-4.86954546	-3.87076139
5	-3.09905934	-4.12120819	-3.15507460
6	-2.44886494	-4.20380163	-2.53191209
7	-1.68872333	-3.18410230	-1.72587299
8	-1.55090523	-2.68687797	-1.52872789
9	-1.54374242	-2.43998647	-1.50680518
10	-1.55206358	-2.27116656	-1.53415298
11	-1.55605268	-2.17078257	-1.54036212
12	-1.53800988	-2.05223417	-1.52547169
13	-1.51415181	-1.77994215	-1.50033176
14	-1.49578691	-1.98887384	-1.47880554
15	-1.42042422	-1.88227510	-1.39588201
16	-1.30096817	-1.76545191	-1.29298532
17	-1.23375225	-1.81095707	-1.22260630
18	-1.20557702	-1.67435610	-1.18761945
19	-1.17453253	-1.61739886	-1.15278292
20	-1.14249516	-1.64429212	-1.12850511
21	-0.79604113	-1.32527900	-0.78205860

Table D.1 Surface Pressure on Upper Surface of the Main Wing for Selected Acoustic Frequencies

	Frequency (Hz)		
Port No.	0	80	120
1	-1.85465455	-0.36774495	-0.02295004
2	-0.04613832	-0.00621475	-0.01509776
3	1.03348470	0.89445329	0.88308084
4	1.01137447	0.89723092	0.86639851
5	0.98926413	0.90000862	0.84971619
6	0.90890771	0.76699936	0.69731772
7	0.73884541	0.64478862	0.61821514
8	0.62299138	0.60573965	0.58717555
9	0.59075010	0.60563660	0.58752698
10	0.61746269	0.65436542	0.62767458

Table D.2 Surface Pressures on Lower Surface of the Main Wing for Selected Acoustic Frequencies

	Frequency (Hz)		
Port No.	0	80	120
1	0.90300673	0.86834896	0.84168965
2	-0.35882041	-0.42169347	-0.46408644
3	-0.85557115	-0.82734221	-0.84952992
4	-0.68994129	-0.69144195	-0.72489679
5	-0.69862878	-0.69015545	-0.72077543
6	-0.68904597	-0.67202348	-0.69238526
7	-0.70372903	-0.67391056	-0.70244241
8	-0.71794814	-0.68279254	-0.71816200
9	-0.72390527	-0.68239510	-0.71903616
10	-0.72380775	-0.68222433	-0.71851647
11	-0.71718872	-0.67795855	-0.70765424
12	-0.69587183	-0.66936797	-0.69292897
13	-0.67017281	-0.64883959	-0.67001200
14	-0.67313069	-0.64375234	-0.66521770

Table D.3 Pressure Distribution on the Upper Surface of the Flap for Selected Acoustic Frequencies

	Frequency (Hz)		
Port No.	0	80	120
1	1.03780484	1.03859663	1.01726353
2	0.84928012	0.88995486	0.87467885
3	0.74856716	0.79622132	0.78134370
4	0.63463974	0.66436911	0.63974738
5	0.61003399	0.64286327	0.62163967

Table D.4 Pressure Distribution on the Lower Surface of the Flap for Selected Acoustic Frequencies

	Frequency (Hz)		
Port No.	0	80	120
1	-3.37990808	-3.93581939	-3.45285130
2	4.68821621	-5.33861637	-4.76125288
3	-3.75466132	-4.22622013	-3.82639027
4	-2.91841841	-3.37923408	-2.98569489
5	-2.08217549	-2.53224802	-2.14499950

Table D.5 Pressure Distribution on the Upper Surface of the Slat for Selected Acoustic Frequencies

	Frequency (Hz)		
Port No.	0	80	120
1	0.84668100	0.85548079	0.87409008
2	0.90374237	0.90942347	0.88765883

Table D.6 Pressure Distribution on the Lower Surface of the Slat for Selected Acoustic Frequencies

APPENDIX E: FORTRAN COMPUTER CODES

```
PROGRAM WAKEIGN
c This is finally the best program version for the odu data 11/24/03
c
ccccccccccccccccccccccccccccccccccccccccccccccccccccccccccccccccc
c                                                                 c
c This program computes the stability characteristics             c
c for a disturbance which is neutrally stable. The                c
c assumption is that the gas medium is incompressible but         c
c is viscous. The governing equations are expressed for           c
c each grid line in the boundary layer. The equations are         c
c then represented as a system of equations in block              c
c tridiagonal form. Thensystem of equations is then solvedc
c by employing a tridiagonal solver, which uses Gaussian          c
c Elimination with partial pivoting.                              c
c                                                                 c
ccccccccccccccccccccccccccccccccccccccccccccccccccccccccccccccccc
c
      double complex a( 6,6 ),xident( 6,6 )
      double complex aa( 6,6,150 ),bb( 6,6,150 )
      double complex cc( 6,6,150 ),dd( 6,150 )
      double complex dadz( 6,6 ), axa( 6,6 )
      double complex lambda1,lambda2,lambda3,kk
      common/flow/t(301),tp(301),tpp(301), etastep(301)
      double complex omega,alpha,sum
      double complex ai/(0.0,1.0)/
      double complex alphmat( 350 ),omegmat( 350 )
      dimension h( 201 ),zz( 201 ),pp(101)
      double complex velwall( 2 ),waveno( 2 ),dely,delx,slope
      dimension array1(350),array2(350),array3(350)
      OPEN(UNIT=1,FILE='OMEGA',FORM='BINARY',STATUS='OLD')
      OPEN(UNIT=2,FILE='ALPHA',FORM='BINARY',STATUS='OLD')
      OPEN(UNIT=3,FILE='WAVE',FORM='BINARY',STATUS='OLD')
      OPEN(UNIT=7,FILE='AMPLT',FORM='BINARY',STATUS='OLD')
c
c *** Initialize Flow Field Parameters ***
c
      IALPHA=1
      IOMEGA=0
      NPOINTS = 201
      REFLEN =(18. * 2.54)/100.
      PI = 3.141592654
      XNU = 15.75E-06
      VINF = 10.0
      RN = VINF * REFLEN / XNU
      infnty = 100
      ibegin = 2
      epsilon = 1.0e-04
      BETA = 0.0
      ALPHMAT( 1 ) = ( 100.0 , 0.0)
      if(iomega.eq.1)then
      dal=-0.002
       do 29 i = 2,100
       alphmat( i ) = alphmat(i-1) + dal
 29      continue
      endif
```

```
      OMEGMAT( 1 ) = 94.9
      OMEGMAT( 1 ) = 97.0
      nstep = 100
       d = 0.0055
       zmax = 0.3750
         dom = -0.50
         if(ialpha.eq.1)then
         do 1011 i = 2,30
         omegmat( i ) = omegmat(i-1) + dom
 1011      continue
         endif
         dn = zmax / (npoints-1)
c
c **** Store values of eta into array etastep ****
c
      etastep( 1 ) = 0.0
      do 22 i = 2,201
      etastep( i ) = etastep( i-1 ) + dn
 22   continue
c
      call wakslat(
     I               etastep , npoints,
     O               t , tp , tpp )
c
      print 81
 81   format(10x,'The Eigenvalues of the Slat Wake Shear Layer')
      eta = -dn
      do 83 ib = 1,51
      eta = eta + dn
c+++    print 82,eta,t(ib),tp(ib),tpp(ib)
  82  format(3x,'eta=',f5.2,2x,'u=',f8.4,2x,'up=',f8.4,
     1       2x,'upp=',f8.4)
  83  continue
c
c*** Initialize the Identity Matrix ***
c
      do 5 i = 1,6
      do 4 j = 1,6
      xident( i,j ) = ( 0.0,0.0 )
 4    continue
      xident( i,i ) = ( 1.0,0.0 )
 5    continue
c
c *** Loop through different values of omega to
c *** calculate the corresponding value of alpha
c
      do 1500 ivalue = 1,30
      IF( IALPHA.EQ.1 )THEN
      IF( IVALUE.EQ.1 )THEN
      ALPHA =  ALPHMAT( IVALUE )
      ELSE
      ALPHA = ALPHMAT( IVALUE-1 )
      ENDIF
c
      OMEGA = OMEGMAT( IVALUE   )
      ENDIF
c
```

```
c *** Initialize the array A ***
c *** First fill the whole array with zeros
c
      do 10 i = 1,6
      do 10 j = 1,6
      a( i,j )     = ( 0.0,0.0 )
      dadz( i,j )  = ( 0.0,0.0 )
      axa( i,j )   = ( 0.0,0.0 )
 10   continue
c
c *** Define the grid and the spacing between grid lines
c
      h( 1 )  = 0.0
      zz( 1 ) = 0.0
      do 88 kstep = 2, nstep + 1
      zz(kstep)=(d*(kstep-1.)/nstep)/(1.-(kstep-1.)/nstep
     1          +d/zmax )
      h(kstep)=zz(kstep) - zz(kstep-1)
 88   continue
c
ccccccccccccccccccccccccccccccccccccccccccccccccc
c                                                 c
c **** Determine shear-layer velocities and       c
c **** their derivatives on the grid line         c
c                                                 c
ccccccccccccccccccccccccccccccccccccccccccccccccc
c
      DO 1000 NTIMES = 1,20
      DO 1000 ITER = 1,2
c
      do 940 i = 1,6
      do 940 j = 1,nstep + 2
      dd( i,j ) = 0.0
 940  continue
c
ccccccccccccccccccccccccccccccccccccccccccccccccccc
c                                                   c
c Construct block tridiagonal matrix. Proceed in the    c
c positive z direction from grid line to grid line      c
c starting at the wall and stopping at the edge of the  c
c boundary layer.                                       c
c                                                   c
ccccccccccccccccccccccccccccccccccccccccccccccccccc
c
c     Now go back and selectively store non-zero
c     values in specific array location. These
c     values do not change as a function of distance
c     z in the boundary layer. They remain fixed for
c     a specific interation step.
c
      kk=alpha*alpha+beta*beta + ai*rn*(alpha - omega)
      lambda1 = -sqrt( kk )
      if( real(lambda1).gt.0.)lambda1=-lambda1
      lambda2 = lambda1
      lambda3 = -sqrt( alpha*alpha+beta*beta )
      if( real(lambda3).gt.0.)lambda3 = -lambda3
      a( 1,5 ) = ( 1.,0. )
```

```
      a( 2,6 ) = ( 1.,0. )
      a( 3,1 ) = 0. + ai*( -alpha )
      a( 3,2 ) = 0. + ai*( -beta )
      a( 4,5 ) = 0. + ai*( -alpha/rn )
      a( 4,6 ) = 0. + ai*( -beta/rn )
      a( 5,4 ) = 0. + ai*( alpha*rn )
      a( 6,4 ) = 0. + ai*( beta*rn )
c
c ***  Store boundary conditions at the far field
c
      aa( 1,1,nstep+2 ) = 0. + ai*(-alpha/lambda1 )
      aa( 1,2,nstep+2 ) = 0. + ai*(-alpha/lambda2 )
      aa( 1,3,nstep+2 ) = (-1.,0.0 )
      aa( 1,4,nstep+2 ) = rn/(lambda3*lambda3-
     1  kk )*(lambda3-alpha*alpha/lambda1-alpha*beta/
     2  lambda2) + ai*(0.0)
      aa( 1,5,nstep+2 ) = ( 0.0,0.0 )
      aa( 1,6,nstep+2 ) = ( 0.0,0.0 )
c
      aa( 2,1,nstep+2 ) = lambda1 + ai*( 0.0 )
      aa( 2,2,nstep+2 ) = ( 0.0,0.0 )
      aa( 2,3,nstep+2 ) = ( 0.0,0.0 )
      aa( 2,4,nstep+2 ) = 0.0 + ai*(alpha*rn/
     1  (lambda3*lambda3-kk)*(lambda3-lambda1) )
      aa( 2,5,nstep+2 ) = (-1.0,0.0)
      aa( 2,6,nstep+2 ) = (0.0,0.0)
c
      aa( 3,1,nstep+2 ) = (0.0,0.0)
      aa( 3,2,nstep+2 ) = lambda2 + ai*(0.0)
      aa( 3,3,nstep+2 ) = ( 0.0, 0.0 )
      aa( 3,4,nstep+2 ) = 0.0 + ai*(beta*rn/
     1   (lambda3*lambda3-kk)*(lambda3-lambda2) )
      aa( 3,5,nstep+2 ) = ( 0.0,0.0 )
      aa( 3,6,nstep+2 ) = (-1.0,0.0 )
c
c*******************************************************
c
      istep = 0
       do 900 kstep = 2, nstep+1
c
       zvalue = zz( kstep )
c
       call newgrid(
     I               zvalue,
     O               u , up , upp )
      if(kstep.eq.1)then
      u   = t( 1 )
      up  = tp( 1 )
      upp = tpp( 1 )
      endif
c
c  Now store into array A those values which change
c  from grid line to grid line
c
      a( 4,3 ) = -(alpha*alpha+beta*beta) /rn
     1           + ai*(-alpha*u+omega )
      a( 5,1 ) = alpha*alpha+beta*beta
```

```
     1           + ai*(rn*(alpha*u-omega) )
      a( 5,3 ) = rn*up + ai*( 0.0 )
      a( 6,2 ) = alpha*alpha+beta*beta
     1           + ai*(rn*(alpha*u - omega) )
c
c    Store first derivatives of elements from array A
c
      dadz( 4,3 ) = 0. + ai*(-alpha*up )
      dadz( 5,1 ) = 0. + ai*(alpha*rn*up )
      dadz( 5,3 ) = rn*upp + ai*( 0.0 )
      dadz( 6,2 ) = 0. + ai*( alpha*rn*up )
c
c  Multiply the matrix A by itself
c
      do 800 i = 1,6
      do 800 j = 1,6
      sum = 0.0
      do 762 n = 1,6
c
      sum = sum + a( i,n ) * a( n,j )
 762  continue
      axa( i,j ) = sum
 800  continue
c
c    Construct the block arrays AA , BB and CC
c
      do 700 i = 1,6
      do 700 j = 1,6
c
c ************************************************************
c
      aa(i,j,kstep)=-xident(i,j)-(h(kstep)/2.)*a(i,j)
     1              -(h(kstep)*h(kstep)/12.)*(dadz(i,j)
     2              + axa(i,j) )
 700  continue
c
 880  CONTINUE
      if(kstep.eq.1) goto 890
      do 600 i = 1,6
      do 600 j = 1,6
c
      bb(i,j,kstep)= xident(i,j)-(h(kstep)/2.)*a(i,j)
     1             +(h(kstep)*h(kstep)/12.)*(dadz(i,j)
     2             +axa(i,j) )
 600  continue
 890  continue
      istep = kstep + 1
 900  continue
 901  continue
c
c  Set boundary conditions at the wall
c
      do 200 i = 1,3
      do 200 j = 1,6
c
      if( i.eq.j )then
      bb( i,j,1 ) = 1.
```

```
      else
      bb( i,j,1 ) = 0.
      endif
c
      cc( i,j,1 ) = 0.
 200  continue
c
      do 550 kstep = 2,nstep+1
      do 500 i = 4,6
      do 500 j = 1,6
c
c   Store the top three rows of matrix AA into the bottom
c   three rows of the matrix BB for the identical grid line
c
      bb( i,j,kstep - 1) = aa( i-3,j,kstep )
c
c   Store the bottom three rows of matrix AA into the top
c   three rows of matrix AA
c
      aa( i-3,j,kstep ) = aa( i,j,kstep )
c
c   Fill the bottom three rows of matrix AA with zeros
c
      aa( i,j,kstep ) = 0.0
c
c   Store the top three rows of matrix BB into the bottom
c   three rows of matrix CC
c
      cc( i,j,kstep - 1 ) = bb( i-3,j,kstep )
c
c   Store the bottom three rows of matrix BB into the top
c   three rows of matrix BB
c
      bb( i-3,j,kstep ) = bb( i,j,kstep )
c
c   Fill the top three rows of matrix CC with zeros
c
      cc( i-3,j,kstep-1 ) = 0.
 500  continue
 550  continue
c
c Store the far-field boundary conditions
c
      do 627 i = 4,6
      do 627 j = 1,6
      bb( i,j,nstep+1 ) = aa( i-3,j,nstep+2 )
 627  continue
c
c  Set the pressure at the wall equal to 1. Make the right hand
c  side of the system of equations nonhomogeneous.
c
      bb( 1,1,1 ) = ( 0.0,0.0 )
      bb( 1,4,1 ) = ( 1.0,0.0 )
      dd( 1,1 )   = ( 1.0,0.0 )
c
      iorder = 6
c
```

```
      CALL TRIDIAG( aa,bb,cc,dd,iorder,nstep+1 )
c
c   Apply Newton-Raphson Algorithm
c
c ***** STORE THE VELOCITY AT THE WALL ***
c
      velwall( iter ) = dd( 1,1 )
      V0 = REAL(velwall( iter ))
c       PRINT *,ITER,NTIMES
c       PRINT *,ALPHA
c       PRINT *,V0
      if( abs( V0 ).le.epsilon )goto 1200
      if(ialpha.eq.1)then
      waveno( iter ) = alpha
      if( iter.gt.1 )goto 1003
      alpha = alpha + 0.01
      goto 1000
1003    continue
      dely =  velwall(iter)-velwall(iter-1)
      delx = waveno(iter)-waveno(iter-1)
      slope = dely/delx
      waveno( 1 ) = waveno( 1 ) - REAL(velwall( 1 ))/slope
      alpha=waveno(1)
      endif
      if(iomega.eq.1)then
      waveno(iter) = omega
      if( iter.gt.1 )goto 1004
      omega = omega + .001
      goto 1000
1004    continue
      dely = velwall(iter)-velwall(iter-1)
      delx = waveno(iter)-waveno(iter-1)
      slope = dely/delx
      waveno( 1 ) = waveno( 1 ) - (velwall( 1 )/slope)
      omega = waveno( 1 )
      endif
1000    continue
1200    continue
      alphmat( ivalue ) = alpha
      omegmat( ivalue ) = omega
      write(6,*) alphmat( ivalue ),omegmat( ivalue )
c
      IF( IVALUE.EQ.30)THEN
      DO 909 I2=1,101
      PP(I2)=REAL( DD(1,I2) )
 909    CONTINUE
      WRITE(7) (PP(I1),I1=1,101)
      ENDIF
c
1500    continue
      if( ialpha.eq.1)then
      do 1520 kr = 1,30
      array1( kr ) = real( omegmat( kr ) )
      array2( kr ) = -aimag( alphmat( kr ) )
      array3( kr ) = real( alphmat( kr ) )
1520  continue
      endif
```

```
c
ccccccccccccccccccccccccccccccccccccccccccccccccccccccc
c                                                       c
c Store the amplitudes of the perturbation velocity     c
c in the longitudinal direction only. This is done      c
c to see if the eigenvalues are influenced mainly       c
c by either the wake or the boundary layer.             c
c                                                       c
ccccccccccccccccccccccccccccccccccccccccccccccccccccccc
c
      if( iomega.eq.1)then
      do 1521 kr = 1,72
      array1( kr ) = real( alphmat( kr ) )
      array2( kr ) = aimag( omegmat( kr ) )
1521  continue
      endif
c
      write(1) (array1(i),i=30,1,-1)
      write(2) (array2(i),i=30,1,-1)
      write(3) (array3(i),i=30,1,-1)
      stop
      end
      subroutine newgrid(
     I                    zvalue,
     O                    u , up , upp )
      common/flow/t(301),tp(301),tpp(301),etastep(301)
      do 100 i = 1,201
      if( (zvalue.ge.etastep(i)).and.
     1    (zvalue.le.etastep(i+1)) )then
      j = i
      goto 110
      endif
 100  continue
 110  continue
      u=( (t(j+1)-t(j))/(etastep(j+1)-etastep(j)) )*
     1  (zvalue-etastep(j)) + t(j)
      up=( (tp(j+1)-tp(j))/(etastep(j+1)-etastep(j)) )*
     1   (zvalue-etastep(j)) + tp(j)
      upp=((tpp(j+1)-tpp(j))/(etastep(j+1)-etastep(j)) )*
     1    (zvalue-etastep(j)) + tpp(j)
      return
      end
      SUBROUTINE TRIDIAG(A,B,C,D,N,IL)
c
      DOUBLE COMPLEX A(6,6,150),B(6,6,150),C(6,6,150),D(6,150)
      DOUBLE COMPLEX AA(10,10),DD(10),SUM
c
      DO 91 I = 2,IL
      DO 10 I1 = 1,N
      DO 10 J1 = 1,N
 10   AA(I1,J1) = B(I1,J1,I-1)
      DO 30 I1=1,N
c
      DO 20 J1=1,N
 20   DD(J1) = C(J1,I1,I-1)
      CALL PIVOT( AA,DD,N )
      DO 30 J1 = 1,N
```

```
 30   C(J1,I1,I-1) = DD(J1)
C
      IF( I.EQ.2)THEN
      DO 40 J1 = 1,N
 40   DD(J1) = D(J1,I-1)
      CALL PIVOT( AA,DD,N )
      DO 50 J1=1,N
 50   D(J1,I-1) = DD(J1)
      ENDIF
C
      DO 70 I2=1,N
      DO 70 J2=1,N
      SUM=0.0
      DO 60 I3 = 1,N
 60   SUM = SUM+A(I2,I3,I)*C(I3,J2,I-1)
 70   B(I2,J2,I) = B(I2,J2,I)-SUM
C
      DO 90 I2=1,N
      SUM = 0.0
      DO 80 J2=1,N
80    SUM = SUM+A(I2,J2,I)*D(J2,I-1)
      D(I2,I) = D(I2,I) - SUM
90    CONTINUE
      DO 100 J2 = 1,N
 100  DD(J2) = D(J2,I)
      DO 110 I2=1,N
      DO 110 J2=1,N
 110  AA(I2,J2) = B(I2,J2,I)
      CALL PIVOT(AA,DD,N)
      DO 120 I2=1,N
 120  D(I2,I) = DD(I2)
91    CONTINUE
C
c BACK SUBSTITUTION
C
      DO 150 I = 2,IL
      I1 = IL-I+1
C
      DO 150 I2=1,N
      SUM=0.0
      DO 140 J2=1,N
 140  SUM = SUM +C(I2,J2,I1)*D(J2,I1+1)
      D(I2,I1) = D(I2,I1)-SUM
 150  CONTINUE
C

      RETURN
      END
C
c *** SUBROUTINE TO SOLVE EQUATION AX=D USING GAUSSIAN ELIMINATION
c *** WITH PARTIAL PIVOTING
C
      SUBROUTINE PIVOT(A,D,N)
C
      INTEGER PIVOT1,N1(6),PIVOT2
C
      DOUBLE COMPLEX A(10,10),D(10),B(10,10),U(10)
```

```
      DOUBLE COMPLEX AA,DD,SUM
C
      DO 1 I = 1,N
      N1( I ) = I
      DO 1 J=1,N
C
  1   B(I,J) = A(I,J)
C
C  FIND THE LARGEST TERM IN THE MATRIX
C
      DO 35 I =1,N-1
C
      PIVOT1 = I
      PIVOT2 = I
C
      DO 10 K=I,N
      DO 10 J=I,N
C
      IF(CABS(A(K,J)).GT.CABS( A(PIVOT1,PIVOT2)))THEN
      PIVOT1 = K
      PIVOT2 = J
      ENDIF
C
 10   CONTINUE
C
C EXCHANGE THE ROWS
C
      DO 20 J = I,N
C
      AA = A(I,J)
      A(I,J) = A(PIVOT1,J)
 20   A(PIVOT1,J) = AA
C
      DD = D(I)
      D(I) = D(PIVOT1)
      D(PIVOT1) = DD
C
C  EXCHANGE THE COLUMNS
C
      DO 25 J =1,N
      AA=A(J,I)
      A(J,I)=A(J,PIVOT2)
 25   A(J,PIVOT2)=AA
C
      N11=N1(I)
      N1(I) = N1(PIVOT2)
      N1(PIVOT2)= N11
      DO 35 I1=I+1,N
      DO 30 J =I+1,N
      A(I1,J) = A(I1,J) - A(I1,I)*A(I,J)/A(I,I)
 30   CONTINUE
C
      D(I1) = D(I1) - A(I1,I)*D(I)/A(I,I)
 35   CONTINUE
C
C BACK SUBSTITUTION
C
```

```
      D(N) = D(N)/A(N,N)
c
      DO 50 I = 2,N
c
      I1 = N-I+1
c
      SUM = 0.0
c
      DO 40 J=I1+1,N
 40   SUM=D(J)*A(I1,J)+SUM
c
      D(I1) = (D(I1)-SUM)/A(I1,I1)
  50  CONTINUE
      DO 55 I=1,N
      J=N1(I)
 55   U(J)=D(I)
      DO 56 I= 1,N
 56   D(I)=U(I)
c
      DO 60 I = 1,N
      DO 60 J = 1,N
c
 60   A(I,J) = B(I,J)
c
      RETURN
      END
      SUBROUTINE WAKSLAT(
     I                    ETA , NVALUES ,
     O                    S , SP , SPP )
c
ccccccccccccccccccccccccccccccccccccccccccccccccccccccccc
c                                                       c
c The purpose of this program is to determine the first  c
c and second derivatives of a velocity profile taken     c
c near the trailing edge of the leading edge slat. These c
c derivatives will be used in a linear stability program c
c to compute the amplification rate for a disturbance    c
c in the flow.                                           c
c                                                       c
ccccccccccccccccccccccccccccccccccccccccccccccccccccccccc
c
      DIMENSION ETA(201),SP(201),SPP(201),S(201)
c
      dimension h(0:200),v(0:200),z(0:200),a(0:200,0:200),y(0:200)
      dimension vpp(0:200),x(201),sd(0:200)
      open(unit=4,file='cbl10l',form='formatted',status='old')
c This program was originally set up for blayerb
c
c Read profile data from file
c
      npoints = 50
      do 70 k = 0,npoints
      read(4,*)z( k ),v( k )
 70   continue
c
      h( 0 ) = 0.0
      do 100 i = 1,npoints
```

```
      h( i ) = z( i ) - z( i-1 )
 100  continue
c
c     Initialize the A matrix
c
      do 120 i=0,npoints
      do 120 j=0,npoints
      a( i,j ) = 0.0
 120  continue
c
      a( 0,0 ) = 1.0
      a( npoints,npoints ) = 1.0
      y( 0 ) = 0.0
      y( npoints ) = 0.0
      do 150 k    = 1,npoints-1
      a(k,k-1 )   =  h( k )/6.0
      a(k,k )     = (h( k ) + h( k+1 ))/3.0
      a(k,k+1 )   =  h( k+1 )/6.0
      y( k )      = (v(k+1)-v(k))/h(k+1) - (v(k)-v(k-1))/h(k)
 150  continue
c
      call secder(
     I              z , v, npoints,
     O              sd)
c
      call crout(
     I            a , npoints, y ,
     O            x )
c
      do 23 i = 0,npoints
      vpp( i ) =  x( i+1 )
 23   continue
c
c       do 27 i = 0, npoints
c       vpp( i ) = sd( i )
c  27   continue
c
      DO 500 J=1,NVALUES
      ZP = ETA( J )
      DO 400 K=1,npoints
      IF( (ZP.GE.Z(k-1)).AND.(ZP.LE.Z(K)) )then
      I=K
      goto 403
      endif
 400  continue
 403  continue
      AX = (h(i)-(zp-z(i-1)))/h(i)
      BX = ((z(i)-zp)**3+h(i)*h(i)*(zp-z(i-1))-h(i)**3)/6.*h(i)
      CX = (zp-z(i-1))/h(i)
      DX = ((zp-z(i-1))**3-h(i)*h(i)*(zp-z(i-1)))/6.*h(i)
      AXP = -1./h(i)
      BXP = (-3.0*(z(i)-zp)**2 + h(i)*h(i))/6.*h(i)
      CXP = 1./h(i)
      DXP = (3.0*(zp-z(i-1))**2 - h(i)*h(i) )/6.*h(i)
      AXPP = 0.0
      BXPP = (z(i)-zp)/h(i)
      CXPP = 0.0
```

```
      DXPP = (zp-z(i-1))/h(i)
      S(J)   =  AX*v(i-1)  + BX*vpp(i-1)  + CX*v(i)   + DX*vpp(i)
      SP(J)  =  AXP*v(i-1) + BXP*vpp(i-1)  + CXP*v(i)  + DXP*vpp(i)
      SPP(J)= AXPP*v(i-1) + BXPP*vpp(i-1) + CXPP*v(i) + DXPP*vpp(i)
 500  CONTINUE
      RETURN
      END
      SUBROUTINE CROUT(
     I                  a , npoints, y ,
     O                  x )
      dimension ep(201),dp(201),fp(201),cp(201)
      dimension a(0:200,0:200),x(201), y(0:200)
      dimension c(201)
      nn=npoints+1
      do 95 i=0,npoints
      c( i+1 ) = y( i )
  95  continue
      dp( 1 ) = a( 0,0 )
      cp( 1 ) = c( 1 )/dp( 1 )
      do 100 i=2,nn
      ep( i )   = a( i-1,i-2 )
      fp( i-1 ) = a( i-2,i-1 )/dp(i-1)
      dp( i )   = a( i-1,i-1 ) - ep( i )*fp( i-1 )
      cp( i )   = (c( i )-ep( i )*cp(i-1))/dp( i )
 100  continue
      x( nn ) = cp( nn )
      do 200 i = nn-1,1,-1
      x( i ) = cp( i ) - fp( i )*x( i+1 )
200   continue
      return
      end
      SUBROUTINE SECDER(
     I                   Z , V , NPOINTS ,
     O                   SD )
c
      DIMENSION Z(0:200),V(0:200),SD(0:200)
c
c   DEFINE 2ND DERIVATIVE AT END POINTS OF BOUNDARY LAYER
c
      SD( 0 ) = 0.0
      SD( NPOINTS ) = 0.0
      DO 900 I = 2,NPOINTS-1
c
      DEL1 =  Z( I ) - Z( I-1 )
      DEL2 =  Z( I + 1 ) - Z( I )
c
      IF( DEL1 .LE. DEL2 ) THEN
       SLOPE = ( V(I+1)-V(I) )/( Z(I+1)-Z(I) )
       ZINT  = Z( I ) + DEL1
       VHIGH  = SLOPE * (ZINT - Z( I )) + V( I )
       VLOW  = V( I-1 )
       VMED  = V( I )
       DEL = DEL1
      ELSE
       SLOPE = ( V( I )-V( I-1 ) )/( Z(I ) - Z(I-1) )
       ZINT  = Z( I ) - DEL2
       VLOW = SLOPE * ( ZINT - Z(I-1)) + V( I-1 )
```

```
        VMED = V( I )
        VHIGH = V( I+1 )
        DEL = DEL2
      ENDIF
C
      SD( I ) = (VHIGH - 2*VMED + VLOW )/( DEL*DEL )
 900  CONTINUE
      RETURN
      END
```

```
program thetay
c
ccccccccccccccccccccccccccccccccccccccccccccccccccccccc
c                                                      c
c  The purpose of this program is to compute the       c
c  momentum thickness across the confluent region      c
c  normal to the surface of the trailing edge flap.    c
c                                                      c
ccccccccccccccccccccccccccccccccccccccccccccccccccccccc
c
      dimension theta( 7 )
      dimension vnorm(7,18),a(18),b(18),c(18),d(18),e(18),
     1           f(18),g(18),z(18),znorm(18)
      data a/ 0.00000,11.05816,10.79232,11.10773,11.03616,11.15512,
     1          11.59377,10.80650,11.09702,10.78732,11.14810,11.41552,
     2          13.09675,12.26638,12.97934,14.23173,14.08337,18.78206/
      data b/ 0.00000,11.40156,11.02176,10.91680,11.16851,11.34064,
     1          11.13865,10.97040,11.03614,11.10188,11.03596,11.57488,
     2          11.47737,12.42107,12.68506,13.77649,14.51156,18.55580/
      data c/ 0.00000,11.00718,10.94495,11.02455,11.06764,11.66765,
     1          10.80685,11.38263,10.96128,11.06053,10.95329,11.87613,
     2          11.64616,13.02145,13.04585,14.20211,14.19076,18.09000/
      data d/ 0.00000,10.88758,11.16527,11.17175,11.06920,11.19136,
     1          11.34198,11.37843,11.16228,11.24938,11.24490,12.32567,
     2          12.30503,13.27690,14.12219,14.61935,15.02811,19.24026/
      data e/ 0.00000,11.16750,10.93124,10.91649,11.07020,11.20668,
     1          11.06489,11.09676,10.92771,11.41814,11.12449,11.36487,
     2          12.53095,13.72581,13.76077,14.22396,14.94804,19.00509/
      data f/ 0.00000,10.93126,11.30647,11.43667,11.19822,11.64462,
     1          11.14037,11.14668,11.05201,11.36254,11.13729,11.52353,
     2          11.91421,12.57541,12.66935,14.04845,13.73031,17.88990/
      data g/ 0.00000,11.02123,10.85338,11.17108,10.67645,10.94792,
     1          11.23722,10.82814,11.00897,11.08196,11.59209,11.14640,
     2          11.80933,12.42074,13.29088,14.04700,14.54922,17.78331/
      data z/ 0.00,13.99,13.98,13.97,13.96,13.95,13.94,13.93,13.92,
     1          13.91,13.90,13.80,13.70,13.60,13.50,13.40,13.30,12.72/
c
c  Specify the freestream velocity (meters/second)
c
      uinf = 19.41881
      zmax = (0.50/2.54) + (13.99 - 12.52)
      npoints = 18
c
c Compute the normalized distance from the wall
c
      znorm(1) = 0.0
      do 30 k = 2,18
      znorm(k) = (0.50/2.54) + (13.99 - z(k))/zmax
 30   continue
c
      do 34 i = 1,18
      vnorm( 1,i ) = a( i )/uinf
      vnorm( 2,i ) = b( i )/uinf
      vnorm( 3,i ) = c( i )/uinf
      vnorm( 4,i ) = d( i )/uinf
      vnorm( 5,i ) = e( i )/uinf
      vnorm( 6,i ) = f( i )/uinf
```

```
      vnorm( 7,i ) = g( i )/uinf
 34   continue
c
c  Perform the integration to compute the momentum thickness
c
      do 120 i = 1,7
      sum = 0.0
      do 100 j = 2,npoints
      deltaz = znorm( j ) - znorm( j-1 )
      sum = sum + vnorm(i,j)*(1-vnorm(i,j))*deltaz
 100  continue
      theta( i ) = sum
 120  continue
      print 104,(theta(n),n=1,7)
 104  format(5x,7f9.4 )
      stop
      end
```

```
      program lift
      dimension tapuppw( 21 ) , taploww( 10 )
      dimension tapuppf( 14 ) , taplowf( 5 )
      dimension tapupps( 5 )  , taplows( 2 )
      dimension xflap1(20),cpflap1(20),xflap2(19),cpflap2(19)
      dimension xslat1(5),cpslat1(5),xslat2(7),cpslat2(7)
      dimension xwing1(21),cpwing1(21),xwing2(10),cpwing2(10)
      character ihead*10
      open(unit=1,file='wing',form='formatted',status='old')
      data tapuppw/0.0000, 0.1128, 0.4618, 0.7915, 1.1973, 1.8217,
     1            2.4319, 2.9578, 3.5486, 4.4506, 5.5030, 6.4057,
     2            7.3678, 8.2370, 9.9148,11.7881,12.7296,13.1866,
     3           13.6304,13.9826,14.3795/
      data taploww/0.1002, 0.6151, 0.8973, 1.4458, 2.0258, 3.0050,
     1            5.2701, 7.3433,10.2531,12.9509/
      data tapuppf/0.0000, 0.0541, 0.1650, 0.2266, 0.4907, 0.8160,
     1             1.1862, 1.6348, 2.0364, 2.7149, 3.2550, 3.9512,
     2             4.4727, 4.7348/
      data taplowf/0.0999, 0.1926, 0.9242, 1.8160, 3.4779/
      data tapupps/0.0000, 0.0296, 0.1403, 0.6318, 1.264/
      data taplows/0.1501, 0.5563/
c
c  Store the value of the wing chord length( inches )
c
      chord = 14.9
      delslat = 30.0
      delflap = 30.0
      aoa = 19.0
      rho = 1.1766
      v = 20.0
      q = 0.5*rho*v*v
      degrad = 3.141592654/180.
      sum = 0.0
c
c Read data from the main wing
c
       read( 1,'(A10)' )ihead
       do 40 k = 1,21
       read( 1,22)xwing1(k),cpwing1(k)
22     format(2f13.8)
40     continue
       read( 1,'(A10)' )ihead
       do 50 k = 1,10
       read( 1,22)xwing2(k),cpwing2(k)
50     continue
c
c Use the trapezoidal rule to perform the numerical integration
c over both the top and lower surfaces to get the total lift on
c the main wing.
c
      top = 0.0
      do 100 i = 1,20
      dchord = ( tapuppw( i + 1 ) - tapuppw( i ) )/chord
      top = top + ( (cpwing1(i+1) + cpwing1(i))/2 ) * dchord
 100  continue
c
      bottom = 0.0
```

```
      do 150 i = 1,9
      dchord = ( taploww( i + 1 ) - taploww( i ) )/chord
      bottom = bottom+( (cpwing2(i+1)+cpwing2(i))/2.0 ) * dchord
 150  continue
c
c Calculate the Lift Force
c
      force = ( bottom - top )*cos( aoa * degrad )
      print 501, force
  501 format( 10x, 'Lift coeff. on main wing is ',f8.5)
c
      sum = sum + force
c
      do 62 i=1,11
      read( 1,22)xbuffer,ybuffer
62    continue
c
c Read data from the flap
c
      read( 1,'(A10)' )ihead
c
      kk = 0
      do 65 k =1,15
      if( k.eq.4 )then
      read( 1,22 )xbuffer,ybuffer
      goto 65
      end if
      kk = kk + 1
      read( 1,22 )xflap1( kk ),cpflap1( kk )
65    continue
      do 66 i = 1,6
      read( 1,22 )xbuffer,ybuffer
66    continue
c
      read( 1,'(A10)' )ihead
c
      do 67 k = 1,5
      read( 1,22 )xflap2( k ),cpflap2( k )
67    continue
c
      do 68 k = 1,16
      read( 1,22 )xbuffer,ybuffer
68    continue
c
c Use the trapezoidal rule to perform the numerical integration
c over both the top and lower surfaces to get the total lift on
c the trailing edge flap.
c
c  Store the value of the flap chord length( inches )
c
      chord = 5.4
      top = 0.0
      do 101 i = 1,13
      dchord = ( tapuppf( i + 1 ) - tapuppf( i ) )/chord
      top = top + ( (cpflap1(i+1) + cpflap1(i))/2 ) * dchord
 101  continue
c
```

```
      bottom = 0.0
      do 151 i = 1,4
      dchord = ( taplowf( i + 1 ) - taplowf( i ) )/chord
      bottom = bottom+( (cpflap2(i+1)+cpflap2(i))/2.0 ) * dchord
 151  continue
c
c Calculate the Lift Force
c
      force = ( bottom - top )*cos( (delflap+aoa) * degrad )
      print 502, force
  502 format( 10x, 'Lift coeff. on flap is ',f8.5)
c
      sum = sum + force
c
c Read data from the slat
c
      read( 1,'(A10)' )ihead
c
      do 73 k = 1,5
      read( 1,22 )xslat1(k),cpslat1(k)
73    continue
c
      do 75 k = 1,16
      read( 1,22 )xbuffer,ybuffer
75    continue
c
      read( 1,'(A10)' )ihead
      do 77 k = 1,2
      read( 1,22 )xslat2(k),cpslat2(k)
77    continue
c
c Use the trapezoidal rule to perform the numerical integration
c over both the top and lower surfaces to get the total lift on
c the leading edge slat.
c
c  Store the value of the slat chord length( inches )
c
      chord = 2.6
      top = 0.0
      do 102 i = 1,4
      dchord = ( tapupps( i + 1 ) - tapupps( i ) )/chord
      top = top + ( (cpslat1(i+1) + cpslat1(i))/2 ) * dchord
 102  continue
c
      bottom = 0.0
      do 152 i = 1,1
      dchord = ( taplows( i + 1 ) - taplows( i ) )/chord
      bottom = bottom+( (cpslat2(i+1)+cpslat2(i))/2.0 ) * dchord
 152  continue
c
c Calculate the Lift Force
c
      force = ( bottom - top )*cos( (delslat-aoa) * degrad )
      print 503, force
  503 format( 10x, 'Lift coeff. on slat is ',f8.5)
c
      sum = sum + force
```

```
      print 504,sum
504   format( 10x, 'Total Lift coeff is ' ,f8.5)
      stop
      end
```

```
      PROGRAM RDWING
      c                                                               c
      ccccccccccccccccccccccccccccccccccccccccccccccccccccccccccccccccc
      c                                                               c
      c  The purpose of this program is to read the pressure          c
      c  coefficient data from the multi-element airfoil model.       c
      c  The relative chord location of the pressure orifice is       c
      c  also read in as input. Some manipulation is done to          c
      c  rearrange the order of the data.                             c
      c  A set of binary output files are created, which does         c
      c  contain the pressure coefficients and the orifice            c
      c  locations. These files are subsequently read by MATLAB       c
      c  utilities for further processing and plotting.               c
      c                                                               c
      ccccccccccccccccccccccccccccccccccccccccccccccccccccccccccccccccc
      c                                                               c
            dimension xwing1(21),cpwing1(21),xwing2(31),cpwing2(31)
            dimension xflap1(20),cpflap1(20),xflap2(19),cpflap2(19)
            dimension xslat1(5),cpslat1(5),xslat2(7),cpslat2(7)
            dimension xxx(30),yyy(30)
            character ihead*10
            open(unit=1,file='wing',form='formatted',status='old')
            open(unit=2,file='wing1',form='binary',status='old')
            open(unit=3,file='wing2',form='binary',status='old')
            open(unit=4,file='flap1',form='binary',status='old')
            open(unit=5,file='flap2',form='binary',status='old')
            open(unit=6,file='slat1',form='binary',status='old')
            open(unit=7,file='slat2',form='binary',status='old')
      ccccccccccccccccccccccccccccccccccccccccccccccccccccccccccccccccc
      c      xwing1  - array containing chord location of ports on upper
      c            surface of wing
      c      xwing2  - array containing chord location of ports on lower
      c            surface of wing
      c      cpwing1 - array containing pressure coefficients on upper
      c            surface of wing
      c      cpwing2 - array containing pressure coefficients on lower
      c            surface of wing
      c      xflap1  - array containing chord locations of ports on upper
      c            surface of flap
      c      xflap2  - array containing chord locations of ports on lower
      c            surface of flap
      c      cflap1  - array containing pressure coefficients on upper
      c            surface of flap
      c      cflap2  - array containing pressure coefficients on lower
      c            surface of flap
      c      xslat1  - array containing chord locations of ports on upper
      c            surface of flap
      c      xslat2  - array containing chord locations of ports on lower
      c            surface of flap
      c      cslat1  - array containing pressure coefficients on upper
      c            surface of flap
      c      cslat2  - array containing pressure coefficients on lower
      c            surface of flap
      c ccccccccccccccccccccccccccccccccccccccccccccccccccccccccccccccccc
            read( 1,'(A10)' )ihead
            do 40 k = 1,21
            read( 1,22)xwing1(k),cpwing1(k)
```

```
22      format(2f13.8)
40      continue
        read( 1,'(A10)' )ihead
        do 50 k = 1,10
        read( 1,22)xwing2(k),cpwing2(k)
50      continue
c
c Store data for the lower wing in reverse order
c
      do 169 k = 1,10
      xxx(11-k)=xwing2(k)
      yyy(11-k)=cpwing2(k)
169   continue
      do 190 k=1,10
      xwing2(k)=xxx(k)
      cpwing2(k)=yyy(k)
190   continue
      do 191 k=11,31
      xwing2(k)=xwing1(k-10)
      cpwing2(k)=cpwing1(k-10)
191   continue
c
      do 62 i=1,11
      read( 1,22)xbuffer,ybuffer
62    continue
c
c Read data from the flap
c
      read( 1,'(A10)' )ihead
c
      kk = 0
      do 65 k =1,15
      if( k.eq.4 )then
      read( 1,22 )xbuffer,ybuffer
      goto 65
      end if
      kk = kk + 1
      read( 1,22 )xflap1( kk ),cpflap1( kk )
65    continue
      do 66 i = 1,6
      read( 1,22 )xbuffer,ybuffer
66    continue
c
      read( 1,'(A10)' )ihead
c
      do 67 k = 1,5
      read( 1,22 )xflap2( k ),cpflap2( k )
67    continue
c
      do 68 k = 1,16
      read( 1,22 )xbuffer,ybuffer
68    continue
c
c Store data for the lower flap in reverse order
c
      do 69 k = 1,5
      xxx(6-k)=xflap2(k)
```

```
      yyy(6-k)=cpflap2(k)
69    continue
      do 90 k=1,5
      xflap2(k)=xxx(k)
      cpflap2(k)=yyy(k)
90    continue
      do 91 k=6,19
      xflap2(k)=xflap1(k-5)
      cpflap2(k)=cpflap1(k-5)
91    continue
c
c Read data from the slat
c
      read( 1,'(A10)' )ihead
c
      do 73 k = 1,5
      read( 1,22 )xslat1(k),cpslat1(k)
73    continue
c
      do 75 k = 1,16
      read( 1,22 )xbuffer,ybuffer
75    continue
c
      read( 1,'(A10)' )ihead
      do 77 k = 1,2
      read( 1,22 )xslat2(k),cpslat2(k)
77    continue
c
c Store data from the lower slat in reverse order
c
      temp=xslat2(1)
      xslat2(1)=xslat2(2)
      xslat2(2)=temp
      temp=cpslat2(1)
      cpslat2(1)=cpslat2(2)
      cpslat2(2)=temp
      do 79 k = 3,7
      xslat2( k )  = xslat1( k-2 )
      cpslat2( k ) = cpslat1( k-2 )
79    continue
c
c Write data to MATLAB files
c
      write( 2 ) xwing2
      write( 3 ) cpwing2
      write( 4 ) xflap2
      write( 5 ) cpflap2
      write( 6 ) xslat2
      write( 7 ) cpslat2
      stop
      end
```

```
      PROGRAM SKINFRC
c
ccccccccccccccccccccccccccccccccccccccccccccccccccccccccccc
c                                                           c
c The pirpose of this program is to estimate the skin       c
c friction drag coefficient on the surface of the model     c
c using an empirical equation based on the Coles Wake       c
c Law. This requires that both the momentum thickness       c
c and shape factor be calculated.                           c
c                                                           c
ccccccccccccccccccccccccccccccccccccccccccccccccccccccccccc
      dimension theta( 7 ),deltap(7),H(7),CF(7)
      dimension vnorm(7,18),a(18),b(18),c(18),d(18),e(18),
     1           f(18),g(18),z(18),znorm(18)
      data a/ 0.00000,11.05816,10.79232,11.10773,11.03616,11.15512,
     1          11.59377,10.80650,11.09702,10.78732,11.14810,11.41552,
     2          13.09675,12.26638,12.97934,14.23173,14.08337,18.78206/
      data b/ 0.00000,11.40156,11.02176,10.91680,11.16851,11.34064,
     1          11.13865,10.97040,11.03614,11.10188,11.03596,11.57488,
     2          11.47737,12.42107,12.68506,13.77649,14.51156,18.55580/
      data c/ 0.00000,11.00718,10.94495,11.02455,11.06764,11.66765,
     1          10.80685,11.38263,10.96128,11.06053,10.95329,11.87613,
     2          11.64616,13.02145,13.04585,14.20211,14.19076,18.09000/
      data d/ 0.00000,10.88758,11.16527,11.17175,11.06920,11.19136,
     1          11.34198,11.37843,11.16228,11.24938,11.24490,12.32567,
     2          12.30503,13.27690,14.12219,14.61935,15.02811,19.24026/
      data e/ 0.00000,11.16750,10.93124,10.91649,11.07020,11.20668,
     1          11.06489,11.09676,10.92771,11.41814,11.12449,11.36487,
     2          12.53095,13.72581,13.76077,14.22396,14.94804,19.00509/
      data f/ 0.00000,10.93126,11.30647,11.43667,11.19822,11.64462,
     1          11.14037,11.14668,11.05201,11.36254,11.13729,11.52353,
     2          11.91421,12.57541,12.66935,14.04845,13.73031,17.88990/
      data g/ 0.00000,11.02123,10.85338,11.17108,10.67645,10.94792,
     1          11.23722,10.82814,11.00897,11.08196,11.59209,11.14640,
     2          11.80933,12.42074,13.29088,14.04700,14.54922,17.78331/
      data z/ 0.00,13.99,13.98,13.97,13.96,13.95,13.94,13.93,13.92,
     1          13.91,13.90,13.80,13.70,13.60,13.50,13.40,13.30,12.72/
c
c  Specify the freestream velocity (meters/second)
c
      uinf = 20.0
      zmax = (0.50/2.54) + (13.99 - 12.52)
      npoints = 9
c
c Compute the normalized distance from the wall
c
      znorm(1) = 0.0
      do 30 k = 2,18
      znorm(k) = (0.50/2.54) + (13.99 - z(k))/zmax
 30   continue
c
      do 34 i = 1,18
      vnorm( 1,i ) = a( i )/uinf
      vnorm( 2,i ) = b( i )/uinf
      vnorm( 3,i ) = c( i )/uinf
      vnorm( 4,i ) = d( i )/uinf
      vnorm( 5,i ) = e( i )/uinf
```

```
      vnorm( 6,i ) = f( i )/uinf
      vnorm( 7,i ) = g( i )/uinf
 34   continue
c
c  Perform the integration to compute the momentum thickness
c
      do 120 i = 1,7
      sum = 0.0
      do 100 j = 2,npoints
      deltaz = znorm( j ) - znorm( j-1 )
      sum = sum + vnorm(i,j)*(1. - vnorm(i,j)) * deltaz
 100  continue
      theta( i ) = sum
 120  continue
c
c  Perform the integration to compute the displacement thickness
c
      do 130 i = 1,7
      sum = 0.0
      do 127 j =2,npoints
      deltaz = znorm( j ) - znorm( j-1 )
      sum = sum + ( 1. - vnorm(i,j) ) * deltaz
 127  continue
      deltap( i ) = sum
 130  continue
c
c  Compute the shape factor H
c
      do 135 i = 1,7
      H( i ) = deltap( i ) / theta( i )
 135  continue
c
c  Compute the estimate of the skin friction coefficient
c
      do 150 i = 1,7
      R = uinf * theta( i )/15.75E-06
c     CF(i)=0.058*R**0.268*(0.93 - 1.95*log( H(i) ) )**1.705
      CF(i)=(0.3*exp(-1.33*H(i)))/(log( R ))**(1.74 + 0.31)
 150  continue
c
      print 104,(CF(n),n=1,5)
 104  format(5x,5f14.10 )
      stop
      end
```

```
      program funfreq
c
ccccccccccccccccccccccccccccccccccccccccccc
c                                          c
c The purpose of this program is to read   c
c from a formatted file the power spectrum c
c data from the TSI hot-film system. This  c
c data will be written to a binary file    c
c which will read into a Matlab program.   c
c The power spectrum data will then be     c
c plotted.                                 c
c Data are read from ten records and then  c
c averaged.                                c
c                                          c
ccccccccccccccccccccccccccccccccccccccccccc
c
      dimension array1(1024),array2(1024)
      dimension ff(1024),amp(1024)
      character ihead*10
      open(unit=1,file='spec1',form='formatted',status='old')
      open(unit=2,file='spec2',form='formatted',status='old')
      open(unit=3,file='spec3',form='formatted',status='old')
      open(unit=4,file='spec4',form='formatted',status='old')
      open(unit=5,file='spec5',form='formatted',status='old')
      open(unit=6,file='spec6',form='formatted',status='old')
      open(unit=7,file='spec7',form='formatted',status='old')
      open(unit=8,file='spec8',form='formatted',status='old')
      open(unit=9,file='spec9',form='formatted',status='old')
      open(unit=10,file='spec10',form='formatted',status='old')
      open(unit=11,file='xxx',form='binary',status='old')
      open(unit=12,file='yyy',form='binary',status='old')
c
c     freqncy - the frequency of the a spectral component
c     amplt   - the power amplitude at a specific frequency
c
c Read the character header records
c
c Initalize arrays
c
      do 9 i = 1,1024
      ff( i ) = 0.0
      amp( i ) = 0.0
 9    continue
c
      nunits=10
c
      do 60 iunit=1,nunits
c
      do 10 i = 1,6
      read(iunit, '(A10)')ihead
 10   continue
c
       icount=0
       do 40 k = 1,1024
```

```
c
      read(iunit,12,iostat=iocheck,end=41)ibin,freqncy,amplt
 12   format(9x,I4,16x,E12.6,16x,E12.6)
 41   array1( k ) = freqncy
      array2( k ) = amplt
 40   continue
      do 50 j = 1,1024
      ff( j ) = ff( j ) + array1( j )
      amp( j ) = amp( j ) + array2( j )
 50   continue
 60   continue
      do 70 i = 1,1024
      ff( i ) = ff( i )/real( nunits )
      amp( i ) = amp( i )/real( nunits )
70    continue
c
100   continue
c
      xmax = -1000.0
      do 92 k = 1,1024
      if( amp(k).ge.xmax)then
      xmax=amp(k)
      index=k
      goto 92
      endif
 92   continue
      print 93,xmax,ff(index)
 93   format(10x,'The maximum amplitude', f7.3,2x,'occurred at',
     1                ' frequency',2x,f10.4)
      write(11)ff
      write(12)amp
      stop
      end
```

APPENDIX F: ALGORITHMS FOR COMPUTING SPECIFIC QUANTITIES

F.1 Determination of Lift Coefficient on Main Wing

A computer program in FORTRAN was written to compute the lift force coefficient on the main wing of a multi-element airfoil. This computation was accomplished by numerically integrating the measured surface pressure coefficients along the centerline of the main wing. Emphasis was placed on the main wing since the more notable increments in static pressure coefficients were found to occur on the this component of the three-element airfoil. The integrated force on the main wing can be resolved into components that are either perpendicular or parallel to the free stream direction and are denoted as the lift force and drag force, respectively. The chordwise position is denoted by c, whereas C is t he chord length and L is the lift force.

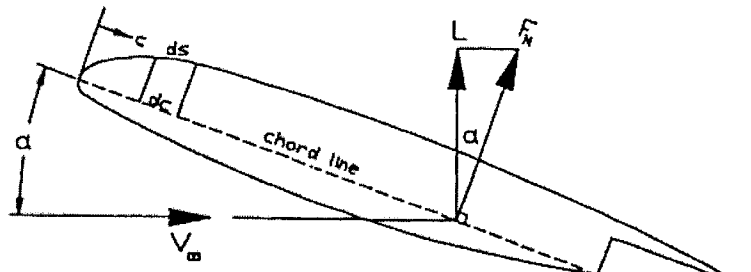

From Landman, D. 1998 – Reprinted with permission from author

The normal force is designated as F_N and acts perpendicular to the model chordline. The differential normal force is the surface static pressure multiplied by the incremental area

formed by the product of the differential chord length and a unit span length. The normal force is shown in Equation F.1-1.

$$F_N = \int P_{lower} - P_{upper} dc \qquad (F.1-1)$$

As shown in the associated drawing, the lift force can be found by resolving the normal force in the direction of the free stream direction. The equation for the lift force is shown in Equation F.1-2.

$$L = F_N \cos\alpha \qquad (F.1-2)$$

The pressure coefficient is determined by using the well-known formulation found in Equation (F.1-3).

$$C_P = \frac{P - P_\infty}{q} \qquad (F.1-3)$$

The lift coefficient is then calculated by performing the following numerical integration as is shown in Equation F.1-4.

$$C_P = \frac{L}{qS} = \frac{\cos\alpha}{C} \int_0^C (C_{P_{lower}} - C_{P_{upper}}) dc \qquad (F.1-4)$$

The numerical integration of the pressure coefficients was performed using the trapezoidal rule.

F.2 Determination of Momentum Thickness

To establish an indication of the effect of the external excitation on the flow field above the trailing-edge flap a FORTRAN program was written to perform the required numerical integration for calculation of the momentum thickness. The integration was performed by summing the products of the local incremental momentum thickness at a point in the profile and its corresponding differential distance normal to the model surface. The momentum thickness was obtained using Equation F.2-1.

$$\theta = \int_0^{\delta} \frac{u}{U_\infty}\left(1 - \frac{u}{U_\infty}\right) dz \qquad \text{(F.2-1)}$$

In the above equation the momentum thickness is designated as θ and δ is the total distance normal to the surface over which the integration was performed. The quantities u and U_∞ are the local flow and freestream velocities, respectively. The normalized differential distance from the surface is dz. The computer algorithm that was employed in the analysis is shown in Equation F.2-2.

$$\theta = \sum_{i=1}^{N} \frac{u_i}{U\infty} \times \left(1 - \frac{u_i}{U\infty}\right) \times \Delta z \qquad \text{(F.2-2)}$$

In this equation N is the total number of data points used in the integration.

F.3 Computation of Cross-Correlation Coefficient

In this experiment, the spectral analysis was performed by the TSI® Data Acquisition Program (DAP) software combined with the IFA (Intelligent Flow Analyzer) 100 anemometer and IFA 200 digitizer. In performing the spectral analysis two consecutive blocks of time-history data, each made up of a sequence of N real-valued data points, were combined to form a sequence of complex numbers using Equations F.3-1 to F.3-3.

$$x_1 = v_0, v_1, v_2 \ldots v_{N-1} \qquad \text{(F.3-1)}$$

$$x_2 = v_N, v_{N+1}, v_{N+2} \ldots v_{2N-1} \qquad \text{(F.3-2)}$$

$$x(n) = x_1(n) + jx_2(n) \quad \text{where} \quad n = 0,1,2 \ldots N-1 \qquad \text{(F.3-3)}$$

Because of the linear property of Fourier Transforms, the transform of x in Equation (F.3-3) is found from Equation F.3-4.

$$X(m) = X_1(m) + jX_2(m) \qquad \text{where } m = 0,1,2 \ldots 2N-1 \qquad \text{(F.3-4)}$$

However, because this analysis was predicated on the supposition that the time-history data were periodic, the frequency spectrum would also be periodic with a period corresponding to 2N or 2048 spectral samples. Therefore, the Equation F.3-5 is likewise true. The asterisk denotes the complex conjugate.

$$X(m) = X^*(2N-m) \qquad \text{(F.3-5)}$$

The first block is declared real, whereas the second adjoining block is considered imaginary.

As a first step, the discrete Fourier Transform is computed using the sequence of digitized hot-wire data. Equation F.3-6 shows how this was computed.

$$G(n) = \sum_{k=0}^{N-1} g(k) e^{\frac{-2\pi jk}{N}} \quad n = 0,1,..., N-1 \qquad (F.3-6)$$

The cross-correlation was then computed by convolving the Fourier transforms from both sensors using Equation 5.7-7.

$$H(n) = G(n) * F(n) \qquad (5.7-7)$$

PERMISSION TO PUBLISH REPRINTS

American Institute of Aeronautics and Astronautics

14 June 2002

Mr. Ira J. Walker
4 Newgate Village Road
Hampton, VA 23666

Dear Mr. Walker:

AIAA is pleased to grant permission for you to reprint the following figures in your Ph.D. dissertation for Old Dominion University:

- Bhattacharjee, S., et al., "Modification of Vortex Interactions in a Reattaching Separated Flow," *AIAA Journal*, Vol. 24, no. 4, 1986, (Figs. 1, 2a, 2b, 2c, 5, 6, 10).
- Smith, A. M. O., "High-Lift Aerodynamics," *Journal of Aircraft*, Vol. 12, No. 6, 1975 (Figs. 35, 38).
- Mack, M. D., and McMasters, J. H., "High Reynolds Number Testing in Support of Transport Airplane Development," AIAA Paper 92-3982, 1992 (Figs. 5, 13).
- Nakayama, A., et al., "Experimental Investigation of Flowfield About a Multielement Airfoil," *AIAA Journal*, Vol. 28, no. 1, 1990 (Figs. 10, 12).

Appropriate credit should be given to AIAA, either on the page containing the reprinted figures or in the figure legends (e.g., "Originally published in 'Paper Title,' Author, Paper number or journal, etc. Copyright © 19xx by the American Institute of Aeronautics and Astronautics, Inc. Reprinted with permission.").

Thank you for your inquiry.

Sincerely yours,

Norma Brennan

Norma Brennan
AIAA Publications

1801 Alexander Bell Drive • Suite 500 • Reston, VA 20191–4344
Phone 703/264-7500 • FAX 703/264-7551 • Web Site: http://www.aiaa.org

Permissions Department
Two Penn Plaza
New York NY 10121
Phone 212 904 2574
Fax 212 904 6285

McGraw-Hill Education

PERMISSION LICENSE: PRINT REPUBLICATION

Request ID/Invoice Number: IRA21424

Date: June 06, 2002

To: Ira Walker
Old Dominion University
Norfolk, VA 23529
"Licensee"

McGraw-Hill Material

Author: Frank White
Title: Viscous Fluid Flow
Description of material: Figure 4-5(a) and (b) on page 232 and Figure 6-4 on page 400, only.

Fee: $0.00

Licensee Work:

Author: Ira Walker
Title: An Experimental Study of Flow-Control Techniques on a Multi-Element Airfoil (PhD dissertation)
Publisher: Old Dominion University
Publication Date: 2002
Distribution Territory: USA
Languages: English

Permission for the use described above is granted under the following conditions:

1. The permission fee of $0.00 must be received by The McGraw-Hill Companies on or before, and MUST BE ACCOMPANIED BY A SIGNED COPY OF THIS AGREEMENT. A check should be made payable to The McGraw-Hill Companies, and sent to The Permissions Department, The McGraw-Hill

Companies, Two Penn Plaza, NY, NY 10121-2298. Please include the invoice number indicated at the top of this form on your check.

2. No adaptations, deletions, or changes will be made in the material without the prior written consent of The McGraw-Hill Companies.

3. This permission is non-exclusive, non-transferable, and limited to the use specified herein. The McGraw-Hill Companies expressly reserves all rights in this material.

4. A credit line must be printed on the first page on which the material appears. This credit must include the author, title, copyright date, and publisher, and indicate that the material is reproduced with permission of The McGraw-Hill Companies.

5. This permission does not allow the use of any material, including but not limited to photographs, charts, and other illustrations, which appears in a McGraw-Hill Companies' work copyrighted in or credited to the name of any person or entity other than The McGraw-Hill Companies. Should you desire permission to use such material, you must seek permission directly from the owner of that material, and if you use such material you agree to indemnify The McGraw-Hill Companies against any claim from the owners of that material.

Please sign both copies and return one with payment to the McGraw-Hill Permissions Department, 2 Penn Plaza, 9th Floor, New York, NY 10121.

For McGraw-Hill:

_____

Nicole Rajnauth
Permissions Department
McGraw-Hill Education

For Licensee:

Name_____

Title _____

VITA

Ira James Walker
Lecturer, Department of Mathematics
Hampton University
Queen and Tyler Streets
Hampton, VA 23668

Office: (757) 727-5550 E-mail: ira.walker@hamptonu.edu
Rank: Lecturer (full-time) Discipline: Mathematics

Education and Degrees

Present Ph.D candidate in Aerospace Engineering
Old Dominion University
1980 M.S. Physics
Old Dominion University
1974 B.S. in General Science
Villanova University

RESEARCH SPECIALTIES:

Aerodynamic research was conducted in the Old Dominion University wind tunnel facility and included experiments in the field of fluid mechanics as it pertains to the study of high-lift airfoil characteristics. Various types of instrumentation were used to obtain measurements of flow field quantities and static surface pressures. Different techniques were used to control the flow field surrounding a scaled wing model to improve the aerodynamic lift.

Wind tunnel research was done as a project engineer in support of the High Speed Aerodynamics Division at the NASA Langley Research Center in Hampton Virginia. Experiments were conducted in the supersonic facility on a variety of test articles to ascertain the aerodynamic characteristics of various aircraft configurations. Responsibilities included the supervision of experiments and the evaluation and documentation of test results.

Technical support was also provided to the NASA/LaRC Atmospheric Sciences Division in the development of empirical models and data analysis software for the processing of satellite imagery data.

Nimbus 7 satellite data were reduced to develop empirical models to estimate the amount of emitted heat flux from satellite-viewed targets on the Earth-Atmospheric system. Work was provided in the design, implementation and documentation of large-scale computer application programs for the analysis and management of remotely-sensed data to estimate the net radiation budget of the Earth-Atmospheric system.